

Finite-ranged interactions and multiband effects in quantum point contacts

A functional renormalization group study

Lukas Ralf Weidinger



Munich 2020

Finite-ranged interactions and multiband effects in quantum point contacts

A functional renormalization group study

Lukas Ralf Weidinger

A dissertation submitted
to the Faculty of Physics at the
Ludwig-Maximilians-Universität München
for the degree of
DOCTOR RERUM NATURALIUM



Munich, December 15, 2020

First referee: Prof. Dr. Jan von Delft
Second referee: Prof. Dr. Lode Pollet
Day of submission: December 15, 2020
Day of the oral examination: February 25, 2021

Zusammenfassung

(Summary in German)

Seit ihrer Entdeckung im Jahre 1996, hat die 0.7-Anomalie in Quantenpunktkontakten (QPCs) große experimentelle und theoretische Aufmerksamkeit erregt. Dabei hat sich herausgestellt, dass die 0.7-Anomalie, neben ihrer zunächst entdeckten Ausprägung als schulterähnliche Struktur im Leitwert bei endlicher Temperatur, praktisch auch in allen anderen QPC Observablen, wie z.B. Thermopower, Schrottrauschen, etc. zu beobachten ist. Die damit assoziierten anomalen Effekte werden mittlerweile zusammengefasst als 0.7-Physik bezeichnet. Trotz ihrer umfangreichen experimentellen Untersuchung steht die Ursache der 0.7-Anomalie nach wie vor zur Diskussion. Es existieren zahlreiche theoretische Erklärungsversuche, denen unterschiedliche Mechanismen zu Grunde liegen und die sich zum Teil auf unterschiedliche Aspekte der 0.7-Physik konzentrieren. In 2013 hat die von Delft Gruppe die sog. van-Hove ridge Erklärung vorgestellt. Diese erlaubt eine intuitive Erklärung der 0.7-Physik, basierend auf den Eigenschaften der nichtwechselwirkenden lokalen Zustandsdichte (LDOS), welche durch die Geometrie des QPCs festgelegt ist. Zur Untermauerung und dem weiteren Ausbau dieser Idee wurde die funktionale Renormalisierungsgruppe (fRG) verwendet, um zahlreiche QPC Observablen zu berechnen. Diesen Berechnungen wurde ein mikroskopisches Model, bestehend aus einem Hüpfterm, einer QPC Barriere und einem Onsite Wechselwirkungsterm zu Grunde gelegt. Wichtige 0.7-Aspekte, wie z.B. die asymmetrische Magnetfeldabhängigkeit des Leitwerts, wurden mittels dieser Berechnungen untersucht. Nichtsdestotrotz konnte das Markenzeichen der 0.7-Anomalie, nämlich eine ausgeprägte Schulter im Leitwert bei endlicher Temperatur, bislang nicht reproduziert werden.

In dieser Arbeit untersuchen wir QPC Modelle, die anstelle reiner Onsite Wechselwirkungen auch Wechselwirkungen mit endlicher Reichweite enthalten. Dies ist besonders interessant, da es die Zahl der möglichen Wechselwirkungsprozesse drastisch erhöht, und daher womöglich das fehlende Bindeglied darstellt, um die charakteristische 0.7-Schulter im Leitwert aus einem mikroskopischen Model zu erhalten. Neben der unmittelbaren Anwendung im Rahmen von Standard QPCs, stellt die Berücksichtigung von Wechselwirkungen mit endlicher Reichweite auch einen wichtigen Schritt zur Behandlung von längeren QPCs und dem Übergang zu Quantendrähten dar. Für diese ausgedehnteren Systeme ist die endliche Reichweite der Wechselwirkung, wegen der reduzierten Abschirmung in Bereichen von niedriger Elektronendichte, besonders relevant.

Zur Untersuchung endlicher Wechselwirkungsreichweiten erweitern wir die existierende fRG Approximationsmethode der gekoppelte Leiter (CLA) durch eine Ausweitung des räumlichen Feedbacks zwischen unterschiedlichen fRG Kanälen. In einer Reihe von Publikationen wenden wir diese neue, erweiterte CLA Methode (eCLA) in Implementationen von wachsender Komplexität auf QPC- und Quantenpunktmodelle (QD Modelle) an. Den Höhepunkt dieser Arbeiten bildet die semi-dynamische Behandlung von Wechselwirkungen endlicher Reichweite in QPCs. Trotz Problemen unserer Methode bezüglich der Verletzung von Ward Identitäten haben wir vielversprechende Anzeichen dafür gefunden, dass eine endliche Wechselwirkungsreichweite – vergleichbar mit der charakteristischen QPC Länge – ein Schlüsselbestandteil einer ausgeprägten 0.7-Schulter im Leitwert sein könnte.

Neben der Behandlung von QPCs mit endlicher Wechselwirkungsreichweite haben wir unsere verbesserte eCLA Methode auch auf einige weitere Problemstellungen angewendet, von denen zwei besonders erwähnenswert sind. (i) Wir haben bemerkt, dass die erweiterte Rückfüt-

terung zwischen den fRG Kanälen den fRG Fluss stabilisiert und dadurch die Untersuchung von physikalischen Parameterbereichen ermöglicht, die mit vorhergehenden fRG Methoden nicht zugänglich waren. So waren wir beispielsweise in der Lage den Leitwert eines Quantenpunkts zu berechnen, der nur einige wenige Elektronen nahe dem chemischen Potential enthält. (ii) Die Fähigkeit Wechselwirkungen mit endlicher Reichweite zu behandeln ermöglicht es auch (mittels einer geeigneten Abbildung) QPCs mit mehreren wechselwirkenden Bändern zu behandeln. Wir nutzen dies zur Untersuchung des 0.7-Analogs, der bei großem externen Magnetfeld am Schnittpunkt von Subbändern unterschiedlicher Spinspezies auftritt. Anhand unserer fRG Berechnungen waren wir in der Lage die Magnetfeldabhängigkeit des Analogs zu reproduzieren und konnten, darauf aufbauend, die auftretende Formasymmetrie des Leitwerts – je nachdem ob man sich dem Leitwert von größeren oder kleineren Magnetfeldern nähert – mittels eines intuitiven Hartree Arguments erklären.

Zusätzlich zu unseren eCLA Arbeiten haben wir mit der einfacheren CLA Vorgänger-methode eindimensionale ungeordnete Systeme betrachtet und Anzeichen eines möglichen Vielteilchenlokalisierungsübergangs (MBL-Übergangs) untersucht.

Abstract

(Abstract in English)

Since its discovery in 1996, the 0.7-anomaly in quantum point contacts (QPCs) has drawn a lot of experimental and theoretical attention. Initially found as the development of a shoulder-like structure in the conductance with increasing temperature, it soon became clear that virtually all QPC observables like thermal power, shot-noise, etc., show anomalous behavior in the 0.7-region, constituting a whole set of phenomena collectively known as 0.7-physics. Although experimentally well established, the origin of the 0.7-anomaly is still under debate. There exist numerous theoretical explanation attempts, evoking different mechanisms and partially focusing on different aspects of the 0.7-physics. In 2013, the von Delft group presented the so called van-Hove ridge explanation, which provides an intuitive explanation of the 0.7-physics, tracing its root back to the properties of the non-interacting local density of states (LDOS) which is defined by the geometry of the QPC. To develop and corroborate this explanation, the functional renormalization group (fRG) was used to compute various QPC observables starting from a microscopic one-dimensional model comprised of hopping term, QPC barrier and onsite interaction term. Important 0.7-features like the asymmetric magnetic field dependence of the conductance could be studied using those calculations. However, the trademark feature of the 0.7-anomaly – the pronounced shoulder in the finite temperature conductance had not yet been reproduced.

In this thesis, we investigate QPC models that in addition to onsite interactions also include a finite interaction range. This is an interesting endeavor, since it increases the number of interaction processes tremendously, possibly contributing the final step to reproduce the trademark 0.7-shoulder from a microscopic model. Besides this immediate application to standard QPCs, it also constitutes an important step towards the treatment of longer QPCs and the transition to quantum wires. For these longer systems, the finite-ranged character of the interactions is especially significant due to reduced screening in the extended spatial regions of low electron density.

In order to achieve the goal of treating finite interaction ranges, we extend a previously used coupled ladder fRG approximation (CLA) scheme, by extending the spatial feedback between different fRG channels. In a series of publications, we apply this new extended CLA (eCLA) scheme in rising levels of sophistication to QPC and quantum dot (QD) models, culminating in a semi-dynamic treatment of finite-ranged interactions in QPCs. Despite methodological problems arising from the violation of Ward identities, we indeed find promising evidence that a finite interaction range, comparable to the characteristic QPC length, is a key ingredient in obtaining a pronounced 0.7-shoulder in the conductance.

Alongside this main application, we also applied our improved eCLA method to various other problems, of which two are especially mention-worthy. (i) We noticed that the extended feedback between fRG channels stabilizes the fRG flow, enabling the study of physical parameter regimes that were not accessible with the previously existing fRG methods. As a prime example, we were able to calculate the conductance of a quantum dot, containing only a few electrons close to the chemical potential. (ii) Being able to treat finite-ranged interactions also enables us (via a suitable mapping) to treat QPC models with multiple interacting bands. We use this to study the 0.7-analog occurring at the intersection of different subbands with opposite spin at large magnetic fields. Using eCLA calculations, we could reproduce the magnetic field dependence of the analog, and devise an intuitive Hartree explanation that

explains the occurring shape-asymmetry depending on whether the 0.7-analog is approached from lower or higher magnetic fields.

Additionally, we investigated one-dimensional disordered systems with the previous CLA method and searched for signs of a possible many-body localization (MBL) transition.

Publications

This dissertation is based on the following journal articles, listed in chronological order:

- P1** *Functional renormalization group approach for inhomogeneous one-dimensional Fermi systems with finite-ranged interactions*
Lukas Weidinger, Florian Bauer, and Jan von Delft
Sec. 3.2 / [arXiv:1609.07423](#) [Phys. Rev. B 95, 035122 \(2017\)](#)
- P2** *Functional renormalization group treatment of the 0.7 analog in quantum point contacts*
Lukas Weidinger, Christian Schmauder, Dennis Schimmel, and Jan von Delft
Sec. 4.2 / [arXiv:1805.06311](#) [Phys. Rev. B 98, 115112 \(2018\)](#)
- P3** *Keldysh Functional Renormalization Group Treatment of Finite-Ranged Interactions in Quantum Point Contacts*
Lukas Weidinger and Jan von Delft
Sec. 5.2 / [arXiv:1912.02700](#)

Acknowledgements

First and foremost, I would like to thank my supervisor Jan von Delft for the opportunity to work with him on a very interesting topic and his great support and guidance over the past several years. I have had the great pleasure of getting to know Jan since the days of my master thesis. Over the course of the past 6 years, he has always had an open door for discussions and has never failed to gently nudge me in the right directions. The completion of this thesis had been delayed due to the arrival of my wonderful daughter Sia and the severe illness of my wife. I sincerely thank Jan for his understanding and his unwavering support in this most challenging time of my life. His great patience and encouragement were monumental in helping me finish this thesis.

I would also like to thank Dennis Schimmel for being my Keldysh and fRG guide, as well as the best office colleague I could have asked for. In countless discussions, he not only helped me with the work done in this thesis, but also shared his deep knowledge of multiple other areas in physics. His great sense of humor and collegiality “Mensa?” always brought a smile to our faces.

Furthermore, I thank Oleg Yevtushenko for working together with me on the disorder investigation. Oleg’s insight and encouragement always got us forward when we were stuck. In this context, I also thank Boris Altshuler for several very useful discussions during his visit to Munich.

I also thank Florian Bauer who helped me during my master thesis and worked together with Jan and me on my first publication.

Moreover, I thank the students who entrusted me to participate in the supervision of their thesis, namely Philipp Rosenberger, Sören Arlt, Christian Schmauder and Andreas Tsevas.

Special thanks goes to my colleagues and fellow PhD students Dima Pimenov, Sebastian Huber, Fabian Kugler, Elias Walter, Bin-Bin Chen, Jheng Wei Li, Katharina Stadler, Andreas Gleis and Julian Thöniss for countless discussions, shared laughter and a great atmosphere in our group.

Lastly, I would like to express my profound gratitude to my family without whom I could never have achieved any of this. My parents, Jutta and Harald, who always supported me throughout my entire life. My amazing wife Sano who has been my biggest inspiration in the last several years and helped me in every way possible to complete this thesis despite her chronic illness. And very specially, our beautiful daughter Sia, who adds the sunshine to our lives.

Contents

Zusammenfassung (Summary in German)	i
Abstract (Abstract in English)	iii
Publications	v
Acknowledgements	vii
Introduction	1
1 Quantum Point Contacts	5
1.1 Physical realizations of QPCs	5
1.1.1 Layered semiconductors	5
1.1.2 Atomic sized break junctions in metals	7
1.1.3 Graphene stripes, gated graphene, and carbon nanotubes	8
1.1.4 Grown Nanowires	11
1.1.5 Cold atoms in optical lattices	11
1.2 Phenomenology of QPCs	13
1.2.1 Conductance quantization	13
1.2.2 Special features of the lowest subband: The 0.7 anomaly	15
1.2.3 Effects involving several subbands: The 0.7 analog	18
1.2.4 Extending the physical setup: Inclusion of spin-orbit interactions	19
1.3 Theoretical explanations beyond the non-interacting model	22
2 Method	27
2.1 Definitions and preliminaries	27
2.1.1 Fourier convention	27
2.1.2 Structure of the Hamiltonian	28
2.1.3 Heisenberg operators	29
2.1.4 Expectation values	29
2.1.5 Keldysh conventions	30
2.1.6 Structure of the bare vertex	31
2.1.7 Definition of Green's functions	32
2.1.8 Compact notation for integration and sums	32
2.1.9 Generating functions and definition of one particle irreducible vertices	33
2.1.10 Time translational invariance	34
2.1.11 Structure of one-particle objects in Keldysh space	35
2.1.12 Form of the bare propagator	35
2.1.13 Equal time in Keldysh formalism	37
2.1.14 A brief look at units	39
2.2 Properties of Green's and vertex functions	39
2.2.1 Dyson equation	39
2.2.2 Permutation of particles	40
2.2.3 Complex conjugation	40

2.2.4	Time reversal	41
2.2.5	Fluctuation-dissipation theorems	44
2.2.6	Causality and related analytic properties in the Keldysh formalism	46
2.2.7	Connection Matsubara - Keldysh formalism	46
2.3	General fRG equations	47
2.3.1	fRG flow equations	47
2.3.2	Choice of flow parameters and initial conditions	48
2.4	Extended Coupled Ladder Approximation	50
2.4.1	Channel decomposition	50
2.4.2	Spin structure	55
2.4.3	Spatial structure	56
2.4.4	Matsubara formulation of the eCLA	59
2.4.5	Keldysh formulation of the eCLA	65
3	Extended Coupled Ladder Approximation in the Matsubara formalism	77
3.1	Overview	77
3.2	Publication: <i>Functional renormalization group approach for inhomogeneous one-dimensional Fermi systems with finite-ranged interactions</i>	79
4	0.7-analog in quantum point contacts	101
4.1	Overview	101
4.2	Publication: <i>Functional renormalization group treatment of the 0.7 analog in quantum point contacts</i>	102
5	Keldysh fRG treatment of finite-ranged interactions in quantum point contacts	111
5.1	Overview	111
5.2	Publication: <i>Keldysh Functional Renormalization Group Treatment of Finite-Ranged Interactions in Quantum Point Contacts</i>	112
5.3	A technical comment	138
6	Application of Keldysh fRG to disordered systems	141
6.1	Setup	141
6.2	Choice of parameters	142
6.3	Data acquisition	143
6.4	Data analysis	144
6.4.1	Quasiparticle decay rate close to the chemical potential	144
6.4.2	Analysis of DOS and LDOS peaks	148
6.5	Conclusion of the disorder study	149
7	Conclusion and Outlook	151
A	Appendix	153
A.1	The Keldysh vertex bubbles at the feedback frequencies	153
A.2	Dependent channel components	154
A.2.1	Matsubara	154
A.2.2	Keldysh	154
A.3	Flow equations for the Keldysh self-energy and the b -components of the vertex	155
A.4	Consistency check of symmetries with flow equations	160
A.4.1	Permutation of particles	160
A.4.2	Complex conjugation	161

A.4.3 Time reversal	162
A.4.4 FDTs	163
A.5 Ladder resumable flow	167
Bibliography	175

Introduction

General motivation

Since several decades, our daily life is unimaginable without semiconductor devices on micrometer scale and below. The size of engineered structures has continuously decreased in the last decades, following an exponential trend which results in the famous Moore's law [Moo65]. The number of transistors within dense integrated circuits doubles roughly every 2 years. However, since the golden days of quantum mechanics in the 1920s, it has been clear that there is a hard boundary for the development of "classical" devices. As soon as the sample dimensions reach the scale of the electronic Fermi-length, quantum effects will dominate the behavior. This is a curse and a blessing at the same time: Although scalability of classical transistors ends, the development of new devices, using their very quantum nature to their advantage has begun. The most anticipated work in this direction would certainly be the realization of highly scalable quantum computers: Up-to now, working implementations of quantum computers were mostly based on systems of trapped ions or macroscopic quantum effects, like superconductivity in Josephson junctions [NM19]. Although stacking of these structures might be possible in the future, nano-fabrication now makes also another setup possible: Electrons confined in artificially manufactured nanostructures could be used as tunable quantum system, suitable for computations [LD98].

In order to develop any of those kinds of systems, a thorough understanding of the effects arising from the interplay of sample geometry and single- as well as multiple-quantum mechanical effects is required. In this work we will focus on the simplest kind of samples imaginable that exhibit quantum effects: A short, point like confinement, the quantum point contact (QPC), between two mesoscopic leads. Already this structurally very simple system offers plenty of experimental phenomenons, in particular the infamous 0.7-anomaly, and poses an immense challenge for theoretical description, being subjected to debate until the present day [Mic11, BKF⁺12, MHW02, RM06, IZ07, Mat04, Rei05, SMS08, AH09, GUJB09, LMS⁺09, ILK⁺13, BHS⁺13].

Apart from naturally arising in bigger quantum devices, QPCs also have found a broad range of applications by themselves, utilizing their various useful properties. These applications include the use as charge detectors [EHG⁺03, FSP⁺93, EHW⁺04, PJT⁺05], fully ballistic field-effect transistors (FETs) [GNC⁺10], and spin polarizers in the context of spin-engineering [YKT⁺18].

Goal and scope of the thesis

The main goal of this thesis is to investigate the role that interactions with finite spatial range play within the physics of QPCs, in particular the 0.7-anomaly. In previous works of our group [BHS⁺13, BHvD14, SBvD17], it was shown that models with short-ranged interactions are sufficient to reproduce important properties of the 0.7-physics, like the magnetic field dependence of the conductance. However, the trademark feature of the 0.7-anomaly, namely the development of a pronounced shoulder at conductance $G = 0.7G_Q$ with increasing temperature could not yet be reproduced. Here and in the following, $G_Q = 2e^2/h$ denotes the QPC conductance quantum. Including a finite-interaction range substantially increases

the possible interaction processes, which is especially important at finite temperatures. We will show evidence that this is an important ingredient that was missing to obtain the finite temperature conductance behavior: A more pronounced shoulder develops when the interaction range is comparable to the characteristic QPC length.

Apart from this direct consequence on the form of the 0.7-shoulder in the conductance of (shorter) QPCs, the inclusion of finite-ranged interactions is also especially important when investigating the transition of a QPC to a longer quantum wire. This transition constitutes a whole project on its own that we do not undertake in this thesis, however, we consider our work an important stepping stone for this endeavor. For a long QPC or a quantum wire, the assumption of effectively short-ranged interactions due to screening processes is especially bad due to the large extent of the spatial region with low Fermi energy. This transition is particularly interesting in the context of investigating a possible occurrence of spontaneous spin polarization within QPCs. Recent experiments [YKT⁺18], allowing the direct measurement of the spin polarization, have shown indications that while shorter QPCs are unpolarized, longer QPCs exhibit spontaneous polarization. For short QPCs this finding is consistent with [SBvD17], where it was shown that for short QPCs the spin polarization is only slowly fluctuating on the typical QPC time scales. Increasing the length of the QPC might lead to the development of a true spontaneous spin polarization. Understanding this development of spontaneous spin polarization in longer QPCs and its relation to the 0.7-physics could settle a discussion on the origin of the 0.7-anomaly that has been going on for decades.

In order to achieve our goal of treating finite-ranged interactions in QPCs we extended the fRG treatment of previous works [BHS⁺13, SBvD17], leading to the development of a scheme we call “extended coupled ladder approximation” (eCLA). Besides from being able to treat finite-ranged interactions, this new scheme also exhibits intrinsic improvement over the previous CLA scheme. Due to the extended feedback between different vertex channels, the fRG flow is more stable, which enables the treatment of larger physical parameter regimes. In particular, we were able to treat a quantum dot (QD) containing only a few electrons close to the chemical potential, see Sec. 3.2. This problem was not accessible via fRG before, see discussion in [HBS⁺15]. Another interesting setup, which we are able to treat with our eCLA method, is a multiband model, including the first few subbands of a QPC. We were able to reproduce the experimental magnetic field dependence of a 0.7-analog occurring for large magnetic fields at the intersection of subbands with different spin. In particular, our calculations also yielded an asymmetry occurring in the experimental magnetic field dependence, depending on whether the analog is approached from higher or lower fields. Guided by our fRG calculations, we could explain this asymmetry intuitively using a simple Hartree argument. Our eCLA method has been also noticed and used successfully by other groups, e.g. the groups of Volker Meden in Aachen and Christoph Karrasch in Berlin. In [MSMK18] they use the eCLA method for the detection of phases in one-dimensional Fermi systems.

This thesis is structured as follows. In Chapter 1, we give a brief introduction to quantum point contacts, discussing the basic setup, different physical implementations, the basic phenomenology as well as theoretical explanations for the occurring phenomena. In Chapter 2, we describe the necessary fRG machinery to treat models with finite-ranged interactions. In particular, we elaborate on the development of the eCLA method. The following three Chapters contain the publications written within this PhD-project, namely Chapter 3.2 on the eCLA in the Matsubara formalism and its static implementation and application to QPCs and QDs, Chapter 4.2 on the 0.7-analog, Chapter 5.2 on the eCLA in the Keldysh formalism and its semi-dynamic implementation and application to a QPC. The last Chapter 6 of this thesis is devoted to an excursion into disordered systems. Concretely, we investigate the

applicability of Keldysh fRG to treat an interacting one-dimensional disordered chain model. Our focus lies here on detecting a possible many body localization (MBL) transition predicted in [BAA06] to occur when temperature is varied. This chapter has not the intention of being a comprehensive study but rather investigates whether Keldysh fRG is applicable at all to this type of system. Furthermore, since the work in this chapter was done in large parts *before* the final Keldysh version of the eCLA was ready, we use in this whole chapter the simpler CLA scheme, developed by Schimmel et al. in [SBvD17, Sch17].

1 Quantum Point Contacts

The main objects of interest in this thesis (apart from a brief excursions into quantum dots in Sec. 3.2 and disordered systems in Sec. 6) will be quantum point contacts. This first chapter gives a brief summary over the most important features of this physical system and consists of three parts. The first part in Sec. 1.1 discusses physical realizations of QPCs. After discussing the standard semiconductor QPC implementation in Sec. 1.1.1 which has been around since the 80's, we give an overview over further implementations Sec. 1.1.2 - Sec. 1.1.5, e.g. in the context of cold atoms, which only arose more recently. In the second part, Sec. 1.2, we discuss the basic phenomenology of QPCs, in particular conductance quantization Sec. 1.2.1, the 0.7-anomaly (Sec. 1.2.2) and 0.7-analog (Sec. 1.2.3) as well as more complicated systems involving spin-orbit interactions. Explanations for non-interacting phenomena, like e.g. the quantization of the conductance are directly given within this section. Finally, the last part of this chapter is dedicated for the discussion of theoretical explanation attempts of QPC phenomena beyond the non-interacting model.

1.1 Physical realizations of QPCs

In this subsection, we want to take a look at physical realizations of QPCs occurring in experiments. Since their first implementation in 2DEGs of layered semiconductors [vWvHB⁺88], there has been an increasing number of systems that realize QPCs. Here we want to briefly present the most important ones, without claim of completeness.

1.1.1 Layered semiconductors

Historically, the first realization of a QPC was implemented by Van Wees et al. in 1988 [vWvHB⁺88]. The idea of their method is still the standard method to realize QPCs: A stacked semiconductor structure is used to create a two-dimensional electron gas (2DEG) at the boundary of two different layers, e.g. GaAs-AlGaAs [SDG⁺79]. By attaching electrodes (“gates”) on the top of the sample (see Fig. 1.1(a)) one can additionally create a potential landscape within this 2DEG. In case of the QPC, this is simply a narrow constriction, which in [vWvHB⁺88] was implemented via a so called split-gate, i.e. a electrode with a very fine slit separating the source and drain regions of the sample. In more recent experiments [ILK⁺13], the usage of multiple gates enables a very flexible adjustment of the form of the constriction, see Fig. 1.1(b). The negative charging of the gates depletes the 2DEG beneath them and induces a constriction with a saddle-like potential in the 2DEG, see Fig. 1.2(a). If now a voltage bias is applied between source and drain, electrons will flow through this constriction, with a current depending on how “open” the potential is. While one would classically expect a smooth conductance $G = \frac{dI}{dV}$, the quantum nature of the system leads to a quantization of the transversal confinement. Assuming this confinement to be parabolic, one obtains discrete energy levels $n = 1, 2, \dots$ with a spacing set by the curvature in y -direction, indicated in Fig. 1.2(a). These discrete energy levels lead to a quantization of the conductance: Whenever one of them crosses the chemical potential μ , another conductance channel opens up. This effect is the hallmark of reaching the quantum domain, and can be understood in a non-interacting quantum mechanical picture [Lan57]. Additionally to this quantization

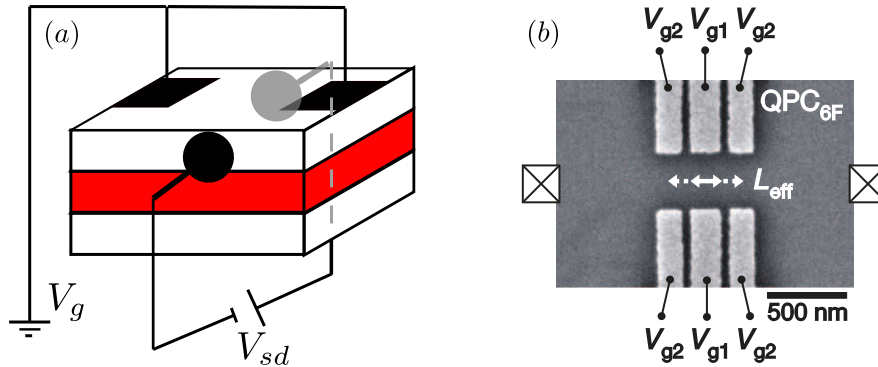


Figure 1.1 (a) Schematics of an experimental implementation of a layered semiconductor QPC. The 2DEG is depicted in red, the electrodes (gates on the top, source-drain electrodes on the side) in black. (b) electron microscope picture of the surface of a QPC, reproduced from [ILK⁺13]. The device here has three pairs of attached gates, enabling the tuning of the effective QPC length.

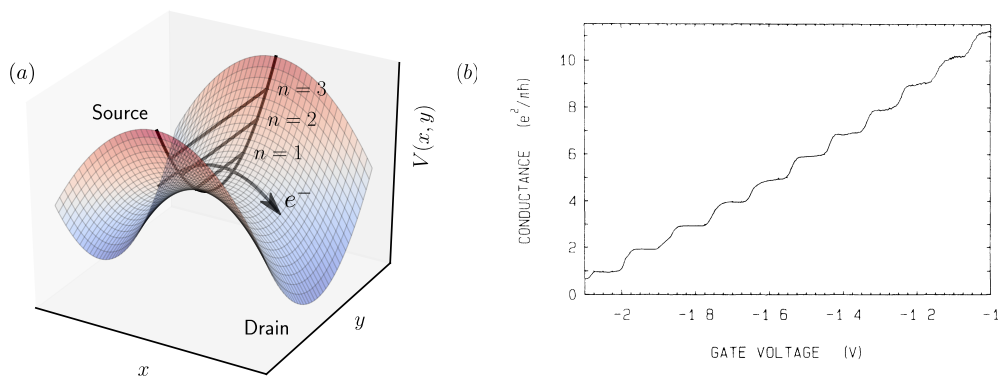


Figure 1.2 (a) Illustration of the parabolic saddlepoint potential $V(x, y)$ in the center of the QPC with positive y -curvature and negative x -curvature. The horizontal lines indicate the transversal energy levels $n = 1, 2, \dots$ in the center of the QPC. (b) First measurement of a quantized QPC conductance as function of gate voltage by Van Wees et al., reproduced from [vWvHB⁺88].

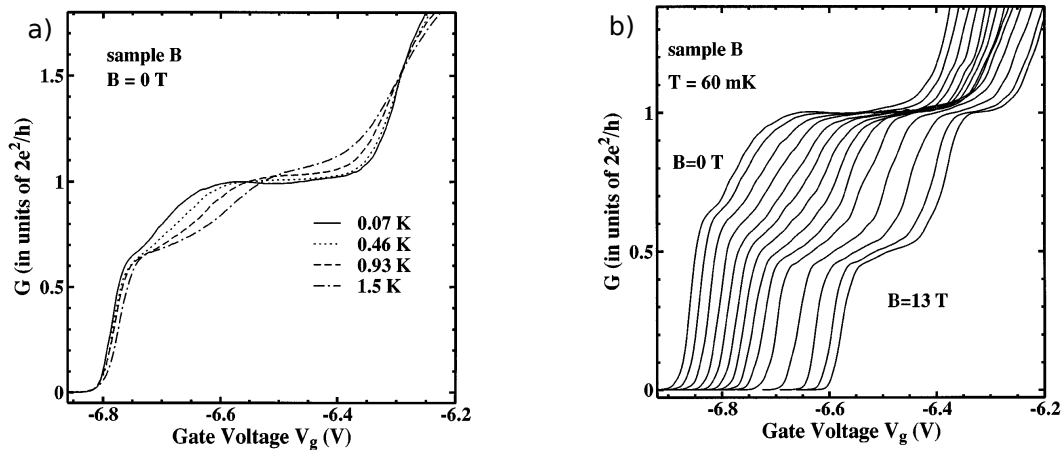


Figure 1.3 First observation of the 0.7 anomaly by Thomas et al., reproduced from [TNS+96]. (a) With increasing temperature, a conductance shoulder emerges around $G = 0.7G_Q$. (b) With increasing magnetic field this shoulder develops into a spin split plateau.

staircase which can be explained non-interactingly, one observes additional effects which can consensually only be understood in an interacting description. The prime example here is the 0.7-anomaly: With increasing temperature, the first conductance step develops a shoulder-like structure around $G = 0.7G_Q$. This effect was first observed by Thomas et al. in 1996, see Fig. 1.3. In Sec. 1.2.2 we will discuss this feature in more detail.

1.1.2 Atomic sized break junctions in metals

In 1995, it was experimentally shown by Krans et al. [KvRF+95] that a conductance quantization similar to the one in standard (i.e. semiconductor) quantum point contacts can be observed at break junctions of fine metal wires. Their setup consisted of a fine sodium wire, attached to two electrodes whose positions could be varied using Piezo electric elements, see inset of Fig. 1.4. Upon applying an increasing voltage at the Piezo elements, the wire was bent until it broke. After that the distance between the two break junctions could be adjusted freely. By studying the conductance as function of this distance, a conduction staircase was obtained, similar to the one encountered above, see Fig. 1.4. Note, however, that there are two qualitative differences. (i) The form of the conductance steps does not match the “clean” form encountered in [vWvHB+88]. Rather than smooth short steps, one observes here either very sharp and abrupt or very elongated steps. In [KvRF+95], it was argued that these effects stem from a rearrangement in the contact area of the atomic tip of the break junction. (ii) Additionally, the conductance itself exhibits a more complex quantization structure. In contrast to standard QPCs, both $2e^2/h$ and $4e^2/h$ steps occur. This effect can be traced back to the three dimensional structure of the break junction and can be understood within the simple approximation of assuming cylindrical contact points, following an argument given by [KvRF+95]. In this case the eigenfunctions $\psi(\mathbf{r})$ of the system are characterized by

$$\psi(\mathbf{r}) \sim J_m(r/r_{mn})e^{im\phi}e^{ikz}, \quad (1.1)$$

where r, ϕ, z are standard cylindrical coordinates, k is the momentum in the non-quantized z direction (along the axis of the point contact), and J_m denotes the m -th Besselfunction of first kind. The constants r_{mn} are determined by imposing the quantization condition $J_m(a/r_{mn}) \stackrel{!}{=} 0$, i.e. by demanding that the electron wavefunction should vanish outside of the cylindrical contact of radius a . Therefore, they are given by $r_{mn} = a\gamma_{mn}$, where γ_{mn} are

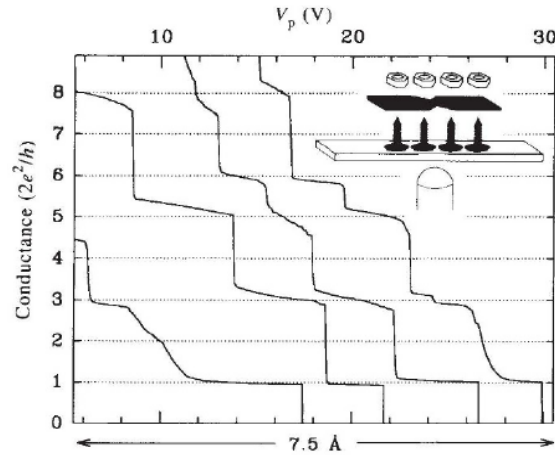


Figure 1.4 First observation of conductance quantization in a metallic (quantum) point contact, reproduced from [KvRF⁺95]. The conductance is plotted as function of the distance between the source and drain electrodes in the break junction (lower horizontal axis). This distance can be varied changing the voltage of a Piezo element (upper horizontal axis). Note that here $2e^2/h$ as well as $4e^2/h$ conductance steps occur. Inset: Schematic of the experimental setup.

the zeros of the m -th Besselfunction. Since this zeros fulfill $\gamma_{mn} = \gamma_{-mn}$, they are degenerate for $m \neq 0$. Thus, only energies with $m = 0$ are non degenerate, yielding conductance steps of $2e^2/h$, whereas all others are twofold degenerate leading to steps of $4e^2/h$ in the conductance.

1.1.3 Graphene stripes, gated graphene, and carbon nanotubes

After the (re-)discovery of graphene in 2004 [NGM⁺04], quasi 1d experiments using thin graphene stripes, so called “nano ribbons” became possible [TVJ⁺11]. Here, the central constriction is not gate defined, but arises naturally by the quasi 1d nature of the sample itself, see Fig. 1.5(a). These constrictions were realized by attaching electrodes on a graphene sheet and applying an electric current between them. The resulting annealing process leads to constrictions with widths down to 250nm.

In 2011, the conductance quantization hallmark was observed in a narrow graphene strip, again by the Van Wees group [TVJ⁺11], see Fig. 1.5(b). Especially in the hole-branch (blue line) one can observe distinct conductance plateaus at $1G_Q$, $2G_Q$ and $3G_Q$. In the electron branch (red line) quantization is less pronounced, however, one can still observe the first and the onset of the second plateau. While a 0.7 anomaly is not observable in the zero magnetic field data, at finite magnetic field the system shows behavior resembling 0.7 physics, see Fig. 1.5. For small magnetic fields, a shoulder develops around $0.6G_Q$. This effect happens for field strengths where the Zeeman splitting is still much smaller than the observed structure. It is very probable that the cause of this effect is the same mechanism as the 0.7-anomaly explained below in Sec. 1.2.2.

Additionally to being beautiful examples of how quantum effects arise in low dimensional systems, graphene based setups are somewhat more involved than the standard QPC above. In particular, theory predicts that the quantization of the conductance should depend on the boundary of the graphene strip [NFDD96, Wak01, BF06, PCG06, MnR.JFRP06]. The pure cases are the following: For an armchair edge, quantization occurs in multiples of the conductance quantum G_Q . However, for a zigzag edge, quantization is predicted to occur multiples of $2G_Q$. The cause of this prediction lies again in the different degeneracies: While

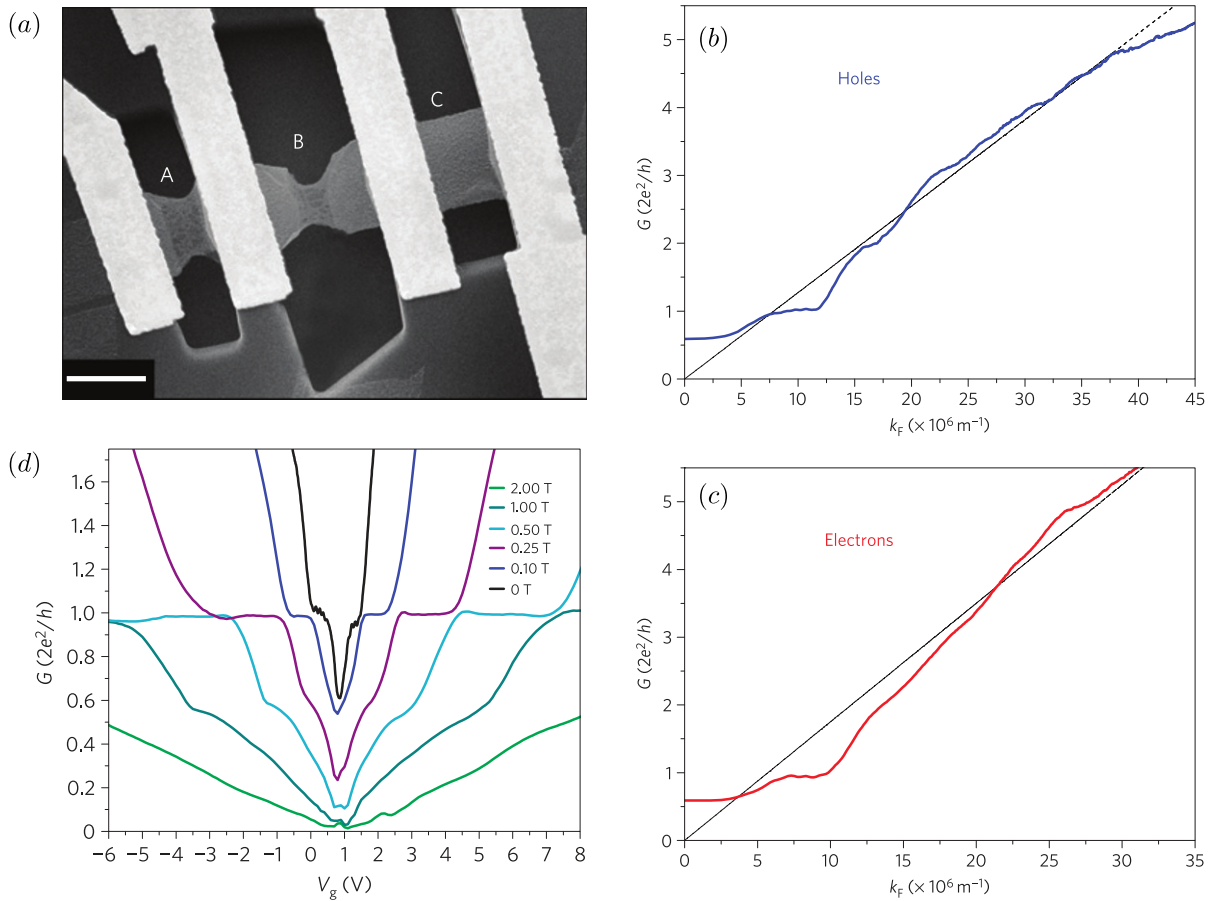


Figure 1.5 (a) Scanning electron microscopy picture of a graphene stripe with attached electrodes [TVJ⁺11]. Segment “C” is just the full unconfined strip, whereas segments “A” and “B” show constrictions of varying size. (b,c) Observed quantization of the conductance G as a function of the Fermi momentum k_F , for the hole branch (blue) and the electron branch (red). The conductance is quantized in integer plateaus, clearly pronounced for the first plateau and then becoming weaker with increasing plateau number. (d) Conductance as function of gate voltage and finite magnetic field. Note the structure at $G/G_Q \approx 0.6$, developing at small magnetic fields and resembling the 0.7-shoulder in regular QPCs. Figures (a)-(d) were reproduced from [TVJ⁺11].

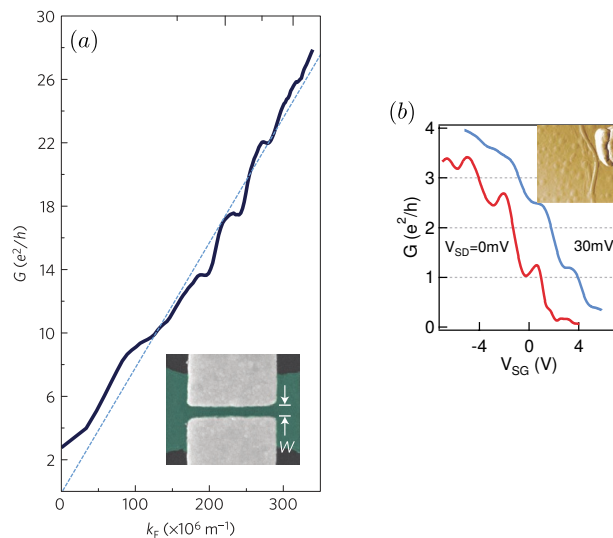


Figure 1.6 (a) Conductance quantization of a gated graphene sheet, reproduced from [KCL⁺16]. Between $G = 10G_Q - 22G_Q$ one can observe clear conductance steps with height $G = 4G_Q$, i.e. the valley symmetry of graphene is in this regime conserved. (b) Conductance quantization of a single-walled carbon nanotube, reproduced from [BMM⁺05]. Interestingly, quantization occurs here with steps $G = 0.5G_Q$, indicating that spin-symmetry is broken.

in the armchair case electrons are only spin degenerate, the zigzag edge also preserves the valley degeneracy between the two Dirac points of the graphene structure. In [TVJ⁺11], see Fig.1.5(b), only the “usual” G_Q quantization was observed. This implies that the valley degeneracy is broken, probably due to a mixture of armchair and zigzag edges as well as the presence of disorder in the system.

In fact, it turned out that the preservation of valley symmetry and a corresponding observation of $2G_Q$ conductance steps is quite hard to realize. It was first achieved only in 2016 by Kim et al. [KCL⁺16], using gate defined constriction on a graphene sheet instead of nano ribbons, see Fig. 1.6(a).

Another natural candidate system for the realization of QPCs are carbon nanotubes [Iij91, BKdV⁺93]. It was shown by Frank et al. [FPWH98] that carbon nanotubes exhibit quantized conductance. In their experimental setup, the conductance of a single carbon nanotube was found to be either 0 or $G_Q = 2e^2/h$. At first look, this result is surprising since theory predicts two degenerate bands [TD94]. Therefore, together with spin-degeneracy one would expect a conductance step from 0 to $2G_Q$. However, the carbon-nanotube used in the experiment was multi-walled, i.e. had additional inner structure, which might affect the overall conductance behavior of the nanotube. Subsequently, there have also been experiments with single-walled tubes, e.g. by Biercuk et al. [BMM⁺05], however, unsuspected conductance behavior was observed also here. Here, neither steps of G_Q nor $2G_Q$ were found, but steps of $0.5G_Q$, see Fig. 1.6(b)! This seems to indicate that spin-symmetry can be broken in this setup. Up to now, no fully satisfying explanation of this anomalous quantization has been given. However, we want to note here that in recent experiments with longer QPCs, indications for spontaneous spin-polarization were observed experimentally [YKT⁺18]. Thus it seems plausible that for sufficiently long nanotubes spontaneous spin-polarization might also arise, causing the observed anomalous quantization behavior.

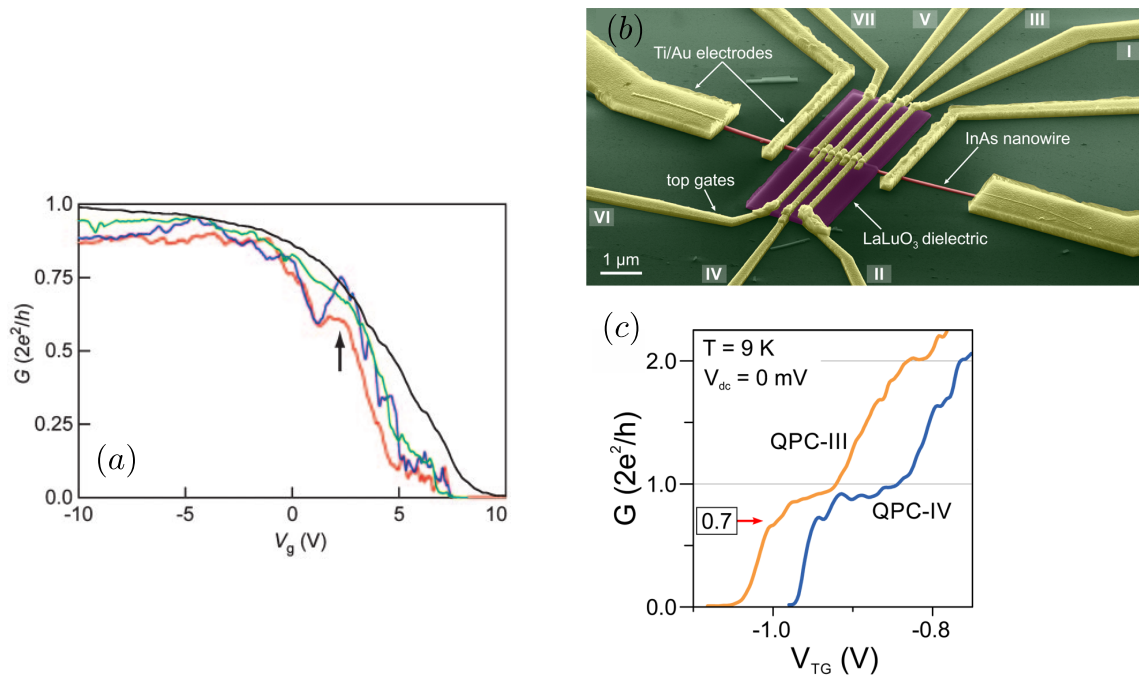


Figure 1.7 (a) First observation of quantized conductance in a nanowire, observed by Lu et al., reproduced from [LXT⁺05]. (b) Highly controllable multigate nanowire device, reproduced from [HPS⁺16], and (c) observed conductance within that device. Note that in both (a) and (c) a pronounced 0.7-shoulder is observable.

1.1.4 Grown Nanowires

Similar to using carbon nanotubes, one can also consider another very natural approach to QPCs by using grown nanowires that are quasi one-dimensional themselves. Conductance quantization in such a grown wire was first observed in 2005 by Lu et al. [LXT⁺05], who used an InAs Nanowire of 20nm diameter and lengths up to 1 μm , see Fig. 1.7(a). Due to advances in growing and gating techniques now highly controllable devices can be manufactured, e.g. like the one described in Heedt et al. [HPS⁺16], see Fig. 1.7(b). Noticeably, already in the first device of Lu that exhibited conductance quantization also the 0.7-anomaly in the first substep could be observed, see Fig. 1.7(a). In the more recent measurements by Heedt et al., the 0.7-feature is very clear, see Fig. 1.7(c).

We note here that for pure cylindrical nanowires without gates the quantization scheme is more evolved than for the standard QPC case, due to the appearance of degenerate angular modes. The argument for this is the same as the one given above in Sec.1.1.2 for metal point contacts. However, in both setups of Refs. [LXT⁺05, HPS⁺16] the attached top/back gates break the cylinder symmetry and therefore the degeneracy of angular modes. Conductance quantization occurs then in the “usual” steps of G_Q , rather than $2G_Q$. However, in an experiment by Ford et al. [FKK⁺12] with lesser attached gates, one can indeed observe the additional angular degeneracy for the conductance of modes with non zero magnetic quantum number ($m \neq 0$).

1.1.5 Cold atoms in optical lattices

More recently, Krinner et al. [KSH⁺14] managed to construct an implementation of a QPC within the framework of cold atoms, also reaching the hallmark of conductance quantization, and in fact exhibiting a whole conductance staircase, see Fig. 1.8(b). This is the first setup

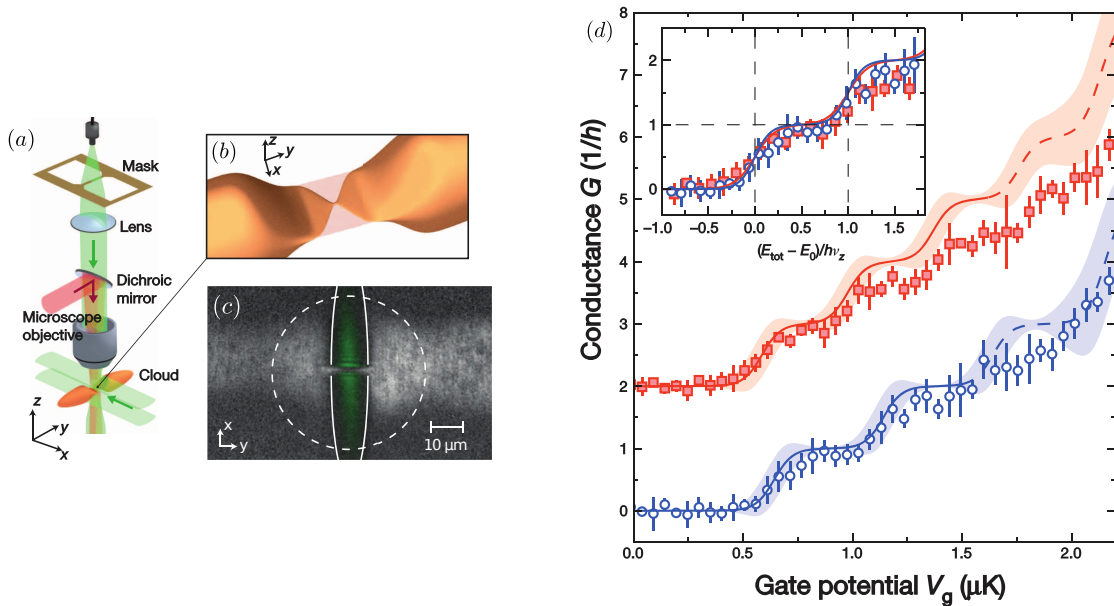


Figure 1.8 (a),(b) Schematics of the experimental setup used for the cold atom QPC experiment in [KSH⁺14]. (c) Image of the resulting QPC constriction. (d) Quantized conductance observed in the steady state of the setup in (a), for a tighter (red curve, for clarity offset by $2\tilde{G}_Q$) and a wider QPC constriction (blue curve). Note the possible candidate for a 0.7-shoulder in the first conductance step of the blue data. The inset shows the conductance curves for a frequency axis scaled by ν_z , demonstrating the overall universality of the (non-interacting) conductance quantization. Figures (a)-(d) were reproduced from [KSH⁺14]

exhibiting conductance quantization using neutral matter (fermionic ${}^6\text{Li}$ -Atoms) instead of charged particles. Therefore, in this context, we will mean with conductance the particle and not the charge conductance, correspondingly quantized in multiples of $\tilde{G}_Q = 1/h$.

The experimental setup consisted of an optical trap, realizing two large cylindrical reservoirs and a central constriction, see Fig. 1.8(a). While the overall trapping potential is cigar shaped, the TEM_{01} -Mode of a green laser is used to create a narrow 2-dimensional central region. Another laser is used to project the image of a small slit upon this 2-dimensional region, effectively creating the 1-dimensional constriction of the QPC, c.f. the schematic in Fig. 1.8(b). Remarkably, and in contrast to standard QPCs, this constriction can also be directly observed optically, see Fig. 1.8(c). The resulting conductance of this setup is shown in Fig. 1.8(d), for a smaller (red) and a larger (blue) transversal confinement width. A whole staircase of conductance steps with heights \tilde{G}_Q is observable. While the authors lay no claim to observing the 0.7-anomaly in their setup, we want to point out that the blue curve in Fig. 1.8(d) in fact shows a shoulder like feature around $0.7\tilde{G}_Q$. This is even more interesting, since, complementary to all our previous QPC realizations, the interaction used in Fig. 1.8(d) is weakly *attractive* instead of repulsive. Later on, when the authors tune their interactions to zero (as it is amazingly possible in the cold atom setup) the general quantization structure stays the same but the 0.7-shoulder vanishes, c.f. Extended Data Figure 2 of [KSH⁺14]. This illustrates the possibility to check theories developed in the context of solid state QPC in a highly adjustable setup: Quantities like interactions (via Feshbach resonances) [Fes58, IAS⁺98], effective spin degrees of freedom (modeled by different hyperfine states) and the potential landscape and can all be tuned very flexible, see e.g. [KEB17].

Additionally, this kind of setup offers the accessibility of new observables, which are only very hardly accessible in the “classical” QPC context. For example, the cold atom setup

enables also the study of QPCs with a spin resolved bias [KLH⁺16], i.e. only one spin species feels a potential difference between source and drain. This can be used to measure spin resolved conductances and investigate the so called spin-drag, i.e. the interaction induced current of the other spin species in the case of a spin-dependent bias [KEB17].

1.2 Phenomenology of QPCs

In this subsection, we will summarize different interesting experimental observations that have been observed in QPCs since the initial implementation [vWvHB⁺88] to very recent experiments [YKT⁺17]. Whenever these observations can be explained within a non-interacting description, we will point this out and detail the most important steps. Theoretical explanations beyond the non-interacting level will be discussed in the following Sec. 1.3.

1.2.1 Conductance quantization

For starters, let us first look at the above mentioned hallmark of entering the quantum realm, namely quantization of the conductance itself, see Fig. 1.2(b). This effect can be understood in a non-interacting picture, and its form was predicted within Landauer's transport theory already in 1957 [Lan57], i.e. over thirty years before its initial observation. For the case of vanishing interactions, the current that flows through the system can be written as:

$$I = e \sum_n \int d\omega \rho(\omega) v(\omega) T_n(\omega) [f_L(\omega) - f_R(\omega)], \quad (1.2)$$

where e is the electron charge, $\rho(\omega)$ is the density of states, $v(\omega)$ the group velocity, $T_n(\omega)$ is the frequency dependent transmission of the n -th conduction channel, and $f_{L/R}(\omega) = 1/(1 + e^{\beta(\omega - \mu_{L/R})})$ are the Fermi functions of the left/right lead, with $\beta_{L/R} = 1/T_{L/R}$ being the reciprocal temperatures (we set the Boltzmann constant $k_B = 1$). If we assume that temperature is constant and the chemical potentials of the left and right lead are given as

$$\mu_{L/R} = \mu \pm \frac{eV_{sd}}{2}, \quad (1.3)$$

where μ is an average chemical potential and V_{sd} is the source drain bias voltage, we can write the equilibrium linear response conductance as

$$G = \frac{dI}{dV_{sd}} = e \sum_n \int d\omega \rho(\omega) v(\omega) T_n(\omega) \partial_{V_{sd}} [f_L(\omega) - f_R(\omega)] \quad (1.4)$$

$$= -e^2 \sum_n \int d\omega \rho(\omega) v(\omega) T_n(\omega) f'(\omega) \quad (1.5)$$

where $f(\omega)$ is the Fermi distribution associated with the average chemical potential μ . The essence of Landauer's argument for the conductance quantization in 1d is the following (for a more detailed discussion, see for example [Bau14]): The product of the density of states $\rho(\omega) = \frac{1}{2\pi} \frac{dk}{d\omega}$ and the electron group velocity $v(\omega) = \frac{1}{\hbar} \frac{d\omega}{dk}$ is constant. This implies that the conductance of the system is essentially given by the sum of the transmissions T_n of the different channels. Since the transmission T_n by definition lies always between 0 and 1, the conductance as a whole is quantized in integer multiples of $G_Q = 2e^2/h$ (the factor 2 stems from the spin degeneracy of T_n for zero magnetic field). Furthermore, the form of this quantization can be beautifully understood by the properties of the saddle point potential, see Fig. 1.2(a). The confining quadratic potential $V(x, y)$ in the transversal

direction leads to a quantization of the y -direction with the x -dependent harmonic oscillator energies $E_n(x) = \hbar\omega(x)(n + \frac{1}{2})$. Upon varying the potential height, each time one of those energies crosses the chemical potential another one of the transversal modes contributes to the conductance in (1.5), see Fig. 1.2(b). Integrating out the y -direction (and nominally also the z -direction) one can obtain a purely one-dimensional model with only the x -direction remaining. The resulting effective potential $V(x)$ is by default dependent on the exact form of the saddle-point constriction. For further details see also Sec. IV.A in our publication 3.2 below. However, to capture the qualitative physics of a QPC, the exact knowledge of $V(x, y)$ and in extension $V(x)$ is not required. One can simply make the ansatz $V(x) = a_0 + a_2x^2 + a_4x^4 + \dots$ as a generic Taylor expansion of a symmetric potential barrier, with the parameters a_0, \dots as fit parameters. In order to determine which structure for $V(x)$ (from here on called the “bare potential”) is suitable to describe the experiment best, one can look at the higher conductance steps of a QPC. Here, interaction effects are less important due to the screening performed through the electrons of the lower, already filled subbands. In Heyder [Hey14], this was carried out and it was shown that a simple parabolic barrier fits the smooth form of the conductance steps of the higher subbands best. Any introduction of an anharmonicity would lead to additional resonance structures in the conductance. This was shown numerically by Heyder [Hey14, HBS⁺15] and is explained by Schimmel [Sch17], using non-interacting scattering theory. Therefore, we consider a QPC potential which (around its barrier top) is of the quadratic form

$$V(x) = V_g - \frac{1}{2} \frac{m^*}{\hbar^2} \Omega_x^2 x^2, \quad (1.6)$$

where V_g is the gate voltage, m^* the effective electron mass in GaAs, and Ω_x is the curvature of the QPC in x -direction. Using the particularly simple form of the transmission for such a pure parabolic barrier [Con68] (which is dependent on spin σ due to a possible present magnetic field B)

$$T_\sigma(\omega) = \frac{1}{1 + \exp(-2\pi(\omega - V_g - \frac{\sigma}{2}B)/\Omega_x)}, \quad (1.7)$$

one can compute the form of the conductance steps analytically as done by Büttiker [Büt90]. In case of zero magnetic field and zero temperature, one obtains a conductance step in the form of a Fermi function where the curvature Ω_x sets the width of the step:

$$g = G/G_Q = \left[e^{2\pi V_g/\Omega_x} + 1 \right]^{-1}, \quad (1.8)$$

c.f. blue line in Fig. 1.9(a). In the following, we take a moment to discuss how this non-interacting form changes for varying temperature, magnetic field and bias voltage. This is particularly useful, in order to distinguish non-interacting from interacting effects observed in QPC experiments.

In Fig. 1.9(a), we show the dependence of the conductance on temperature. With increasing temperatures, the conductance step becomes smeared out. Due to the interaction with the thermal bath, electrons with energy below the barrier may receive thermal energy and manage to cross the barrier. On the other hand, incoming electrons with sufficient energy to pass the barrier, may be reflected due to loss of energy to the thermal bath. Both effects lead to a broadening of the conductance step. Note, however, that overall the step remains symmetric around the $g = 0.5$ point.

In Fig. 1.9(b), the magnetic field is increased, which leads to a different QPC barrier height for the two spin species. Therefore, the respective spin resolved curves are shifted in

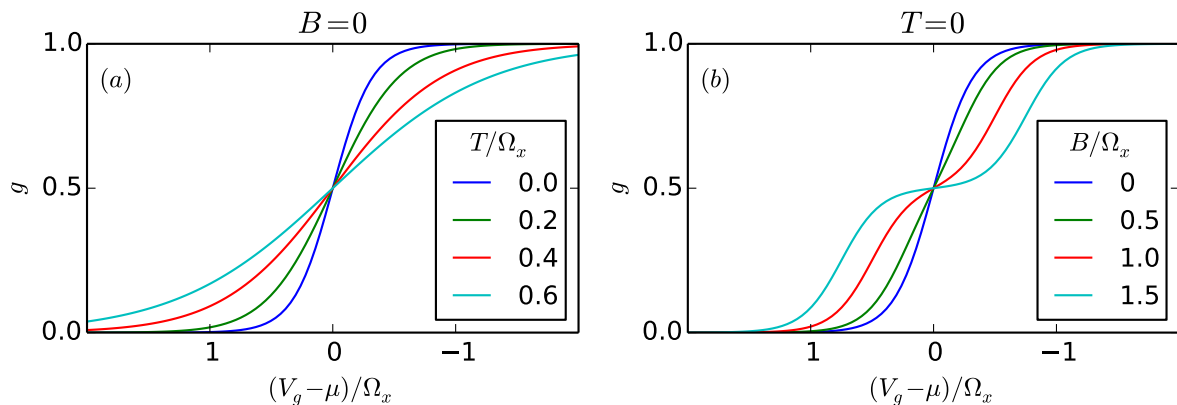


Figure 1.9 Conductance $g = G/G_Q$ as function of gate voltage V_g for a single subband. (a) With varying temperature the conductance is smeared out symmetrically around the $g = 0.5$ point. (b) Finite magnetic field lifts the spin degeneracy and leads to a development of a spin-split plateau. Note that also here the splitting occurs symmetrically around the $g = 0.5$ point

gate voltage, leading to the development of a spin split plateau. Again the symmetry around $g = 0.5$ remains conserved in the non-interacting case. So far, we have only studied the linear response conductance, i.e. the conductance at vanishing bias voltage $V_{sd} = 0$.

In Fig. 1.10, we show the behavior of the conductance with increasing V_{sd} at different gate voltages V_g . For a more closed setup with $g < 0.5$, increasing the bias voltage leads to an increase in the conductance, while for a more open setup with $g > 0.5$ it leads to a decrease. This can be easily understood considering the symmetric form of the applied bias (1.3). Without loss of generality, we can assume that $V_{sd} \geq 0$. In general, an infinitesimal increase of the bias voltage $\delta V_{sd} > 0$ will lift the left chemical potential slightly up and shift the right chemical potential slightly down. Therefore, the net current from the left to the right lead will slightly increase. The magnitude of this increase (and therefore the conductance), however, depends on the position of the left and right chemical potential and therefore the finite bias voltage. In an open QPC, a small but finite increase in the bias voltage leads to the following effects: The left chemical potential is shifted upwards and $T(\mu_L)$ changes only lightly, therefore having no large impact on the conductance. On the other hand, the right chemical potential is shifted downwards and $T(\mu_R)$ decreases due to the QPC barrier. This leads to a decrease in the conductance. Thus the net effect of an increase in bias in the open QPC regime is to decrease the conductance (see the cyan and magenta lines in Fig. 1.10). In the closed QPC, this effect is reversed. Now the shift of the right chemical potential has no impact since $T(\mu_R)$ is small anyway. However the transmission amplitude $T(\mu_L)$ is significantly increased by shifting μ upwards, therefore yielding an increase in conductance. Thus the net effect of a finite bias increase in the closed QPC regime is to increase the conductance (see the green and blue lines in Fig. 1.10).

1.2.2 Special features of the lowest subband: The 0.7 anomaly

Additionally to the quantization staircase in Fig. 1.2(b), which can be understood in a non-interacting setup, there are a several observations which can only be explained by taking interactions into account. First and foremost among those is the so called “0.7 anomaly”. This structure was pointed out first by Thomas et al. [TNS⁺96] in 1996. While the higher conductance steps follow beautifully the non-interacting form given in (1.8), the

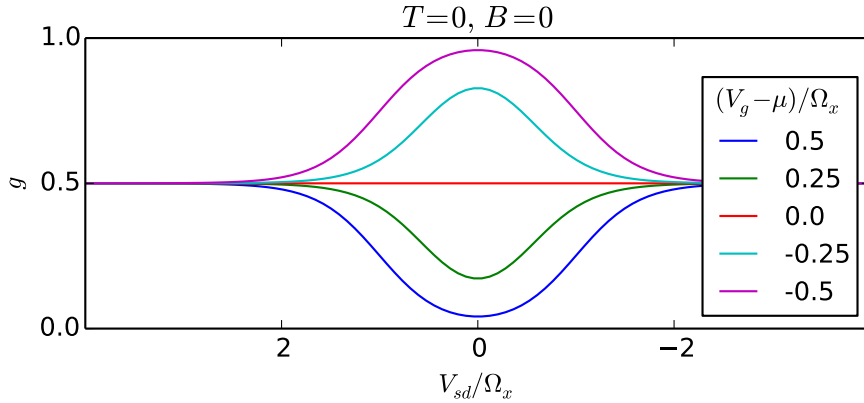


Figure 1.10 Conductance as function of bias voltage V_{sd} for several values of the gate voltage V_g . Note that for a closed QPC an increase in V_{sd} leads to an increase of conductance, while for an open QPC it leads to a decrease.

first step shows a peculiarity. The dimensionless conductance $g = G/G_Q$, where $G_Q = 2e^2/h$ is the conductance quantum, exhibits a shoulder like structure at roughly $g \approx 0.7$, see Fig. 1.3(a). In particular, this structure gets more pronounced with increasing temperature. Subsequent studies showed that virtually all observables (shot noise [RSG⁺04, DZM⁺06], thermal power [ANP⁺00], thermal conductance [CNP⁺06], ...) show anomalous behavior (i.e. different than non-interacting behavior) while the gate-voltage is turned through the 0.7 (also called “subopen”) region. Here, we show the most prominent example for this behavior, namely the conductance as function of temperature [TNS⁺96, BHS⁺13], magnetic field [TNS⁺96, BHS⁺13] and bias voltage [KBH⁺00, CLGG⁺02]. In this section, we focus on the experimental features of the 0.7-anomaly. A theoretical explanation for the 0.7-physics as given in [BHS⁺13] is discussed in Sec. 1.3 below.

The conductance in Fig. 1.3 shows clearly the development of a pronounced shoulder at $g = 0.7$ with increasing temperature. Although the degree to which this step develops varies for different devices, the occurrence of a shoulder-like 0.7-feature is universal and was observed in a multitude of experiments, see e.g. [TNS⁺96, Mic11, BHS⁺13, ILK⁺13]. Newer measurements at very low temperatures indicate that the shoulder can actually vanish for $T \rightarrow 0$, yielding again a convex conductance step, see Fig. 1.11(b) .

The conductance as function of an in plane magnetic field B also exhibits interesting behavior. While the non-interacting formula (1.8) suggests a symmetric splitting (a finite magnetic field adds a linear Zeeman term to the gate potential, i.e. in (1.8) $V_g \rightarrow V_g + \frac{\sigma}{2}B$, where $\sigma \in \{+, -\}$ is the electron spin), the experimental curves show that the splitting exhibits a pronounced asymmetry, see Figs. 1.3(b) and 1.11(a). The shape of the first substep is almost of the same form as in the non-interacting case. The second substep, however, is shifted to higher gate voltages and its form is much more broadened. In the case of very large in plane magnetic fields, the opposite spin components of different subbands can become degenerate, yielding new interesting effects. We discuss this case in Sec. 1.2.3 below.

The conductance as function of finite bias voltage and for different values of the gate voltage can be seen in Fig. 1.12(a). To study the influence of a finite bias voltage let us first look at the behavior of the higher conductance steps around $V_{sd} = 0$. Here, the finite bias influence resembles strongly the non-interacting shape displayed in Fig. 1.10, again indicating that interactions play a less important role for the higher steps. Therefore, we focus in

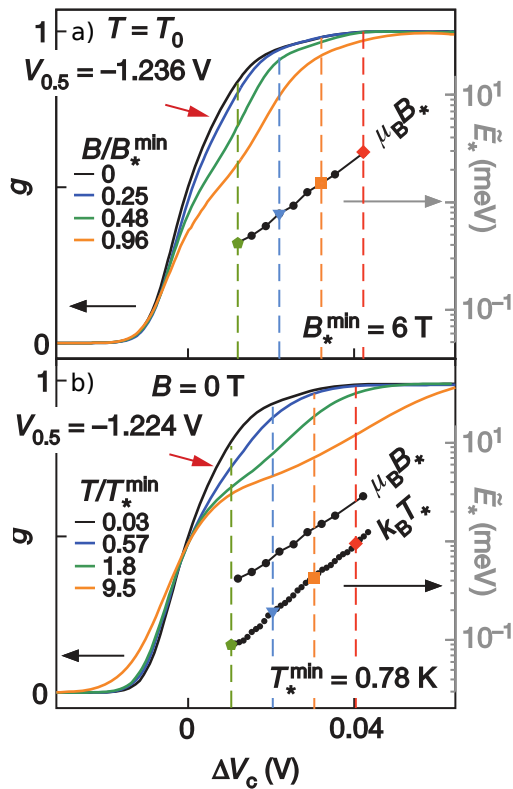


Figure 1.11 Measurements of the first conductance step, reproduced from [BHS⁺13]. Development of the 0.7 anomaly for varying magnetic fields (a) and temperatures (b). Note that for very small temperature and zero magnetic field the 0.7-shoulder vanishes.

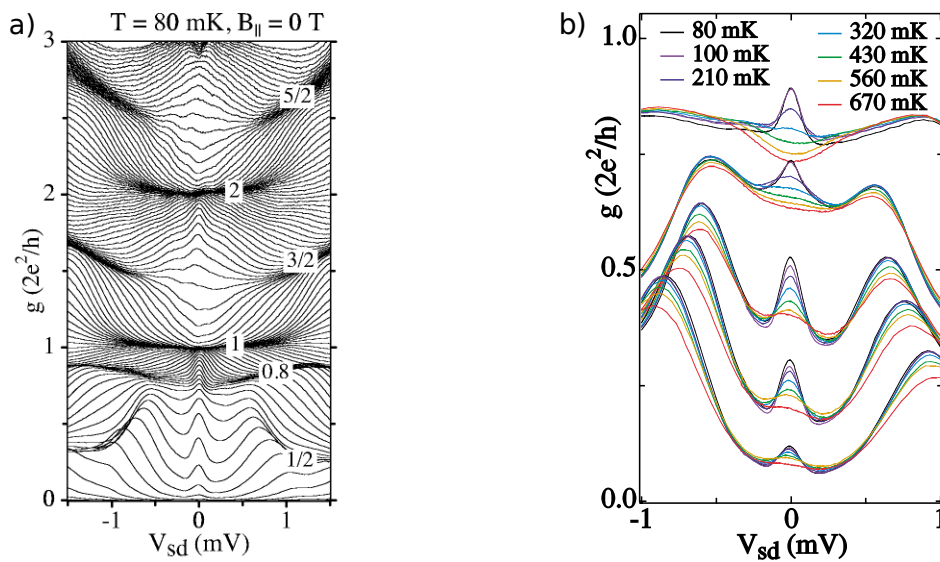


Figure 1.12 (a) Measured bias dependence of the conductance for various gate voltages. Note the zero bias anomaly (ZBA) occurring at $V_{sd} = 0$ and small conductance g . (b) Temperature dependence of the ZBA and the side peaks. Figures (a) and (b) were reproduced from [CLGG⁺02]

the following discussion on the first conductance step, i.e. only the first transversal mode is contributing. For all gate voltages, the conductance exhibits a sharp decrease when going from $V_{sd} = 0$ to a small finite bias. This is particularly interesting for gate voltages where $g < 0.5$, since for these gate voltages a non-interacting treatment predicts an increase of the conductance with increasing bias voltage, see the discussion in Sec. 1.2.1. This feature is called a zero bias anomaly (ZBA) and resembles the ZBA induced by the Kondo effect in quantum dots. In particular, it also gets suppressed with increasing temperature, see Fig. 1.13(b). Due to these similarities, it was argued (see e.g. [ILK⁺13]) that the 0.7-anomaly might also be caused by the Kondo effect, even though the development of a localized magnetic moment in a QPC seems unlikely.

Additional interesting features of the first conductance step are the sidepeaks, see Fig 1.12(a,b) around $V_{sd} = 0.6\text{mV}$, as well as the behavior at large bias voltage $V_{sd} = 1.5\text{mV}$ where the conductance approaches - independently of the gate voltage - a value around $g \approx 0.2 - 0.3$. The latter feature, first observed in [PNMM⁺91] (and sometimes addressed as the “0.25-anomaly” [CGP⁺08]) is interesting, since a non-interacting treatment yields a value of $g \approx 0.5$ for large bias. Similar to the 0.7 anomaly, the origin of the 0.25 anomaly is still under debate [dPPBW04, KRA⁺08, CGP⁺08, IZ09]. However, as pointed out by Schimmel [Sch17], the occurrence of the sidepeaks at $V_{sd} = 0.6\text{mV}$ is also very interesting. This feature is consistently present in a large variety of experiments (see e.g. [CLGG⁺02, RYF⁺10]) and to our knowledge, its origin is not known. It is not even apparent if it is necessarily the result of interactions or if some modification of the non-interacting model that was missed up to now could also be responsible. A non-equilibrium Keldysh fRG treatment performed in [Sch17], using a standard QPC model with short ranged-interactions (see Sec. 5.2 below), did not show any indications of this sidepeaks.

1.2.3 Effects involving several subbands: The 0.7 analog

After it was discovered that the 0.7 anomaly in the first conductance step exhibits clearly the influence of interactions, several other attempts were made to observe further non-interacting behavior. The natural candidates for this are always the energetically lowest electrons, since the interactions of the energetically higher ones will be effectively screened by the lower lying electrons. Indeed, we have seen above that the higher conductance steps resemble almost perfectly the non-interacting shape given by (1.8). In the standard setup (i.e. zero magnetic field and strong confinement) this lowest electrons are the spin degenerate ones of the first subband. In order to observe different interacting behavior, one has to find a way to change this configuration of the lowest lying electron levels. This can be done in several ways. More recently, [HCC⁺18] implemented an experiment with a very weak confining potential. This leads to a very small subband spacing, almost making the first two subbands degenerate. It was shown that this leads to the development of a quasi one-dimensional Wigner crystal where the electrons form a loose zig-zag chain formation in the QPC. Interestingly, it was conjectured [MML07] that the change from the normal groundstate, which is for a not too long QPC still Fermi-liquid like (instead of exhibiting 1d Luttinger behavior, as it is the case in infinitely expanded systems), to this type of Wigner crystal is a quantum phase transition.

A second, maybe more straight forward approach, is to apply a strong in plane magnetic field to the QPC sample. Besides a diamagnetic contribution (which again can be understood nicely in a non-interacting model, see [GTP⁺03]), this leads to a lifting of the energy degeneracy of single subbands of spin up and down electrons via a Zeeman shift, see Fig. 1.13. For low magnetic fields (blue region in Fig. 1.13), this leads exactly to the behavior in the first substep, that was already explored in the 0.7-anomaly section above. However, by making the applied magnetic field sufficiently large, we can introduce another degeneracy in the system,

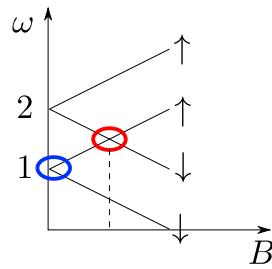


Figure 1.13 Illustration of the development of the QPC energy levels with increasing magnetic field. The region of the 0.7-analog at the intersection of the spin-up branch of the first subband and the spin-down branch of the second subband is marked in red, whereas the region of the ordinary 0.7-anomaly is marked in blue.

namely at the intersection of the spin 1-up and the spin 2-down spin-subbands, see red region in Fig. 1.13. When - while opening the QPC - this region crosses the chemical potential, the screening potential caused by lower lying subbands is still small, since only the 1-down electrons are occupied. Indeed, here one notices another interacting effect. At the crossing appears a structure that resembles the 0.7-anomaly in the first substep, see Fig. 1.14, solid ellipse. For this reason it is called the 0.7-analog [GTP⁺03].

However, opposed to all similarities, there are also differences to the 0.7-anomaly. The most striking one is certainly the appearing asymmetry of the structure. If the crossing point is approached from higher magnetic fields a clear shoulder is visible, see green curve in Fig. 1.14. At lower fields, however, no shoulder is visible and the conductance curves looks almost symmetric, see red and blue curves in Fig. 1.14. In section 4.2 of this work, we first reproduce this feature in the conductance via fRG-calculations and then also give an intuitive physical explanation, in terms of a simple Hartree picture.

1.2.4 Extending the physical setup: Inclusion of spin-orbit interactions

In this last part of the phenomenological QPC section, we take a brief look at physical setups that exhibit an additional kind of spin symmetry breaking, namely spin-orbit coupling. While in the previous sections, spin symmetry was broken by the introduction of an external magnetic field via a Zeeman term $\sim \mathbf{B} \cdot \boldsymbol{\sigma}$, we discuss here setups which exhibit an additional Rashba spin-orbit term, proportional to the electron momentum $\sim k\sigma_y$. This spin-orbit coupling can be used in many ways to produce new interesting physical setups.

The most direct setting is to include it directly within a QPC, and study the effects that emerge from the interplay of Zeeman-field, Rashba-term and electron interactions. In [GBHvD14], this setup was studied by using similar methods as in [BHS⁺13] and consequently our study 3.2. Besides interesting effects that emerge from the interplay of SOI and Zeeman terms already in a non-interacting setup, the implications on the interaction induced 0.7-physics are immense. In particular, for increasing spin orbit strength (perpendicular to the external magnetic field) spin-mixing is introduced, yielding an avoided crossing and consequential development of a spin gap. For intermediate spin-orbit strengths, this accentuates the asymmetric shape of the conductance w.r.t. increasing external magnetic field B , see Fig. 1.15(a-b). However, the dependence of the conductance on B is still linear (although with increased Lande-factor, due to interactions). For large spin orbit strengths one can observe several changes, see Fig. 1.15(c). A feature one immediately notices, is the drop of the conductance in the usual plateau region after the double step. This feature is already there in the non-interacting model and is due to the development of the above mentioned

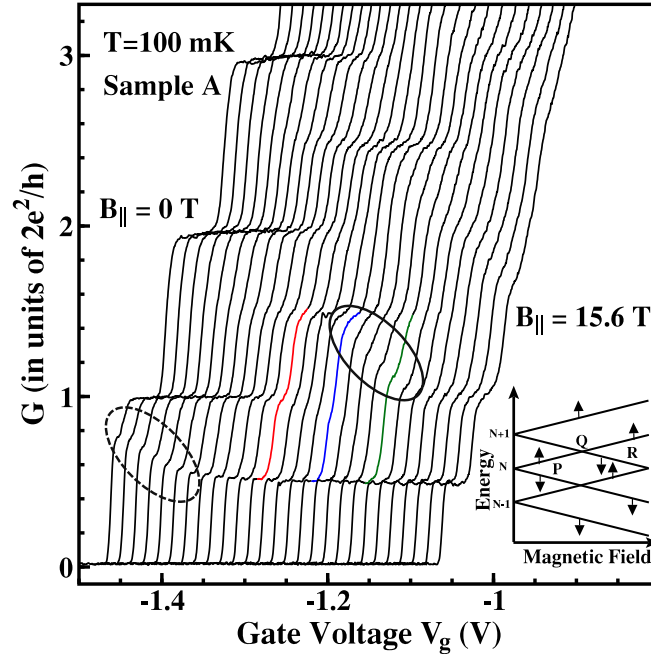


Figure 1.14 Conductance as function of gate voltage for increasing magnetic fields as measured in [GTP⁺03], reproduced from our publication in Sec. 4.2. The dashed and solid ellipses mark the 0.7-region and the similar shoulder structure appearing at the 0.7-analog, respectively. Note the asymmetry in the magnetic field dependence of the 0.7-analog, depending whether it is approached from lower or higher magnetic fields.

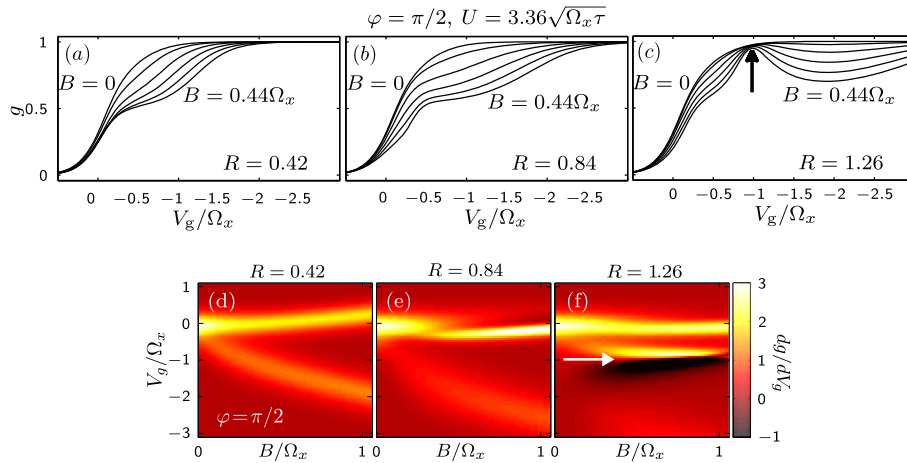


Figure 1.15 (a-c) Development of the magnetic field dependence of the QPC conductance with increasing dimensionless SOI strength R . (d-f) QPC transconductance in presence of SOI. Note that at large R , the splitting of the double step is not linear in B but almost constant (see arrow in (f)). Figures (a)-(f) were reproduced from [GBHvD14]

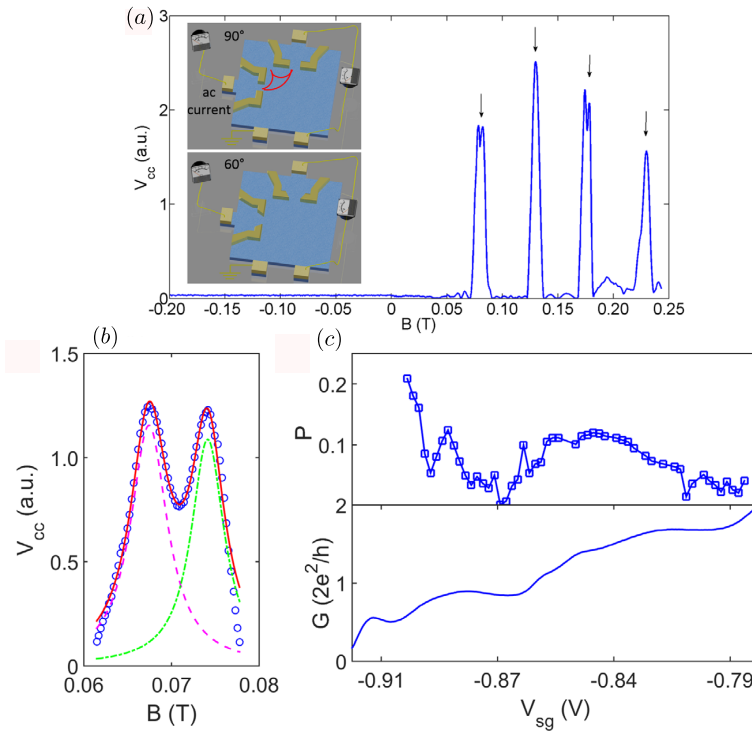


Figure 1.16 Detection of spin polarization via spin orbit interactions, reproduced from [YKT⁺18]. (a) Detector voltage as function of perpendicular magnetic field. Note the splitting of odd peaks arising from SOI. Inset: Focusing geometries with longer (90deg shape of split gates) and shorter QPC (60deg shape of split gates). (b) First focusing peak (blue circles) with fitted Lorentzian subpeaks (green and magenta curves). Note that the amplitude difference of the subpeaks, indicating a spin polarization of the QPC. (c) Resulting polarization (computed from the amplitude of the subpeaks in (b)) and conductance as function of gate voltage.

spin gap. However, there is another striking feature, that arises only within the interacting model. In contrast to the intermediate case, the dependence on B of the double step in the conductance is almost constant instead of linear. This difference can be seen especially good by comparing the corresponding transconductances, see Fig. 1.15(d,f). In [GBHvD14], it is shown that this feature can be beautifully understood by analyzing the dependence of the (non-interacting) van-Hove ridge on spin orbit strength at finite external magnetic field. The essence of this van-Hove ridge type of argument to make predictions about the influence of interactions, is the same as in [BHS⁺13], and is discussed in detail below in Sec. 1.3.

In a more recent experiment [YKT⁺18], the effect of spin-orbit interactions was used to analyze the spin-components of the transmitted electrons of a QPC. For this purpose a setups consisting of two QPCs were used, see Fig. 1.16(a), inset.

One QPC acts as injector with tunable gate voltage, while the other acts as receptor, with a gate voltage fixed to the middle of the first conductance plateau. Outside the QPCs, an external magnetic field perpendicular to the QPC plane is applied, leading the injected electrons to follow cyclotron orbits. These cyclotron orbits differ slightly for spin-up and spin-down electrons due to the effect of spin-orbit interactions (due to the SOI introduced splitting of the Fermi surface), therefore affecting the form of the detected focussing peaks with varying magnetic field, see Fig. 1.16(a). For odd peaks (i.e. peaks with an even number of reflections on the wall of the setup), this leads to a splitting of the focussing peak into a (mainly) up- and a (mainly) down-component. For even peaks, this effect is compensated

by the odd number of reflections on the wall, leading to an eventual refocusing of up- and down-electrons at the detector.

This possibility to distinguish between up- and down-electrons in the detector offers the very interesting opportunity to observe a possible spin-polarization of the injector. This is *highly relevant* for insights in the 0.7-physics, since a lot of theoretical descriptions see a spontaneous spin-splitting as the main cause of the 0.7-anomaly [TNS⁺96, Rei05]. Other interpretations, as the van Hove ridge interpretation advocated by our group do not per se rely on such a spontaneous splitting. The experimental result in [YKT⁺18], seems to be very Solomonic in this regard. While spontaneous polarization is absent for short QPCs, it is observable for longer QPCs, via a resulting amplitude difference of the focusing peaks, see Fig. 1.16(b,c). This seems to be consistent with the theoretical findings in [SBvD17], where it is shown for *short QPCs* that the van Hove ridge scenario -while not leading to a true, static spontaneous polarization - also implies a “slowly fluctuating polarization”. The time an electron needs to transverse the QPC is of the same order as the time of spin fluctuations within the QPC barrier. This quasi polarization could be seen as the precursor to a truly static polarization in longer QPCs.

Within this thesis, we focus on the treatment and the influence of longer-ranged interactions in QPCs. We consider our work an important step on the way to obtaining a theoretical description of the transition from shorter to longer QPCs and the possible onset of spontaneous polarization. On the one hand, it is a physical necessity to treat longer interaction ranges in longer QPCs. Longer barrier regions with small Fermi energy limit the amount of possible screening. In particular, descriptions with purely onsite-interaction models as in [BHS⁺13, SBvD17] will not be enough. In the limit to very long one-dimensional systems (quantum wires), one even expects the formation of Wigner crystals [Sch93]. On the other hand, while developing the necessary fRG machinery to include this longer interaction ranges, we noticed that our improved long-range feedback method developed in Sec. 3.2 also helps to improve the convergence of the fRG flow in general. This enables, independent of which interaction model (onsite/finite-range) is chosen, the better treatment of longer QPC barriers, where the fRG-treatment becomes difficult due to the large density of states at the chemical potential.

1.3 Theoretical explanations beyond the non-interacting model

Over the years, the rich physics involved in the 0.7 anomaly has invoked a lot of explanation attempts, which all are more or less good in explaining certain features of the anomaly, but fail in others. Possible explanations (this list is by no means complete) involve spontaneous spin polarization [TNS⁺96, SYB03, Rei05], inelastic scattering [SMS08, LMS⁺09, BHS⁺13], the Kondo effect [MHW02, RM06] and Wigner crystallization [Mat04, GmcUJB09]. Each of this explanations has its advantages and disadvantages. Here we will give a short review of the three most prominent:

Spontaneous spin polarization has been the first attempt to explain the 0.7-anomaly, suggested by Thomas et al. in the same work, where they published the experimental finding of the 0.7-anomaly [TNS⁺96]. The idea stems from the form of the conductance curve at finite magnetic fields B : When B is increased, the 0.7-shoulder develops gradually in the 0.5-spin split step, that is expected to occur due to the Zeeman shift. The 0.7-shoulder at zero magnetic field is then interpreted as the spin polarized remnant of the finite magnetic field splitting. In this sense, the spontaneous polarization is analog to the remaining non-vanishing magnetization in a ferromagnet at zero external magnetic field. Prominent criticism of

this picture is that in one dimension the Mermin-Wagner theorem applies, prohibiting a spontaneous breaking of continuous symmetries, like spin orientation. However it is under debate whether this theorem can be applied so strictly in the given setup, which after all is only approximately one-dimensional. Suggestions are that (similar to graphene in 2d), the system can adopt a slight zig-zag structure to avoid the violation of the Mermin-Wagner theorem. Concrete calculations to support the spontaneous spin polarization hypotheses were carried out e.g. in [SYB03]. They used a zero temperature DFT approach which seems to indeed show spontaneous spin-polarization of the energy levels. However, as was pointed out by Bauer [Bau14], this sort of DFT calculations tend in general to converge preferably towards polarized phases, missing out on the possibility of an unpolarized phase in between. Furthermore, only local quantities like the renormalized local potentials are accessible, which prohibits a direct computation of transport observables like the linear conductance.

As discussed above in Sec. 1.2.4, a recent experiment carried out in the Pepper group was able to shine more light on the question whether spontaneous spin polarization occurs. Using a 2DEG sample with strong spin-orbit interactions (SOI), they were able to measure directly the spin polarization of the QPC, by analyzing electron trajectories in an applied out-of plane magnetic field. They found that longer QPCs show indeed an onset of spin polarization, while shorter QPCs remain unpolarized. Therefore, spontaneous spin polarization may certainly play an important role in the physics of (longer) QPCs but to promote it as the single source of the 0.7-anomaly may not be the whole truth.

Another, explanation attempt utilizes the Kondo-effect to explain the anomalous conductance behavior [MHW02, RM06]. The source of this view is mainly rooted in the finite bias properties of the QPC conductance, see Sec. 1.2.2 above. The behavior of the QPC's zero bias anomaly resembles somewhat the zero bias anomaly displayed by the Kondo effect in quantum dots, see e.g. [COK98]. The claim of this explanation attempt is that a (quasi-) localized spin forms within the QPC that acts as a magnetic impurity, instigating the Kondo effect. To validate this claim, density functional calculations were carried out, similar to the ones used in the spin polarized setup above. Again DFT yields an access of one spin species, however, now the data is interpreted even bolder. It is claimed that in the middle of the QPC this access is exactly given by one spin 1/2, effectively yielding a localized magnetic moment in the QPC center. More recent experiments seem to be in disagreement with this localization theory. In [KOS⁺15] the authors present a novel method using NMR measurements to investigate the spin properties of a QPC in the 0.7 regime. They find no evidence of a localized spin and in fact, they support the thesis that their measurements can be perfectly understood in the context of the next and final explanation of the 0.7 anomaly, which we present below.

Our preferred explanation for the 0.7-anomaly is consensually referred to as “inelastic scattering” [SMS08, LMS⁺09] - or also “Van-Hove ridge” explanation. It's main idea is that the anomalous properties in the 0.7-regime can be traced back to a large density of states whose apex lies on the scale of Ω_x above the band-bottom of the QPC. This shift of the 1d-divergent Van-Hove singularity away from the band edge is a geometry induced effect of the QPC barrier, see Fig. 1.17(b). We stress here that this is not a interaction effect, but can be understood perfectly well in a single-particle picture. However, the effect of this large density of states becomes only prominent once interactions are taken into account. This can already be seen in a simple Hartree-argument. To first order in the interaction, the self-energy in the QPC is given by

$$\Sigma_{ii}^{\sigma} \sim U n_i^{\sigma} = U \int_{-\infty}^{\mu} d\omega' \mathcal{A}(\omega'), \quad (1.9)$$

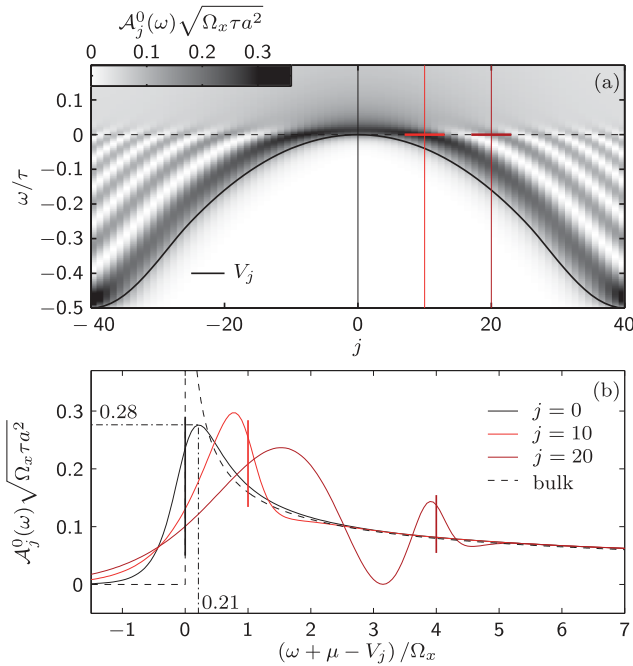


Figure 1.17 Local density of states $\mathcal{A}_j(\omega)$ of a QPC barrier, reproduced from [BHvD14], (a) as colorplot of site j and frequency ω and (b) $\mathcal{A}_j(\omega)$ at different sites j . Note that at the QPC center ($j = 0$) the LDOS attains its maximum at a small but finite value above 0. The oscillating structure in the flanks of the QPC are due to Friedel oscillations.

where μ is the chemical potential, U a (here for simplicity onsite) interaction strength and $\mathcal{A}_i^\sigma(\omega) = -\frac{1}{\pi} \text{Im} G_{ii}^\sigma(\omega)$ is the local density of states (LDOS) at site i . This first order self-energy is frequency independent and therefore just leads to an effective non-interacting model with renormalized barrier. Since the interactions are repulsive, this effective barrier is higher than the bare one. Furthermore, this effective barrier is highest, where \mathcal{A} is biggest, i.e. in the area around a conductance of $g \approx 0.7$, leading to a pronounced reduction in that part of the conductance curve. While it turns out that this simple Hartree argument alone is not enough to explain the 0.7-anomaly, it already gives us an intuitive idea what the 0.7 anomaly is rooted in: An enhanced density of states at the chemical potential in the 0.7-regime.

A more refined treatment of the physical setup, including higher order (and therefore dynamic) contributions to the self-energy, leads to a more realistic conductance behavior, especially for finite temperatures. Increasing temperature opens up the window for possible scattering processes within the QPC. At zero temperature, all states below the chemical potential are occupied, all above are empty. Therefore, an incoming electron at the chemical potential can only scatter with other electrons at the chemical potential. All inelastic processes in which an electron only gives a part of its energy to create particle-hole excitations are not possible. At finite temperature, the occupation of electron levels within the QPC is given by a Fermi distribution, therefore making a lot more processes possible.

Having this picture of the 0.7 anomaly in mind, the function renormalization group (fRG) (see Sec. 2.3 below) yields a natural tool to reinforce and complement this argument via direct calculations of the QPC conductance. Due to the involved nature of the problem, this still poses a major challenge in itself and was done in several steps in our group, going from static to dynamic Matsubara implementations (only reliably usable for zero temperature and non-dynamic quantities) to a more recent Keldysh implementation.

Having access to dynamical quantities, in particular the frequency resolved density of states as well as transversal times of electrons through the QPC, peaked recently in an extended insight into the QPC mechanics: Schimmel et al. [SBvD17] noticed that all three of the major explanations presented above can be unified, via evoking a dynamical spin polarization, which is semi-static on the time scale that electrons need to traverse the QPC. This timescale is of the same order as spin-fluctuations occurring in the QPC. The explanation for this is actually quite intuitive. For a not too long QPC (to avoid Luttinger behavior), the natural degrees of freedom in the QPC are just Fermi-liquid like particle-hole excitations. Therefore, changing the spin in the center of the QPC by $1/2$ corresponds to the transport of an electron from the middle to the edge of the QPC. Thus, on the timescale that an external incoming electron needs to traverse the QPC, the other spins appear to be semi-static in the sense that they cannot change their direction completely in that time.

2 Method

In the first part of this chapter, various definitions and preliminaries used throughout this thesis are stated. In the second part, our original work on the extended Coupled Ladder Approximation in an efficient combined Matsubara/Keldysh formulation (in a similar way as introduced by Karrasch [Kar10]) is presented. Here, the focus lies on the treatment of symmetries and the derivation of the eCLA flow equations. This effectively combines the eCLA parts in the method sections of our publications P1, Sec. 3.2 (Sec. II.A-C,E) and P3, Sec. 5.2 (Sec. III.A.1-2,B.1-3) below, which the reader may skip on subsequent reading.

2.1 Definitions and preliminaries

In this section, definitions and known relations for various quantities used throughout this thesis are stated. The formal fRG framework, within which we work, has been established earlier and has been described in meticulous detail in the works by Karrasch [Kar10], Jakobs [Jak09] and Bauer [Bau14]. Hence, here it will only be commented on briefly and also only necessary definitions and important formulas used in our original work will be discussed. The adopted conventions for Green's functions, two-particle vertices, etc. are consistent with the ones used in our publications P1, Sec. 3.2 - P3, Sec. 5.2 below.

2.1.1 Fourier convention

Real time

For a function $f(t'|t)$ of m incoming particles at real times $t = (t_1, \dots, t_m)$ and m outgoing ones at real times $t' = (t'_1, \dots, t'_m)$, we define its real-frequency Fourier transform $f(\omega'|\omega)$,¹ with $\omega = (\omega_1, \dots, \omega_m)$ and $\omega' = (\omega'_1, \dots, \omega'_m)$, via

$$f(\omega', \omega) = \int dt \int dt' e^{i(\omega't' - \omega t)} f(t', t), \quad (2.1a)$$

with $\omega t = \omega_1 t_1 + \dots + \omega_m t_m$ and the integration over multi-indices $\int dt = \int dt_1 \dots \int dt_m$ and correspondingly for $\omega't'$ and $\int dt'$.² The inverse Fourier transform of (2.1a) is given by

$$f(t', t) = \frac{1}{(2\pi)^{2m}} \int d\omega \int d\omega' e^{-i(\omega't' - \omega t)} f(\omega', \omega). \quad (2.1b)$$

Imaginary time

For a function $f(\tau'|\tau)$ of m incoming particles at imaginary times $i\tau = (i\tau_1, \dots, i\tau_m)$ and m outgoing ones at imaginary times $i\tau' = (i\tau'_1, \dots, i\tau'_m)$, with $\tau_i, \tau'_i \in [0, \beta]$, we define its discrete, imaginary-frequency Fourier components $f(\omega'_n|\omega_n)$, with $\omega_n = (\omega_{n_1}, \dots, \omega_{n_m})$ and $\omega'_n = (\omega'_{n_1}, \dots, \omega'_{n_m})$, with imaginary Matsubara frequencies³ $\omega_n = iT\pi(2n+1)$, with $n \in \mathbb{Z}$,

¹ To simplify notation, we use the same symbol for a function and its Fourier transform. Which one is meant will be clear from the context or from its specified argument.

² Here and in the following, an integration without specified boundaries always runs from $-\infty$ to ∞ .

³ We consider here only the fermionic case, which suffices for our applications.

via

$$f(\omega'_n, \omega_n) = \int d\tau \int d\tau' e^{(\omega'_n \tau' - \omega_n \tau)} f(\tau', \tau), \quad (2.2a)$$

where $\omega_n \tau = \omega_{n_1} \tau_1 + \dots + \omega_{n_m} \tau_m$ and the integration over multi-indices $\int d\tau = \int d\tau_1 \dots \int d\tau_m$ and correspondingly for $\omega'_n \tau'$ and $\int d\tau'$. The inverse Fourier transform of (2.2a) is given by

$$f(\tau', \tau) = \frac{1}{\beta^{2m}} \sum_{\omega_n} \sum_{\omega'_n} e^{-(\omega'_n \tau' - \omega_n \tau)} f(\omega'_n, \omega_n), \quad (2.2b)$$

where $\sum_{\omega_n} = \sum_{\omega_{n_1}} \dots \sum_{\omega_{n_m}}$, etc.

2.1.2 Structure of the Hamiltonian

In this thesis, we will consider Hamiltonians of the generic form

$$H = H_0 + H_{\text{int}} = \sum_{q'_1 q_1} \left(h_{q'_1 q_1} + \sigma \frac{B}{2} \right) c_{q'_1}^\dagger c_{q_1} + \frac{1}{4} \sum_{q'_1 q'_2 q_1 q_2} \bar{v}_{q'_1 q'_2 | q_1 q_2} c_{q'_1}^\dagger c_{q'_2}^\dagger c_{q_2} c_{q_1}, \quad (2.3)$$

with the quadratic part H_0 and the interacting part H_{int} . The indices q'_1, \dots, q_2 are composite quantum numbers $q = (i, \sigma, s)$ consisting of site $i \in \mathbb{Z}$, spin $\sigma \in \{+, -\}$ and band index $s \in \mathbb{N}$. All our applications will use a real Hamiltonian, i.e. $h, \bar{v} \in \mathbb{R}$, and in particular the quadratic part is symmetric

$$h_{q_1 q_2} = h_{q_2 q_1}. \quad (2.4)$$

The interaction $\bar{v}_{q'_1 q'_2 | q_1 q_2}$ is antisymmetric, i.e. it is invariant under exchange of two incoming or two outgoing particles,

$$\bar{v}_{q'_1 q'_2 | q_1 q_2} = -\bar{v}_{q'_2 q'_1 | q_1 q_2} = -\bar{v}_{q'_1 q'_2 | q_2 q_1}. \quad (2.5a)$$

Furthermore, the interaction is invariant w.r.t. swapping incoming and outgoing particles,

$$\bar{v}_{q'_1 q'_2 | q_1 q_2} = \bar{v}_{q_1 q_2 | q'_1 q'_2}. \quad (2.5b)$$

As we will discuss in Sec. 2.2.4, this property is related to time-reversal symmetry.

In addition to the properties (2.4) - (2.5b) that affect all quantum numbers on an equal footing, we also assume that $h_{q'_1 q_1}$ and $\bar{v}_{q'_1 q'_2 | q_1 q_2}$ are $SU(2)$ symmetric in spin space. In particular, we have spin conservation and spin flip symmetry

$$\bar{v}_{\sigma'_1 \sigma'_2 | \sigma_1 \sigma_2} \sim \delta_{\sigma'_1 + \sigma'_2 | \sigma_1 + \sigma_2}, \quad (2.6a)$$

$$\bar{v}_{\sigma'_1 \sigma'_2 | \sigma_1 \sigma_2} = \bar{v}_{\bar{\sigma}'_1 \bar{\sigma}'_2 | \bar{\sigma}_1 \bar{\sigma}_2}, \quad (2.6b)$$

where $\bar{\sigma} = -\sigma$ denotes the flipped spin.

In most of our applications,⁴ the Hamiltonian (2.3) will consist of a finite, one-dimensional central region connected to two non-interacting leads on both ends, see Fig. 2.1. Therefore we also often decompose the Hamiltonian via

$$H = H_L + H_{LC} + H_c + H_{CR} + H_R, \quad (2.7)$$

⁴ except for some disorder calculations in Sec. 6 that use a finite system

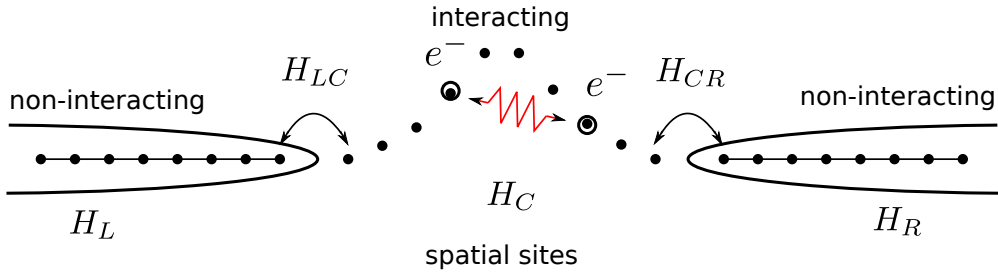


Figure 2.1 Schematic of our generic physical setup, consisting of an interacting, inhomogeneous center region described by H_C , connected via the coupling terms H_{LC} and H_{CR} on both sides to non-interacting leads H_L and H_R .

where $H_{L/R}$ are the Hamiltonians of the left/right lead, H_c is the Hamiltonian of the central region and H_{LC} and H_{CR} are the respective couplings. In the following, we use the convention that the central region lies between sites $-N$ and N , i.e. it consists of $2N + 1$ sites.

2.1.3 Heisenberg operators

For an operator A we define the time dependent operator $A_H(t)$ for a real time t in the Heisenberg picture as

$$A_H(t) = e^{-iH(t-t_i)} A e^{-iH(t-t_i)}, \quad (2.8)$$

where t_i is some initial time (in our applications $t_i = -\infty$) and H is the Hamiltonian of the system. For Matsubara calculations, we consider the evolution in imaginary time $t = i\tau$ via

$$A_{\mathcal{H}}(\tau) = e^{-\mathcal{H}(\tau_i-\tau)} A e^{-\mathcal{H}(\tau-\tau_i)}, \quad (2.9)$$

where we use the modified Matsubara Hamiltonian $\mathcal{H} = H - \mu N$, with the number operator N and the chemical potential μ . This facilitates the treatment of imaginary time τ and inverse temperature β on the same footing.

In the following, we will sometimes drop the subscript H or \mathcal{H} for sake of compactness. If not specified otherwise, time dependent operators are always meant to be understood in the Heisenberg picture.

2.1.4 Expectation values

The expectation value of an observable A at time t is generically given by

$$\langle A \rangle(t) := \text{Tr}[A\rho(t)], \quad (2.10)$$

where $\rho(t)$ is the density matrix of the system. If we know the value of $\rho_0 = \rho(t_i)$ for an initial time t_i and assume the Hamiltonian to be time independent (as will be the case for all our applications), the time dependence of $\rho(t)$ is given by the Heisenberg equation of motion

$$\rho(t) = e^{-iH(t-t_i)} \rho_0 e^{-iH(t_i-t)}. \quad (2.11)$$

Therefore, the expectation value of A is given by

$$\langle A \rangle(t) = \text{Tr}[A_H(t)\rho_0] = \langle A_H(t) \rangle, \quad (2.12)$$

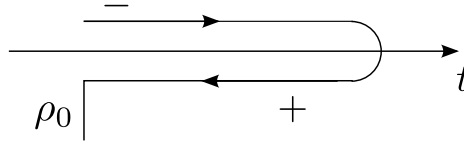


Figure 2.2 Double time contour with forward “-” branch and backward “+” branch and initial distribution ρ_0

where in the last step we have introduced the general notation $\langle \cdot \rangle := \text{Tr}[\cdot \rho_0]$.

In thermal equilibrium, the density matrix is of Gibbs form

$$\rho_0 = \rho_{\text{eq}} \equiv \frac{e^{-\beta(H-\mu N)}}{\text{Tr} e^{-\beta(H-\mu N)}}, \quad (2.13)$$

with $\beta = 1/T$ being the inverse temperature (we set the Boltzmann constant $k_B = 1$), μ the chemical potential and N being the number operator. In this case, ρ_0 commutes with the Hamiltonian and therefore yields a constant density matrix $\rho(t) = \rho_0$ for all times t .

In the non-equilibrium steady-state approach, we assume that at $t_i \rightarrow -\infty$ our system was in a product state

$$\rho_0 = \rho_0^c \otimes \rho_0^L \otimes \rho_0^R, \quad (2.14)$$

consisting of some initial state of the finite central region ρ_0^c which we do not further specify, as well as the initial state of the infinite leads in thermal equilibrium

$$\rho_0^\alpha = \frac{e^{-\beta(H_\alpha - \mu_\alpha N_\alpha)}}{\text{Tr} e^{-\beta(H_\alpha - \mu_\alpha N_\alpha)}}, \quad (2.15)$$

where H_α , N_α , and μ_α with $\alpha \in \{L, R\}$ are the Hamiltonian, number operator, and the chemical potential of the left/right lead, respectively. Since $t_i \rightarrow -\infty$, the value of the initial density matrix of the *finite* central region ρ_0^c does not matter⁵: At the time where we observe the system, the influence of the initial state of the central region is already decayed and a steady-state with constant current through the central region has emerged.

2.1.5 Keldysh conventions

Contour and Keldysh indices

In the following, we specify the conventions used for contour and Keldysh indices. We denote indices living on the forward contour by “-” and indices on the backward contour by “+”, see Fig. 2.2. As convention for the Keldysh rotation of a tensor object A we use

$$A^{\alpha\alpha'} = \sum_{j,j'} (D^{-1})^{\alpha|j} A^{jj'} D^{j'|\alpha'}, \quad (2.16)$$

where $j = (j_1, \dots, j_n)$ with $j_i \in \{-, +\}$ are multi-indices in contour space, and $\alpha = (\alpha_1, \dots, \alpha_n)$ with $\alpha_i \in \{1, 2\}$ are multi-indices in Keldysh space. Furthermore, we use

⁵ We assume here that all eigenstates of the central region are coupled to the leads and therefore the initial distribution of the central region can decay.

the definition

$$D^{j|\alpha} = \prod_{k=1}^n D^{j_k|\alpha_k}, \quad (2.17)$$

where the elementary 2×2 rotation matrix between contour- and Keldysh space is defined by

$$D = \begin{pmatrix} D^{-|1} & D^{-|2} \\ D^{+|1} & D^{+|2} \end{pmatrix} = \frac{1}{\sqrt{2}} \begin{pmatrix} 1 & 1 \\ -1 & 1 \end{pmatrix}, \quad (2.18a)$$

and correspondingly

$$D^{-1} = \begin{pmatrix} (D^-)^{1|-} & (D^-)^{1|+} \\ (D^-)^{2|-} & (D^-)^{2|+} \end{pmatrix} = \frac{1}{\sqrt{2}} \begin{pmatrix} 1 & -1 \\ 1 & 1 \end{pmatrix}. \quad (2.18b)$$

2.1.6 Structure of the bare vertex

The interaction \bar{v} of the Hamiltonian introduced in Sec. 2.1.2, gives rise to a two-particle bare vertex ν in the action.

Matsubara

In the Matsubara case, this bare vertex is given by

$$\nu_{q'_1 q'_2 | q_1 q_2}(\tau'_1, \tau'_2 | \tau_1, \tau_2) = \delta(\tau'_1 - \tau'_2) \delta(\tau'_2 - \tau_1) \delta(\tau_1 - \tau_2) \bar{v}_{q'_1 q'_2 | q_1 q_2} \quad (2.19)$$

and correspondingly in frequency space

$$\nu_{q'_1 q'_2 | q_1 q_2}(\omega'_{n_1}, \omega'_{n_2} | \omega_{n_1}, \omega_{n_2}) = \beta \delta_{n'_1 + n'_2 | n_1 + n_2} \bar{v}_{q'_1 q'_2 | q_1 q_2}. \quad (2.20)$$

Keldysh

In the Keldysh case, one obtains an additional $(\mathbb{Z}_2)^4$ Keldysh structure, stemming from the doubling of the time contour, see Sec. 2.1.5. Expressing the bare vertex in contour space by symmetrically placing one interaction component on the forward and one on the backward branch yields

$$\nu_{q'_1 q'_2 | q_1 q_2}^{j'_1 j'_2 | j_1 j_2}(t'_1, t'_2 | t_1, t_2) = (-j'_1) \delta(t'_1 - t'_2) \delta(t'_2 - t_1) \delta(t_1 - t_2) \delta_{j'_1 = j'_2 = j_1 = j_2} \bar{v}_{q'_1 q'_2 | q_1 q_2}. \quad (2.21)$$

Rotation into Keldysh space yields correspondingly

$$\nu_{q'_1 q'_2 | q_1 q_2}^{\alpha'_1 \alpha'_2 | \alpha_1 \alpha_2}(t'_1, t'_2 | t_1, t_2) = \begin{cases} \delta(t'_1 - t'_2) \delta(t'_2 - t_1) \delta(t_1 - t_2) \frac{1}{2} \bar{v}_{q'_1 q'_2 | q_1 q_2}, & \text{if } \alpha'_1 + \alpha'_2 + \alpha_1 + \alpha_2 \text{ odd} \\ 0 & \text{else,} \end{cases} \quad (2.22)$$

which reads in frequency space

$$\nu_{q'_1 q'_2 | q_1 q_2}^{\alpha'_1 \alpha'_2 | \alpha_1 \alpha_2}(\omega'_{n_1}, \omega'_{n_2} | \omega_{n_1}, \omega_{n_2}) = \begin{cases} 2\pi \delta(\omega'_{n_1} + \omega'_{n_2} - \omega_{n_1} - \omega_{n_2}) \frac{1}{2} \bar{v}_{q'_1 q'_2 | q_1 q_2}, & \text{if } \alpha'_1 + \alpha'_2 + \alpha_1 + \alpha_2 \text{ odd} \\ 0 & \text{else.} \end{cases} \quad (2.23)$$

In the following, we will use the notation ν also for the reduced bare vertex, i.e. the bare vertex without frequency structure. For this reduced quantity, we have $\nu = \bar{\nu}$ in the Matsubara and

$$\nu^{\alpha'_1 \alpha'_2 | \alpha_1 \alpha_2} = \begin{cases} \frac{1}{2} \bar{\nu} & \text{for } \alpha'_1 + \alpha'_2 + \alpha_1 + \alpha_2 \text{ odd} \\ 0 & \text{else} \end{cases} \quad (2.24)$$

in the Keldysh case.

2.1.7 Definition of Green's functions

We define the general n -particle Green's function as

$$G_{k'k} = \begin{cases} (-1)^n \langle T_\tau [c_{q'_1}(\tau'_1) \cdots c_{q'_n}(\tau'_n) c_{q_n}^\dagger(\tau_n) \cdots c_{q_1}^\dagger(\tau_1)] \rangle & \text{Matsubara} \\ (-i)^n \langle T_c [c_{q'_1}^{j'_1}(t'_1) \cdots c_{q'_n}^{j'_n}(t'_n) c_{q_n}^{\dagger j_n}(t_n) \cdots c_{q_1}^{\dagger j_1}(t_1)] \rangle & \text{Keldysh,} \end{cases} \quad (2.25)$$

where $k = (\tau, q)$ in the Matsubara case and $k = (t, j, q)$ in the Keldysh case. The symbols T_τ and T_c denote time ordering, either on the imaginary time axis or on the real double time contour. Operators with later times (in the Keldysh case with times further along the double contour, see Fig. 2.2) are placed to the left of operators with earlier times.⁶ At equal time, creation operators are ordered to the left of annihilation operators. As usual, T and T_c yield an overall “ $-$ ” sign if the resulting time ordering is an odd permutation of the initial order, and a “ $+$ ” sign if it is an even one.

2.1.8 Compact notation for integration and sums

In the following, we will frequently have to integrate over real or imaginary times and correspondingly integrate over real frequencies or sum over Matsubara frequencies. To be able to use an efficient combined notation, we will write

$$\int d\mathfrak{k} = \begin{cases} \int dt & \text{Keldysh,} \\ \int d\tau & \text{Matsubara,} \end{cases} \quad (2.26)$$

and

$$\sum_\omega = \begin{cases} \frac{1}{\beta} \sum_{\omega_n} & \text{Matsubara,} \\ \frac{1}{2\pi} \int d\omega & \text{Keldysh.} \end{cases} \quad (2.27)$$

Notation-wise, we will often combine these integrations/summations with a summation over all other quantum numbers

$$\sum_k = \sum_{\tilde{q}} \begin{cases} \int d\mathfrak{k} & \text{time} \\ \sum_\omega & \text{frequency,} \end{cases} \quad (2.28)$$

with the composite index k consisting of time \mathfrak{k} or frequency ω and the rest of the appropriate indices q . In the Matsubara case, $q = (i, \sigma, s)$, it consists of the indices for site, spin and

⁶ Therefore, on the double time contour, the forward branch is internally time-ordered, while the backward branch is internally anti-time-ordered.

band. In the Keldysh case, we have an additional time contour index j or Keldysh index α , i.e. $q = (j, q)$ or $q = (\alpha, q)$, respectively.

2.1.9 Generating functions and definition of one particle irreducible vertices

In this subsection, we use an efficient combined Matsubara/Keldysh notation similar to the one introduced by Karrasch in Ref. [Kar10]. While most of our conventions are the same as in [Kar10], we differ in the definition of the vertex functions in the Keldysh formalism, in order to be consistent with the conventions introduced in Ref. [Jak09], which were used in previous publications [HBSvD17, SBvD17] of our group. All factors in curly brackets $\{\dots\}$ are only present in the Keldysh formulation. Furthermore we define the scalar product

$$(\bar{\psi}, \psi') = \{i\} \sum_k \bar{\psi}_k \psi'_k. \quad (2.29)$$

The Green's functions defined in (2.25) can also be obtained by using a generating function. To establish this formalism, we first define the partition function

$$Z = \int D\bar{\psi}\psi \exp[S], \quad (2.30)$$

where $\{\psi\}$ is a set of fermionic Grassmann variables, carrying appropriate time and quantum labels q , and the action $S = S_0 - \{i\}S_{\text{int}}$ consists of a quadratic part

$$S_0 = i \sum_{k,k'} \bar{\psi}_k [G_0^{-1}]_{kk'} \psi_{k'} \quad (2.31)$$

and an interaction part

$$S_{\text{int}} = \frac{1}{4} \sum_{k'_1 k'_2 k_1 k_2} \nu_{k'_1 k'_2 k_1 k_2} \bar{\psi}_{k'_1} \bar{\psi}_{k'_2} \psi_{k_2} \psi_{k_1}. \quad (2.32)$$

The specific form of the bare propagator G_0 resulting from the lead - central region - lead structure of the Hamiltonian (2.7) is given in Sec. 2.1.12. In the Keldysh case, we have $Z = 1$ since, in the absence of external sources, any evolution on the forward branch is exactly rewound on the backwards branch. By coupling the fields $\bar{\psi}, \psi$ to external sources $\bar{\eta}, \eta$, we can define the generating function

$$W(\bar{\eta}, \eta) = \frac{1}{Z} \int D\bar{\psi}\psi \exp \left(S_0 - \{i\}S_{\text{int}} - (\bar{\psi}, \eta) - (\bar{\eta}, \psi) \right). \quad (2.33)$$

Using this generating function, the m -particle Green's functions defined in (2.25) can be obtained from W via

$$G_{k'k} = \{-i\}^m \frac{\delta^m}{\delta \bar{\eta}_{k'_1} \dots \delta \bar{\eta}_{k'_m}} \frac{\delta^m}{\delta \eta_{k_m} \dots \delta \eta_{k_1}} W(\bar{\eta}, \eta) \Big|_{\bar{\eta}=\eta=0}. \quad (2.34)$$

If we furthermore define $W^c = \ln W$, we can obtain the *connected* m -particle Green's functions as

$$G_{k'k}^c = \{-i\}^m \frac{\delta^m}{\delta \bar{\eta}_{k'_1} \dots \delta \bar{\eta}_{k'_m}} \frac{\delta^m}{\delta \eta_{k_m} \dots \delta \eta_{k_1}} W^c(\bar{\eta}, \eta) \Big|_{\bar{\eta}=\eta=0}. \quad (2.35)$$

Applying a Legendre transformation on W^c in $(\bar{\eta}, \eta)$, we obtain the generating function Γ for the one-particle irreducible (1PI) vertices

$$\Gamma(\bar{\phi}, \phi) = -W^c(\bar{\eta}, \eta) - (\bar{\phi}, \eta) - (\bar{\eta}, \phi) + (\bar{\phi}, G_0^{-1}\phi), \quad (2.36)$$

with the conjugate fields

$$\phi_k = -\{-i\} \frac{\delta}{\delta \bar{\eta}_k} W^c, \quad (2.37a)$$

$$\bar{\phi}_k = \{-i\} \frac{\delta}{\delta \eta_k} W^c. \quad (2.37b)$$

From this function the 1PI vertices can be obtained via

$$\gamma_{k'_1 k} = \{(-i)(-1)^m\} \frac{\delta}{\delta \bar{\phi}_{k'_1} \dots \bar{\phi}_{k'_m}} \frac{\delta}{\delta \phi_{k_m} \dots \phi_{k_1}} \Gamma(\bar{\phi}, \phi) \Big|_{\bar{\phi}=\phi=0}. \quad (2.38)$$

Note that the definition (2.38) differs from the one given in Ref. [Kar10]: Instead of $\{-i\}^m$ we set the prefactor to $\{(-i)(-1)^m\}$, in order to obtain the same vertex conventions in the Keldysh formalism as in Ref. [Jak09]. Correspondingly, this implies for the self-energy

$$\Sigma_{k'_1 | k_1} = -\{-1\} \gamma_{k'_1 | k_1}. \quad (2.39)$$

This choice of sign ensures that the Dyson equations take the form as given in (2.73, 2.74).

2.1.10 Time translational invariance

Since we consider only equilibrium or steady-state applications, all our objects will be translationally invariant in time, or correspondingly the sum of incoming and outgoing frequencies will be preserved. Therefore, we can define reduced objects depending on one frequency less than the original ones. For these reduced objects, we will use the following conventions (we suppress here all indices except frequencies):

Keldysh

$$G(\omega'_1, \dots, \omega'_n | \omega_1, \dots, \omega_n) \equiv 2\pi \delta(\omega'_1 + \dots + \omega'_n - \omega_1 - \dots - \omega_n) \times G(\omega'_2, \dots, \omega'_n | \omega_1, \dots, \omega_n), \quad (2.40a)$$

$$\gamma(\omega'_1, \dots, \omega'_n | \omega_1, \dots, \omega_n) \equiv 2\pi \delta(\omega'_1 + \dots + \omega'_n - \omega_1 - \dots - \omega_n) \times \gamma(\omega'_2, \dots, \omega'_n | \omega_1, \dots, \omega_n), \quad (2.40b)$$

Matsubara

$$G(\omega'_{n_1}, \dots, \omega'_{n_m} | \omega_{n_1}, \dots, \omega_{n_m}) \equiv \beta \delta_{n'_1 + \dots + n'_m - n_1 - \dots - n_m} \times G(\omega'_{n_2}, \dots, \omega'_{n_m} | \omega_{n_1}, \dots, \omega_{n_m}) \quad (2.41a)$$

$$\gamma(\omega'_{n_1}, \dots, \omega'_{n_m} | \omega_{n_1}, \dots, \omega_{n_m}) \equiv \beta \delta_{n'_1 + \dots + n'_m - n_1 - \dots - n_m} \times \gamma(\omega'_{n_2}, \dots, \omega'_{n_m} | \omega_{n_1}, \dots, \omega_{n_m}). \quad (2.41b)$$

2.1.11 Structure of one-particle objects in Keldysh space

In contour space, the four components of the one-particle Green's function and the self-energy are linearly dependent

$$G^{--} - G^{-+} - G^{+-} + G^{++} = 0, \quad (2.42a)$$

$$\Sigma^{--} + \Sigma^{-+} + \Sigma^{+-} + \Sigma^{++} = 0. \quad (2.42b)$$

The rotation to Keldysh space (2.16), makes use of this dependence, yielding⁷

$$0 = G^{11} = \frac{1}{2} \left(G^{--} - G^{-+} - G^{+-} + G^{++} \right), \quad (2.43a)$$

$$G^A = G^{12} = \frac{1}{2} \left(G^{--} + G^{-+} - G^{+-} - G^{++} \right), \quad (2.43b)$$

$$G^R = G^{21} = \frac{1}{2} \left(G^{--} - G^{-+} + G^{+-} - G^{++} \right), \quad (2.43c)$$

$$G^K = G^{22} = \frac{1}{2} \left(G^{--} + G^{-+} + G^{+-} + G^{++} \right). \quad (2.43d)$$

and

$$\Sigma^K = \Sigma^{11} = \frac{1}{2} \left(\Sigma^{--} - \Sigma^{-+} - \Sigma^{+-} + \Sigma^{++} \right) \quad (2.44a)$$

$$\Sigma^R = \Sigma^{12} = \frac{1}{2} \left(\Sigma^{--} + \Sigma^{-+} - \Sigma^{+-} - \Sigma^{++} \right) \quad (2.44b)$$

$$\Sigma^A = \Sigma^{21} = \frac{1}{2} \left(\Sigma^{--} - \Sigma^{-+} + \Sigma^{+-} - \Sigma^{++} \right) \quad (2.44c)$$

$$0 = \Sigma^{22} = \frac{1}{2} \left(\Sigma^{--} + \Sigma^{-+} + \Sigma^{+-} + \Sigma^{++} \right). \quad (2.44d)$$

Therefore, instead of four components we only have to keep track of three, the so called retarded, advanced and Keldysh components.

2.1.12 Form of the bare propagator

The generic Hamiltonian stated above in Sec. 2.1.2 yields an action of the form given by Eqs. (2.31),(2.32), where the spatial range of the composite indices k'_1, \dots, k_2 contains the whole system. The bare propagator G_0 , e.g. in the Matsubara formalism, is then determined by

$$G_0(\omega_n) = \frac{1}{\omega_n - \mathcal{H}_0}, \quad (2.45)$$

where

$$[\mathcal{H}_0]_{q'q} = [H_0 - \mu N]_{q'q} = h_{q'q} + \sigma \frac{B}{2} - \mu \quad (2.46)$$

is the full one-particle part of the Matsubara Hamiltonian, including the leads.

In our applications, it suffices to compute both the bare propagator $(G_0)_{k'k}$ and the full propagator $G_{k'k}$ with the indices k', k lying in the central region. Since only the central region of the system contains interactions, the contribution of the leads can be integrated out analytically and absorbed into a self-energy contribution Σ_{lead} , see c.f. [Kar06]. Therefore,

⁷ Eqs. (2.43a),(2.44d) only hold, if the time arguments t', t of $G(t', t) / \Sigma(t', t)$ do not coincide. For the case of equal times, see the discussion in Sec. 2.1.13.

the bare Matsubara propagator (2.45) with k', k in the central region can be written as

$$(G_0)_{k'k}(\omega_n) = \left[\frac{1}{\omega_n - \mathcal{H}_{0c} - \Sigma_{\text{lead}}(\omega_n)} \right]_{k'k}, \quad (2.47)$$

where $\mathcal{H}_{0c} = H_{0c} - \mu N_c$ is the one-particle part of the Matsubara Hamiltonian of the central region without the leads and the lead self-energy is given by

$$\Sigma_{\text{lead}ij}^p(\omega_n) = \left(\delta_{-Ni} \delta_{-Nj} + \delta_{Ni} \delta_{Nj} \right) f^p(\omega_n + \mu), \quad (2.48)$$

with the composite spin and band index $p = (\sigma, s)$. The form of the function $f^p(\omega)$ depends on the Hamiltonian of the leads and their coupling terms to the central region. In case of a tight-binding chain as lead, the Hamiltonian of the left lead takes the form

$$H_L = -\tau \sum_{j < -N-1, \sigma, p} [a_{jp}^\dagger a_{j+1p} + a_{j+1p}^\dagger a_{jp}] + \sum_{j < -N} a_{jp}^\dagger a_{jp} \left(\frac{\sigma}{2} B + V_s \right), \quad (2.49)$$

with τ being the hopping amplitude and V_s the overall band offset depending on the index s . The Hamiltonian for the right lead H_R looks analogous, with site index $j > N$. Computing the self-energy contribution of the leads to the one-dimensional central region $[-N, N]$, one obtains⁸ (c.f. [Kar06])

$$f^p(\omega) = \frac{1}{2} \left[\omega^p - i \sqrt{4\tau^2 - (\omega^p)^2} \right], \quad (2.50)$$

with

$$\omega^p = \omega - \frac{\sigma}{2} B - V_s. \quad (2.51)$$

In the Keldysh case, one can proceed analogously [Jak09]. Here one obtains for the bare propagator connecting two sites within the central region

$$G_0^R = \frac{1}{\omega - H_{0c} - \Sigma_{\text{lead}}^R(\omega)}, \quad (2.52a)$$

$$G_0^A = [G_0^R]^\dagger, \quad (2.52b)$$

$$G_0^K = G_0^R \Sigma_{\text{lead}}^K G_0^A, \quad (2.52c)$$

where Σ_{lead}^R and Σ_{lead}^K are given by

$$\Sigma_{\text{lead}}^{Rp}(\omega)_{ij} = \left(\delta_{-Ni} \delta_{-Nj} + \delta_{iN} \delta_{jN} \right) f^p(\omega), \quad (2.53)$$

and

$$\Sigma_{\text{lead}}^{Kp}(\omega)_{ij} = -i \left(\delta_{-Ni} \delta_{-Nj} (1 - 2n_l(\omega)) + \delta_{iN} \delta_{jN} (1 - 2n_r(\omega)) \right) \Gamma^p(\omega), \quad (2.54)$$

with

$$\Gamma^p(\omega) = -2 \text{Im} f^p(\omega) \quad (2.55)$$

$$= \theta(2\tau - |\omega^p|) \sqrt{4\tau^2 - (\omega^p)^2}, \quad (2.56)$$

⁸ Here and in the following, $\sqrt{\dots}$ always denotes the principal branch of the complex square root. In particular, for a complex number z with positive real part, $\sqrt{-z} = i\sqrt{z}$.

and $n_{l/r}(\omega)$ denotes the initial equilibrium Fermi distribution with chemical potential $\mu_{l/r}$ and temperature $T_{l/r}$ of the left/right lead.

In the case of thermal equilibrium, which will be the relevant case for all applications in this thesis (except the non-equilibrium fRG flow equations given in Sec. 2.4.5 and App. A.3), the Keldysh component of any single particle propagator (non-interacting or interacting) fulfills the fluctuation-dissipation theorem (2.105).

There is a small caveat concerning the lead self-energy and hybridization function. In a fRG approach, it can be advantageous to introduce the flow parameter Λ also in the lead part of the quadratic action, in order to obtain a smoother fRG flow. This implies that the form of $f^p(\omega)$ in (2.50) and correspondingly the form of $\Gamma^p(\omega)$ in (2.56) is modified by the flow parameter. In our applications below, this is the case for the Keldysh hybridization flow, see Sec. 2.3.2. The modified forms $f^{p\Lambda}(\omega)$ and $\Gamma^{p\Lambda}(\omega)$ are specified in Eq. (2.130).

2.1.13 Equal time in Keldysh formalism

In this subsection, we take a brief look on what happens in the case of equal times occurring in propagators. This deserves a small subsection by itself, since [Jak09, Sch17] comment only novercally on this case. Let us look at a small example to illustrate the arising problem. Consider the first order (Hartree) contribution to the self-energy

$$\Sigma_{k'_1 k_1} = -\{i\} \sum_{k'_2, k_2} (G_0)_{k_2 k'_2} \nu_{k'_1 k'_2 | k_1 k_2}. \quad (2.57)$$

For concreteness, we look at the retarded component $\Sigma^R = \Sigma^{12}$. If we compute it in Keldysh space, we obtain

$$\Sigma_{q'_1 q_1}^R(\omega) = -\frac{i}{4\pi} \sum_{q'_2, q_2} \int d\omega' [(G_0)^{11} + (G_0)^{22}]_{q_2 q'_2}(\omega') \bar{v}_{q'_1 q'_2 | q_1 q_2}, \quad (2.58)$$

where we used the structure of the bare vertex (2.23). If we now naively insert the Keldysh structure of the Green's function (2.43), we obtain the wrong result

$$\Sigma_{q'_1 q_1}^R(\omega) = \frac{1}{4\pi i} \sum_{q'_2, q_2} \bar{v}_{q'_1 q'_2 | q_1 q_2} \int d\omega' (G_0)_{q_2 q'_2}^K(\omega'), \quad (2.59)$$

or after transforming to contour space

$$\Sigma_{q'_1 q_1}^R(\omega) = \frac{1}{8\pi i} \sum_{q'_2, q_2} \bar{v}_{q'_1 q'_2 | q_1 q_2} \int d\omega' [G_0^{--} + G_0^{-+} + G_0^{+-} + G_0^{++}]_{q_2 q'_2}(\omega'). \quad (2.60)$$

Now let us do the computation directly in contour space. We obtain

$$\Sigma_{q'q}^{++}(\omega) = -\frac{1}{2\pi i} \sum_{q'_2, q_2} \int d\omega' \bar{v}_{q'q'_2 | qq_2} (G_0)_{q_2 q'_2}^{++}(\omega'), \quad (2.61a)$$

$$\Sigma_{q'q}^{--}(\omega) = \frac{1}{2\pi i} \sum_{q'_2, q_2} \int d\omega' \bar{v}_{q'q'_2 | qq_2} (G_0)_{q_2 q'_2}^{--}(\omega'), \quad (2.61b)$$

$$\Sigma_{q'q}^{-+}(\omega) = \Sigma^{+-}(\omega) = 0, \quad (2.61c)$$

where we used the structure of the bare vertex in contour space (2.21). If we furthermore use

$$\Sigma^R(\omega) = \frac{1}{2} [\Sigma^{--} - \Sigma^{-+} - \Sigma^{+-} - \Sigma^{++}] (\omega), \quad (2.62)$$

from Eq. (2.44b), we get the retarded self-energy

$$\Sigma_{q'q}^R(\omega) = \frac{1}{4\pi i} \sum_{q'_2 q_2} \bar{v}_{q'q'_2|qq_2} \int d\omega' [(G_0)^{--} + (G_0)^{++}]_{q_2 q'_2}(\omega'), \quad (2.63)$$

in contrast to the naive result (2.60).

To check that (2.63) is indeed the correct formula, we can evaluate the contour Green's functions. Using time translational invariance, we get for the evaluation at equal times

$$(G_0)_{q_2 q'_2}^{--}(t, t) = (G_0)_{q_2 q'_2}^{--}(0, 0) = (-i) \langle T_c [a_{q_2}^-(0) a_{q'_2}^{-\dagger}(0)] \rangle_0 = i \langle a_{q_2}^\dagger a_{q'_2} \rangle_0 \quad (2.64a)$$

$$(G_0)_{q_2 q'_2}^{++}(t, t) = (G_0)_{q_2 q'_2}^{++}(0, 0) = (-i) \langle T_c [a_{q_2}^+(0) a_{q'_2}^{+\dagger}(0)] \rangle_0 = i \langle a_{q_2}^\dagger a_{q'_2} \rangle_0 \quad (2.64b)$$

$$(G_0)_{q_2 q'_2}^{-+}(t, t) = (G_0)_{q_2 q'_2}^{-+}(0, 0) = (-i) \langle T_c [a_{q_2}^-(0) a_{q'_2}^{+\dagger}(0)] \rangle_0 = i \langle a_{q_2}^\dagger a_{q'_2} \rangle_0 \quad (2.64c)$$

$$(G_0)_{q_2 q'_2}^{+-}(t, t) = (G_0)_{q_2 q'_2}^{+-}(0, 0) = (-i) \langle T_c [a_{q_2}^+(0) a_{q'_2}^{-\dagger}(0)] \rangle_0 = -i \langle a_{q_2}^\dagger a_{q'_2} \rangle_0. \quad (2.64d)$$

Thus, using

$$\begin{aligned} \frac{1}{2\pi} \int d\omega' [(G_0)_0^{--} + (G_0)_0^{++}]_{q_2 q'_2} &= [(G_0)_0^{--} + (G_0)_0^{++}]_{q_2 q'_2}(t, t) \\ &= 2i \langle a_{q_2}^\dagger a_{q'_2} \rangle_0 = 2i \delta_{q_2 q'_2} (n_0)_{q_2}, \end{aligned} \quad (2.65)$$

with the non-interacting particle number $(n_0)_q$, we get for (2.63)

$$\Sigma_{q'q}^R(\omega) = \sum_{q_2} \bar{v}_{q'q'_2|qq_2} (n_0)_{q_2}. \quad (2.66)$$

In case of a spin conserving Hamiltonian with a purely constant onsite and one-band interaction

$$\bar{v}_{j'j'_2|jj_2}^{\sigma'\sigma'_2|\sigma\sigma_2} = U \delta_{j'=j'_2=j_2} \left(\delta_{\sigma'\sigma} \delta_{\sigma'_2\sigma_2} - \delta_{\sigma'\sigma_2} \delta_{\sigma'_2\sigma} \right), \quad (2.67)$$

we obtain

$$\Sigma_{ji}^{R\sigma}(\omega) = \delta_{ij} U (n_0)_{j\bar{\sigma}}, \quad (2.68)$$

with $(n_0)_{j\bar{\sigma}}$ being the number of spin $\bar{\sigma}$ particles on site j . This is indeed the correct and well known Hartree result.

This small example shows that one has to be careful applying the Keldysh structure (2.43) and (2.44) when dealing with equal times. Indeed, the arising problem that was illustrated here stems from the wrong assumption

$$\frac{1}{2\pi} \int d\omega G_0^{11}(\omega) = G_0^{11}(t, t) = 0. \quad (2.69)$$

At equal times we have instead (using the relations (2.64))

$$(G_0)_{q'q}^{11}(t, t) = \frac{1}{2} (G_0^{--} - G_0^{-+} - G_0^{+-} + G_0^{++})_{q'q}(t, t) = \frac{i}{2} \langle \{a_q^\dagger, a_{q'}\} \rangle_0 = \frac{i}{2} \delta_{q'q}. \quad (2.70)$$

2.1.14 A brief look at units

At the end of this section, it is a good point to take a step back and take a brief look at the units of the various objects defined in the last subsections. In our chosen formulation we have, in rough order of appearance (we call the unit of energy here E)

$$[H] = [h] = [\bar{v}] = E, \quad (2.71a)$$

$$[c], [c^\dagger] = [c(\mathfrak{k})] = [c^\dagger(\mathfrak{k})] = 0, \quad (2.71b)$$

$$[\nu(\mathfrak{k}'_1, \mathfrak{k}'_2 | \mathfrak{k}_1, \mathfrak{k}_2)] = E^4, \quad (2.71c)$$

$$[\nu(\omega'_1, \omega'_2 | \omega_1, \omega_2)] = 0, \quad (2.71d)$$

$$[S] = [S_0] = [S_{\text{int}}] = [W] = [W^c] = [\Gamma] = 0, \quad (2.71e)$$

$$[G(\mathfrak{k}', \mathfrak{k})] = 0, \quad (2.71f)$$

$$[G(\omega', \omega)] = \frac{1}{E^{2m}}, \quad (2.71g)$$

$$[\bar{\psi}(\mathfrak{k})] = [\psi(\mathfrak{k})] = 0, \quad (2.71h)$$

$$[\bar{\eta}(\mathfrak{k})] = [\eta(\mathfrak{k})] = E, \quad (2.71i)$$

$$[\bar{\phi}(\mathfrak{k})] = [\phi(\mathfrak{k})] = 0, \quad (2.71j)$$

$$\left[\frac{\delta}{\delta \bar{\eta}(\mathfrak{k})} \right] = \left[\frac{\delta}{\delta \eta(\mathfrak{k})} \right] = 0, \quad (2.71k)$$

$$\left[\frac{\delta}{\delta \bar{\phi}(\mathfrak{k})} \right] = \left[\frac{\delta}{\delta \phi(\mathfrak{k})} \right] = E, \quad (2.71l)$$

$$[\gamma(\mathfrak{k}', \mathfrak{k})] = E^{2m}, \quad (2.71m)$$

$$[\gamma(\omega', \omega)] = 0, \quad (2.71n)$$

$$[\gamma(\omega'_2, \dots, \omega'_n | \omega_1, \dots, \omega_n)] = E, \quad (2.71o)$$

$$[G(\omega'_2, \dots, \omega'_n | \omega_1, \dots, \omega_n)] = \frac{1}{E^{2n-1}}, \quad (2.71p)$$

where \mathfrak{k} is either t or τ and ω is either a continuous real (Keldysh) or discrete imaginary frequency (Matsubara). The last two lines (2.71o) - (2.71p) are the reduced quantities from (2.40, 2.41) with one lesser frequency.

2.2 Properties of Green's and vertex functions

In this section, we discuss exact properties of Green's and vertex functions. In particular, we take a look at their various symmetries and analytic properties.

2.2.1 Dyson equation

We can express the full propagator using the bare propagator and the self-energy via the Dyson equation, which reads in the Keldysh case

$$G^R(\omega) = G_0^R + G_0^R \Sigma^R G^R, \quad (2.72)$$

and therefore

$$G^R = \frac{1}{[G_0^R]^{-1} - \Sigma^R}. \quad (2.73)$$

Completely analogously, we obtain for the Matsubara propagator

$$G = \frac{1}{[G_0]^{-1} - \Sigma}. \quad (2.74)$$

2.2.2 Permutation of particles

Let $P \in S_n$ be a permutation of $\{1, \dots, n\}$ and $(-1)^P$ the sign of the permutation. Then, as a direct consequence of the representations (2.34) and (2.36), we get the properties

$$G_{Pk'|k} = G_{k'|Pk} = (-1)^P G_{k'|k}, \quad (2.75a)$$

$$\gamma_{Pk'|k} = \gamma_{k'|Pk} = (-1)^P \gamma_{k'|k}, \quad (2.75b)$$

for both the Matsubara $k = (\omega_n, q)$ and Keldysh $k = (\omega, j, q)$ formulations.

2.2.3 Complex conjugation

Matsubara

In the Matsubara formalism, straight forward complex conjugation of the definition of the multi-particle Green's function (2.25) yields

$$G_{q'q}(\tau', \tau)^* = G_{qq'}(-\tau, -\tau'), \quad (2.76)$$

or correspondingly in frequency space

$$G_{q'q}(\omega'_n, \omega_n)^* = G_{qq'}(-\omega_n, -\omega'_n). \quad (2.77)$$

Analogously, one obtains for the multi-particle vertex

$$\gamma_{q'q}(\omega'_n, \omega_n)^* = \gamma_{qq'}(-\omega_n, -\omega'_n). \quad (2.78)$$

Keldysh

In the Keldysh formalism, by complex conjugating the definition of (2.25), one obtains for the Green's function the following relation in contour space

$$G_{q'q}^{j'j}(t', t)^* = (-1)^n G_{qq'}^{\bar{j}\bar{j}'}(t, t'). \quad (2.79)$$

In Keldysh and frequency space, this leads to the following relations, see Ref. [Jak09]

$$G_{q'q}^{\alpha'|\alpha}(\omega'|\omega)^* = (-1)^{n+\sum_k(\alpha'_k+\alpha_k)} G_{q|q'}^{\alpha|\alpha'}(\omega|\omega'), \quad (2.80a)$$

$$\gamma_{q'q}^{\alpha'|\alpha}(\omega'|\omega)^* = (-1)^{1+\sum_k(\alpha'_k+\alpha_k)} \gamma_{q|q'}^{\alpha|\alpha'}(\omega|\omega'), \quad (2.80b)$$

where α'_k, α_k denote indices in Keldysh space.

In the one-particle case, this yields the well known relations

$$(G^R)^\dagger = G^A, \quad (2.81a)$$

$$(G^K)^\dagger = -G^K, \quad (2.81b)$$

$$(\Sigma^R)^\dagger = \Sigma^A, \quad (2.81c)$$

$$(\Sigma^K)^\dagger = -\Sigma^K. \quad (2.81d)$$

2.2.4 Time reversal

In thermal equilibrium, the type of system that we are interested in exhibits a special symmetry behavior under time-reversal, even when the Hamiltonian itself – in the case of finite magnetic field – is not time-reversal invariant. For the choice of the single particle basis $|q\rangle = |i, \sigma, s\rangle$, this symmetry takes for the multi-particle Green's function the form

$$G_{qq'}^{\{jj'\}}(\mathbf{k}, \mathbf{k}') = G_{\tilde{q}\tilde{q}'}^{\{jj'\}}(\mathbf{k}, \mathbf{k}') \Big|_{\tilde{H}}, \quad (2.82)$$

where the contour indices $\{jj'\}$ are only there in the real time formalism, the tilded quantities are the time-reversed versions of their normal counterparts, and on the r.h.s. $|_{\tilde{H}}$ indicates that the time dependence should be evaluated using the time-reversed Hamiltonian. Note that the formulation (2.82) places a requirement on both the Hamiltonian and the basis $|q\rangle$ used for the single-particle states. It does *not* hold for arbitrary single particle states $|q\rangle$.

To give (2.82) a precise meaning, we define the anti-unitary⁹ time-reversal operator Θ . The action of this operator on the single particle basis states $|p, \sigma\rangle$, with $p = (i, s)$ being the combined quantum numbers of site index i and band index s , and with the spin index $\sigma \in \{-, +\}$, is given by

$$\Theta|p, \sigma\rangle = e^{i\frac{\pi}{2}\sigma}|p, \bar{\sigma}\rangle. \quad (2.83)$$

Correspondingly, its action on creation and annihilation operators takes the form

$$\Theta a_{p,\sigma}^\dagger \Theta^\dagger = e^{i\frac{\pi}{2}\sigma} a_{p,\bar{\sigma}}^\dagger, \quad (2.84a)$$

$$\Theta a_{p,\sigma} \Theta^\dagger = e^{-i\frac{\pi}{2}\sigma} a_{p,\bar{\sigma}}. \quad (2.84b)$$

To simplify notation, we denote the time-reversed states and operators via a tilde, $|\tilde{q}\rangle = \Theta|q\rangle$ and $\tilde{A} = \Theta A \Theta^\dagger$. To prove (2.82) we slightly generalize the argument given by Jakobs in [Jak09] to our more general type of systems. All of the Hamiltonians in our applications below (Secs. 3.2 - 6) are of the general form discussed in Sec. 2.1.2. In particular, all terms that do not explicitly contain the magnetic field are assumed to obey spin conservation, and spin flip symmetry, see Eq. (2.6). Using this property, direct computation shows that the time-reversed Hamiltonian \tilde{H} is equal to the Hamiltonian H with reversed magnetic field:

$$\tilde{H}(B) = H(-B). \quad (2.85)$$

In order to show now (2.82), we note that we can relate the action of the anti-unitary operator Θ on the basis states $|q\rangle$ to a unitary operator, namely $\Omega = e^{-i\pi S_x}$, which is the operator that rotates states by an angle of π in spin space around the x -axis. Its action on the single particle z -axis eigenstates is given by

$$\Omega|p, \sigma\rangle = -i|p, \bar{\sigma}\rangle. \quad (2.86)$$

We note that $\Omega|p, \sigma\rangle$ is proportional to $\Theta|p, \sigma\rangle$, in particular we have

$$|\tilde{q}\rangle = \Theta|p, \sigma\rangle = e^{i\pi(\sigma+\frac{1}{2})}\Omega|p, \sigma\rangle = e^{i\pi(\sigma+\frac{1}{2})}\Omega|q\rangle. \quad (2.87)$$

⁹ Note that the conjugate of a anti-linear operator Θ is defined by $\langle\psi_1|\Theta\psi_2\rangle = \langle\psi_2|\Theta^\dagger\psi_1\rangle$, and therefore the anti-unitary relations take the same form as the unitary ones, namely $\Theta^\dagger\Theta = \Theta\Theta^\dagger = 1$.

Using this proportionality and the relations (2.84), we get

$$G_{\bar{q}'\bar{q}}\Big|_{\tilde{H}} = e^{i\pi\sum_k(\sigma'_k - \sigma_k)} G_{\Omega q|\Omega q'}\Big|_{\Omega H\Omega^\dagger} = G_{\Omega q|\Omega q'}\Big|_{\Omega H\Omega^\dagger}, \quad (2.88)$$

where we used spin conservation $\sum_k(\sigma'_k - \sigma_k) = 0$. Furthermore

$$\begin{aligned} G_{\Omega q'|\Omega q}\Big|_{\Omega H\Omega^\dagger} &= ((-1)\{i\})^n \text{Tr} \left[e^{-\beta(\Omega H\Omega^\dagger - \mu N)} \mathcal{T}[a_{\Omega q'_1} \dots a_{\Omega q'_n} a_{\Omega q_n}^\dagger \dots a_{\Omega q_1}^\dagger] \right] \\ &= ((-1)\{i\})^n \text{Tr} \left[\Omega e^{-\beta(H - \mu N)} \Omega^\dagger \mathcal{T}[\Omega a_{q'_1} \Omega^\dagger \dots \Omega a_{q'_n} \Omega^\dagger \Omega a_{q_n}^\dagger \Omega^\dagger \dots \Omega a_{q_1}^\dagger \Omega^\dagger] \right] \\ &= ((-1)\{i\})^n \text{Tr} \left[e^{-\beta(H - \mu N)} \mathcal{T}[a_{q'_1} \dots a_{q'_n} a_{q_n}^\dagger \dots a_{q_1}^\dagger] \right] \\ &= G_{q'|q}, \end{aligned} \quad (2.89)$$

where $\mathcal{T} \in \{T, T_c\}$ for the Keldysh or Matsubara formalism. Therefore (2.82) is fulfilled for our Hamiltonian H and choice of single particle basis $|q\rangle = (i, \sigma, s)$.

Matsubara

In the Matsubara formalism, we can directly profit from relation (2.82), by computing for the m -particle Green's function (2.25)

$$\begin{aligned} G_{q'q}(\tau'|\tau) &= (-1)^m \langle T[a(\tau'_1) \dots a(\tau'_m) a^\dagger(\tau_m) \dots a^\dagger(\tau_1)] \rangle \\ &= (-1)^m (-1)^P \text{Tr} \left[\rho_{\text{eq}} \hat{a}(\tau_{P(1)}) \dots \hat{a}(\tau_{P(2m)}) \right] \\ &= (-1)^m (-1)^P \text{Tr} \left[\Theta \rho_{\text{eq}} \Theta^\dagger \Theta \hat{a}(\tau_{P(1)}) \Theta^\dagger \dots \Theta \hat{a}(\tau_{P(2m)}) \Theta^\dagger \right]^* \end{aligned} \quad (2.90)$$

where in the second line we have relabeled the times $(\tau'_1, \dots, \tau'_m, \tau_m, \tau_1)$ as $(\tau_1, \dots, \tau_{2m})$, $P \in S_N(2m)$ is a suitable permutation with sign $(-1)^P$, and $\hat{a} \in \{a, a^\dagger\}$ as appropriate. In the third line, we used the general property

$$\text{Tr}[A] = \text{Tr}[\Theta A \Theta^\dagger]^*, \quad (2.91)$$

as well as the identity $\Theta^\dagger \Theta = 1$. Furthermore, if we use

$$\begin{aligned} \Theta \hat{a}_q(\tau) \Theta^\dagger &= \Theta \left[e^{\tau H} \hat{a}_q e^{-\tau H} \right] \Theta^\dagger = \Theta e^{\tau H} \Theta^\dagger \Theta \hat{a}_q \Theta^\dagger \Theta e^{-\tau H} \Theta^\dagger \\ &= e^{\tau \tilde{H}} \hat{a}_{\bar{q}} e^{-\tau \tilde{H}} = \hat{a}_{\bar{q}}(\tau) \Big|_{\tilde{H}}, \end{aligned} \quad (2.92)$$

we obtain from (2.90)

$$G_{q'q}(\tau'|\tau) = (-1)^m (-1)^P \text{Tr} \left[\tilde{\rho} \hat{a}(\tau_{P(1)}) \Big|_{\tilde{H}} \dots \hat{a}(\tau_{P(2m)}) \Big|_{\tilde{H}} \right]^* \quad (2.93)$$

$$= \left[G_{\bar{q}'\bar{q}}(\tau'|\tau) \right]^* \stackrel{(2.76)}{=} G_{\bar{q}'\bar{q}}(-\tau | -\tau') \Big|_{\tilde{H}} \stackrel{(2.82)}{=} G_{q'q}(-\tau | -\tau'). \quad (2.94)$$

Therefore, we see that this symmetry is indeed of a time-reversal character: All incoming and outgoing indices are swapped and the times acquire a minus sign. In frequency space, this takes the particular easy form

$$G_{q'q}(\omega'_n|\omega_n) = G_{q'q}(\omega_n|\omega'_n), \quad (2.95a)$$

i.e., simply all incoming and outgoing arguments are swapped. For the vertex, the analogous relation

$$\gamma_{q'q}(\omega'_n|\omega_n) = \gamma_{qq'}(\omega_n|\omega'_n) \quad (2.95b)$$

holds.

Keldysh

In the Keldysh formalism, the use of the time-reversal property (2.82) proves to be more tricky. If one carries out the analog computation to (2.90), one obtains the relation

$$\tilde{G}_{qq'}^{jj'}(t, t') = G_{\tilde{H}}^{\bar{j}'\bar{j}}(-t'|-t) \stackrel{(2.82)}{=} G_{q'q}^{\bar{j}'\bar{j}}(-t'|-t), \quad (2.96)$$

where the contour tilde Green's function \tilde{G} is defined as the standard one in (2.25), but with the difference that the forward “-”-branch is now internally anti-time-ordered while the backward “+”-branch is time-ordered. Due to the appearance of \tilde{G} instead of G , we can not easily get a relation of the form (2.95), as it is the case in the Matsubara formalism. However, it turns out that there is another connection between \tilde{G} and G , that can be derived from the Kubo-Martin-Schwinger (KMS) relation, see (2.102) below. Combining the two relations (2.96) and (2.102) yields again a symmetry relation for the Green's function G , namely the multi-particle fluctuation dissipation theorem (FDT). We will discuss the FDT in Sec. 2.2.5 below.

For now, we just want to comment on the special case of one-particle quantities. Here, the internal time ordering of the contour branches does not really matter, since any desired ordering can be achieved by putting the incoming and outgoing parts on different branches. Concretely we have the relation

$$\tilde{G}_{q'_1q_1}^{j'_1j_1}(t'_1|t_1) = \tilde{G}_{q_1q'_1}^{\bar{j}'_1\bar{j}_1}(t'_1|t_1), \quad (2.97)$$

and therefore we obtain with the general multi-particle property (2.96)

$$G_{q'q}^{j'j}(t'|t) \stackrel{(2.97)}{=} \tilde{G}_{q'q}^{\bar{j}'\bar{j}}(t'|t) = G_{qq'}^{j'j}(-t'|-t). \quad (2.98)$$

Transforming this to frequency yields

$$G_{q'q}^{j'j}(\omega'|\omega) = G_{qq'}^{j'j}(\omega|\omega'), \quad (2.99)$$

i.e. the incoming and outgoing arguments are swapped, except the contour indices. The same relation also holds in Keldysh space, one simply has to exchange the contour indices (j', j) with Keldysh indices (α', α). Furthermore, due to time translational invariance, the one-particle quantities are diagonal in frequency, thus we can write compactly

$$G_{q'_1q_1}^{R/A/K}(\omega) = G_{q_1q'_1}^{R/A/K}(\omega). \quad (2.100)$$

At this point, two remarks are in order. (i) Note that (2.100) for $G^{R/A}(\omega)$ is consistent with the (2.95), since $G^{R/A}(\omega)$ are related to $G(\omega)$ via analytic continuation, see the discussion in Sec. 2.2.7 below. (ii) The transposition property in (2.95, 2.100) can also be understood diagrammatically without explicitly referring to time-reversal symmetry but just by using the fact that the Hamiltonian in all our applications (Sec. 3.2 - Sec. 6) is not only hermitian but actually real and symmetric. In the following, we sketch the argument in the Keldysh

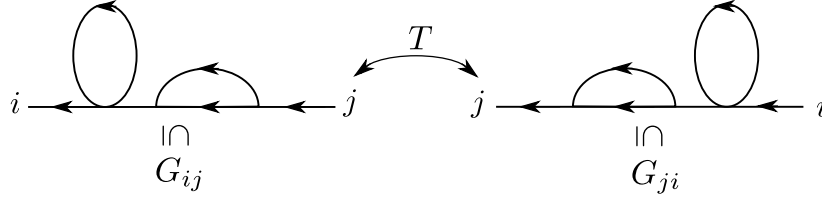


Figure 2.3 Illustration of a diagram that contributes to G_{ij} and after the exchange T of all internal incoming and outgoing spatial and spin indices yields a diagram contributing to G_{ji} .

formalism, the Matsubara argument is completely analogous. From the form of the bare propagator discussed in Sec. 2.1.12 one can easily see that the transposition symmetry (2.100) holds for $G_0^R(\omega)$. Thermal equilibrium implies via the well known one-particle fluctuation-dissipation theorem (2.105) that it is also true for $G_0^K(\omega)$. Furthermore, also the bare interaction is symmetric under exchange of incoming and outgoing site and spin indices, see (2.5b). Let us now consider any diagram consisting of bare propagators and bare vertices that contributes to the propagator $G_{ij}^R(\omega)$. By exchanging the incoming and outgoing spatial indices at all internal bare propagators and bare vertices, we obtain a diagram contributing to G_{ji}^R without changing the value of the diagram, see Fig. 2.3. The same holds true vice versa and therefore we obtain $G_{ij}^R = G_{ji}^R$. Via the Dyson equation (2.73) one sees immediately that the same must hold for the one-particle self-energy $\Sigma^R(\omega)$.

2.2.5 Fluctuation-dissipation theorems

In case of thermal equilibrium, one can show in general that for the one-particle quantities so called fluctuation-dissipation theorems (FDTs) hold, connecting the retarded and advanced components with the Keldysh component. If additionally Eq. (2.82) holds, one can show a similar statement (which we also call FDT) for two-particle quantities, see [Jak09].

The basis for both the single- and the multi-particle FDTs is the Kubo-Martin-Schwinger (KMS) relation [Kub57, MS59, Kub66]

$$\text{Tr} \left[\rho_{\text{eq}} A(t_A - i\beta) B(t_B) \right] = \text{Tr} \left[\rho_{\text{eq}} B(t_B) e^{\beta\mu N} A(t_A) e^{-\beta\mu N} \right]. \quad (2.101)$$

Using this relation, one can derive a connection between the Green's function G and the tilde Green's function \tilde{G} , introduced in Sec. 2.2.4 which takes the form

$$e^{\beta\Delta^{j|j'}(\omega|\omega')} G_{q|q'}^{j|j'}(\omega|\omega') = (-1)^{m^{j|j'}} \tilde{G}_{q|q'}^{\bar{j}|\bar{j}'}(\omega|\omega'), \quad (2.102)$$

see [Jak09]. The functions $\Delta^{j|j'}$ and $m^{j|j'}$ are defined as

$$m^{j|j'} = \sum_{k:j'_k=+} 1 - \sum_{k:j_k=+} 1, \quad (2.103)$$

i.e. $m^{j|j'}$ measures how many more particles are incoming than outgoing on the backward branch and

$$\Delta^{j|j'}(\omega|\omega') = \sum_{k:j'_k=+} (\omega'_k - \mu) - \sum_{k:j_k=+} (\omega_k - \mu). \quad (2.104)$$

One-particle quantities

In case of the one-particle Green's function and one-particle self-energy, we can use (2.102) together with the trivial connection (2.97) between \tilde{G} and G to obtain the well known one-particle FDTs

$$G^K(\omega) = (1 - 2n_F(\omega)) (G^R(\omega) - G^A(\omega)), \quad (2.105a)$$

$$\Sigma^K(\omega) = (1 - 2n_F(\omega)) (\Sigma^R(\omega) - \Sigma^A(\omega)), \quad (2.105b)$$

with the Fermi distribution

$$n_F(\omega) = \frac{1}{1 + e^{\beta(\omega - \mu)}}. \quad (2.106)$$

In thermal equilibrium, the Keldysh component is thus completely determined by the knowledge of the retarded and advanced component.

Multi-particle quantities

In the general multi-particle case, we can use (2.102) together with the previous connection (2.96) between \tilde{G} and G obtained by the time-reversal property. This yields the multi-particle FDTs derived in [Jak09], which take the form

$$\text{Re } G_{\epsilon_n^{j'|j}}^{j'|j}(\omega', \omega) = - \left[1 - 2n_F(\Delta^{j'|j}(\omega|\omega') + \mu) \right] \text{Re } G_{-\epsilon_n^{j|j'}}^{j|j'}(\omega|\omega'), \quad (2.107a)$$

$$\text{Im } G_{-\epsilon_n^{j'|j}}^{j'|j}(\omega', \omega) = - \left[1 - 2n_F(\Delta^{j'|j}(\omega|\omega') + \mu) \right] \text{Im } G_{\epsilon_n^{j|j'}}^{j|j'}(\omega|\omega'), \quad (2.107b)$$

where

$$\epsilon_n^{j'|j} = (-1)^{1+n+m^{j'|j}}, \quad (2.108)$$

and

$$A_\epsilon^{j'j} = \sum_{\substack{\alpha', \alpha \\ (-1)^{\sum_k (\alpha'_k + \alpha_k)} = \epsilon}} D^{j'|\alpha'} A^{\alpha'|\alpha} (D^{-1})^{\alpha|j}, \quad (2.109)$$

for an arbitrary multi-particle quantity A . An analogous statement holds for the n -particle vertices

$$\text{Re } \gamma_{\epsilon_1^{j'|j}}^{j'|j}(\omega'|\omega) = - \left[1 - 2n_F(\Delta^{j'|j}(\omega'|\omega) + \mu) \right] \text{Re } \gamma_{-\epsilon_1^{j|j'}}^{j|j'}(\omega'|\omega), \quad (2.110a)$$

$$\text{Im } \gamma_{-\epsilon_1^{j'|j}}^{j'|j}(\omega'|\omega) = - \left[1 - 2n_F(\Delta^{j'|j}(\omega'|\omega) + \mu) \right] \text{Im } \gamma_{\epsilon_1^{j|j'}}^{j|j'}(\omega'|\omega), \quad (2.110b)$$

with

$$\epsilon_1^{j'|j} = -(-1)^{1+m^{j'|j}}. \quad (2.111)$$

The form of this symmetries will further simplify in the context of our fRG approximations, due to simplifications of the two-particle vertex, see Sec. 2.4.5 below.

2.2.6 Causality and related analytic properties in the Keldysh formalism

In our subsequent studies, it is often useful to consider the analytical properties of the continuous Keldysh Green's functions and vertex quantities as functions of frequencies. Using a redundancy in the description of the Keldysh contour, one can obtain certain ‘‘causality’’ relations [Jak09]. In particular, one gets that

$$G^{1\dots 1|1\dots 1} = 0 \quad (2.112)$$

vanishes identically and that the reduced quantities (being functions of one frequency argument less, in a sense analog to the definitions in (2.40))

$$G^{1\dots 1 \overset{\text{m-th pos.}}{2} 1\dots 1|1\dots 1}(\omega'_1, \dots, \cancel{\omega'_m}, \dots, \omega'_n | \omega_1, \dots, \omega_n), \quad (2.113a)$$

$$G^{1\dots 1|1\dots \overset{\text{m-th pos.}}{2} 1\dots 1}(\omega'_1, \dots, \omega'_n | \omega_1, \dots, \cancel{\omega_m}, \dots, \omega_n), \quad (2.113b)$$

are analytic in the lower half plane (l.h.p.) for the frequencies $\omega'_1, \dots, \omega'_n$ and analytic in the upper half plane (u.h.p.) for the frequencies $\omega_1, \dots, \omega_n$.

Analogous statements can be derived for the two-particle vertex [Jak09]. In particular, they imply that

$$\gamma^{2\dots 2|2\dots 2} = 0, \quad (2.114)$$

and that

$$\gamma^{2\dots 2 \overset{\text{m-th pos.}}{1} 2\dots 2|2\dots 2}(\omega'_1, \dots, \cancel{\omega'_m}, \dots, \omega'_n | \omega_1, \dots, \omega_n), \quad (2.115a)$$

$$\gamma^{2\dots 2|2\dots \overset{\text{m-th pos.}}{1} 2\dots 2}(\omega'_1, \dots, \omega'_n | \omega_1, \dots, \cancel{\omega_m}, \dots, \omega_n), \quad (2.115b)$$

are analytic in the lower half plane (l.h.p.) for the frequencies $\omega'_1, \dots, \omega'_n$ and analytic in the upper half plane (u.h.p.) for the frequencies $\omega_1, \dots, \omega_n$.

2.2.7 Connection Matsubara - Keldysh formalism

In the one-particle case, there is an easy connection between the Matsubara and the Keldysh propagator, namely

$$G(\omega_n) = G^R(\omega_n) \text{ for } \text{Im } \omega_n > 0, \quad (2.116a)$$

and

$$G(\omega_n) = G^A(\omega_n) \text{ for } \text{Im } \omega_n < 0. \quad (2.116b)$$

Therefore, one can obtain the retarded Green's function $G^R(\omega)$ for real frequencies $\omega \geq \mu$ from $G(\omega_n)$ by analytic continuation from positive Matsubara frequencies, and the advanced Green's function $G^A(\omega)$ for real frequencies $\omega < \mu$ from $G(\omega_n)$ by analytic continuation from negative Matsubara frequencies, see Fig. 2.4.

For multi-particle Green's functions there is in general no simple relation like (2.116) between the thermal Green's function and the Keldysh Green's functions, see e.g. the discussion in [Wel05]. One of the main reasons for this is that with four or more time arguments, not all possible correlation functions can be expressed via the simple double time contour description.

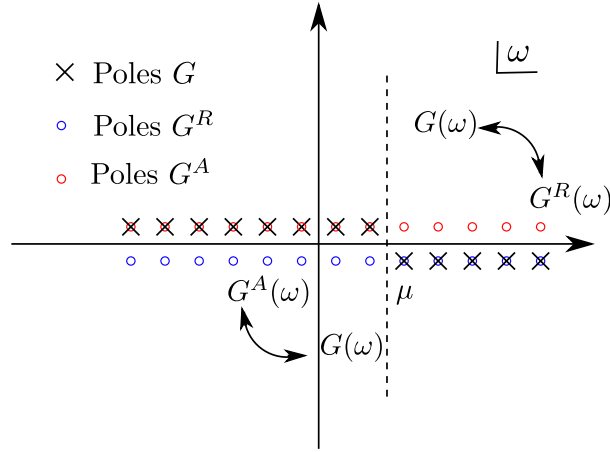


Figure 2.4 Illustration of the analytic continuation of $G(\omega)$ to either $G^R(\omega)$ for $\omega > \mu$ or $G^A(\omega)$ for $\omega < \mu$.

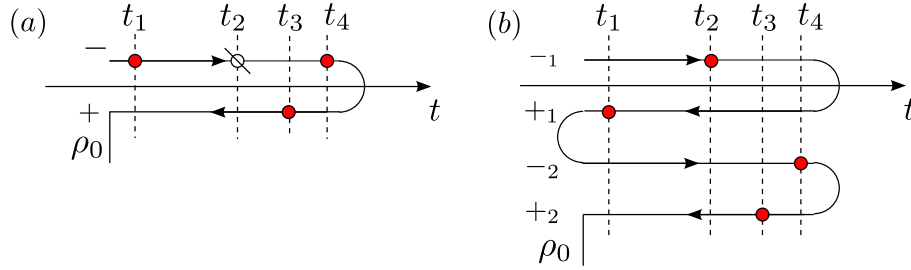


Figure 2.5 Illustration of the correlation function (2.117) that can not be represented on the usual double contour (a). On the four branch contour (b) this is possible without a problem.

For example, for times $t_1 < t_2 < t_3 < t_4$ the correlator

$$\langle a^\dagger(t_3)a^\dagger(t_4)a(t_1)a(t_2) \rangle \quad (2.117)$$

cannot be represented on the double time contour, see Fig. 2.5(a). However, if one allows for a multi-contour description (i.e. multiple forward and backward branches) this problem can be resolved, see Fig. 2.5(b). However, then the number of different contour components grows, making the description more complicated.

2.3 General fRG equations

In this short section, we briefly review the concept of the functional Renormalization Group (fRG) and explain the specific choice of our used flow parameters.

2.3.1 fRG flow equations

By introducing an artificial flow parameter Λ into the quadratic part of the action G_0^Λ ,¹⁰ and computing the derivative of the generating function of the vertices Γ^Λ (2.36) w.r.t. Λ , one can derive an infinite hierarchy of flow equations for the vertex functions $\gamma_{k'k}^\Lambda$, see Ref. [Wet93, MSH⁺12]. A meticulous derivation via generating functionals can be found in

¹⁰ In the following the superscript, Λ indicates the dependence of an object on the flow parameter Λ .

[Kar10, Bau14]. Alternatively, the flow equations can also be obtained in a diagrammatic approach [Jak09], or as done very recently by Kugler [KvD18b, KvD18c, KvD18a], by taking derivatives of the parquet-equations w.r.t. an introduced flow parameter. In our chosen conventions, the flow equations for the one- and two-particle vertex take the following form

$$\frac{\partial}{\partial \Lambda} \Sigma_{k'_1 k_1}^\Lambda = -\{i\} \sum_{k'_2 k_2} S_{k_2 k'_2}^\Lambda \gamma_{k'_1 k'_2 | k_1 k_2}^\Lambda \quad (2.118a)$$

and

$$\begin{aligned} \frac{\partial}{\partial \Lambda} \gamma_{k'_1 k'_2 | k_1 k_2}^\Lambda &= \{i\} \sum_{k'_3 k_3} S_{k_3 k'_3}^\Lambda \gamma_{k'_1 k'_2 k'_3 | k_1 k_2 k_3}^\Lambda \\ &+ \{i\} \sum_{k'_3 k'_4 k_3 k_4} \gamma_{k'_1 k'_2 | k_3 k_4}^\Lambda \left[S_{k_3 k'_3}^\Lambda G_{k_4 k'_4}^\Lambda \right] \gamma_{k'_3 k'_4 | k_1 k_2}^\Lambda \\ &+ \{i\} \sum_{k'_1 k'_4 k_1 k_2} \gamma_{k'_1 k'_4 | k_3 k_2}^\Lambda \left[S_{k_3 k'_3}^\Lambda G_{k_4 k'_4}^\Lambda + G_{k_3 k'_3}^\Lambda S_{k_4 k'_4}^\Lambda \right] \gamma_{k'_3 k'_2 | k_1 k_4}^\Lambda \\ &- \{i\} \sum_{k'_3 k'_4 k_3 k_4} \gamma_{k'_1 k'_3 | k_1 k_4}^\Lambda \left[S_{k_3 k'_3}^\Lambda G_{k_4 k'_4}^\Lambda + G_{k_3 k'_3}^\Lambda S_{k_4 k'_4}^\Lambda \right] \gamma_{k'_4 k'_2 | k_3 k_2}^\Lambda, \end{aligned} \quad (2.118b)$$

where the single scale operator is given by

$$S^\Lambda = \{-\} G^\Lambda \partial_\Lambda [G_0^{\Lambda-1}] G^\Lambda. \quad (2.119)$$

Note that due to the highly symmetric form of S in terms of G , the symmetries that we stated earlier for the propagator G , namely complex conjugation (Sec. 2.2.3), time-reversal (Sec. 2.2.4), and FDTs (Sec. 2.2.5) hold in the same form also for S .

2.3.2 Choice of flow parameters and initial conditions

So far, we have not specified how the flow parameter is concretely realized. This is done differently in the Matsubara and Keldysh context.

Matsubara formalism

In the Matsubara case, we use a frequency cutoff as flow parameter, introduced in the bare propagator of the central region via:

$$G_0^\Lambda(\omega_n) = \theta_T(|\omega_n| - \Lambda) G_0(\omega_n), \quad (2.120)$$

with Λ being a positive number, starting from an initial value $\Lambda_{\text{ini}} = \infty$ and flowing towards its final value $\Lambda_{\text{fin}} = 0$, and θ_T being a step function broadened on the scale of temperature

$$\theta_T(\omega) = \begin{cases} 0, & \omega < -\pi T \\ \frac{1}{2} + \frac{1}{2\pi T} \omega, & |\omega| \leq \pi T \\ 1, & \omega > \pi T. \end{cases} \quad (2.121)$$

Therefore $G_0^{\Lambda_{\text{ini}}} = 0$, and $G_0^{\Lambda_{\text{fin}}} = G_0$, i.e. the full bare propagator is recovered. The analytical initial conditions for the self-energy and two-particle vertex are in this case simple to determine,

namely

$$\Sigma^{\Lambda_{\text{ini}}} = 0, \quad (2.122\text{a})$$

$$\gamma^{\Lambda_{\text{ini}}} = \nu. \quad (2.122\text{b})$$

Numerically, we can not set $\Lambda_{\text{ini}} = \infty$, but rather we set it to a large number, much bigger than any scale involved in the system, but still finite. Therefore, one has to include the flow from $\Lambda = \infty$ to $\Lambda = \Lambda_{\text{ini}} < \infty$ analytically. In this case, one obtains a modified numerical initial condition for the self-energy, while the initial condition for the two-particle vertex stays the same (see e.g. [Bau14])

$$\Sigma_{q',q}^{\Lambda_{\text{ini}}} = \frac{1}{2} \sum_p \bar{v}_{q',p|q,p} + \mathcal{O}(\Lambda_{\text{ini}}^{-1}), \quad (2.123\text{a})$$

$$\gamma^{\Lambda_{\text{ini}}} = \nu. \quad (2.123\text{b})$$

Zero temperature limit

A special case occurs in the limit of vanishing temperature $T \rightarrow 0$. In our concrete implementations of the Matsubara fRG flow in our publication P1, Sec. 3.2, this will be the only case we study due to its simpler structure. In this case, on the one hand the step function (2.121) becomes sharp, on the other hand the Matsubara frequencies become dense. Therefore, one has to take some care when computing the derivative w.r.t. the flow parameter Λ . In this derivative, combinations of δ and θ functions arise, which can be evaluated using Morris lemma [Mor94], which states that

$$\lim_{\epsilon \rightarrow 0} \delta_\epsilon(\omega) f(\theta_\epsilon(\omega)) = \delta(\omega) \int_0^1 f(t) dt, \quad (2.124)$$

if δ_ϵ and θ_ϵ are series of approximating functions

$$\lim_{\epsilon \rightarrow 0} \delta_\epsilon(\omega) = \delta(\omega), \quad (2.125\text{a})$$

$$\lim_{\epsilon \rightarrow 0} \theta_\epsilon(\omega) = \theta(\omega). \quad (2.125\text{b})$$

Using this, one obtains in the $T = 0$ case for the single-scale propagator appearing in the flow of the self-energy (2.118a)

$$S^\Lambda(\omega_n) = \delta(|\omega_n| - \Lambda) \tilde{G}^\Lambda(\omega_n), \quad (2.126)$$

where

$$\tilde{G}^\Lambda(\omega_n) = \frac{1}{(G_0)^{-1}(\omega_n) - \Sigma^\Lambda(\omega_n)}. \quad (2.127)$$

Note that G_0 in the denominator of (2.127) does not depend on the flow parameter Λ . Analogously, one obtains for the products of single-scale and full propagators in the flow of the two-particle vertex (2.118b)

$$S^\Lambda(\omega_{n_1}) G^\Lambda(\omega_{n_2}) = \delta(|\omega_{n_1}| - \Lambda) \theta(|\omega_{n_2}| - \Lambda) \tilde{G}(\omega_{n_1}) \tilde{G}(\omega_{n_2}). \quad (2.128)$$

Keldysh formalism

In our Keldysh studies, we choose a hybridization flow, as described in detail in [Jak09, Sch17]. In this case, the flow parameter Λ is introduced as an artificial decay mechanism in our

system via

$$G_0^\Lambda = \frac{1}{\omega - H_{0c} - \Sigma_{\text{lead}}^\Lambda + \frac{i}{2}\Lambda}. \quad (2.129)$$

Note that also the lead self-energy depends on Λ , since we use the artificial decay term $i/2\Lambda$ in the denominator of the bare propagator on all sites of the system including the leads. The resulting components of the lead self-energy $\Sigma_{\text{lead}}^{R\Lambda}$ and $\Sigma_{\text{lead}}^{K\Lambda}$ are still of the form (2.53) and (2.54), however the functions $f^p(\omega)$ and $\Gamma^p(\omega)$ have to be replaced by

$$f^{p\Lambda}(\omega) = f^p\left(\omega + i\frac{\Lambda}{2}\right), \quad (2.130a)$$

$$\Gamma^{p\Lambda}(\omega) = -2 \text{Im} f^p\left(\omega + i\frac{\Lambda}{2}\right). \quad (2.130b)$$

The advantage of this hybridization flow compared to the frequency cutoff scheme used in the Matsubara context is that it can be seen as describing an actually physical system in each step of the flow. Therefore, conservation laws, fluctuation-dissipation theorems and analytical properties must hold¹¹ not just for the final result (as in the frequency cutoff flow) but throughout the entire flow. Especially in the context of the real-frequency Keldysh approach this turned out to be a major advantage [Jak09, Sch17].

Analogous to the Matsubara case, the numerical initial conditions amount to

$$\Sigma_{q',q}^{R\Lambda_{\text{ini}}}(\omega) = \frac{1}{2} \sum_p \bar{v}_{q'p|qp}, \quad (2.131a)$$

$$\Sigma_{q',q}^{K\Lambda_{\text{ini}}}(\omega) = 0, \quad (2.131b)$$

$$\gamma_{\text{ini}}^\Lambda = \nu. \quad (2.131c)$$

2.4 Extended Coupled Ladder Approximation

In this section, we will describe the derivation of the extended Coupled Ladder Approximation (eCLA) which we developed to be able to treat finite-ranged interactions in QPCs.

2.4.1 Channel decomposition

Our starting ground are the fRG equations for self-energy and vertex (2.118) in a second-order truncation, i.e. we neglect the three-particle vertex $\gamma_{k'_1 k'_2 k'_3 | k_1 k_2 k_3}^\Lambda$. In this truncation, the fRG equation for the vertex (2.118b) exhibits three natural channels, depending on the form of the frequency argument. To make this explicit, one can replace the four fermionic frequency arguments of the vertex (which are dependent, due to frequency conservation) by three independent bosonic frequencies, defined as

$$\Pi = \omega'_1 + \omega'_2 = \omega_1 + \omega_2 \quad (2.132a)$$

$$X = \omega_2 - \omega'_1 = \omega'_2 - \omega_1 \quad (2.132b)$$

$$\Delta = \omega_2 - \omega'_2 = \omega'_1 - \omega_1. \quad (2.132c)$$

¹¹ That is, if they are not broken by further approximations.

Correspondingly the fermionic frequencies $\omega'_1, \dots, \omega_2$ can be expressed as

$$\omega'_1 = \frac{1}{2}(\Pi - X + \Delta), \quad (2.133a)$$

$$\omega'_2 = \frac{1}{2}(\Pi + X - \Delta), \quad (2.133b)$$

$$\omega_1 = \frac{1}{2}(\Pi - X - \Delta), \quad (2.133c)$$

$$\omega_2 = \frac{1}{2}(\Pi + X + \Delta). \quad (2.133d)$$

Using the bosonic frequencies (2.132), the flow equation for the vertex (2.118b) can be written as [Jak09]

$$\begin{aligned} \frac{\partial}{\partial \Lambda} \gamma_{k'_1 k'_2 | k_1 k_2}^\Lambda(\Pi, X, \Delta) = \{i\} \sum_{\omega} \{ & \\ & \gamma_{k'_1 k'_2 | k_3 k_4}^\Lambda \left(\Pi, \omega + \frac{X - \Delta}{2}, \omega - \frac{X - \Delta}{2} \right) \left[S_{k_3 | k'_3}^\Lambda \left(\frac{\Pi}{2} - \omega \right) G_{k_4 k'_4}^\Lambda \left(\frac{\Pi}{2} + \omega \right) \right] \\ & \gamma_{k'_3 k'_4 | k_1 k_2}^\Lambda \left(\Pi, \frac{X + \Delta}{2} + \omega, \frac{X + \Delta}{2} - \omega \right) \end{aligned} \quad (2.134a)$$

$$\begin{aligned} & + \gamma_{k'_1 k'_4 | k_3 k_2}^\Lambda \left(\frac{\Pi + \Delta}{2} + \omega, X, \frac{\Pi + \Delta}{2} - \omega \right) \left[S_{k_3 k'_3}^\Lambda \left(\omega - \frac{X}{2} \right) G_{k_4 k'_4}^\Lambda \left(\omega + \frac{X}{2} \right) + [G \leftrightarrow S] \right] \\ & \gamma_{k'_3 k'_2 | k_1 k_4}^\Lambda \left(\omega + \frac{\Pi - \Delta}{2}, X, \omega - \frac{\Pi - \Delta}{2} \right) \end{aligned} \quad (2.134b)$$

$$\begin{aligned} & - \gamma_{k'_1 k'_3 | k_1 k_4}^\Lambda \left(\omega + \frac{\Pi - X}{2}, \omega - \frac{\Pi - X}{2}, \Delta \right) \left[S_{k_3 k'_3}^\Lambda \left(\omega - \frac{\Delta}{2} \right) G_{k_4 k'_4}^\Lambda \left(\omega + \frac{\Delta}{2} \right) + [G \leftrightarrow S] \right] \\ & \gamma_{k'_4 k'_2 | k_3 k_2}^\Lambda \left(\frac{\Pi + X}{2} + \omega, \frac{\Pi + X}{2} - \omega, \Delta \right) \}, \end{aligned} \quad (2.134c)$$

and correspondingly the flow of the self energy is given by

$$\frac{\partial}{\partial \Lambda} \Sigma_{k'_1 k_1}^\Lambda(\omega) = -\{i\} \sum_{\omega'} S_{k_2 k'_2}^\Lambda(\omega') \gamma_{k'_1 k'_2 | k_1 k_2}^\Lambda(\omega' + \omega, \omega' - \omega, 0), \quad (2.135)$$

where ω in (2.135) can either be a real Keldysh or imaginary Matsubara frequency. The k 's here denote composite indices, comprised of all appropriate indices except frequencies which are displayed explicitly. Here and in the following, we often apply the Einstein sum convention for reasons of compactness, i.e. we do not write explicit sum symbols for the internal indices. Furthermore, from here on, we suppress the superscript Λ . Note that the flow equation (2.134) consists of three parts ‘‘channels’’, each characterized by a special role of one of the three frequency arguments Π, X, Δ . In order to emphasize this, we have colored the special bosonic frequencies for each channel in (2.134) in a different colors. The bubble parts of (2.134), i.e. the parts in square brackets containing only S and G , depend only on this specific frequency. This motivates the following approximation called channel decomposition, which assumes that each channel is only dependent on its specific frequency and independent of the other two bosonic frequencies, see e.g. [Kar06, Jak09, Bau14]. Concretely, we make the ansatz

$$\gamma(\Pi, X, \Delta) \approx \nu + \varphi^P(\Pi) + \varphi^X(X) + \varphi^D(\Delta), \quad (2.136)$$

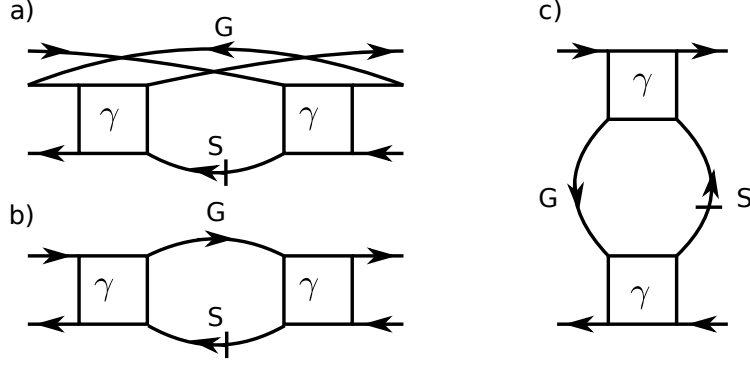


Figure 2.6 Schematic of the three different channels, the particle-particle channel (a), and the exchange and the direct part of the particle-hole channel (b) and (c).

which we insert on the l.h.s. of the flow equation (2.134). On the r.h.s. of (2.134) we simplify (2.136) even further by using instead of γ a reduced $\tilde{\gamma}^A$ for each channel $A \in \{P, X, D\}$

$$\tilde{\gamma}^A = \nu + \varphi^A(\Pi) + \phi^B + \phi^C, \quad (2.137)$$

where the contributions of the other two channels B and C ¹² are approximated by static values ϕ^B , ϕ^C in order to avoid frequency mixing between channels. On the specific choice of ϕ we comment below, see the discussion to Eq. (2.145). Using (2.137) on the r.h.s. of (2.134), we end up with the following flow equations for φ^A with $A \in \{P, X, D\}$

$$\frac{\partial}{\partial \Lambda} (\varphi^P)_{k'_1 k'_2 | k_1 k_2}^\Lambda(\Pi) = (\tilde{\gamma}^P)_{k'_1 k'_2 | k_3 k_4}^\Lambda(\Pi) (\hat{I}^{pp})_{k_3 k_4 | k'_3 k'_4}^\Lambda(\Pi) (\tilde{\gamma}^P)_{k'_3 k'_4 | k_1 k_2}^\Lambda(\Pi), \quad (2.138a)$$

$$\frac{\partial}{\partial \Lambda} (\varphi^X)_{k'_1 k'_2 | k_1 k_2}^\Lambda(X) = (\tilde{\gamma}^X)_{k'_1 k'_4 | k_3 k_2}^\Lambda(X) (I^{ph})_{k_3 k_4 | k'_3 k'_4}^\Lambda(X) (\tilde{\gamma}^X)_{k'_3 k'_2 | k_1 k_4}^\Lambda(X), \quad (2.138b)$$

$$\frac{\partial}{\partial \Lambda} (\varphi^D)_{k'_1 k'_2 | k_1 k_2}^\Lambda(\Delta) = -(\tilde{\gamma}^D)_{k'_1 k'_3 | k_1 k_4}^\Lambda(\Delta) (I^{ph})_{k_3 k_4 | k'_3 k'_4}^\Lambda(\Delta) (\tilde{\gamma}^D)_{k'_4 k'_2 | k_3 k_2}^\Lambda(\Delta), \quad (2.138c)$$

with the bubble terms

$$(\hat{I}^{pp})_{k_3 k_4 | k'_3 k'_4}^\Lambda(\Pi) = \{i\} \sum_{\omega} \left[S_{k_3 | k'_3}^\Lambda \left(\frac{\Pi}{2} - \omega \right) G_{k_4 k'_4}^\Lambda \left(\frac{\Pi}{2} + \omega \right) \right], \quad (2.139a)$$

$$(I^{ph})_{k_3 k_4 | k'_3 k'_4}^\Lambda(X) = \{i\} \sum_{\omega} \left[S_{k_3 | k'_3}^\Lambda \left(\omega - \frac{X}{2} \right) G_{k_4 k'_4}^\Lambda \left(\omega + \frac{X}{2} \right) + [G \leftrightarrow S] \right]. \quad (2.139b)$$

The notation pp - and ph -bubble stands for “particle-particle” and “particle-hole”, and stems from the direction of the internal lines, see Fig. 2.6. Using the channel decomposition (2.136), the flow of the self-energy takes the form

$$\begin{aligned} \frac{\partial}{\partial \Lambda} \Sigma_{k'_1 k_1}^\Lambda(\omega) = & -\{i\} \sum_{\omega'} S_{k_2 k'_2}^\Lambda(\omega') \left[\nu_{k'_1 k'_2 | k_1 k_2} + (\varphi^P)_{k'_1 k'_2 | k_1 k_2}^\Lambda(\omega' + \omega) \right. \\ & \left. + (\varphi^X)_{k'_1 k'_2 | k_1 k_2}^\Lambda(\omega' - \omega) + (\varphi^D)_{k'_1 k'_2 | k_1 k_2}^\Lambda(0) \right]. \end{aligned} \quad (2.140)$$

The reasoning behind the approximation of the channel decomposition (2.136) is to assume that most of the frequency dependence of a channel is captured in its specific prominent bosonic frequency, while the dependence on the other two bosonic frequency arguments is

¹² $B, C \in \{P, X, D\} \setminus \{A\}$ and $B \neq C$

not as pronounced. This requirement is in general only fulfilled for small and intermediate interaction strengths, as the error introduced by the approximations (2.136) and (2.137) is of third order in the interaction strength. This is no real setback for the fRG scheme presented here, since by neglecting the three-particle vertex in (2.134), we use a second-order truncation anyway. However, due to the overall perturbative nature of our fRG approach, the interaction strength in our applications in Sec. 3.2 - Sec. 6 can not be increased arbitrarily. Despite this limitation, it was shown in the past that for our type of systems the use of second-order truncation in conjunction with the channel-decomposition (2.136) usually yields reliable results up to intermediate interaction strengths. In Ref. [KHP⁺08], second-order fRG schemes with and without channel decomposition were compared and shown to yield similar results for the single impurity Anderson model (SIAM). Furthermore, Schimmel et al. showed in [SBvD17] that second-order fRG with the presented channel decomposition scheme (2.136) yields results for the spectral function in QPC systems that are very similar to the ones obtained using state of the art DMRG techniques. In recent and more advanced versions of fRG, such as mfRG, the single-frequency-per-channel has to be dropped. There, full description of dependence on all three frequencies is needed, e.g. using the parametrization of [].

Note that even though in (2.136) the different channel components of φ seem to be independent, the X- and D-channel are related via the particle permutation symmetry (2.75b). Explicitly, we have e.g. for the permutation of the outgoing particles

$$\begin{aligned}
& \gamma_{k'_1 k'_2 | k_1 k_2}(\Pi, X, \Delta) \\
&= \gamma_{k'_1 k'_2 | k_1 k_2} \left(\frac{1}{2}(\Pi - X + \Delta), \frac{1}{2}(\Pi + X - \Delta) \middle| \frac{1}{2}(\Pi - X - \Delta), \frac{1}{2}(\Pi + X + \Delta) \right) \\
&= -\gamma_{k'_2 k'_1 | k_1 k_2} \left(\frac{1}{2}(\Pi + X - \Delta), \frac{1}{2}(\Pi - X + \Delta) \middle| \frac{1}{2}(\Pi - X - \Delta), \frac{1}{2}(\Pi + X + \Delta) \right) \\
&= -\gamma_{k'_2 k'_1 | k_1 k_2}(\Pi, \Delta, X)
\end{aligned} \tag{2.141}$$

and therefore we obtain for φ^A with $A \in \{\Pi, X, \Delta\}$ the relations

$$(\varphi^P)_{k'_1 k'_2 | k_1 k_2}(\Pi) = -(\varphi^P)_{k'_2 k'_1 | k_1 k_2}(\Pi) \tag{2.142a}$$

$$(\varphi^X)_{k'_1 k'_2 | k_1 k_2}(X) = -(\varphi^D)_{k'_2 k'_1 | k_1 k_2}(X). \tag{2.142b}$$

Analogous one obtains for the permutation of the incoming particles

$$(\varphi^P)_{k'_1 k'_2 | k_1 k_2}(\Pi) = -(\varphi^P)_{k'_1 k'_2 | k_2 k_1}(\Pi) \tag{2.143a}$$

$$(\varphi^X)_{k'_1 k'_2 | k_1 k_2}(X) = -(\varphi^D)_{k'_1 k'_2 | k_2 k_1}(-X). \tag{2.143b}$$

One can show (see App. A.4) that the relations (2.142) and (2.143) are conserved under the fRG flow (2.134) and (2.135)). Therefore, since the initial vertices $\varphi^{A\Lambda_{\text{ini}}} = 0$ obey them, also all $\varphi^{A\Lambda}$ with finite Λ will fulfill them. Further relations between the components of the φ^A are introduced by the complex conjugation symmetry (Sec. 2.2.3), thermal equilibrium and time-reversal properties (Sec. 2.2.4-2.2.5). Additionally to those physical symmetries, the approximated fRG flow equations (2.138) introduce further (artificial) relations between the φ^A components by themselves. In particular, they reduce the number of independent Keldysh components, c.f. Eq. (2.202). We study these properties in detail below.

We also want to remark that by utilizing the particle permutation symmetry (2.75b) as above in (2.142,2.143), we could have used in (2.138) the symmetrized version

$$I^{pp} = \frac{1}{2}(\hat{I}^{pp} + \hat{I}^{pp}[G \leftrightarrow S]) \quad (2.144)$$

instead of \hat{I} , where $\hat{I}^{pp}[G \leftrightarrow S]$ is defined as \hat{I}^{pp} in (2.139), just with interchanged roles of G and S . In the following, we will usually use I^{pp} instead of \hat{I}^{pp} due to the explicit symmetry of G and S .

The only thing left at this point, in order to completely specify our approximation scheme, is to make a concrete choice for the static feedback components ϕ^P , ϕ^X and ϕ^D in (2.137). The simplest approach, which we also want to follow in this work, is to treat the ϕ^A with $A \in \{P, X, D\}$ as an effective additional contribution to the bare vertex ν . In order for this to be valid, we require the ϕ^A to be real and, in the Keldysh case, to have the same Keldysh structure as the bare vertex, see (2.22). In [Jak09] a particularly elegant choice of the ϕ^A in thermal equilibrium was suggested, namely

$$\phi^P = \varphi^P(\Pi_f), \quad \phi^X = \varphi^X(X_f), \quad \phi^D = \varphi^D(\Delta_f), \quad (2.145)$$

with a particular choice of so called feedback frequencies Π_f , X_f and Δ_f . In the Keldysh formulation, the appropriate choice for these feedback frequencies is

$$\Pi_f = 2\mu, \quad X_f = \Delta_f = 0. \quad (2.146)$$

For these special frequencies, the ϕ^A defined in (2.145) are real and, as we will show below in 2.4.5, exhibit the same Keldysh structure as the bare vertex (2.22).

In the Matsubara case, we set the feedback frequencies to

$$\Pi_f = X_f = \Delta_f = 0. \quad (2.147)$$

Note that (2.147) is completely analogous to the choice (2.146). The apparent difference in the choice of Π_f only stems from the different choice of the zero point in frequencies for the Matsubara and Keldysh formalism. In the Matsubara formulation, the zero point is set to the chemical potential μ , while in the Keldysh formulation the zero point is chosen independent of μ (we usually choose the middle of the non-interacting energy band as zero). The effect of the choices (2.146) or (2.147) therefore is the same: In the integrand of the I^{ph} bubble, both G and S are evaluated at the same frequency, while the frequency arguments of G and S in the integrand of the I^{pp} bubble become symmetric around the chemical potential.

In the Matsubara case, it is immediately apparent that the choice (2.147) yields the correct structure for the ϕ^A by simply using the symmetry (2.77), as well as the corresponding symmetry for the single-scale propagator $S(\omega_n)^* = S(-\omega_n)$, which can easily be deduced from the definition (2.119). We get for the integrand of I^{pp} (c.f. Eq. (2.144))

$$G\left(\frac{\Pi_f}{2} - \omega_n\right)S\left(\frac{\Pi_f}{2} + \omega_n\right) + [G \leftrightarrow S] = G(-\omega_n)S(\omega_n) + [G \leftrightarrow S] \quad (2.148)$$

$$= \left(G(-\omega_n)S(\omega_n) + [G \leftrightarrow S]\right)^* = \left[G\left(\frac{\Pi_f}{2} - \omega_n\right)S\left(\frac{\Pi_f}{2} + \omega_n\right) + [G \leftrightarrow S]\right]^*. \quad (2.149)$$

and analog for the integrand of I^{ph}

$$\begin{aligned}
& \sum_{\omega} \left[S\left(\omega - \frac{X_f}{2}\right) G\left(\omega + \frac{X_f}{2}\right) + [G \leftrightarrow S] \right] = \sum_{\omega} \left[S(\omega) G(\omega) + [G \leftrightarrow S] \right] \\
& = \sum_{\omega} \left[S(-\omega) G(-\omega) + [G \leftrightarrow S] \right]^* = \sum_{\omega} \left[S(\omega) G(\omega) + [G \leftrightarrow S] \right]^* \\
& \sum_{\omega} \left[S\left(\omega - \frac{X_f}{2}\right) G\left(\omega + \frac{X_f}{2}\right) + [G \leftrightarrow S] \right]^*. \tag{2.150}
\end{aligned}$$

Therefore, the bubbles $I^{pp}(\Pi_f)$, $I^{ph}(X_f)$, $I^{ph}(D_f)$ and with them also ϕ^P , ϕ^X and ϕ^D are real and thus the latter can be seen as effective addition to the bare vertex ν .

In the Keldysh case, the corresponding computations are somewhat more complicated, however the idea is the same. In thermal equilibrium, one can show that the bubbles are real at the feedback frequencies (see App. A.1). Therefore, also the feedback terms ϕ^P , ϕ^X , ϕ^D are real. Using the explicit form of the vertex Keldysh structure (2.202) and the FDTs (2.237) furthermore yields that the feedback terms have the same Keldysh structure as the bare vertex.

2.4.2 Spin structure

Before discussing the more complicated spatial structure, we first take a look at the spin structure of the fRG flow (2.138, 2.140). For any quantity $A^{\sigma'_1 \sigma'_2 | \sigma_1 \sigma_2}$ with spin indices $\sigma'_1, \dots, \sigma_2$ we define

$$A^{\sigma\sigma} := A^{\sigma\sigma|\sigma\sigma}, \tag{2.151a}$$

$$A^{\sigma\tau} := A^{\sigma\tau|\sigma\tau}, \tag{2.151b}$$

with $\sigma, \tau = \uparrow, \downarrow$. Using spin conservation as well as the particle permutation symmetries (2.143, 2.142), we can reduce the number of independent channel and spin components of φ to seven, namely

$$(\varphi^P)^{\uparrow\downarrow}, (\varphi^P)^{\sigma\sigma} \tag{2.152a}$$

$$(\varphi^X)^{\uparrow\downarrow}, \tag{2.152b}$$

$$(\varphi^D)^{\uparrow\downarrow}, (\varphi^D)^{\sigma\sigma}, \tag{2.152c}$$

with $\sigma = \uparrow, \downarrow$. In terms of this spin components, the flow of the self-energy (2.140) can be written as

$$\begin{aligned}
\frac{\partial}{\partial \Lambda} \Sigma_{k'_1 k_1}^{\uparrow}(\omega) = & -\{i\} \sum_{\omega'} \left\{ \right. \\
& S_{k_2 k'_2}^{\uparrow}(\omega') \left[\nu_{k'_1 k'_2 | k_1 k_2}^{\uparrow\uparrow} + (\varphi^P)_{k'_1 k'_2 | k_1 k_2}^{\uparrow\uparrow}(\omega' + \omega) - (\varphi^D)_{k'_2 k'_1 | k_1 k_2}^{\uparrow\uparrow}(\omega' - \omega) + (\varphi^D)_{k'_1 k'_2 | k_1 k_2}^{\uparrow\uparrow}(0) \right] \\
& + S_{k_2 k'_2}^{\downarrow}(\omega') \left[\nu_{k'_1 k'_2 | k_1 k_2}^{\uparrow\downarrow} + (\varphi^P)_{k'_1 k'_2 | k_1 k_2}^{\uparrow\downarrow}(\omega' + \omega) + (\varphi^X)_{k'_1 k'_2 | k_1 k_2}^{\uparrow\downarrow}(\omega' - \omega) + (\varphi^D)_{k'_1 k'_2 | k_1 k_2}^{\uparrow\downarrow}(0) \right] \left. \right\}, \tag{2.153a}
\end{aligned}$$

and

$$\begin{aligned} \frac{\partial}{\partial \Lambda} \Sigma_{k'_1 k_1}^\downarrow(\omega) = & -\{i\} \sum_{\omega'} \left\{ \right. \\ & S_{k_2 k'_2}^\uparrow(\omega') \left[\nu_{k'_2 k'_1 | k_2 k_1}^{\uparrow\downarrow} + (\varphi^P)_{k'_2 k'_1 | k_2 k_1}^{\uparrow\downarrow}(\omega' + \omega) + (\varphi^X)_{k'_2 k'_1 | k_2 k_1}^{\uparrow\downarrow}(\omega - \omega') + (\varphi^D)_{k'_2 k'_1 | k_2 k_1}^{\uparrow\downarrow}(0) \right] \\ & \left. + S_{k_2 k'_2}^\downarrow(\omega') \left[\nu_{k'_1 k'_2 | k_1 k_2}^{\downarrow\downarrow} + (\varphi^P)_{k'_1 k'_2 | k_1 k_2}^{\downarrow\downarrow}(\omega' + \omega) - (\varphi^D)_{k'_2 k'_1 | k_1 k_2}^{\downarrow\downarrow}(\omega' - \omega) + (\varphi^D)_{k'_1 k'_2 | k_1 k_2}^{\downarrow\downarrow}(0) \right] \right\}, \end{aligned} \quad (2.153b)$$

where we used (2.143, 2.142) and the symmetry properties of the bare interaction (2.5a). Furthermore, using the $\tilde{\gamma}$ components

$$(\tilde{\gamma}^P)_{k'_1 k'_2 | k_1 k_2}^{\sigma\sigma}(\Pi) = \left[\nu + (\varphi^P)(\Pi) + (\phi^D) \right]_{k'_1 k'_2 | k_1 k_2}^{\sigma\sigma} - (\phi^D)_{k'_2 k'_1 | k_1 k_2}^{\sigma\sigma}, \quad (2.154)$$

$$(\tilde{\gamma}^P)_{k'_1 k'_2 | k_1 k_2}^{\uparrow\downarrow}(\Pi) = \left[\nu + (\varphi^P)(\Pi) + (\phi^X) + (\phi^D) \right]_{k'_1 k'_2 | k_1 k_2}^{\uparrow\downarrow}, \quad (2.155)$$

$$(\tilde{\gamma}^X)_{k'_1 k'_2 | k_1 k_2}^{\uparrow\downarrow}(X) = \left[\nu + (\varphi^X)(X) + (\phi^P) + (\phi^D) \right]_{k'_1 k'_2 | k_1 k_2}^{\uparrow\downarrow}, \quad (2.156)$$

$$(\tilde{\gamma}^D)_{k'_1 k'_2 | k_1 k_2}^{\sigma\sigma}(\Delta) = \left[\nu + (\varphi^D)(\Delta) + (\phi^P) \right]_{k'_1 k'_2 | k_1 k_2}^{\sigma\sigma} - (\phi^D)_{k'_2 k'_1 | k_1 k_2}^{\sigma\sigma}, \quad (2.157)$$

$$(\tilde{\gamma}^D)_{k'_1 k'_2 | k_1 k_2}^{\uparrow\downarrow}(\Delta) = \left[\nu + (\varphi^D)(\Delta) + (\phi^P) + (\phi^X) \right]_{k'_1 k'_2 | k_1 k_2}^{\uparrow\downarrow}, \quad (2.158)$$

$$(2.159)$$

the fRG flow of the vertex components (2.152) is given by

$$\frac{\partial}{\partial \Lambda} (\varphi^P)_{k'_1 k'_2 | k_1 k_2}^{\sigma\sigma}(\Pi) = (\tilde{\gamma}^P)_{k'_1 k'_2 | k_3 k_4}^{\sigma\sigma}(\Pi) (I^{pp})_{k_3 k_4 | k'_3 k'_4}^{\sigma\sigma}(\Pi) (\tilde{\gamma}^P)_{k'_3 k'_4 | k_1 k_2}^{\sigma\sigma}(\Pi), \quad (2.160a)$$

$$\frac{\partial}{\partial \Lambda} (\varphi^P)_{k'_1 k'_2 | k_1 k_2}^{\uparrow\downarrow}(\Pi) = 2(\tilde{\gamma}^P)_{k'_1 k'_2 | k_3 k_4}^{\uparrow\downarrow}(\Pi) (I^{pp})_{k_3 k_4 | k'_3 k'_4}^{\uparrow\downarrow}(\Pi) (\tilde{\gamma}^P)_{k'_3 k'_4 | k_1 k_2}^{\uparrow\downarrow}(\Pi), \quad (2.160b)$$

$$\frac{\partial}{\partial \Lambda} (\varphi^X)_{k'_1 k'_2 | k_1 k_2}^{\uparrow\downarrow}(X) = (\tilde{\gamma}^X)_{k'_1 k'_4 | k_3 k_2}^{\uparrow\downarrow}(X) (I^{ph})_{k_3 k_4 | k'_3 k'_4}^{\uparrow\downarrow}(X) (\tilde{\gamma}^X)_{k'_3 k'_2 | k_1 k_4}^{\uparrow\downarrow}(X), \quad (2.160c)$$

$$\frac{\partial}{\partial \Lambda} (\varphi^D)_{k'_1 k'_2 | k_1 k_2}^{\uparrow\uparrow}(\Delta) = - \left[(\tilde{\gamma}^D)_{k'_1 k'_3 | k_1 k_4}^{\uparrow\uparrow}(\Delta) (I^{ph})_{k_3 k_4 | k'_3 k'_4}^{\uparrow\uparrow}(\Delta) (\tilde{\gamma}^D)_{k'_4 k'_2 | k_3 k_2}^{\uparrow\uparrow}(\Delta) \right. \quad (2.160d)$$

$$\left. + (\tilde{\gamma}^D)_{k'_1 k'_3 | k_1 k_4}^{\uparrow\downarrow}(\Delta) (I^{ph})_{k_3 k_4 | k'_3 k'_4}^{\downarrow\downarrow}(\Delta) (\tilde{\gamma}^D)_{k'_2 k'_4 | k_2 k_3}^{\uparrow\downarrow}(-\Delta) \right], \quad (2.160e)$$

$$\frac{\partial}{\partial \Lambda} (\varphi^D)_{k'_1 k'_2 | k_1 k_2}^{\downarrow\downarrow}(\Delta) = - \left[(\tilde{\gamma}^D)_{k'_1 k'_3 | k_1 k_4}^{\downarrow\downarrow}(\Delta) (I^{ph})_{k_3 k_4 | k'_3 k'_4}^{\downarrow\downarrow}(\Delta) (\tilde{\gamma}^D)_{k'_4 k'_2 | k_3 k_2}^{\downarrow\downarrow}(\Delta) \right. \quad (2.160f)$$

$$\left. + (\tilde{\gamma}^D)_{k'_3 k'_1 | k_4 k_1}^{\uparrow\downarrow}(-\Delta) (I^{ph})_{k_3 k_4 | k'_3 k'_4}^{\uparrow\uparrow}(\Delta) (\tilde{\gamma}^D)_{k'_4 k'_2 | k_3 k_2}^{\uparrow\downarrow}(\Delta) \right], \quad (2.160g)$$

$$\frac{\partial}{\partial \Lambda} (\varphi^D)_{k'_1 k'_2 | k_1 k_2}^{\uparrow\downarrow}(\Delta) = - \left[(\tilde{\gamma}^D)_{k'_1 k'_3 | k_1 k_4}^{\uparrow\uparrow}(\Delta) (I^{ph})_{k_3 k_4 | k'_3 k'_4}^{\uparrow\uparrow}(\Delta) (\tilde{\gamma}^D)_{k'_4 k'_2 | k_3 k_2}^{\uparrow\downarrow}(\Delta) \right. \quad (2.160h)$$

$$\left. + (\tilde{\gamma}^D)_{k'_1 k'_3 | k_1 k_4}^{\uparrow\downarrow}(\Delta) (I^{ph})_{k_3 k_4 | k'_3 k'_4}^{\downarrow\downarrow}(\Delta) (\tilde{\gamma}^D)_{k'_4 k'_2 | k_3 k_2}^{\downarrow\downarrow}(\Delta) \right]. \quad (2.160i)$$

2.4.3 Spatial structure

For our choice of systems, the second-order truncation with channel decomposition is unfortunately not yet enough to enable a numerical treatment. For QPC applications, we usually use $N_{\text{tot}} = 61$ sites for the interacting central region in order to be able to resolve the QPC

barrier properly. The resulting N_{tot}^4 different spatial components (plus additional frequency, spin, band and Keldysh structure) are too many to be stored in the RAM memory of current processors. Therefore, we have to introduce another approximation scheme, to reduce the number of spatial indices. Our guideline for this will be to only keep spatial components which are at least generated in second-order perturbation theory in the interaction. Components that are generated only in higher order will not be kept systematically. This idea was first implemented by Bauer et al. for the case of onsite interactions in the so called Coupled Ladder Approximation (CLA) [BHvD14]. Here, we extend this idea to the case of finite-ranged interactions and correspondingly call it the extended Coupled Ladder Approximation (eCLA).

In order to formulate the eCLA efficiently, it is advantageous to introduce a new notation for the spatial indices of any channel dependent quantity Ξ^A , with $A \in \{P, X, D\}$ that exhibits four spatial indices. In (2.160), these quantities (there $\Xi \in \{\varphi, \tilde{\gamma}, I\}$) are of the form

$$(\Xi^A)_{j'_1 j'_2 | j_1 j_2}, \quad (2.161)$$

with indices running in the range $-N \leq j'_1, \dots, j_2 \leq N$ (the number of total sites is $N_{\text{tot}} = 2N + 1$). In particular, the index ranges are independent of the channel $A \in \{P, X, D\}$. Now we introduce channel dependent indices

$$(\Xi^P)_{ji}^{lk} = (\Xi^P)_{j(j+l)|i(i+k)}, \quad (2.162a)$$

$$(\Xi^X)_{ji}^{lk} = (\Xi^X)_{j(i+k)|i(j+l)}, \quad (2.162b)$$

$$(\Xi^D)_{ji}^{lk} = (\Xi^D)_{j(i+k)|(j+l)i}, \quad (2.162c)$$

where we refer to l, k as short and j, i as long indices with ranges

$$-L \leq l, k \leq L, \quad (2.163a)$$

$$\max(-N, -N - l) \leq j \leq \min(N, N + l), \quad (2.163b)$$

$$\max(-N, -N - k) \leq i \leq \min(N, N + k), \quad (2.163c)$$

with the feedback length L . If one chooses $L = 2N$, the description (2.162) is equivalent to the original description (2.161). If, however, L is chosen smaller than $2N$, this introduces an additional approximation that sets all old vertex components in (2.161) which cannot be described by (2.162) to zero.

By comparison with the terms generated in second order perturbation theory (c.f. second order diagrams in Pub. 1 in Sec. 3.2), we see that all spatial components which are generated in second order in the interaction, are included in our description (2.162) if the feedback length L is chosen at least as large as the interaction range L_U (we assume that the Coulomb interaction U_{ji} between to sites is only finite if $|j - i| \leq L_U$). Correspondingly, the CLA scheme used by Bauer et al. is a special case of our description. In order to reduce the eCLA to the CLA, we have to set the feedback length to zero, $L = 0$ and omit all the $(\phi^D)^{\uparrow\downarrow}$ contributions (those are not contained in the CLA description since, in the case of onsite interactions, they do not contribute in second order).

In the following, we will often use block matrix multiplication for spatial indices

$$[A \cdot B]_{ji}^{lk} = \sum_{l', j'} A_{jj'}^{l'l'} B_{j'i}^{l'k}, \quad (2.164)$$

as well as the spatial transformations

$$(A^T)_{ji}^{lk} = A_{ij}^{kl}, \quad (2.165a)$$

$$(A^{I_1})_{ji}^{lk} = A_{(j+l)i}^{(-l)k}, \quad (2.165b)$$

$$(A^{I_2})_{ji}^{lk} = A_{j(i+k)}^{l(-k)}, \quad (2.165c)$$

$$(A^I)_{ji}^{lk} = A_{(j+l)(i+k)}^{(-l)(-k)}. \quad (2.165d)$$

Note that the I and T transformations commute, i.e. $(A^T)^I = (A^I)^T$, and that one has

$$(AB)^T = B^T A^T, \quad (2.166a)$$

$$(AB)^I = A^I B^I. \quad (2.166b)$$

For an efficient notation of the flow equations, we also introduce for a two spatial index quantity Y_{ji} the notation

$$Y_j^l = Y_{j(j+l)}. \quad (2.167)$$

Furthermore, we define the transformations

$$[Y^T]_{ji} = Y_{ij}, \quad (2.168a)$$

$$(Y^I)_j^l = Y_{(j+l)}^{-l}. \quad (2.168b)$$

$$(2.168c)$$

Note that, in particular, we have for two spatial index quantities

$$(Y^I)_j^l = (Y^T)_j^l. \quad (2.169)$$

For the occurring products of two index Y and four index quantities A , we introduce the notation

$$[A \cdot Y]_j^l = A_{ji}^{lk} Y_i^k, \quad (2.170a)$$

$$\text{Tr}[A \times Y]_{ji} = A_{ji}^{lk} Y_{(i+k)(j+l)}. \quad (2.170b)$$

For these products, the following symmetries hold

$$(A \cdot Y)^I = A^I \cdot Y^I, \quad (2.171a)$$

$$\left[\text{Tr}[A \times Y] \right]^T = \text{Tr}[A^T \times Y^T]. \quad (2.171b)$$

Furthermore, we will adapt the following convention for the bare vertex: Whenever we write an expression like

$$[\bar{v} + \Xi^A]_{ji}^{lk}, \quad (2.172)$$

where Ξ^A is a channel dependent vertex quantity, the bare vertex is to be evaluated with the spatial structure appropriate for channel A , i.e. explicitly we have

$$[\bar{v} + \Xi^P]_{ji}^{lk} = [\bar{v} + \Xi^P]_{j(j+l)|i(i+k)}, \quad (2.173a)$$

$$[\bar{v} + \Xi^X]_{ji}^{lk} = [\bar{v} + \Xi^X]_{j(i+k)|i(j+l)}, \quad (2.173b)$$

$$[\bar{v} + \Xi^D]_{ji}^{lk} = [\bar{v} + \Xi^D]_{j(i+k)|(j+l)i}. \quad (2.173c)$$

Having introduced the short index description (2.162), as well as the explicitly formulated spin structure (2.160) of the flow equations, we have everything at hand to formulate the eCLA flow equations for the Matsubara case. In the real-frequency Keldysh formulation, we still have to resolve the Keldysh structure of the flow. Therefore, let us take a look at the easier Matsubara formulation first.

2.4.4 Matsubara formulation of the eCLA

In this subsection, we specify the eCLA flow equations to the Matsubara case. For this, we combine the short index description (2.162) with the explicit spin structure of the fRG flow (2.160). Furthermore, we discuss the special cases of magnetic field, as well as zero temperature. In the latter case, we also argue that a static approximation is sufficient and discuss its specific form.

In order to connect with our publication P1 in Sec. 3.2,¹³ we introduce the following vertex bubble quantities

$$(W^P)_{ji}^{lk\sigma\sigma'}(\Pi) = (I^{pp})_{j(j+l)|i(i+k)}^{\sigma\sigma'}(\Pi) = \frac{T}{2} \sum_n \left[S_{ji}^\sigma(\omega_n) G_{(j+l)(i+k)}^{\sigma'}(\Pi - \omega_n) + [S \leftrightarrow G] \right] \quad (2.174a)$$

$$(W^X)_{ji}^{lk\sigma\sigma'}(X) = (I^{ph})_{j(i+k)|i(j+l)}^{\sigma\sigma'}(X) = T \sum_n \left[S_{ji}^\sigma(\omega_n) G_{(i+k)(j+l)}^{\sigma'}(\omega_n + X) + [S \leftrightarrow G] \right]. \quad (2.174b)$$

For our generic fRG flow, we will only need six of these vertex bubbles, namely

$$(W^P)^{\sigma\sigma}, (W^P)^{\uparrow\downarrow}, (W^X)^{\sigma\sigma}, (W^X)^{\uparrow\downarrow}, \quad (2.175)$$

with $\sigma = \uparrow, \downarrow$. Furthermore, we introduce the abbreviations

$$P = \varphi^P, \quad \tilde{P} = \tilde{\gamma}^P, \quad (2.176a)$$

$$X = \varphi^X, \quad \tilde{X} = \tilde{\gamma}^X, \quad (2.176b)$$

$$D = \varphi^D, \quad \tilde{D} = \tilde{\gamma}^D, \quad (2.176c)$$

which enable us to write down the fRG flow a little more compactly and is the same notation as used in P1, Sec. 3.2.

Before we write down the flow equations, we first take a look at the symmetries of Green's and vertex functions (as discussed in Sec. 2.2) and see what form they take in our new spatial index notation. We only state here symmetries relating to our choice of kept spin components.

¹³ Instead of exactly repeating the flow equations of P1, here we give a slightly different representation. This has two reasons. (i) In P1, we gave a formulation containing dependent spin components, whereas we use here only the independent spin components (2.160) to formulate the flow. Thus, the equations here are closer to our actual implementation of the flow, where one wants to work only with the independent components, to reduce numerical costs. (ii) Furthermore, we introduce here a notation that is free of all spatial indices, making the structure of the flow much more transparent.

The eliminated spin components can always be obtained via particle permutation as discussed in Sec. 2.4.1. We give their explicit form in App. A.2. The whole¹⁴ set of symmetries can then be summarized as follows

- **Particle permutation**

$$P^{\sigma\sigma} = P^{I\sigma\sigma} = -P^{I_1\sigma\sigma} = -P^{I_2\sigma\sigma}, \quad (2.177a)$$

$$D^{\sigma\sigma}(\Delta) = D^{TI\sigma\sigma}(-\Delta). \quad (2.177b)$$

- **Complex conjugation**

$$\Sigma_{ji}^\sigma(\omega_n) = \left[\Sigma_{ij}^\sigma(-\omega_n) \right]^*, \quad (2.178a)$$

$$P^{\sigma\sigma'}(\Pi) = \left[(P^T)^{\sigma\sigma'}(-\Pi) \right]^*, \quad (2.178b)$$

$$X^{\uparrow\downarrow}(X) = \left[(X^T)^{\uparrow\downarrow}(-X) \right]^*, \quad (2.178c)$$

$$D^{\sigma\sigma'}(\Delta) = \left[(D^I)^{\sigma\sigma'}(\Delta) \right]^*. \quad (2.178d)$$

- **Time reversal**

$$\Sigma_{ji}^\sigma(\omega_n) = \Sigma_{ij}^\sigma(\omega_n), \quad (2.179a)$$

$$P^{\sigma\sigma'} = (P^T)^{\sigma\sigma'}, \quad (2.179b)$$

$$X^{\uparrow\downarrow} = (X^T)^{\uparrow\downarrow}, \quad (2.179c)$$

$$D^{\sigma\sigma'}(\Delta) = (D^I)^{\sigma\sigma'}(-\Delta). \quad (2.179d)$$

For the bubbles (2.175) we have in general

$$W = W^T, \quad (2.180a)$$

$$W(\Omega) = W^*(-\Omega), \quad (2.180b)$$

$$(W^P)^{\sigma\sigma}(\Pi) = (W^P)^{I\sigma\sigma}(\Pi), \quad (2.180c)$$

$$(W^X)^{\sigma\sigma}(X) = (W^X)^{I\sigma\sigma}(-X), \quad (2.180d)$$

where $\Omega \in \{\Pi, X, \Delta\}$. These bubble symmetries can be seen immediately from their definition and the symmetry properties (complex conjugation and time-reversal) of the propagators, see (2.77), (2.95a).

All the symmetries in (2.177) – (2.179) can be checked to be consistent with the fRG flow, see App. A.4. Furthermore, all the vertex symmetries in (2.177) – (2.179) also hold for the corresponding tilded vertex objects. This is immediately clear from the definition of the tilded objects (2.137) and the choice of the feedback in (2.147). Of course it can also be checked explicitly, using the explicit form of the tilded quantities below in (2.187). In the following derivation of the final form of the flow equations, we first write down the r.h.s. in the form resulting immediately from combining (2.160) with our short index notation for spatial indices (2.162). Then, in a final step, we will simplify the r.h.s. of the flow equation using

¹⁴ To the knowledge of the author; the reader is welcome to search for more symmetries.

the symmetries displayed above (2.177) – (2.179). Note that if one wants to check if these symmetries are actually consistent with the fRG flow, one actually *can* use the symmetry simplified version of the r.h.s. of the flow, as long the initial conditions satisfy the symmetries. This is done explicitly in App. A.4.

In order to use our short-index notation (2.162) efficiently, we furthermore split the flow of the self-energy (2.153) in a static and a dynamic part

$$\frac{\partial}{\partial \Lambda} \Sigma = \frac{\partial}{\partial \Lambda} \Sigma_s + \frac{\partial}{\partial \Lambda} \Sigma_d, \quad (2.181)$$

with

$$\frac{\partial}{\partial \Lambda} (\Sigma_s)_{j(j+l)}^\uparrow = - \sum_{\omega'} \left\{ S_{i(i+k)}^\uparrow(\omega') [\bar{v} + D(0)]_{ji}^{\uparrow\uparrow lk} + S_{i(i+k)}^\downarrow(\omega') [\bar{v} + D(0)]_{ji}^{\uparrow\downarrow lk} \right\}, \quad (2.182a)$$

$$\frac{\partial}{\partial \Lambda} (\Sigma_s)_{j(j+l)}^\downarrow = - \sum_{\omega'} \left\{ S_{i(i+k)}^\uparrow(\omega') [(\bar{v} + D(0))^{TI}]_{ji}^{\uparrow\downarrow lk} + S_{i(i+k)}^\downarrow(\omega') [\bar{v} + D(0)]_{ji}^{\downarrow\downarrow lk} \right\}, \quad (2.182b)$$

and

$$\begin{aligned} \frac{\partial}{\partial \Lambda} (\Sigma_d)_{ji}^\uparrow(\omega) = & - \sum_{\omega'} \left\{ S_{(i+k)(j+l)}^\uparrow(\omega') P_{ji}^{\uparrow\uparrow lk}(\omega' + \omega) - S_{(j+l)(i+k)}^\uparrow(\omega') (D^{TI})_{ji}^{\uparrow\uparrow lk}(\omega' - \omega) \right. \\ & \left. + S_{(i+k)(j+l)}^\downarrow(\omega') P_{ji}^{\uparrow\downarrow lk}(\omega' + \omega) + S_{(j+l)(i+k)}^\downarrow(\omega') X_{ji}^{\uparrow\downarrow lk}(\omega' - \omega) \right\}, \end{aligned} \quad (2.183a)$$

$$\begin{aligned} \frac{\partial}{\partial \Lambda} (\Sigma_d)_{ji}^\downarrow(\omega) = & - \sum_{\omega'} \left\{ S_{(i+k)(j+l)}^\uparrow(\omega') (P^I)_{ji}^{\uparrow\downarrow lk}(\omega' + \omega) + S_{(j+l)(i+k)}^\uparrow(\omega') (X^{TI})_{ji}^{\uparrow\downarrow lk}(\omega' - \omega) \right. \\ & \left. + S_{(i+k)(j+l)}^\downarrow(\omega') P_{ji}^{\downarrow\downarrow lk}(\omega' + \omega) - S_{(j+l)(i+k)}^\downarrow(\omega') (D^{TI})_{ji}^{\downarrow\downarrow lk}(\omega' - \omega) \right\}. \end{aligned} \quad (2.183b)$$

Using the symmetry relations (2.177) - (2.179) and the product notation introduced in (2.170), we can write the self-energy flow compactly in a spatial index free notation as

$$\frac{\partial}{\partial \Lambda} \Sigma_s^\uparrow = - \left\{ [\bar{v} + D(0)]^{\uparrow\uparrow} \cdot \hat{S}^\uparrow + [\bar{v} + D(0)]^{\uparrow\downarrow} \cdot \hat{S}^\downarrow \right\}, \quad (2.184a)$$

$$\frac{\partial}{\partial \Lambda} \Sigma_s^\downarrow = - \left\{ [(\bar{v} + D(0))^T]^{\uparrow\downarrow} \cdot \hat{S}^\uparrow + [\bar{v} + D(0)]^{\downarrow\downarrow} \cdot \hat{S}^\downarrow \right\}, \quad (2.184b)$$

where

$$\hat{S} = \sum_{\omega'} S(\omega') = T \sum_n S(\omega_n). \quad (2.185)$$

Note that due to the complex conjugation symmetry $S(-\omega_n) = S(\omega_n)^*$, \hat{S} and therefore also Σ_s are real numbers.

Furthermore, we have for the dynamic part of the self-energy

$$\frac{\partial}{\partial \Lambda} \Sigma_d^\uparrow(\omega) = -T \sum_n \left\{ \text{Tr} \left[\left(P^{\uparrow\uparrow}(\omega_n + \omega) - D^{\uparrow\uparrow}(\omega - \omega_n) \right) \times S^\uparrow(\omega_n) \right] \right. \\ \left. + \text{Tr} \left[\left(P^{\uparrow\downarrow}(\omega_n + \omega) + X^{\uparrow\downarrow}(\omega_n - \omega) \right) \times S^\downarrow(\omega_n) \right] \right\}, \quad (2.186a)$$

$$\frac{\partial}{\partial \Lambda} \Sigma_d^\downarrow(\omega) = -T \sum_n \left\{ \text{Tr} \left[\left((P^I)^{\uparrow\downarrow}(\omega_n + \omega) + (X^I)^{\uparrow\downarrow}(\omega - \omega_n) \right) \times S^\uparrow(\omega_n) \right] \right. \\ \left. + \text{Tr} \left[\left(P^{\downarrow\downarrow}(\omega_n + \omega) - D^{\downarrow\downarrow}(\omega - \omega_n) \right) \times S^\downarrow(\omega_n) \right] \right\}. \quad (2.186b)$$

Using the explicit form of the tilded vertex quantities

$$\tilde{P}_{ji}^{\sigma\sigma lk}(\Pi) = \left[\bar{v}_{j(j+l)|i(i+k)}^{\sigma\sigma|\sigma\sigma} + P_{ji}^{\sigma\sigma lk}(\Pi) - (\phi^D)_{j(i+k)}^{\sigma\sigma(i+k-j)(j+l-i)} + (\phi^D)_{j(i+k)}^{\sigma\sigma(i-j)(j+l-i-k)} \right], \quad (2.187a)$$

$$\tilde{P}_{ji}^{\uparrow\downarrow lk}(\Pi) = \left[\bar{v}_{j(j+l)|i(i+k)}^{\uparrow\downarrow|\uparrow\downarrow} + P_{ji}^{\uparrow\downarrow lk}(\Pi) + (\phi^X)_{ji}^{\uparrow\downarrow(i+k-j)(j+l-i)} + (\phi^D)_{j(i+k)}^{\uparrow\downarrow(i-j)(j+l-i-k)} \right], \quad (2.187b)$$

$$\tilde{X}_{ji}^{\uparrow\downarrow lk}(X) = \left[\bar{v}_{j(i+k)|i(j+l)}^{\uparrow\downarrow|\uparrow\downarrow} + X_{ji}^{\uparrow\downarrow lk}(X) + (\phi^P)_{ji}^{\uparrow\downarrow(i+k-j)(j+l-i)} + (\phi^D)_{j(j+l)}^{\uparrow\downarrow(i-j)(i+k-j-l)} \right], \quad (2.187c)$$

$$\tilde{D}_{ji}^{\sigma\sigma lk}(\Delta) = \left[\bar{v}_{j(i+k)|(j+l)i}^{\sigma\sigma|\sigma\sigma} + D_{ji}^{\sigma\sigma lk}(\Delta) + (\phi^P)_{j(j+l)}^{\sigma\sigma(i+k-j)(i-j-l)} - (\phi^D)_{j(j+l)}^{\sigma\sigma(i-j)(i+k-j-l)} \right], \quad (2.187d)$$

$$\tilde{D}_{ji}^{\uparrow\downarrow lk}(\Delta) = \left[\bar{v}_{j(i+k)|(j+l)i}^{\uparrow\downarrow|\uparrow\downarrow} + D_{ji}^{\uparrow\downarrow lk}(\Delta) + (\phi^P)_{j(j+l)}^{\uparrow\downarrow(i+k-j)(i-j-l)} + (\phi^X)_{j(j+l)}^{\uparrow\downarrow(i-j)(i+k-j-l)} \right], \quad (2.187e)$$

the vertex flow can be written for the P- and X-channel very compactly as

$$\frac{\partial}{\partial \Lambda} P^{\sigma\sigma}(\Pi) = \tilde{P}^{\sigma\sigma}(\Pi) \cdot (W^P)^{\sigma\sigma}(\Pi) \cdot \tilde{P}^{\sigma\sigma}(\Pi), \quad (2.188a)$$

$$\frac{\partial}{\partial \Lambda} P^{\uparrow\downarrow}(\Pi) = 2\tilde{P}^{\uparrow\downarrow}(\Pi) \cdot (W^P)^{\uparrow\downarrow}(\Pi) \cdot \tilde{P}^{\uparrow\downarrow}(\Pi), \quad (2.188b)$$

$$\frac{\partial}{\partial \Lambda} X^{\uparrow\downarrow}(X) = \tilde{X}^{\uparrow\downarrow}(X) \cdot (W^X)^{\uparrow\downarrow}(X) \cdot \tilde{X}^{\uparrow\downarrow}(X). \quad (2.188c)$$

Using (2.165), we can write down an interim form of the D-channel as

$$\frac{\partial}{\partial \Lambda} D^{\uparrow\uparrow}(\Delta) = - \left[\tilde{D}^{\uparrow\uparrow}(\Delta) \cdot (W^X)^{TI\uparrow\uparrow}(\Delta) \cdot \tilde{D}^{\uparrow\uparrow}(\Delta) + \tilde{D}^{\uparrow\downarrow}(\Delta) \cdot (W^X)^{TI\downarrow\downarrow}(\Delta) \cdot (\tilde{D}^{TI})^{\uparrow\downarrow}(-\Delta) \right], \quad (2.189a)$$

$$\frac{\partial}{\partial \Lambda} D^{\downarrow\downarrow}(\Delta) = - \left[\tilde{D}^{\downarrow\downarrow}(\Delta) \cdot (W^X)^{TI\downarrow\downarrow}(\Delta) \cdot \tilde{D}^{\downarrow\downarrow}(\Delta) + (\tilde{D}^{TI})^{\uparrow\downarrow}(-\Delta) \cdot (W^X)^{TI\uparrow\uparrow}(\Delta) \cdot \tilde{D}^{\uparrow\downarrow}(\Delta) \right], \quad (2.189b)$$

$$\frac{\partial}{\partial \Lambda} D^{\uparrow\downarrow}(\Delta) = - \left[\tilde{D}^{\uparrow\uparrow}(\Delta) \cdot (W^X)^{TI\uparrow\uparrow}(\Delta) \cdot \tilde{D}^{\uparrow\downarrow}(\Delta) + \tilde{D}^{\uparrow\downarrow}(\Delta) \cdot (W^X)^{TI\downarrow\downarrow}(\Delta) \cdot \tilde{D}^{\downarrow\downarrow}(\Delta) \right]. \quad (2.189c)$$

This interim form (2.189) can be further simplified by using symmetry relations for the bubbles (2.180) as well as for the vertex quantities (2.177) - (2.179). We obtain

$$\begin{aligned} \frac{\partial}{\partial \Lambda} D^{\uparrow\uparrow}(\Delta) = & - \left[\tilde{D}^{\uparrow\uparrow}(\Delta) \cdot (W^X)^{\uparrow\uparrow}(-\Delta) \cdot \tilde{D}^{\uparrow\uparrow}(\Delta) \right. \\ & \left. + \tilde{D}^{\uparrow\downarrow}(\Delta) \cdot (W^X)^{\downarrow\downarrow}(-\Delta) \cdot (\tilde{D}^T)^{\uparrow\downarrow}(\Delta) \right], \end{aligned} \quad (2.190a)$$

$$\begin{aligned} \frac{\partial}{\partial \Lambda} D^{\downarrow\downarrow}(\Delta) = & - \left[\tilde{D}^{\downarrow\downarrow}(\Delta) \cdot (W^X)^{\downarrow\downarrow}(-\Delta) \cdot \tilde{D}^{\downarrow\downarrow}(\Delta) \right. \\ & \left. + (\tilde{D}^T)^{\uparrow\downarrow}(\Delta) \cdot (W^X)^{\uparrow\uparrow}(-\Delta) \cdot \tilde{D}^{\uparrow\downarrow}(\Delta) \right], \end{aligned} \quad (2.190b)$$

$$\begin{aligned} \frac{\partial}{\partial \Lambda} D^{\uparrow\downarrow}(\Delta) = & - \left[\tilde{D}^{\uparrow\uparrow}(\Delta) \cdot (W^X)^{\uparrow\uparrow}(-\Delta) \cdot \tilde{D}^{\uparrow\downarrow}(\Delta) \right. \\ & \left. + \tilde{D}^{\uparrow\downarrow}(\Delta) \cdot (W^X)^{\downarrow\downarrow}(-\Delta) \cdot \tilde{D}^{\downarrow\downarrow}(\Delta) \right]. \end{aligned} \quad (2.190c)$$

Having derived the flow equations, the last piece of input we need for actual computations are the explicit form of the initial conditions which read

$$\Sigma_{j_1 j_1}^{\Lambda_{\text{ini}} \sigma_1} = \frac{1}{2} \sum_{j_2, \sigma_2} \bar{v}_{j_1 j_2 | j_1 j_2}^{\sigma_1 \sigma_2 | \sigma_1 \sigma_2}, \quad (2.191a)$$

$$P^{\Lambda_{\text{ini}}} = X^{\Lambda_{\text{ini}}} = D^{\Lambda_{\text{ini}}} = 0. \quad (2.191b)$$

Before we continue to derive the explicit flow equations for the Keldysh formulation in the next subsection, we take a look at a few special cases of the Matsubara flow.

Zero magnetic field

In the case of zero magnetic field, we have an additional symmetry between spin up and down components by flipping all spins

$$A^{\sigma'_1 \dots \sigma'_n | \sigma'_1 \dots \sigma'_n} = A^{\bar{\sigma}'_1 \dots \bar{\sigma}'_n | \bar{\sigma}'_1 \dots \bar{\sigma}'_n}, \quad (2.192)$$

where A is any spin dependent quantity and $\bar{\sigma} = -\sigma$. Therefore for magnetic field $B = 0$, we only have to compute the five vertex quantities

$$P^{\uparrow\uparrow}, P^{\uparrow\downarrow}, X^{\uparrow\downarrow}, D^{\uparrow\uparrow}, D^{\uparrow\downarrow}. \quad (2.193)$$

Furthermore, we get for the components with mixed spins the additional symmetry relations

$$P^{\uparrow\downarrow} = P^{I\uparrow\downarrow}, \quad (2.194a)$$

$$X^{\uparrow\downarrow}(X) = X^{I\uparrow\downarrow}(-X), \quad (2.194b)$$

$$D^{\uparrow\downarrow} = D^{T\uparrow\downarrow}. \quad (2.194c)$$

Note that for zero magnetic field only *two* bubble evaluations are needed, e.g.

$$(W^P)^{\uparrow\uparrow}, (W^X)^{\uparrow\uparrow}. \quad (2.195)$$

Zero temperature

Although we have formulated the Matsubara flow equations for arbitrary finite temperatures, we usually use it only to determine the conductance at zero temperature. At finite temperature, the conductance contains both single-particle as well as two-particle contributions evaluated at real frequencies, see Sec. 5.2 below. In order to obtain the needed information within the Matsubara formalism, one would have to perform an analytic continuation from the purely imaginary Matsubara frequencies to the real frequency axis. While this is numerically per se

an ill-defined question, due to the finite number of discrete Matsubara frequencies available in a computation, it turned out that in the QPC case it is especially difficult to extract meaningful information. This problem was studied in detail by Heyder et al. [Hey14] who showed that even smallest numerical errors and the general analytic continuation ambiguity lead to large errors in the conductance.

At zero temperature, the conductance contains only information of the self-energy at the chemical potential, which can be obtained without problem from our fRG scheme defined above, by taking the appropriate $T \rightarrow 0$ limit, see the discussion in Sec. 2.3.2 above. Bauer et al. even showed in [BHvD14] that for zero temperature a static approximation of the vertices (and correspondingly also the self-energy) in the fRG-flow leads to reasonable results for a QPC setup with onsite interactions. For this reason, we focused in our publication P1, Sec. (3.2), solely on the zero temperature case in a static approximation to investigate the effect of finite-ranged interactions in a QPC. Therefore, at the end of this subsection we take a brief look on how to perform the $T \rightarrow 0$ limit of the Matsubara flow. In the limit of vanishing temperature, the Matsubara frequencies become continuous. From our definition in Sec. (2.1.1) it follows that that

$$T \sum_{\omega_n} f(\omega_n) \rightarrow \frac{1}{2\pi i} \int_{\text{Im-axis}} d\omega f(\omega) = \frac{1}{2\pi} \int d\omega f(i\omega), \quad (2.196)$$

where $f(\omega)$ is a function defined on the imaginary axis. While this limit can be performed without difficulty for the self-energy flow (2.184) and (2.186), the limiting procedure for the flow of the vertex quantities requires more care, see the discussion in Sec. 2.3.2. The resulting explicit $T \rightarrow 0$ limit of the bubble terms (2.174) is given by

$$\begin{aligned} (W^P)_{ji}^{lk\sigma\sigma'}(\Pi) &= \frac{1}{4\pi} \int d\omega \left[S_{ji}^\sigma(i\omega) G_{(j+l)(i+k)}^{\sigma'}(\Pi - i\omega) + [G \leftrightarrow S] \right] \\ &= \frac{1}{4\pi} \int d\omega \delta(|\omega| - \Lambda) \theta(|\Pi - i\omega| - \Lambda) \left[\tilde{G}_{ji}^\sigma(i\omega) \tilde{G}_{(j+l)(i+k)}^{\sigma'}(\Pi - i\omega) + [(\Pi - i\omega) \leftrightarrow (i\omega)] \right] \\ &= \frac{1}{4\pi} \sum_{\omega=\pm\Lambda} \theta(|\Pi - i\omega| - \Lambda) \left[\tilde{G}_{ji}^\sigma(i\omega) \tilde{G}_{(j+l)(i+k)}^{\sigma'}(\Pi - i\omega) + [(\Pi - i\omega) \leftrightarrow (i\omega)] \right]. \end{aligned} \quad (2.197)$$

and analogously one obtains

$$(W^X)_{ji}^{lk\sigma\sigma'}(X) = \frac{1}{2\pi} \sum_{\omega=\pm\Lambda} \theta(|X - i\omega| - \Lambda) \left[\tilde{G}_{ji}^\sigma(-i\omega) \tilde{G}_{(j+l)(i+k)}^{\sigma'}(X - i\omega) + [(X - i\omega) \leftrightarrow (i\omega)] \right]. \quad (2.198)$$

Zero temperature and static approximation

In the zero temperature limit, a static treatment of the vertex already leads to reasonable results, see e.g. [Kar06, BHvD14]. In such a static treatment, we approximate all vertex quantities by their value at the feedback frequency instead of treating them dynamically. In this case, the vertex bubble terms become especially simple

$$(W^P)_{ji}^{\sigma\sigma'lk}(0) = \frac{1}{2\pi} \text{Re} \left[\tilde{G}_{ji}^\sigma(i\Lambda) \tilde{G}_{(j+l)(i+k)}^{\sigma'}(i\Lambda)^* \right], \quad (2.199a)$$

$$(W^X)_{ji}^{\sigma\sigma'lk}(0) = \frac{1}{\pi} \text{Re} \left[\tilde{G}_{ji}^\sigma(i\Lambda) \tilde{G}_{(j+l)(i+k)}^{\sigma'}(i\Lambda) \right]. \quad (2.199b)$$

In particular they are both real, as they should be, see the discussion in Sec. 2.4.1.

Furthermore, the resulting self-energy will be also static since the (former) dynamic part of self-energy takes the form

$$\frac{\partial}{\partial \Lambda} \Sigma_d^\uparrow(i\omega) = -\left\{ \text{Tr} \left[\left((P^{\uparrow\uparrow})(0) - D^{\uparrow\uparrow}(0) \right) \times \hat{S}^\uparrow \right] + \text{Tr} \left[\left((P^{\uparrow\downarrow})(0) + X^{\uparrow\downarrow}(0) \right) \times \hat{S}^\downarrow \right] \right\}, \quad (2.200a)$$

$$\frac{\partial}{\partial \Lambda} \Sigma_d^\downarrow(i\omega) = -\left\{ \text{Tr} \left[\left((P^{I\uparrow\downarrow})(0) + X^{I\uparrow\downarrow}(0) \right) \times \hat{S}^\uparrow \right] + \text{Tr} \left[\left((P^{\downarrow\downarrow})(0) - D^{\downarrow\downarrow}(0) \right) \times \hat{S}^\downarrow \right] \right\}, \quad (2.200b)$$

i.e. it is independent of the external frequency ω .

2.4.5 Keldysh formulation of the eCLA

In this subsection, we derive the form of the eCLA within the Keldysh formalism. The resulting flow equations are similar to the ones in the Matsubara formalism, however, extended by the additional overlaying Keldysh structure. Since the Keldysh formulation offers, in principle, the option to investigate non-equilibrium systems (though we will not apply it for this purpose in this work), we take some extra effort to first describe the general eCLA setup (suitable also for non-equilibrium systems) and then specialize it to the case of equilibrium.

General (non-equilibrium) eCLA setup

Before we derive the actual flow equations, we take a closer look at the form of the Keldysh structure for the vertex and bubble quantities. For the vertex Keldysh structure, we will use the same matrix notation as in [Jak09], namely

$$A^{\alpha'_1 \alpha'_2 | \alpha_1 \alpha_2} = \left(\begin{array}{cc|cc} (11|11) & (11|21) & (11|12) & (11|22) \\ (21|11) & (21|21) & (21|12) & (21|22) \\ \hline (12|11) & (12|21) & (12|12) & (12|22) \\ (22|11) & (22|21) & (22|12) & (22|22) \end{array} \right), \quad (2.201)$$

for any quantity $A^{\alpha'_1 \alpha'_2 | \alpha_1 \alpha_2}$ with four Keldysh indices $\alpha'_1, \alpha'_2, \alpha_1, \alpha_2 \in \{1, 2\}$. Using the spin resolved flow equations (2.153) and (2.160), one can show that the Keldysh structure for the vertex objects (in our chosen truncated approximation) is of the structure [Jak09]

$$\varphi^P = \left(\begin{array}{cc|cc} 0 & d & d & 0 \\ a & b & b & a \\ \hline a & b & b & a \\ 0 & d & d & 0 \end{array} \right), \quad \varphi^X = \left(\begin{array}{cc|cc} 0 & d & a & b \\ a & b & 0 & d \\ \hline d & 0 & b & a \\ b & a & d & 0 \end{array} \right), \quad \varphi^D = \left(\begin{array}{cc|cc} 0 & a & d & b \\ a & 0 & b & d \\ \hline d & b & 0 & a \\ b & d & a & 0 \end{array} \right) \quad (2.202)$$

where generically $a^A, b^A, d^A \in \mathbb{C}$ with $A \in \{P, X, D\}$. Utilization of the general vertex symmetries as portrait in Sec. 2.2, yields additional relations between the individual components.¹⁵ Analogous to the spin structure in Sec. 2.4.2, where we used the particle exchange symmetry to reduce the number of vertex spin components to an independent subset, we utilize the general vertex symmetries (complex conjugation, particle exchange) to reduce the Keldysh components in (2.202) to an independent subset. All remaining independent symmetries yield then only relations within the spatial and frequency structure of a particular component with

¹⁵ As in the Matsubara case, one can check that these symmetries are conserved under the fRG flow, see App. A.4. As long as the initial conditions fulfill them, it does not matter if the r.h.s. of the flow equation is simplified using these symmetries, as long as the l.h.s. is not modified.

fixed Keldysh and spin structure, i.e. they do not relate components that differ in Keldysh or spin structure.

Using the general symmetry under complex conjugation (2.80b), we have

$$\begin{aligned}
& (\bar{v} + \varphi^P + \varphi^X + \varphi^D)_{q'q}^{\alpha'\alpha}(\Pi, X, \Delta) \\
&= \gamma_{q'q}^{\alpha'\alpha} \left(\frac{1}{2}(\Pi - X + \Delta), \frac{1}{2}(\Pi + X - \Delta) \middle| \frac{1}{2}(\Pi - X - \Delta), \frac{1}{2}(\Pi + X + \Delta) \right) \\
&= (-1)^{\alpha'\alpha} \gamma_{qq'}^{\alpha\alpha'} \left(\frac{1}{2}(\Pi - X - \Delta), \frac{1}{2}(\Pi + X + \Delta) \middle| \frac{1}{2}(\Pi - X + \Delta), \frac{1}{2}(\Pi + X - \Delta) \right)^* \\
&= (-1)^{\alpha'\alpha} (\bar{v} + \varphi^P + \varphi^X + \varphi^D)_{qq'}^{\alpha\alpha'}(\Pi, X, -\Delta)^*, \tag{2.203}
\end{aligned}$$

where we used the notation

$$(-1)^{\alpha'\alpha} = (-1)^{1+\sum_k(\alpha'_k+\alpha_k)}. \tag{2.204}$$

Therefore, we obtain for the individual channels

$$(\varphi^P)_{q'q}^{\alpha'\alpha}(\Pi) = (-1)^{\alpha'\alpha} (\varphi^P)_{qq'}^{\alpha\alpha'}(\Pi)^*, \tag{2.205a}$$

$$(\varphi^X)_{q'q}^{\alpha'\alpha}(X) = (-1)^{\alpha'\alpha} (\varphi^X)_{qq'}^{\alpha\alpha'}(X)^*, \tag{2.205b}$$

$$(\varphi^D)_{q'q}^{\alpha'\alpha}(\Delta) = (-1)^{\alpha'\alpha} (\varphi^D)_{qq'}^{\alpha\alpha'}(-\Delta)^*. \tag{2.205c}$$

If we apply this symmetry relations to the components a , d and b from (2.202), we obtain

$$a_{q'q}^P(\Pi) = d_{qq'}^P(\Pi)^*, \tag{2.206a}$$

$$a_{q'q}^X(X) = d_{qq'}^X(X)^*, \tag{2.206b}$$

$$a_{q'q}^D(\Delta) = a_{qq'}^D(-\Delta)^*, \tag{2.206c}$$

$$d_{q'q}^D(\Delta) = d_{qq'}^D(-\Delta)^*, \tag{2.206d}$$

$$b_{q'q}^P(\Pi) = -b_{qq'}^P(\Pi)^*, \tag{2.206e}$$

$$b_{q'q}^X(X) = -b_{qq'}^X(X)^*, \tag{2.206f}$$

$$b_{q'q}^D(\Delta) = -b_{qq'}^D(-\Delta)^*. \tag{2.206g}$$

Note that flipping q and q' does not change the spin-structure of any of the kept spin components (2.152). Therefore, we can eliminate all d components in the P- and the X-channel by replacing them with appropriate a^* components. Displaying the spin structure and writing this symmetries finally in the short index notation for spatial indices, we get from (2.206) for the kept spin components the following set of symmetries

$$(a^P)^{\sigma\sigma'} = (d^P)^{T\sigma\sigma'}, \tag{2.207a}$$

$$(a^X)^{\uparrow\downarrow} = (d^X)^{T\uparrow\downarrow}, \tag{2.207b}$$

$$(a^D)^{\sigma\sigma'}(\Delta) = (a^D)^{I\sigma\sigma'}(-\Delta), \tag{2.207c}$$

$$(d^D)^{\sigma\sigma'}(\Delta) = (d^D)^{I\sigma\sigma'}(-\Delta), \tag{2.207d}$$

$$(b^P)^{\sigma\sigma'} = -(b^P)^{T\sigma\sigma'}, \tag{2.207e}$$

$$(b^X)^{\uparrow\downarrow} = -(b^X)^{T\uparrow\downarrow}, \tag{2.207f}$$

$$(b^D)^{\sigma\sigma'}(\Delta) = -(b^D)^{I\sigma\sigma'}(-\Delta), \tag{2.207g}$$

where the first two a -symmetries can be used to replace the d -component in the P- and

X-channel. Using particle exchange, we obtain - analog to the Matsubara case - the additional symmetries

$$(a^P)^{\sigma\sigma} = (a^P)^{I\sigma\sigma} = -(a^P)^{I_1\sigma\sigma}$$

$$= -(a^P)^{I_2\sigma\sigma}, \quad (2.208a)$$

$$(a^D)^{\sigma\sigma}(\Delta) = (d^D)^{TI\sigma\sigma}(-\Delta), \quad (2.208b)$$

$$(b^P)^{\sigma\sigma} = (b^P)^{I\sigma\sigma} = -(b^P)^{I_1\sigma\sigma}$$

$$= -(b^P)^{I_2\sigma\sigma}, \quad (2.208c)$$

$$(b^D)^{\sigma\sigma}(\Delta) = (b^D)^{TI\sigma\sigma}(-\Delta). \quad (2.208d)$$

Therefore, we can additionally eliminate the $(d^D)^{\sigma\sigma}$ component. The independent spin and Keldysh components can be summarized as

$$(a^P)^{\sigma\sigma}, (a^P)^{\uparrow\downarrow}, \quad (2.209a) \quad (b^P)^{\sigma\sigma}, (b^P)^{\uparrow\downarrow}, \quad (2.209d)$$

$$(a^X)^{\uparrow\downarrow}, \quad (2.209b) \quad (b^X)^{\uparrow\downarrow}, \quad (2.209e)$$

$$(a^D)^{\sigma\sigma}, (a^D)^{\uparrow\downarrow}, (d^D)^{\uparrow\downarrow}, \quad (2.209c) \quad (b^D)^{\sigma\sigma}, (b^D)^{\uparrow\downarrow}. \quad (2.209f)$$

In App. A.2, we state how the dependent components are related to the independent ones (2.209).

As in the Matsubara case, we first derive the flow equation for the self-energy, split in a static and dynamic part. For this, we combine the spatial structure from the Matsubara case (before we applied any equilibrium specific symmetries) (2.182) and (2.183) with the Keldysh structure according to Eq. (2.153). Using the Keldysh structure of the single scale propagator S (which is the same as for the full propagator G (2.43)) and the two-particle vertex (2.202), we readily obtain for the static component of the self-energy

$$\begin{aligned} \frac{\partial}{\partial\Lambda}\Sigma_s^{R\uparrow} = & -i\{(b^D)^{\uparrow\uparrow}(0) \cdot (\hat{S}^{R\uparrow} + \hat{S}^{A\uparrow}) + [\frac{1}{2}\bar{v} + a^D(0)]^{\uparrow\uparrow} \cdot \hat{S}^{K\uparrow}\} \\ & + (b^D)^{\uparrow\downarrow}(0) \cdot (\hat{S}^{R\downarrow} + \hat{S}^{A\downarrow}) + [\frac{1}{2}\bar{v} + a^D(0)]^{\uparrow\downarrow} \cdot \hat{S}^{K\downarrow}\}, \end{aligned} \quad (2.210a)$$

$$\begin{aligned} \frac{\partial}{\partial\Lambda}\Sigma_s^{R\downarrow} = & -i\{(b^D)^{TI\uparrow\downarrow}(0) \cdot (\hat{S}^{R\uparrow} + \hat{S}^{A\uparrow}) + [\frac{1}{2}\bar{v} + a^D(0)]^{TI\uparrow\downarrow} \cdot \hat{S}^{K\uparrow}\} \\ & + (b^D)^{\downarrow\downarrow}(0) \cdot (\hat{S}^{R\downarrow} + \hat{S}^{A\downarrow}) + [\frac{1}{2}\bar{v} + a^D(0)]^{\downarrow\downarrow} \cdot \hat{S}^{K\downarrow}\}, \end{aligned} \quad (2.210b)$$

where analogous to (2.185)

$$\hat{S} = \sum_{\omega} S(\omega) = \frac{1}{2\pi} \int d\omega S(\omega), \quad (2.211)$$

and we have used the efficient notation for the spatial indices introduced in (2.170). Using the propagator (2.81) and vertex symmetries (2.207) and (2.208), as well as the fact that $a^D(0)$ is real, we can write this as

$$\begin{aligned} \frac{\partial}{\partial\Lambda}\Sigma_s^{R\uparrow} = & -i\{(b^D)^{\uparrow\uparrow}(0) \cdot (\hat{S}^{R\uparrow} + (\hat{S}^R)^{T\uparrow*}) + [\frac{1}{2}\bar{v} + a^D(0)]^{\uparrow\uparrow} \cdot \hat{S}^{K\uparrow}\} \\ & + (b^D)^{\uparrow\downarrow}(0) \cdot (\hat{S}^{R\downarrow} + (\hat{S}^R)^{T\downarrow*}) + [\frac{1}{2}\bar{v} + a^D(0)]^{\uparrow\downarrow} \cdot \hat{S}^{K\downarrow}\}, \end{aligned} \quad (2.212a)$$

$$\begin{aligned} \frac{\partial}{\partial\Lambda}\Sigma_s^{R\downarrow} = & -i\{- (b^D)^{TI\uparrow\downarrow}(0) \cdot (\hat{S}^{R\uparrow} + (\hat{S}^R)^{T\uparrow*}) + [\frac{1}{2}\bar{v} + a^D(0)]^{TI\uparrow\downarrow} \cdot \hat{S}^{K\uparrow}\} \\ & + (b^D)^{\downarrow\downarrow}(0) \cdot (\hat{S}^{R\downarrow} + (\hat{S}^R)^{T\downarrow*}) + [\frac{1}{2}\bar{v} + a^D(0)]^{\downarrow\downarrow} \cdot \hat{S}^{K\downarrow}\}. \end{aligned} \quad (2.212b)$$

In a similar manner, we obtain for the dynamic part of the self-energy

$$\begin{aligned}
\frac{\partial}{\partial \Lambda} \Sigma_d^{R\uparrow}(\omega) = & -\frac{i}{2\pi} \int d\omega' \{ \\
& \text{Tr} \left[(a^P)^{\uparrow\uparrow}(\omega' + \omega) \times S^{K\uparrow}(\omega') \right] - \text{Tr} \left[(d^D)^{TI\uparrow\uparrow}(\omega' - \omega) \times (S^K)^{T\uparrow}(\omega') \right] \\
& + \text{Tr} \left[(a^P)^{\uparrow\downarrow}(\omega' + \omega) \times S^{K\downarrow}(\omega') \right] + \text{Tr} \left[(a^X)^{\uparrow\downarrow}(\omega' - \omega) \times (S^K)^{T\downarrow}(\omega') \right] \\
& + \text{Tr} \left[(b^P)^{\uparrow\uparrow}(\omega' + \omega) \times S^{A\uparrow}(\omega') \right] - \text{Tr} \left[(b^D)^{TI\uparrow\uparrow}(\omega' - \omega) \times (S^R)^{T\uparrow}(\omega') \right] \\
& + \text{Tr} \left[(b^P)^{\uparrow\downarrow}(\omega' + \omega) \times S^{A\downarrow}(\omega') \right] + \text{Tr} \left[(b^X)^{\uparrow\downarrow}(\omega' - \omega) \times (S^R)^{T\downarrow}(\omega') \right] \}, \tag{2.213}
\end{aligned}$$

and analogously

$$\begin{aligned}
\frac{\partial}{\partial \Lambda} \Sigma_d^{R\downarrow}(\omega) = & -\frac{i}{2\pi} \int d\omega' \{ \\
& \text{Tr} \left[(a^P)^{I\uparrow\downarrow}(\omega' + \omega) \times S^{K\uparrow}(\omega') \right] + \text{Tr} \left[(d^X)^{TI\uparrow\downarrow}(\omega - \omega') \times (S^K)^{T\uparrow}(\omega') \right] \\
& + \text{Tr} \left[(a^P)^{\downarrow\downarrow}(\omega' + \omega) \times S^{K\downarrow}(\omega') \right] - \text{Tr} \left[(d^D)^{TI\downarrow\downarrow}(\omega' - \omega) \times (S^K)^{T\downarrow}(\omega') \right] \\
& + \text{Tr} \left[(b^P)^{I\uparrow\downarrow}(\omega' + \omega) \times S^{A\uparrow}(\omega') \right] + \text{Tr} \left[(b^X)^{TI\uparrow\uparrow}(\omega - \omega') \times (S^R)^{T\uparrow}(\omega') \right] \\
& + \text{Tr} \left[(b^P)^{\downarrow\downarrow}(\omega' + \omega) \times S^{A\downarrow}(\omega') \right] - \text{Tr} \left[(b^D)^{TI\downarrow\downarrow}(\omega' - \omega) \times (S^R)^{T\downarrow}(\omega') \right] \}. \tag{2.214}
\end{aligned}$$

Using again the symmetry relations (2.81), (2.207) and (2.208), this flow equations for the retarded self-energy can be formulated within the subset of kept spin and Keldysh components as

$$\begin{aligned}
\frac{\partial}{\partial \Lambda} \Sigma_d^{R\uparrow}(\omega) = & -\frac{i}{2\pi} \int d\omega' \{ \\
& \text{Tr} \left[(a^P)^{\uparrow\uparrow}(\omega' + \omega) \times S^{K\uparrow}(\omega') \right] - \text{Tr} \left[(a^D)^{\uparrow\uparrow}(\omega - \omega') \times (S^K)^{T\uparrow}(\omega') \right] \\
& + \text{Tr} \left[(a^P)^{\uparrow\downarrow}(\omega' + \omega) \times S^{K\downarrow}(\omega') \right] + \text{Tr} \left[(a^X)^{\uparrow\downarrow}(\omega' - \omega) \times (S^K)^{T\downarrow}(\omega') \right] \\
& + \text{Tr} \left[(b^P)^{\uparrow\uparrow}(\omega' + \omega) \times (S^R)^{T\uparrow}(\omega')^* \right] - \text{Tr} \left[(b^D)^{\uparrow\uparrow}(\omega - \omega') \times (S^R)^{T\uparrow}(\omega') \right] \\
& + \text{Tr} \left[(b^P)^{\uparrow\downarrow}(\omega' + \omega) \times (S^R)^{T\downarrow}(\omega')^* \right] + \text{Tr} \left[(b^X)^{\uparrow\downarrow}(\omega' - \omega) \times (S^R)^{T\downarrow}(\omega') \right] \}, \tag{2.215a}
\end{aligned}$$

and

$$\begin{aligned}
\frac{\partial}{\partial \Lambda} \Sigma_d^{R\downarrow}(\omega) = & -\frac{i}{2\pi} \int d\omega' \{ \\
& \text{Tr} \left[(a^P)^{I\uparrow\downarrow}(\omega' + \omega) \times S^{K\uparrow}(\omega') \right] + \text{Tr} \left[(a^X)^{I\uparrow\downarrow}(\omega - \omega')^* \times (S^K)^{T\uparrow}(\omega') \right] \\
& + \text{Tr} \left[(a^P)^{\downarrow\downarrow}(\omega' + \omega) \times S^{K\downarrow}(\omega') \right] - \text{Tr} \left[(a^D)^{\downarrow\downarrow}(\omega - \omega') \times (S^K)^{T\downarrow}(\omega') \right] \\
& + \text{Tr} \left[(b^P)^{I\uparrow\downarrow}(\omega' + \omega) \times (S^R)^{T\uparrow}(\omega')^* \right] - \text{Tr} \left[(b^X)^{I\uparrow\downarrow}(\omega - \omega')^* \times (S^R)^{T\uparrow}(\omega') \right] \\
& + \text{Tr} \left[(b^P)^{\downarrow\downarrow}(\omega' + \omega) \times (S^R)^{T\downarrow}(\omega')^* \right] - \text{Tr} \left[(b^D)^{\downarrow\downarrow}(\omega - \omega') \times (S^R)^{T\downarrow}(\omega') \right] \}. \tag{2.215b}
\end{aligned}$$

Since we will not need the flow of the Keldysh component of the self-energy in thermal equilibrium later on, we will not display it here. However, the interested reader can find it in App. A.3.

In order to derive the flow equations for the vertex, let us next take a look at the Keldysh structure of the bubble terms (2.139). Generically, we have for the bubble terms

$$(I^{pp})_{j(j+l)|i(i+k)}^{\sigma\sigma'\alpha'_1\alpha'_2|\alpha_1\alpha_2}(\Pi) = \frac{i}{4\pi} \int d\omega \left[S_{ji}^{\sigma\alpha'_1\alpha_1}(\omega) G_{(j+l)(i+k)}^{\sigma'\alpha'_2\alpha_2}(\Pi - \omega) + [S \leftrightarrow G] \right], \quad (2.216)$$

$$(I^{ph})_{j(i+k)|i(j+l)}^{\sigma\sigma'\alpha'_1\alpha'_2|\alpha_1\alpha_2}(X) = \frac{i}{2\pi} \int d\omega \left[S_{ji}^{\sigma\alpha'_1\alpha_1}(\omega) G_{(i+k)(j+l)}^{\sigma'\alpha'_2\alpha_2}(\omega + X) + [S \leftrightarrow G] \right]. \quad (2.217)$$

which is analogous to (2.174) with an additional Keldysh structure. Using the Keldysh structure of the propagators (2.43), we obtain

$$I^{pp} = \frac{i}{4\pi} \int d\omega' \left[\left(\begin{array}{cc|cc} 0 & 0 & 0 & G^A S^A \\ 0 & 0 & G^R S^A & G^K S^A \\ \hline 0 & G^A S^R & 0 & G^A S^K \\ G^R S^R & G^K S^R & G^R S^K & G^K S^K \end{array} \right) + [G \leftrightarrow S] \right], \quad (2.218a)$$

$$I^{ph} = \frac{i}{2\pi} \int d\omega' \left[\left(\begin{array}{cc|cc} 0 & 0 & 0 & 0 \\ 0 & 0 & G^R S^A & G^K S^A \\ \hline 0 & G^A S^R & 0 & G^A S^K \\ 0 & G^K S^R & G^R S^K & G^K S^K \end{array} \right) + [G \leftrightarrow S] \right]. \quad (2.218b)$$

Using additionally the analytic properties from Sec. 2.2.6 and the fact that for large enough frequencies we have $G(\omega) \sim 1/\omega$ and $S(\omega) \sim 1/\omega^2$, we arrive at the following Keldysh structures for the bubble terms

$$I^{pp} = \frac{i}{4\pi} \int d\omega' \left[\left(\begin{array}{cc|cc} 0 & 0 & 0 & G^A S^A \\ 0 & 0 & 0 & G^K S^A \\ \hline 0 & 0 & 0 & G^A S^K \\ G^R S^R & G^K S^R & G^R S^K & G^K S^K \end{array} \right) + [G \leftrightarrow S] \right] \quad (2.219a)$$

$$I^{ph} = \frac{i}{2\pi} \int d\omega' \left[\left(\begin{array}{cc|cc} 0 & 0 & 0 & 0 \\ 0 & 0 & G^R S^A & G^K S^A \\ \hline 0 & G^A S^R & 0 & G^A S^K \\ 0 & G^K S^R & G^R S^K & G^K S^K \end{array} \right) + [G \leftrightarrow S] \right]. \quad (2.219b)$$

Furthermore, analogous to the Matsubara case (2.174), we use the short index notation for the spatial indices

$$(I^{pp})_{ji}^{lk} = (I^{pp})_{j(j+l)|i(i+k)}, \quad (2.220a)$$

$$(I^{ph})_{ji}^{lk} = (I^{ph})_{j(i+k)|i(j+l)}. \quad (2.220b)$$

Then we have the following bubble symmetries

$$\left[(I^{pp})_{\sigma\tau} \right]^{\alpha'_1\alpha'_2|\alpha_1\alpha_2} = \left[(I^{pp})_{I\tau\sigma} \right]^{\alpha'_2\alpha'_1|\alpha_2\alpha_1}, \quad (2.221a)$$

$$\left[(I^{ph})_{\sigma\tau} \right]^{\alpha'_1\alpha'_2|\alpha_1\alpha_2}(X) = \left[(I^{ph})_{T I \tau \sigma} \right]^{\alpha'_2\alpha'_1|\alpha_2\alpha_1}(-X), \quad (2.221b)$$

$$(I)^{\alpha'_1\alpha'_2|\alpha_1\alpha_2} = (-1)^{1+\alpha'_1+\alpha'_2+\alpha_1+\alpha_2} [I^T]^{\alpha_1\alpha_2|\alpha'_1\alpha'_2*}, \quad (2.221c)$$

where the first two relations stem from the $G \leftrightarrow S$ symmetry, and the second relation (for both P- and X-bubble) is induced by the complex conjugation of the propagators (2.81). Ultimately, we will see that by using the symmetries (2.221) for the flow of the a components

we only need to compute the two bubbles

$$I^P := (I^{pp})^{22|21}, \quad I^X := (I^{ph})^{22|12}, \quad (2.222)$$

and then form the combinations

$$(W^P)^{\sigma\sigma'} := (I^P)^{\sigma\sigma'} + (I^P)^{I\sigma'\sigma}, \quad (2.223a)$$

$$(W^X)^{\sigma\sigma'}(X) := (I^X)^{\sigma\sigma'}(X) + (I^X)^{I\sigma'\sigma}(-X)^*. \quad (2.223b)$$

For the flow of the b components (which is not needed in thermal equilibrium applications), one needs to compute additional bubbles, see App. A.3.

With the structure of the bubble terms (2.223), we have everything at hand to derive the flow equations for the vertex in the Keldysh formalism. The simplest way to derive them, is to just add the appropriate Keldysh structure to the unsimplified (i.e. where we have not yet used the Matsubara symmetries) flow equations from the Matsubara case (2.188) - (2.189). Before we write down the flow equations, let us have a look at the specific choice of the feedback. Since we give the flow-equations for a general, i.e. a not necessarily equilibrium setup, there is distinguished choice like (2.145). However, by analogy to (2.145), the most natural choice would probably be something like

$$(\phi^P)^{\alpha'_1\alpha'_2|\alpha_1\alpha_2} = \mathbb{1}^{\alpha'_1\alpha'_2|\alpha_1\alpha_2} \frac{1}{2} (a^P + d^P)(\mu_L + \mu_R), \quad (2.224)$$

$$(\phi^{X/D})^{\alpha'_1\alpha'_2|\alpha_1\alpha_2} = \mathbb{1}^{\alpha'_1\alpha'_2|\alpha_1\alpha_2} \frac{1}{2} (a^{X/D} + d^{X/D})(0), \quad (2.225)$$

where $\mathbb{1}^{\alpha'_1\alpha'_2|\alpha_1\alpha_2}$ reproduces the Keldysh structure of the bare vertex, i.e.

$$\mathbb{1}^{\alpha'_1\alpha'_2|\alpha_1\alpha_2} = \begin{cases} 1 & \text{if } \alpha'_1 + \alpha'_2 + \alpha_1 + \alpha_2 \text{ odd} \\ 0 & \text{otherwise.} \end{cases} \quad (2.226)$$

Though not as mathematically compelling as the equilibrium choice (2.145) (we now fixed the Keldysh structure by hand to have the same form as the one of the bare vertex), this approach conserves the general symmetries from Sec. 2.2 under the fRG flow. Note, however, that with the choice (2.225) the feedback is not necessarily real anymore. A slightly simplified approach was used by Schimmel in Ref. [Sch17], namely (expressed in our notation)

$$(\phi^P)^{\alpha'_1\alpha'_2|\alpha_1\alpha_2} = \mathbb{1}^{\alpha'_1\alpha'_2|\alpha_1\alpha_2} \text{Re } a^P(\mu_L + \mu_R), \quad (2.227)$$

$$(\phi^{X/D})^{\alpha'_1\alpha'_2|\alpha_1\alpha_2} = \mathbb{1}^{\alpha'_1\alpha'_2|\alpha_1\alpha_2} \text{Re } a^{X/D}(0), \quad (2.228)$$

which specifically keeps the feedback real. Since we will not apply the non-equilibrium flow equations in this work, we will not further comment on the specifics of the non-equilibrium feedback.

Having specified the static feedback, we can define the tilded quantities

$$(\tilde{a}^P)_{ji}^{\sigma\sigma lk}(\Pi) = \left[\frac{1}{2} \bar{v}_{j(j+l)|i(i+k)}^{\sigma\sigma|\sigma\sigma} + (a^P)_{ji}^{\sigma\sigma lk}(\Pi) - (\phi^D)_{ji}^{\sigma\sigma(i+k-j)(j+l-i)} + (\phi^D)_{j(i+k)}^{\sigma\sigma(i-j)(j+l-i-k)} \right], \quad (2.229a)$$

$$(\tilde{a}^P)_{ji}^{\uparrow\downarrow lk}(\Pi) = \left[\frac{1}{2} \bar{v}_{j(j+l)|i(i+k)}^{\uparrow\downarrow|\uparrow\downarrow} + (a^P)_{ji}^{\uparrow\downarrow lk}(\Pi) + (\phi^X)_{ji}^{\uparrow\downarrow(i+k-j)(j+l-i)} + (\phi^D)_{j(i+k)}^{\uparrow\downarrow(i-j)(j+l-i-k)} \right], \quad (2.229b)$$

$$(\tilde{a}^X)_{ji}^{\uparrow\downarrow lk}(X) = \left[\frac{1}{2} \bar{v}_{j(i+k)|i(j+l)}^{\uparrow\downarrow|\uparrow\downarrow} + (a^X)_{ji}^{\uparrow\downarrow lk}(X) + (\phi^P)_{ji}^{\uparrow\downarrow(i+k-j)(j+l-i)} + (\phi^D)_{j(j+l)}^{\uparrow\downarrow(i-j)(i+k-j-l)} \right], \quad (2.229c)$$

$$(\tilde{a}^D)_{ji}^{\sigma\sigma lk}(\Delta) = \left[\frac{1}{2} \bar{v}_{j(i+k)|i(j+l)}^{\sigma\sigma|\sigma\sigma} + (a^D)_{ji}^{\sigma\sigma lk}(\Delta) + (\phi^P)_{j(j+l)}^{\sigma\sigma(i+k-j)(i-j-l)} - (\phi^D)_{j(j+l)}^{\sigma\sigma(i-j)(i+k-j-l)} \right], \quad (2.229d)$$

$$(\tilde{a}^D)_{ji}^{\uparrow\downarrow lk}(\Delta) = \left[\frac{1}{2} \bar{v}_{j(i+k)|i(j+l)}^{\uparrow\downarrow|\uparrow\downarrow} + (a^D)_{ji}^{\uparrow\downarrow lk}(\Delta) + (\phi^P)_{j(j+l)}^{\uparrow\downarrow(i+k-j)(i-j-l)} + (\phi^X)_{j(j+l)}^{\uparrow\downarrow(i-j)(i+k-j-l)} \right], \quad (2.229e)$$

$$(\tilde{d}^D)_{ji}^{\uparrow\downarrow lk}(\Delta) = \left[\frac{1}{2} \bar{v}_{j(i+k)|i(j+l)}^{\uparrow\downarrow|\uparrow\downarrow} + (d^D)_{ji}^{\uparrow\downarrow lk}(\Delta) + (\phi^P)_{j(j+l)}^{\uparrow\downarrow(i+k-j)(i-j-l)} + (\phi^X)_{j(j+l)}^{\uparrow\downarrow(i-j)(i+k-j-l)} \right]. \quad (2.229f)$$

With these, we readily obtain for the flow of a^P and a^X

$$\frac{\partial}{\partial \Lambda} (a^P)^{\sigma\sigma}(\Pi) = (\tilde{a}^P)^{\sigma\sigma}(\Pi) \cdot \left[(I^{pp})^{22|12} + (I^{pp})^{22|21} \right]^{\sigma\sigma}(\Pi) \cdot (\tilde{a}^P)^{\sigma\sigma}(\Pi), \quad (2.230a)$$

$$\frac{\partial}{\partial \Lambda} (a^P)^{\uparrow\downarrow}(\Pi) = 2(\tilde{a}^P)^{\uparrow\downarrow}(\Pi) \cdot \left[(I^{pp})^{22|12} + (I^{pp})^{22|21} \right]^{\uparrow\downarrow}(\Pi) \cdot (\tilde{a}^P)^{\uparrow\downarrow}(\Pi), \quad (2.230b)$$

$$\frac{\partial}{\partial \Lambda} (a^X)^{\uparrow\downarrow}(X) = (\tilde{a}^X)^{\uparrow\downarrow}(X) \cdot \left[(I^{ph})^{22|12} + (I^{ph})^{21|22} \right]^{\uparrow\downarrow}(X) \cdot (\tilde{a}^X)^{\uparrow\downarrow}(X). \quad (2.230c)$$

Using the bubble symmetries (2.221) this can be written in terms of the bubbles (2.223) as

$$\frac{\partial}{\partial \Lambda} (a^P)^{\sigma\sigma}(\Pi) = (\tilde{a}^P)^{\sigma\sigma}(\Pi) \cdot (W^P)^{\sigma\sigma}(\Pi) \cdot (\tilde{a}^P)^{\sigma\sigma}(\Pi), \quad (2.231a)$$

$$\frac{\partial}{\partial \Lambda} (a^P)^{\uparrow\downarrow}(\Pi) = 2(\tilde{a}^P)^{\uparrow\downarrow}(\Pi) \cdot (W^P)^{\uparrow\downarrow}(\Pi) \cdot (\tilde{a}^P)^{\uparrow\downarrow}(\Pi), \quad (2.231b)$$

$$\frac{\partial}{\partial \Lambda} (a^X)^{\uparrow\downarrow}(X) = (\tilde{a}^X)^{\uparrow\downarrow}(X) \cdot (W^X)^{\uparrow\downarrow}(X) \cdot (\tilde{a}^X)^{\uparrow\downarrow}(X). \quad (2.231c)$$

For the flow the $a^{\sigma\sigma'}$ and the $d^{\uparrow\downarrow}$ component of the D-channel we obtain

$$\begin{aligned} \frac{\partial}{\partial\Lambda}(a^D)^{\uparrow\uparrow}(\Delta) = & -\left\{(\tilde{a}^D)^{\uparrow\uparrow}(\Delta)\left[(I^{ph})^{22|21} + (I^{ph})^{12|22}\right]^{TI\uparrow\uparrow}(\Delta)(\tilde{a}^D)^{\uparrow\uparrow}(\Delta)\right. \\ & \left. + (\tilde{a}^D)^{\uparrow\downarrow}(\Delta)\left[(I^{ph})^{22|21} + (I^{ph})^{12|22}\right]^{TI\uparrow\downarrow}(\Delta)(\tilde{d}^D)^{TI\uparrow\downarrow}(-\Delta)\right\}, \end{aligned} \quad (2.232a)$$

$$\begin{aligned} \frac{\partial}{\partial\Lambda}(a^D)^{\downarrow\downarrow}(\Delta) = & -\left\{(\tilde{a}^D)^{\downarrow\downarrow}(\Delta)\left[(I^{ph})^{22|21} + (I^{ph})^{12|22}\right]^{TI\downarrow\downarrow}(\Delta)(\tilde{a}^D)^{\downarrow\downarrow}(\Delta)\right. \\ & \left. + (\tilde{d}^D)^{TI\uparrow\downarrow}(-\Delta)\left[(I^{ph})^{22|21} + (I^{ph})^{12|22}\right]^{TI\uparrow\uparrow}(\Delta)(\tilde{a}^D)^{\uparrow\downarrow}(\Delta)\right\}, \end{aligned} \quad (2.232b)$$

$$\begin{aligned} \frac{\partial}{\partial\Lambda}(a^D)^{\uparrow\downarrow}(\Delta) = & -\left\{(\tilde{a}^D)^{\uparrow\uparrow}(\Delta)\left[(I^{ph})^{22|21} + (I^{ph})^{12|22}\right]^{TI\uparrow\uparrow}(\Delta)(\tilde{a}^D)^{\uparrow\downarrow}(\Delta)\right. \\ & \left. + (\tilde{a}^D)^{\uparrow\downarrow}(\Delta)\left[(I^{ph})^{22|21} + (I^{ph})^{12|22}\right]^{TI\downarrow\downarrow}(\Delta)(\tilde{a}^D)^{\downarrow\downarrow}(\Delta)\right\}, \end{aligned} \quad (2.232c)$$

$$\begin{aligned} \frac{\partial}{\partial\Lambda}(d^D)^{\uparrow\downarrow}(\Delta) = & -\left\{(\tilde{d}^D)^{\uparrow\uparrow}(\Delta)\left[(I^{ph})^{21|22} + (I^{ph})^{22|12}\right]^{TI\uparrow\uparrow}(\Delta)(\tilde{d}^D)^{\uparrow\downarrow}(\Delta)\right. \\ & \left. + (\tilde{d}^D)^{\uparrow\downarrow}(\Delta)\left[(I^{ph})^{21|22} + (I^{ph})^{22|12}\right]^{TI\downarrow\downarrow}(\Delta)(\tilde{d}^D)^{\downarrow\downarrow}(\Delta)\right\}. \end{aligned} \quad (2.232d)$$

In terms of (2.223) and using the symmetries (2.207) this can be written compactly as

$$\begin{aligned} \frac{\partial}{\partial\Lambda}(a^D)^{\uparrow\uparrow}(\Delta) = & -\left\{(\tilde{a}^D)^{\uparrow\uparrow}(\Delta) \cdot (W^X)^{\uparrow\uparrow}(-\Delta) \cdot (\tilde{a}^D)^{\uparrow\uparrow}(\Delta)\right. \\ & \left. + (\tilde{a}^D)^{\uparrow\downarrow}(\Delta) \cdot (W^X)^{\downarrow\downarrow}(-\Delta) \cdot (\tilde{d}^D)^{T\uparrow\downarrow}(\Delta)^*\right\}, \end{aligned} \quad (2.233a)$$

$$\begin{aligned} \frac{\partial}{\partial\Lambda}(a^D)^{\downarrow\downarrow}(\Delta) = & -\left\{(\tilde{a}^D)^{\downarrow\downarrow}(\Delta) \cdot (W^X)^{\downarrow\downarrow}(-\Delta) \cdot (\tilde{a}^D)^{\downarrow\downarrow}(\Delta)\right. \\ & \left. + (\tilde{d}^D)^{T\uparrow\downarrow}(\Delta)^* \cdot (W^X)^{\uparrow\uparrow}(-\Delta) \cdot (\tilde{a}^D)^{\uparrow\downarrow}(\Delta)\right\}, \end{aligned} \quad (2.233b)$$

$$\begin{aligned} \frac{\partial}{\partial\Lambda}(a^D)^{\uparrow\downarrow}(\Delta) = & -\left\{(\tilde{a}^D)^{\uparrow\uparrow}(\Delta) \cdot (W^X)^{\uparrow\uparrow}(-\Delta) \cdot (\tilde{a}^D)^{\uparrow\downarrow}(\Delta)\right. \\ & \left. + (\tilde{a}^D)^{\uparrow\downarrow}(\Delta) \cdot (W^X)^{\downarrow\downarrow}(-\Delta) \cdot (\tilde{a}^D)^{\downarrow\downarrow}(\Delta)\right\}, \end{aligned} \quad (2.233c)$$

$$\begin{aligned} \frac{\partial}{\partial\Lambda}(d^D)^{\uparrow\downarrow}(\Delta) = & -\left\{(\tilde{d}^D)^{\uparrow\uparrow}(\Delta) \cdot (W^X)^{TI\uparrow\uparrow}(\Delta) \cdot (\tilde{d}^D)^{\uparrow\downarrow}(\Delta)\right. \\ & \left. + (\tilde{d}^D)^{\uparrow\downarrow}(\Delta) \cdot (W^X)^{TI\downarrow\downarrow}(\Delta) \cdot (\tilde{d}^D)^{\downarrow\downarrow}(\Delta)\right\}. \end{aligned} \quad (2.233d)$$

Due to our choice of the hybridization flow with artificial leads, the initial conditions in non-equilibrium are the same as in the ones in equilibrium (2.131).¹⁶ For completeness, we state them here in terms of our introduced quantities

$$\Sigma_{ji}^{R\sigma}(\omega) = \frac{1}{2} \sum_{j_2, \sigma'} \bar{v}_{jj_2}^{\sigma\sigma'} |_{ij_2}, \quad \Sigma_{ji}^{K\sigma}(\omega) = 0, \quad (2.234a)$$

$$a^P = a^X = a^D = d^D = 0. \quad (2.234b)$$

¹⁶ The reason for this is that, at large flow parameter Λ , the physics is dominated by the artificial leads, which due to their infinite band width are always at half-filling. Therefore the values of the temperatures and the chemical potentials of the actual physical leads do not matter. For details see the argument given by Schimmel in Ref. [Sch17]

Thermal equilibrium

In thermal equilibrium, additionally to the symmetries discussed in the last subsection (2.207) – (2.208), we also have the time-reversal symmetry (2.95a) for the propagators and the self-energy as well as the one- and two-particle FDTs. The former yields the corresponding bubble symmetry

$$W = W^T. \quad (2.235)$$

The latter take the form (2.105) for the self-energy and propagators and were formulated in (2.110) for the vertex in contour space. After some tedious but otherwise straight forward algebra (see App. C in Sec. 5.2 for details), one can obtain the following relations for the Keldysh components of the vertex in (2.202)

$$d = a^*, \quad (2.236)$$

independently of the channel, and

$$b^P = 2i \operatorname{Im}(a^P) \coth\left(\left(\frac{\Pi}{2} - \mu\right)/T\right), \quad (2.237a)$$

$$b^X = -2i \operatorname{Im}(a^X) \coth\left(\frac{X}{2T}\right), \quad (2.237b)$$

$$b^D = 2i \operatorname{Im}(a^D) \coth\left(\frac{\Delta}{2T}\right). \quad (2.237c)$$

Using this additional symmetries (2.236) and (2.237), the general flow equations can be simplified. The flow of the static self-energy (2.212) takes the equilibrium form

$$\frac{\partial}{\partial \Lambda} \Sigma_s^{R\uparrow} = -i \left\{ \left[\frac{1}{2} \bar{v} + a^D(0) \right]^{\uparrow\uparrow} \cdot \hat{S}^{K\uparrow} + \left[\frac{1}{2} \bar{v} + a^D(0) \right]^{\uparrow\downarrow} \cdot \hat{S}^{K\downarrow} \right\} \quad (2.238a)$$

$$\frac{\partial}{\partial \Lambda} \Sigma_s^{R\downarrow} = -i \left\{ \left[\frac{1}{2} \bar{v} + a^D(0) \right]^{T\uparrow\downarrow} \cdot \hat{S}^{K\uparrow} + \left[\frac{1}{2} \bar{v} + a^D(0) \right]^{\downarrow\downarrow} \cdot \hat{S}^{K\downarrow} \right\}. \quad (2.238b)$$

In thermal equilibrium, \hat{S}^K can furthermore be expressed as

$$\hat{S}^K = \frac{i}{\pi} \int d\omega (1 - 2n_F(\omega)) \operatorname{Im} S^R(\omega). \quad (2.239)$$

For the dynamic part of the self-energy one obtains

$$\begin{aligned}
\frac{\partial}{\partial \Lambda} \Sigma_d^{R\uparrow}(\omega) &= \frac{1}{\pi} \int d\omega' \left\{ (1 - 2n_F(\omega')) \right. \\
&\quad \times \left(\text{Tr} \left[\left((a^P)^{\uparrow\uparrow}(\omega' + \omega) - (a^D)^{\uparrow\uparrow}(\omega - \omega') \right) \times \text{Im} S^{R\uparrow}(\omega') \right] \right. \\
&\quad \left. + \text{Tr} \left[\left((a^P)^{\uparrow\downarrow}(\omega' + \omega) + (a^X)^{\uparrow\downarrow}(\omega' - \omega) \right) \times \text{Im} S^{R\downarrow}(\omega') \right] \right) \\
&\quad + \coth \left(\left(\frac{\omega' + \omega}{2} - \mu \right) / T \right) \\
&\quad \times \left(\text{Tr} \left[\text{Im}(a^P)^{\uparrow\uparrow}(\omega' + \omega) \times (S^R)^{\uparrow}(\omega')^* \right] + \text{Tr} \left[\text{Im}(a^P)^{\uparrow\downarrow}(\omega' + \omega) \times (S^R)^{\downarrow}(\omega')^* \right] \right) \\
&\quad - \coth \left(\frac{\omega - \omega'}{2T} \right) \\
&\quad \left. \times \left(\text{Tr} \left[\text{Im}(a^D)^{\uparrow\uparrow}(\omega - \omega') \times (S^R)^{\uparrow}(\omega') \right] - \text{Tr} \left[\text{Im}(a^X)^{\uparrow\downarrow}(\omega' - \omega) \times (S^R)^{\downarrow}(\omega') \right] \right) \right\}, \tag{2.240a}
\end{aligned}$$

and

$$\begin{aligned}
\frac{\partial}{\partial \Lambda} \Sigma_d^{R\downarrow}(\omega) &= \frac{1}{\pi} \int d\omega' \left\{ (1 - 2n_F(\omega')) \right. \\
&\quad \times \left(\text{Tr} \left[\left((a^P)^{I\uparrow\downarrow}(\omega') + (a^X)^{I\uparrow\downarrow}(\omega - \omega')^* \right) \times \text{Im} S^{R\uparrow}(\omega') \right] \right. \\
&\quad \left. + \text{Tr} \left[\left((a^P)^{\downarrow\downarrow}(\omega' + \omega) - (a^D)^{\downarrow\downarrow}(\omega - \omega') \right) \times \text{Im} S^{R\downarrow}(\omega') \right] \right) \\
&\quad + \coth \left(\left(\frac{\omega + \omega'}{2} - \mu \right) / T \right) \\
&\quad \times \left(\text{Tr} \left[\text{Im}(a^P)^{I\uparrow\downarrow}(\omega' + \omega) \times (S^R)^{\uparrow}(\omega')^* \right] + \text{Tr} \left[\text{Im}(a^P)^{\downarrow\downarrow}(\omega' + \omega) \times (S^R)^{\downarrow}(\omega')^* \right] \right) \\
&\quad - \coth \left(\frac{\omega - \omega'}{2T} \right) \\
&\quad \left. \times \left(\text{Tr} \left[\text{Im}(a^D)^{\downarrow\downarrow}(\omega - \omega') \times S^{R\downarrow}(\omega') \right] + \text{Tr} \left[\text{Im}(a^X)^{I\uparrow\downarrow}(\omega - \omega') \times S^{R\uparrow}(\omega') \right] \right) \right\}. \tag{2.240b}
\end{aligned}$$

Furthermore, we do not have to consider the vertex flow of $d^{D\uparrow\downarrow}$ and the b components in thermal equilibrium. Additionally, the flow equations for the a components of the D-channel take the simpler form

$$\begin{aligned}
\frac{\partial}{\partial \Lambda} (a^D)^{\uparrow\uparrow}(\Delta) &= - \left\{ (\tilde{a}^D)^{\uparrow\uparrow}(\Delta) \cdot (W^X)^{\uparrow\uparrow}(-\Delta) \cdot (\tilde{a}^D)^{\uparrow\uparrow}(\Delta) \right. \\
&\quad \left. + (\tilde{a}^D)^{\uparrow\downarrow}(\Delta) \cdot (W^X)^{\downarrow\downarrow}(-\Delta) \cdot (\tilde{a}^D)^{T\uparrow\downarrow}(\Delta) \right\}, \tag{2.241a}
\end{aligned}$$

$$\begin{aligned}
\frac{\partial}{\partial \Lambda} (a^D)^{\downarrow\downarrow}(\Delta) &= - \left\{ (\tilde{a}^D)^{\downarrow\downarrow}(\Delta) \cdot (W^X)^{\downarrow\downarrow}(-\Delta) \cdot (\tilde{a}^D)^{\downarrow\downarrow}(\Delta) \right. \\
&\quad \left. + (\tilde{a}^D)^{T\uparrow\downarrow}(\Delta) \cdot (W^X)^{\uparrow\uparrow}(-\Delta) \cdot (\tilde{a}^D)^{\uparrow\downarrow}(\Delta) \right\}, \tag{2.241b}
\end{aligned}$$

$$\begin{aligned}
\frac{\partial}{\partial \Lambda} (a^D)^{\uparrow\downarrow}(\Delta) &= - \left\{ (\tilde{a}^D)^{\uparrow\uparrow}(\Delta) \cdot (W^X)^{\uparrow\uparrow}(-\Delta) \cdot (\tilde{a}^D)^{\uparrow\downarrow}(\Delta) \right. \\
&\quad \left. + (\tilde{a}^D)^{\uparrow\downarrow}(\Delta) \cdot (W^X)^{\downarrow\downarrow}(-\Delta) \cdot (\tilde{a}^D)^{\downarrow\downarrow}(\Delta) \right\}. \tag{2.241c}
\end{aligned}$$

Furthermore, we can combine (2.237) with (2.206) and (2.207) to obtain symmetries for the kept spin and Keldysh (i.e. the a) components of the vertex. For completeness, we summarize here all resulting symmetries for the kept components¹⁷

¹⁷ For a systematic visualization of these symmetries, see also App. B of Sec. 5.2.

- **Particle exchange**

$$(a^P)^{\sigma\sigma} = (a^P)^{I\sigma\sigma} = -(a^P)^{I_1\sigma\sigma} = -(a^P)^{I_2\sigma\sigma}, \quad (2.242a)$$

- **Complex conjugation**

$$(a^D)^{\sigma\sigma'}(\Delta) = (a^D)^{I\sigma\sigma'}(-\Delta), \quad (2.242b)$$

- **Particle exchange + FDT**

$$(a^D)^{\sigma\sigma} = (a^D)^{T\sigma\sigma}, \quad (2.242c)$$

- **Complex conjugation + FDT**

$$(a^X)^{\uparrow\downarrow} = (a^X)^{T\uparrow\downarrow}, \quad (2.242d)$$

$$(a^P)^{\sigma\sigma'} = (a^P)^{T\sigma\sigma'}. \quad (2.242e)$$

To summarize, the equilibrium flow is given by the flow equations for the self-energy (2.240), the P- and X-channel (2.231), and the D-channel (2.241). The initial conditions are given by (2.234). For a generic flow with finite magnetic field, one has to evaluate the 8 bubble terms

$$(I^P)^{\sigma\sigma'}, (I^X)^{\sigma\sigma'}, \quad (2.243)$$

for all possible spin combinations $\sigma, \sigma' \in \{\uparrow, \downarrow\}$.

Zero magnetic field

In the case of zero magnetic field, it is enough to compute only the two bubble terms

$$(I^P)^{\uparrow\uparrow}, (I^X)^{\uparrow\uparrow}. \quad (2.244)$$

Since most of the computation time is spent on the evaluation of the integrals of the bubble terms (2.243), the zero field case reduces computation time by almost a factor of 4. Furthermore, completely analogous to the Matsubara case (2.193), the vertex components whose flow has to be computed is reduced to 5 (since the $a^{\downarrow\downarrow}$ components can be eliminated), and induces one additional symmetry each for the $a^{\uparrow\downarrow}$ components. Furthermore, it is of course enough to compute for the self-energy only the flow of Σ^{\uparrow} . For details see App. B of Sec. 5.2.

3 Extended Coupled Ladder Approximation in the Matsubara formalism

3.1 Overview

This section contains our first publication aiming at the treatment of finite-ranged interactions in quantum point contacts (QPCs). We devise the Matsubara version of the extended Coupled Ladder Approximation (eCLA), proceeding analogously to the previous work of Bauer et al. in [BHS⁺13, BHvD14]. Guided by the idea to only keep vertex configurations that are already generated in second-order of the bare interaction, we are lead in a natural way to the eCLA scheme which incorporates the necessary inter-channel feedback. Since our understanding -and with it the presentation- of the method has deepened over the last three years, we recommend, for the interested reader, to study the newer introductory part to the eCLA method in Sec. 2.4.

Although we derive the dynamic eCLA fRG equations in the Matsubara formalism, we do not yet aim to achieve a dynamic treatment of the vertex functions in this work. In our presented implementation, both the two-particle vertex and the one-particle self-energy are assumed to be static. This assumption was found to produce reasonable results for the case of zero temperature [BHS⁺13, BHvD14], and is a good stepping stone to a more involved dynamical treatment. Besides simplifying the complexity of the implementation, a static treatment also requires much lesser computational resources and therefore enables the scanning of a wide range of physical parameters.

The results part can be divided into two sections. Firstly, the new eCLA method is applied to models with onsite interactions only, to get an intuition what effects the extension of the interchannel feedback causes by itself. For this task, a newly introduced parameter, the feedback length L , is increased from $L = 0$ (which corresponds – besides a minor detail – to the previous CLA method of [BHvD14]) to finite L constituting a finite spatial feedback between the different fRG channels. For a standard QPC model with onsite interactions, the qualitative results for the conductance stay the same as for the CLA. Quantitatively, it was found that convergence in L is achieved for L being comparable to the characteristic QPC length. Furthermore, we noticed that the extended feedback stabilizes the fRG flow, enabling the study of wider physical parameter regimes. We demonstrate this feature using a quantum dot containing only a few electrons close the chemical potential. For previous fRG schemes this regime was not treatable due to the large density of states at the chemical potential, c.f. the work of Heyder et al. in [HBS⁺15, Hey14]. With a feedback length L on the scale of the width of the quantum dot, the eCLA, however, impressively manages to overcome this convergence issues and yields beautiful results.

Secondly, the eCLA method is applied to a model with finite-ranged interactions. For intermediate interaction ranges, comparable to the characteristic QPC length, the form of the zero temperature conductance does not change qualitatively from the onsite one.¹ A distinctly different conductance shape is only found when increasing the interaction range to the scale of the system size, therefore taking a real long-range tail of the interaction into account. Here the conductance develops additional shoulder / resonance type features. This

¹ This will change when treating finite temperatures, see Sec. 5.2.

conductance features are accompanied by density oscillations occurring in the central QPC region. Analyzing the local density of states (LDOS), these additional structures can be identified as Friedel oscillations of a significantly flattened effective QPC barrier.

A small caveat has to be pointed out here. Our results are accompanied by a fRG artifact, already encountered in previous studies [Eis13, BHvD14], namely an unphysical shift in the energy of the pinch-off of the conductance. While noticeable for short- and intermediate ranged-interactions on the scale of the characteristic QPC length, this shift becomes especially worse for interactions with a real long range tail. At the time of the publication of this paper, we attributed this artifact to the static treatment, however, it also persists (though somewhat mollified) in a semi-dynamic treatment, see Sec. 5.2. Thus, we expect that this kind of artifact is either caused by the applied channel decomposition or by the second-order truncated structure of the fRG flow itself. The artifact might therefore be remedied in a future implementation using multiloop fRG [KvD18b, KvD18c, KvD18a], which does (generically) not rely on a channel decomposition and furthermore incorporates a certain class of contributions (namely the parquet type ones) beyond second order.

We are proud to mention that our eCLA method has also caught the attention and the interest of other groups. A special case of the eCLA is used in [SK17]. In [MSMK18], the eCLA scheme is successfully used in a fRG study of phase transitions in one-dimensional systems. It was found that in order to detect certain phase transitions the extended vertex feedback of the eCLA is of crucial importance.

3.2 Functional renormalization group approach for inhomogeneous one-dimensional Fermi systems with finite-ranged interactions

by

Lukas Weidinger,¹ Florian Bauer,¹ and Jan von Delft¹

¹ Physics Department, Arnold Sommerfeld Center for Theoretical Physics and Center for NanoScience, Ludwig-Maximilians-Universität München, 80333 München, Germany

reprinted on pages [80–99](#)

Phys. Rev. B. **95**, 035122 (2017),

DOI: [10.1103/PhysRevB.95.035122](https://doi.org/10.1103/PhysRevB.95.035122).

with permission from

© 2017 American Physical Society

Functional renormalization group approach for inhomogeneous one-dimensional Fermi systems with finite-ranged interactions

Lukas Weidinger, Florian Bauer, and Jan von Delft

*Arnold Sommerfeld Center for Theoretical Physics and Center for NanoScience,**Ludwig-Maximilians-Universität München, Theresienstrasse 37, D-80333 München, Germany*

(Received 11 October 2016; revised manuscript received 19 December 2016; published 13 January 2017)

We introduce an equilibrium formulation of the functional renormalization group (fRG) for inhomogeneous systems capable of dealing with spatially finite-ranged interactions. In the general third-order truncated form of fRG, the dependence of the two-particle vertex is described by $\mathcal{O}(N^4)$ independent variables, where N is the dimension of the single-particle system. In a previous paper [Bauer *et al.*, *Phys. Rev. B* **89**, 045128 (2014)], the so-called coupled-ladder approximation (CLA) was introduced and shown to admit a consistent treatment for models with a purely onsite interaction, reducing the vertex to $\mathcal{O}(N^2)$ independent variables. In this work, we introduce an extended version of this scheme, called the extended coupled ladder approximation (eCLA), which includes a spatially extended feedback between the individual channels, measured by a feedback length L , using $\mathcal{O}(N^2L^2)$ independent variables for the vertex. We apply the eCLA in a static approximation and at zero temperature to three types of one-dimensional model systems, focusing on obtaining the linear response conductance. First, we study a model of a quantum point contact (QPC) with a parabolic barrier top and on-site interactions. In our setup, where the characteristic length l_x of the QPC ranges between approximately 4–10 sites, eCLA achieves convergence once L becomes comparable to l_x . It also turns out that the additional feedback stabilizes the fRG flow. This enables us, second, to study the geometric crossover between a QPC and a quantum dot, again for a one-dimensional model with on-site interactions. Third, the enlarged feedback also enables the treatment of a finite-ranged interaction extending over up to L sites. Using a simple estimate for the form of such a finite-ranged interaction in a QPC with a parabolic barrier top, we study its effects on the conductance and the density. We find that for low densities and sufficiently large interaction ranges the conductance develops additional features, and the corresponding density shows some fluctuations that can be interpreted as Friedel oscillations arising from a renormalized barrier shape with a rather flat top and steep flanks.

DOI: [10.1103/PhysRevB.95.035122](https://doi.org/10.1103/PhysRevB.95.035122)

I. INTRODUCTION

The functional renormalization group (fRG) is a well established tool for studying interacting many-body systems [1–6]. This technique treats interactions using an RG-enhanced perturbation theory and is known to provide an efficient way to treat correlations. In particular, fRG can be used to treat spatially inhomogeneous systems, represented by a discretized model with N sites. For example, about $N \sim 10^2$ sites are required to represent the electrostatic potential of a quasi-one-dimensional point contact in a manner that is sufficiently smooth to avoid finite-size effects [7]. The corresponding two-particle vertex has $\mathcal{O}(N^4) \sim 10^8$ independent spatial components. To make numerical computations feasible, simplifying approximations have to be made to reduce the number of components used to describe the vertex. Such a scheme, called the coupled-ladder approximation (CLA), was proposed in Ref. [7] for the case of on-site interactions. Bauer, Heyder, and von Delft (BHD) [8] supplied a detailed description of the CLA, which is in principle applicable to systems of arbitrary dimensionality. The CLA is implemented within the context of generic, third-order-truncated fRG, meaning that all vertices with three and higher particle number are set to zero throughout the whole flow. In this paper, we generalize this scheme to be able to treat finite-ranged interactions. Since the central aim of our scheme is to extend the spatial range over which information is fed back into the RG flow, we call our scheme the *extended coupled-ladder approximation* (eCLA).

The basic idea of the CLA, and by extension the eCLA, lies in reducing the number independent components of the vertex by decomposing it into several interaction channels and then establishing a consistent approximation by controlling the amount of feedback between the individual channels. This strategy follows that used in Refs. [4,9] in the context of the single-impurity Anderson model. For a model with short-ranged interactions, this approach reduces the number of independent quantities in the vertex to order $\sim \mathcal{O}(N^2)$. From a perturbative point of view, this treatment is exact in second order in the interaction and amounts to summing up approximate contributions from a large class of diagrams, including mutual feedback between the different interaction channels. The eCLA generalizes the CLA by extending spatial feedback between the channels. As a control parameter for this extended feedback we introduce a feedback length L , where $L = 0$ corresponds to the previous approximation scheme used by BHD, while $L = N - 1$ includes the full fRG flow in second order. L thus serves as a control parameter for the number of independent spatial components of the vertex, which scales as $\sim \mathcal{O}(N^2L^2)$. Moreover, the longer-ranged feedback allows us also to treat interactions with finite range up to L_U sites (with $L_U \leq L$) in a manner that is exact to second order in the interaction.

In this paper, we present a detailed account of the eCLA, and apply it to two one-dimensional (1D) fermionic systems, modeled to describe the lowest 1D subband of a quantum point contact (QPC) or a quantum dot (QD), respectively. We

develop the eCLA for systems described by a Hamiltonian of the form

$$\hat{H} = \sum_{ij,\sigma} h_{ij}^{\sigma} d_{i\sigma}^{\dagger} d_{j\sigma} + \frac{1}{2} \sum_{ij,\sigma\sigma'} U_{ij} \hat{n}_{i\sigma} \hat{n}_{j\sigma'} (1 - \delta_{ij} \delta_{\sigma\sigma'}), \quad (1)$$

where h^{σ} and U are real, symmetric matrices, $d_{j\sigma}^{\dagger}$ creates an electron in single particle state j with spin σ ($=\uparrow, \downarrow$ or $+, -$, with $\bar{\sigma} = -\sigma$), and $n_{j\sigma} = d_{j\sigma}^{\dagger} d_{j\sigma}$. In the context of the applications presented here, we refer to the quantum number j as the “site index.” Our eCLA scheme requires the interaction to have a finite range $L_U \leq L$, such that

$$U_{ij} = 0 \quad \text{if } |i - j| > L_U. \quad (2)$$

Models of this form, but with on-site interactions ($U_{ij} = U\delta_{ij}$), have been used to study both QPC and QD systems [7]. To describe a QPC, h_{ij}^{σ} is taken to represent a one-dimensional tight-binding chain, with a potential barrier with parabolic top, whereas for a QD, it is chosen to represent a double-barrier potential. The noninteracting physics of both models is well known, whereas the effect of interactions, especially for the QPC, are still a topic of ongoing discussions [10–12]. For the QPC, the conductance is quantized [13–15] in units of the conductance quantum $G_Q = 2e^2/h$, but shows an additional shoulder at approximately $0.7G_Q$. This regime, in which other observables show anomalous behavior too [16–18], is commonly known as the “0.7-anomaly.” The latter has been studied in [7] using a model of the above form, with purely on-site interactions. However, to examine the effect of gate-induced screening in a QPC, one needs to consider finite-ranged interactions. This goal serves as the main motivation for developing the eCLA put forth in this paper.

We remark that the QD and QPC models considered here provide a meaningful testing ground for the eCLA, since lowest-order perturbation theory would not yield an adequate treatment of the correlation effects expected to occur: the Kondo effect for QDs and the 0.7-anomaly for QPCs. Although some aspects of the latter can be understood in terms of a simple Hartree picture [7], the interaction strength needed to yield phenomenological behavior typical of the 0.7-anomaly is sufficiently large that lowest-order perturbation theory is inadequate.

The numerical results presented here were all obtained using the eCLA in a static approximation, which neglects the frequency-dependence of the two-particle vertex (after which the approach no longer is exact to second order). Nevertheless, BHD have shown that for a QPC model with on-site interactions, the CLA with a static approximation leads to reasonable results for the conductance step shape, though it does produce some artifacts regarding the pinch-off gate voltage when the interaction strength is increased. We find the same to be true for the static eCLA, with the artifacts becoming more pronounced with increasing interaction range, but the step shape behaving in a physically reasonable manner.

We use the eCLA for three studies of increasing complexity.

(i) We present static eCLA results for a QPC model with short-ranged interaction and successively increase the feedback length L . This systematically improves the treatment of RG feedback between the various fRG channels, and

for sufficiently large L converges to the full solution of the generic, third-order-truncated static fRG. For the models we consider here, where the characteristic length l_x of the parabolic QPC potential barrier varies between approximately 4–10 sites, we find that convergence in L is achieved once L becomes comparable to l_x . For such systems, the eCLA scheme thus speeds up the calculation relative to the full generic, third-order-truncated static fRG by a factor of 10^3 , without any loss of accuracy. (ii) Furthermore, it turns out that the eCLA’s enhanced feedback leads to a more stable fRG flow than the CLA scheme, since each interaction channel acts more strongly to limit the tendencies other channels might have to diverge during the fRG flow. This enables us to study the geometric crossover between a QPC and a QD where the barrier top stays close to the chemical potential. This setup features a high local density of states (LDOS) at the chemical potential, and as a result turns out to be intractable when using the CLA without enhanced feedback [19]. In contrast, the eCLA is able to treat this challenging crossover very nicely. (iii) Finally, we illustrate the potential of the eCLA to deal with finite-ranged interactions in a setting where the physics of screening comes into play, namely, a QPC model with an interaction whose range extends over up to N sites. The purpose of this study is mainly methodological, i.e., we do not aim here to achieve a fully realistic treatment of screening in a QPC. Nevertheless, the results are interesting: for a sufficiently long ranged interaction and sufficiently low density, there exists a parameter regime where we find additional features in the conductance and corresponding $2k_F$ density fluctuations *within* the QPC.

The paper has three main parts. The first part (Sec. II) develops our improved eCLA feedback scheme. The second part (Sec. III) studies its consequences for QPC and QD models with on-site interaction, focusing on the effects of increasing the feedback length L . Finally, the third part (Sec. IV) is devoted to finite-ranged interactions. We estimate the approximate form and strength of the interaction to be used for a 1D depiction of a QPC and show some preliminary results for the conductance and density profile of such a system depending on the screening properties. A detailed study of the physics of long-ranged interactions in QPCs is beyond the scope of this work and left as a topic of future investigation.

II. fRG FLOW EQUATIONS

Before we introduce our new eCLA scheme, we give a short overview over the general idea and the usual approximations made in fRG. Since numerous detailed treatments of fRG are available, and since our work builds on that of BHD, the discussion below is very brief and structured similarly to that in Ref. [8]. The basic idea of fRG is to introduce a flow parameter Λ in the bare propagator of the theory in such a way that for $\Lambda = \Lambda_i = \infty$, the structure of the resulting vertex functions are very simple. With our choice for Λ (described later) all but the two-particle vertex will vanish,

$$\gamma_2^{\Lambda_i} = v \quad \gamma_n^{\Lambda_i} = 0 \quad (n \neq 2), \quad (3)$$

where v is the bare vertex. For the final value of the flow parameter $\Lambda = \Lambda_f = 0$, one recovers the full bare propagator

and hence the full theory:

$$\mathcal{G}_0^\Lambda \rightarrow \mathcal{G}_0, \quad \text{with} \quad \mathcal{G}_0^{\Lambda_i} = 0, \quad \mathcal{G}_0^{\Lambda_f} = \mathcal{G}_0. \quad (4)$$

The RG flow is described by a hierarchy of coupled differential equations for the one particle irreducible (1PI) n -particle vertex functions γ_n ,

$$\frac{d}{d\Lambda} \gamma_n^\Lambda = \mathcal{F}(\Lambda, \mathcal{G}_0^\Lambda, \gamma_1^\Lambda, \dots, \gamma_{n+1}^\Lambda). \quad (5)$$

Integrating this system from $\Lambda = \Lambda_i$ to $\Lambda = 0$ yields in principle a full description of all interaction vertices. In practice, one can of course not treat an infinite hierarchy of flow equations and has to truncate it at some point. In our form of third-order truncated fRG, we incorporate the one- and two-particle vertex into the flow, but set all vertices with three or more particles to zero

$$\frac{d}{d\Lambda} \gamma_n = 0 \quad (n \geq 3). \quad (6)$$

We thus retain only the flow of the self-energy, $\Sigma = -\gamma_1$, and the flow of the two-particle vertex γ_2 . This differential equation can then be solved numerically, using a standard Runge-Kutta method. As we will see shortly, the flow of the vertex consists of three different parquetlike channels, which are coupled to the flow of the self-energy and also directly to each other. This simultaneous treatment moderates competing instabilities in an unbiased way.

In principle, the form of the fRG flow equations depends on the choice of the flow parameter, even if in most cases they take the form stated below. In our work, we choose the Λ dependence of the bare propagator to take the form of an infrared cutoff

$$\mathcal{G}_0^\Lambda(\omega_n) = \Theta_T(|\omega_n| - \Lambda) \mathcal{G}_0(\omega_n), \quad \Lambda_i = \infty, \quad \Lambda_f = 0. \quad (7)$$

We use the Matsubara formalism with the frequencies ω_n defined to be purely imaginary,

$$\omega_n = iT\pi(2n + 1),$$

and Θ_T is a step function broadened on the scale of temperature.

Using this cutoff, one can derive the fRG equations in the standard way, see, e.g., Refs. [5,20] or Ref. [21] for a diagrammatic derivation. The resulting equation for the one-particle vertex is given by

$$\frac{d}{d\Lambda} \gamma_1^\Lambda(q'_1, q_1) = T \sum_{q'_2, q_2} \mathcal{S}_{q'_2, q_2}^\Lambda \gamma_2^\Lambda(q'_2, q'_1; q_2, q_1), \quad (8)$$

where q_i is a shorthand for all quantum numbers and the fermionic Matsubara frequency associated with the legs of a vertex, and the full- and single-scale propagators are defined via

$$\mathcal{G}^\Lambda = [[\mathcal{G}_0^\Lambda]^{-1} - \Sigma^\Lambda]^{-1}, \quad (9a)$$

$$\mathcal{S}^\Lambda = \mathcal{G}^\Lambda \partial_\Lambda [\mathcal{G}_0^\Lambda]^{-1} \mathcal{G}^\Lambda, \quad (9b)$$

respectively. The structure of the vertex consists naturally of three different parquetlike channels

$$\gamma_2^\Lambda = v + \gamma_p^\Lambda + \gamma_x^\Lambda + \gamma_d^\Lambda, \quad (10)$$

where v is the bare vertex and we refer to γ_p^Λ , γ_x^Λ , and γ_d^Λ as the particle-particle channel (P), and the exchange (X) and direct (D) part of the particle-hole channel. These quantities are defined via their flow equations

$$\frac{d}{d\Lambda} \gamma_2^\Lambda = \frac{d}{d\Lambda} (\gamma_p^\Lambda + \gamma_x^\Lambda + \gamma_d^\Lambda), \quad (11)$$

and the initial conditions $\gamma_p^{\Lambda_i} = \gamma_x^{\Lambda_i} = \gamma_d^{\Lambda_i} = 0$. The explicit form of the flow equations is

$$\frac{d}{d\Lambda} \gamma_p^\Lambda(q'_1, q'_2; q_1, q_2) = T \sum_{q'_3, q_3, q'_4, q_4} \gamma_2^\Lambda(q'_1, q'_2; q_3, q_4) \mathcal{S}_{q'_3, q'_4}^\Lambda \mathcal{G}_{q_3, q_4}^\Lambda \gamma_2^\Lambda(q'_3, q'_4; q_1, q_2), \quad (12a)$$

$$\frac{d}{d\Lambda} \gamma_x^\Lambda(q'_1, q'_2; q_1, q_2) = T \sum_{q'_3, q_3, q'_4, q_4} \gamma_2^\Lambda(q'_1, q'_2; q_3, q_4) [\mathcal{S}_{q'_3, q'_4}^\Lambda \mathcal{G}_{q_3, q_4}^\Lambda + \mathcal{G}_{q'_3, q'_4}^\Lambda \mathcal{S}_{q_3, q_4}^\Lambda] \gamma_2^\Lambda(q'_3, q'_4; q_1, q_2), \quad (12b)$$

$$\frac{d}{d\Lambda} \gamma_d^\Lambda(q'_1, q'_2; q_1, q_2) = -T \sum_{q'_3, q_3, q'_4, q_4} \gamma_2^\Lambda(q'_1, q'_2; q_3, q_4) [\mathcal{S}_{q'_4, q'_3}^\Lambda \mathcal{G}_{q_3, q_4}^\Lambda + \mathcal{G}_{q'_4, q'_3}^\Lambda \mathcal{S}_{q_3, q_4}^\Lambda] \gamma_2^\Lambda(q'_4, q'_3; q_3, q_2). \quad (12c)$$

At this point, the channels have a full feedback between them. Later on, however, we will control the amount of feedback between channels by the feedback length L .

A. Frequency parametrization

Since we have energy conservation at each vertex,

$$\begin{aligned} \gamma_1(q'_1, q_1) &\propto \delta_{n'_1, n_1}, \\ \gamma_2(q'_1, q'_2; q_1, q_2) &\propto \delta_{n'_1 + n'_2, n_1 + n_2}, \end{aligned} \quad (13)$$

we can parametrize the frequency dependence of the self-energy with one frequency, and of the vertex with three frequencies. A detailed discussion of the frequency structure is given in Refs. [4,8,9], and since we proceed analogously, we will be very brief here. A convenient choice for the parametrization of the vertex frequency structure is given in terms of the three bosonic frequencies [7]

$$\Pi = \omega_{n'_1} + \omega_{n'_2} = \omega_{n_1} + \omega_{n_2}, \quad (14a)$$

$$X = \omega_{n'_1} - \omega_{n_2} = \omega_{n_1} - \omega_{n'_2}, \quad (14b)$$

$$\Delta = \omega_{n'_1} - \omega_{n_1} = \omega_{n_2} - \omega_{n'_2}. \quad (14c)$$

In order to keep notation short, the frequency information is separated from the site and spin quantum numbers:

$$\begin{aligned} & \gamma_2(j'_1\sigma'_1\omega_{n'_1}, j'_2\sigma'_2\omega_{n'_2}; j_1\sigma_1\omega_{n_1}, j_2\sigma_2\omega_{n_2}) \\ & = \delta_{n'_1+n'_2, n_1+n_2} \gamma_2(j'_1\sigma'_1, j'_2\sigma'_2; j_1\sigma_1, j_2\sigma_2; \Pi, \chi, \Delta). \end{aligned} \quad (15)$$

For convenience, we have here also listed the fermionic frequencies in terms of the bosonic ones:

$$\omega_{n'_1} = \frac{1}{2}(\Pi + X + \Delta), \quad \omega_{n'_2} = \frac{1}{2}(\Pi - X - \Delta), \quad (16a)$$

$$\omega_{n_1} = \frac{1}{2}(\Pi + X - \Delta), \quad \omega_{n_2} = \frac{1}{2}(\Pi - X + \Delta). \quad (16b)$$

B. Coupled-Ladder approximation

The basic idea of the CLA scheme was introduced in Refs. [4,9] for the frequency parametrization of the single-impurity Anderson model and was further developed for inhomogeneous Fermi systems with on-site interaction in Ref. [7]. Here we will go one step further and extend this scheme to treat interacting models with two-particle interactions of finite range, using an idea similar to the singular mode fRG approach introduced in [22]. There, the vertex structure in momentum space was decomposed into fermion bilinears that interact via exchange bosons and it was shown that this decomposition admits a systematic approximation by an expansion using form factors. Here, we will proceed similar in position space, introducing ‘‘short indices’’ k, l that will control the extent of our approximation and act similar to the mentioned form factor expansion.

In the case of third-order truncated fRG, BHD introduced two different approximation schemes. The simpler ‘‘static second-order fRG’’ (sfRG2) neglects the frequency dependence of the vertex; the more elaborate ‘‘dynamic second-order fRG’’ (dfRG2) includes the frequency dependence of the vertex within a channel approximation, reducing this dependence from the generic $\mathcal{O}(N_f^3)$ to $\mathcal{O}(N_f)$, where N_f is the number of used frequencies. In the case of the on-site model, it turned out that static compared to dynamic fRG produces some artifacts concerning the pinch-off point of the conductance of a QPC but yields essentially the same shape for the conductance steps as dynamic fRG. For this reason and since it is a factor of N_f cheaper, we will only compute the static fRG flow in our numerical work. Nevertheless, we will derive here the full dynamic flow equations, and in principle, it should be no problem to implement these too.

The dfRG2 scheme exploits the fact that the bare vertex consists of a density-density interaction

$$\begin{aligned} & v(j'_1\sigma'_1, j'_2\sigma'_2; j_1\sigma_1, j_2\sigma_2) \\ & = \delta_{j'_1 j'_2}^{L_U} U_{j_1 j_2} [(1 - \delta_{j_1 j_2}) \delta_{\sigma_1 \sigma_2} + \delta_{\sigma_1 \bar{\sigma}_2}] \\ & \quad \times (\delta_{j'_1 j_1} \delta_{j'_2 j_2} \delta_{\sigma'_1 \sigma_1} \delta_{\sigma'_2 \sigma_2} - \delta_{j'_1 j_2} \delta_{j'_2 j_1} \delta_{\sigma'_1 \sigma_2} \delta_{\sigma'_2 \sigma_1}), \end{aligned} \quad (17)$$

and parametrizes the vertex in terms of $\mathcal{O}(N^2 L_U^2 N_f)$ independent variables. Here, $\delta_{j'_1 j_2}^{L_U} = 1$ if $|j_1 - j_2| \leq L_U$ and is otherwise set to zero.

Using this vertex, we can now consider a simplified version of the vertex flow equation (12), where the feedback of the vertex flow is neglected: on the r.h.s. we replace $\gamma_2^\Lambda \rightarrow v$. If the feedback of the self-energy were also neglected, this would be equivalent to calculating the vertex in second-order perturbation theory. As a consequence, all generated vertex contributions have one of the following structures:

$$\begin{aligned} P_{ji\sigma\sigma'}^{kl}(\Pi) & := \gamma_p^\Lambda(j\sigma, j+k\sigma'; i\sigma, i+l\sigma'; \Pi) \\ \mathcal{O}(v^2) & \approx \begin{array}{c} \Pi - \omega_{n'} \quad \Pi - \omega_{n''} \quad \Pi - \omega_n \\ \swarrow \quad \quad \quad \searrow \quad \quad \quad \swarrow \\ j\sigma \quad \quad \quad i\sigma \\ \swarrow \quad \quad \quad \searrow \\ j+k\sigma' \quad \quad \quad i+l\sigma' \\ \omega_{n'} \quad \quad \quad \omega_{n''} \quad \quad \quad \omega_n \end{array}, \end{aligned} \quad (18a)$$

$$\begin{aligned} \bar{P}_{ji\sigma\sigma'}^{kl}(\Pi) & := \gamma_p^\Lambda(j\sigma, j+k\sigma'; i\sigma', i+l\sigma; \Pi) \\ \mathcal{O}(v^2) & \approx \begin{array}{c} \Pi - \omega_{n'} \quad \Pi - \omega_{n''} \quad \Pi - \omega_n \\ \swarrow \quad \quad \quad \searrow \quad \quad \quad \swarrow \\ j\sigma \quad \quad \quad i\sigma' \\ \swarrow \quad \quad \quad \searrow \\ j+k\sigma' \quad \quad \quad i+l\sigma \\ \omega_{n'} \quad \quad \quad \omega_{n''} \quad \quad \quad \omega_n \end{array}, \end{aligned} \quad (18b)$$

$$\begin{aligned} X_{ji\sigma\sigma'}^{kl}(X) & := \gamma_x^\Lambda(j\sigma, i+l\sigma'; i\sigma, j+k\sigma'; X) \\ \mathcal{O}(v^2) & \approx \begin{array}{c} X + \omega_{n'} \quad X + \omega_{n''} \quad X + \omega_n \\ \swarrow \quad \quad \quad \searrow \quad \quad \quad \swarrow \\ j\sigma \quad \quad \quad i\sigma \\ \swarrow \quad \quad \quad \searrow \\ j+k\sigma' \quad \quad \quad i+l\sigma' \\ \omega_{n'} \quad \quad \quad \omega_{n''} \quad \quad \quad \omega_n \end{array}, \end{aligned} \quad (18c)$$

$$\begin{aligned} \bar{X}_{ji\sigma\sigma'}^{kl}(X) & := \gamma_x^\Lambda(j\sigma, i+l\sigma'; i\sigma', j+k\sigma; X) \\ \mathcal{O}(v^2) & \approx \begin{array}{c} X + \omega_{n'} \quad X + \omega_{n''} \quad X + \omega_n \\ \swarrow \quad \quad \quad \searrow \quad \quad \quad \swarrow \\ j\sigma \quad \quad \quad i\sigma' \\ \swarrow \quad \quad \quad \searrow \\ j+k\sigma' \quad \quad \quad i+l\sigma' \\ \omega_{n'} \quad \quad \quad \omega_{n''} \quad \quad \quad \omega_n \end{array}, \end{aligned} \quad (18d)$$

$$\begin{aligned} D_{ji\sigma\sigma'}^{kl}(\Delta) & := \gamma_d^\Lambda(j\sigma, i+l\sigma'; j+k\sigma, i\sigma'; \Delta) \\ \mathcal{O}(v^2) & \approx \begin{array}{c} \Delta + \omega_{n'} \quad j\sigma \quad \quad \quad j+k\sigma \quad \omega_{n'} \\ \swarrow \quad \quad \quad \searrow \quad \quad \quad \swarrow \\ \omega_{n''} \quad \mu \quad \quad \quad \mu \quad \Delta + \omega_{n''} \\ \swarrow \quad \quad \quad \searrow \\ i\sigma' \quad \quad \quad i+l\sigma' \\ \omega_n + \Delta \quad \quad \quad \omega_n \end{array}, \end{aligned} \quad (18e)$$

$$\begin{aligned} \bar{D}_{ji\sigma\sigma'}^{kl}(\Delta) & := \gamma_d^\Lambda(j\sigma, i+l\sigma'; j+k\sigma', i\sigma; \Delta) \\ \mathcal{O}(v^2) & \approx \begin{array}{c} \Delta + \omega_{n'} \quad j\sigma \quad \quad \quad j+k\sigma' \quad \omega_{n'} \\ \swarrow \quad \quad \quad \searrow \quad \quad \quad \swarrow \\ \omega_{n''} \quad \sigma' \quad \quad \quad \sigma \quad \Delta + \omega_{n''} \\ \swarrow \quad \quad \quad \searrow \\ i\sigma \quad \quad \quad i+l\sigma' \\ \omega_n + \Delta \quad \quad \quad \omega_n \end{array}, \end{aligned} \quad (18f)$$

These terms depend only on a single bosonic frequency. The upper indices kl are taken to run over the range

$$-L \leq k, l \leq L, \quad (19)$$

where the control parameter L sets the “spatial feedback range.” The bounds on the lower indices depend on the upper indices: if one of the site indices of γ_2 lies outside the region $[-N', N']$ where N' is defined by $N = 2N' + 1$, γ_2 is zero. Therefore i, j run between

$$\max(-N', -N' - l) \leq i \leq \min(N', N' - l), \quad (20)$$

$$\max(-N', -N' - k) \leq j \leq \min(N', N' - k). \quad (21)$$

Analogously to BHD, we now feed back all those terms on the right-hand side (r.h.s.) of the flow equation (12), which conserve the site and spin structure indicated in Eq. (18). As a first consequence, each vertex quantity is fully fed back into its own flow equation. Secondly, the feedback between different quantities is restricted to those site indices that have the appropriate structure. Furthermore, to avoid frequency mixing, the feedback to a given channel from the other two channels is restricted to using only the static, i.e., zero-frequency component of the latter.

This scheme can be expressed by the replacement

$$\gamma_2 \rightarrow \tilde{\gamma}_a \quad (22)$$

on the r.h.s. of channel $a = p, x, d$ in Eq. (12) where $\tilde{\gamma}_a$ is defined as

$$\begin{aligned} \tilde{\gamma}_p(j'_1\sigma'_1, j'_2\sigma'_2; j_1\sigma_1, j_2\sigma_2, \Pi) \\ = \delta_{j'_1 j'_2}^L \delta_{j_1 j_2}^L \gamma_2(j'_1\sigma'_1, j'_2\sigma'_2; j_1\sigma_1, j_2\sigma_2; \Pi, 0, 0), \end{aligned} \quad (23a)$$

$$\begin{aligned} \tilde{\gamma}_x(j'_1\sigma'_1, j'_2\sigma'_2; j_1\sigma_1, j_2\sigma_2, X) \\ = \delta_{j'_1 j'_2}^L \delta_{j_1 j_2}^L \gamma_2(j'_1\sigma'_1, j'_2\sigma'_2; j_1\sigma_1, j_2\sigma_2; 0, X, 0), \end{aligned} \quad (23b)$$

$$\begin{aligned} \tilde{\gamma}_d(j'_1\sigma'_1, j'_2\sigma'_2; j_1\sigma_1, j_2\sigma_2, \Delta) \\ = \delta_{j'_1 j'_2}^L \delta_{j_1 j_2}^L \gamma_2(j'_1\sigma'_1, j'_2\sigma'_2; j_1\sigma_1, j_2\sigma_2; 0, 0, \Delta). \end{aligned} \quad (23c)$$

C. Symmetries

As can readily be checked, these flow equations respect the following symmetry relations:

$$\mathcal{G}_{ij}^{\sigma\Lambda}(\omega_n) = \mathcal{G}_{ji}^{\sigma\Lambda}(\omega_n) = [\mathcal{G}_{ij}^{\sigma\Lambda}(-\omega_n)]^*, \quad (24a)$$

$$\Sigma_{ij}^{\sigma\Lambda}(\omega_n) = \Sigma_{ji}^{\sigma\Lambda}(\omega_n) = [\Sigma_{ij}^{\sigma\Lambda}(-\omega_n)]^*, \quad (24b)$$

$$\begin{aligned} P_{ji\sigma\sigma'}^{kl}(\Pi) &= P_{ij\sigma\sigma'}^{lk}(\Pi) = P_{(j+k)(i+l)\sigma'\sigma}^{(-k)(-l)}(\Pi), \\ \bar{P}_{ji\sigma\sigma'}^{kl}(\Pi) &= \bar{P}_{ij\sigma\sigma'}^{lk}(\Pi) = \bar{P}_{(j+k)(i+l)\sigma'\sigma}^{(-k)(-l)}(\Pi), \\ P_{ji\sigma\sigma'}^{kl}(\Pi) &= -\bar{P}_{j+k i \sigma'\sigma}^{-kl}(\Pi) = -\bar{P}_{j(i+l)\sigma\sigma'}^{k(-l)}(\Pi), \\ P_{\sigma\sigma} &= \bar{P}_{\sigma\sigma}, \end{aligned} \quad (25a)$$

$$\begin{aligned} X_{ji\sigma\sigma'}^{kl}(X) &= X_{ij\sigma\sigma'}^{lk}(X) = [X_{(j+k)(i+l)\sigma'\sigma}^{(-k)(-l)}(X)]^*, \\ \bar{X}_{ji\sigma\sigma'}^{kl}(X) &= \bar{X}_{ij\sigma\sigma'}^{lk}(X) = [\bar{X}_{(j+k)(i+l)\sigma'\sigma}^{(-k)(-l)}(X)]^*, \\ X_{\sigma\sigma} &= \bar{X}_{\sigma\sigma}, \end{aligned} \quad (25b)$$

$$X = -\bar{D}, \quad \bar{X} = -D, \quad (25c)$$

$$\begin{aligned} P_{ji\sigma\sigma'}^{kl}(\Pi) &= [P_{ji\sigma\sigma'}^{kl}(-\Pi)]^*, \\ X_{ji\sigma\sigma'}^{kl}(X) &= [X_{ji\sigma\sigma'}^{kl}(-X)]^*, \\ \bar{X}_{ji\sigma\sigma'}^{kl}(\Delta) &= [\bar{X}_{ji\sigma\sigma'}^{kl}(-\Delta)]^*. \end{aligned} \quad (25d)$$

As a result, all relevant information is contained in a small number of independent frequency-dependent block matrices, which we define as follows:

$$\begin{aligned} P^\Lambda &= P_{\uparrow\downarrow}^\Lambda, P_\sigma^\Lambda = P_{\sigma\sigma}^\Lambda, \\ X^\Lambda &= X_{\uparrow\downarrow}^\Lambda, \\ D^\Lambda &= D_{\uparrow\downarrow}^\Lambda, D_\sigma^\Lambda = D_{\sigma\sigma}^\Lambda, \end{aligned} \quad (26)$$

where the superscript Λ signifies a dependence on the flow parameter.

The flow equations for these matrices can be derived starting from Eq. (12). The replacement (22) restricts the internal quantum numbers on the r.h.s. of the flow equation q_3, q_4, q'_3 , and q'_4 according to the definitions (18):

$$\begin{aligned} \dot{P}_{ji}^{kl\Lambda}(\Pi) &= \dot{\gamma}_p^\Lambda(j\uparrow, j+k\downarrow; i\uparrow, i+l\downarrow; \Pi) \\ &= T \sum_{j' i' k' l', n} [\tilde{\gamma}_p^\Lambda(j\uparrow, j+k\downarrow; i'\uparrow, i'+l'\downarrow; \Pi) \mathcal{S}_{i'j'}^{\uparrow\Lambda}(\omega_n) \mathcal{G}_{i'4l' j+k'}^{\downarrow\Lambda}(\Pi - \omega_n) \tilde{\gamma}_p^\Lambda(j'\uparrow, j'+k'\downarrow; i\uparrow, i+l\downarrow; \Pi) \\ &\quad + \tilde{\gamma}_p^\Lambda(j\uparrow, j+k\downarrow; i'\downarrow, i'+l'\uparrow; \Pi) \mathcal{S}_{i'j'}^{\downarrow\Lambda}(\omega_n) \mathcal{G}_{i'4l' j+k'}^{\uparrow\Lambda}(\Pi - \omega_n) \tilde{\gamma}_p^\Lambda(j'\downarrow, j'+k'\uparrow; i\uparrow, i+l\downarrow; \Pi)], \end{aligned} \quad (27a)$$

$$\begin{aligned} \dot{P}_{ji\sigma}^{kl\Lambda}(\Pi) &= \dot{\gamma}_p^\Lambda(j\sigma, j+k\sigma; i\sigma, i+l\sigma; \Pi) \\ &= T \sum_{j' i' k' l', n} \tilde{\gamma}_p^\Lambda(j\sigma, j+k\sigma; i'\sigma, i'+l'\sigma; \Pi) \mathcal{S}_{i'j'}^{\sigma\Lambda}(\omega_n) \mathcal{G}_{i'4l' j+k'}^{\sigma\Lambda}(\Pi - \omega_n) \tilde{\gamma}_p^\Lambda(j'\sigma, j'+k'\sigma; i\sigma, i+l\sigma; \Pi), \end{aligned} \quad (27b)$$

$$\begin{aligned} \dot{X}_{ji}^{kl\Lambda}(X) &= \dot{\gamma}_x^\Lambda(j\uparrow, i+l\downarrow; i\uparrow, j+k\downarrow; X) \\ &= T \sum_{i' j' l' k', n} \tilde{\gamma}_x^\Lambda(j\uparrow, i'+l'\downarrow; i'\uparrow, j+k\downarrow; X) [\mathcal{S}_{i'j'}^{\uparrow\Lambda}(\omega_n + X) \mathcal{G}_{j+k' i+l'}^{\downarrow\Lambda}(\omega_n) + \mathcal{S}_{j+k' i+l'}^{\downarrow\Lambda}(\omega_n) \mathcal{G}_{i'j'}^{\uparrow\Lambda}(\omega_n + X)] \\ &\quad \times \tilde{\gamma}_x^\Lambda(j'\uparrow, i+l\downarrow; i\uparrow, j'+k'\downarrow; X), \end{aligned} \quad (27c)$$

$$\begin{aligned}
 \dot{D}_{ji\sigma\sigma'}^{kl\Lambda}(\mathbf{X}) &= \dot{\gamma}_d^\Lambda(j\sigma, i+l\sigma'; j+k\sigma, i\sigma'; \Delta) \\
 &= -T \sum_{\substack{i'j'l'k' \\ n, \sigma''}} \tilde{\gamma}_d^\Lambda(j\sigma, i'+l'\sigma''; j+k\sigma, i'\sigma''; \Delta) [\mathcal{S}_{i'+l', j+k'}^{\sigma''\Lambda}(\omega_n) \mathcal{G}_{i'j'}^{\sigma''\Lambda}(\omega_n + \Delta) + \mathcal{G}_{i'+l', j+k'}^{\sigma''\Lambda}(\omega_n) \mathcal{S}_{i'j'}^{\sigma''\Lambda}(\omega_n + \Delta)] \\
 &\quad \times \tilde{\gamma}_d^\Lambda(j'\sigma'', i+l\sigma'; j'+k'\sigma'', i\sigma'; \Delta).
 \end{aligned} \tag{27d}$$

The initial conditions are

$$P^{\Lambda_i} = P_\sigma^{\Lambda_i} = X^{\Lambda_i} = D_{\sigma\sigma'}^{\Lambda_i} = 0. \tag{28}$$

These equations can be compactly written in block-matrix form:

$$\frac{d}{d\Lambda} P^\Lambda(\Pi) = \tilde{P}^\Lambda(\Pi) \cdot W^{p\Lambda}(\Pi) \cdot \tilde{P}^\Lambda(\Pi), \tag{29a}$$

$$\frac{d}{d\Lambda} P_\sigma^\Lambda(\Pi) = \tilde{P}_\sigma^\Lambda(\Pi) \cdot W_\sigma^{p\Lambda}(\Pi) \cdot \tilde{P}_\sigma^\Lambda(\Pi), \tag{29b}$$

$$\frac{d}{d\Lambda} X^\Lambda(\mathbf{X}) = \tilde{X}^\Lambda(\mathbf{X}) \cdot W^{x\Lambda}(\mathbf{X}) \cdot \tilde{X}^\Lambda(\mathbf{X}), \tag{29c}$$

$$\frac{d}{d\Lambda} D_{\sigma\sigma'}^\Lambda(\Delta) = - \sum_{\sigma''} \tilde{D}_{\sigma\sigma''}^\Lambda(\Delta) \cdot W_{\sigma''}^{d\Lambda}(\Delta) \cdot \tilde{D}_{\sigma''\sigma'}^\Lambda(\Delta), \tag{29d}$$

where “ \cdot ” denotes a block-matrix multiplication:

$$[A \cdot B]_{ji}^{kl} = \sum_{j'k'} A_{jj'}^{kk'} B_{j'i}^{k'l} \tag{30}$$

and we have introduced the definitions

$$\begin{aligned}
 \tilde{P}_{ji}^{kl\Lambda}(\Pi) &= \tilde{\gamma}_p^\Lambda(j\uparrow, j+k\downarrow; i\uparrow, i+l\downarrow; \Pi) \\
 &= \delta_{ji}\delta_{kl}U_{jj+k} + P_{ji}^{kl\Lambda}(\Pi) + \delta_{ji+l}^L \delta_{ij+k}^L X_{ji}^{(i+l-j)(j+k-i)\Lambda}(0) + \delta_{ij}^L \delta_{j+ki+l}^L D_{j(i+l)\uparrow\downarrow}^{(i-j)(j+k-i-l)\Lambda}(0),
 \end{aligned} \tag{31a}$$

$$\begin{aligned}
 \tilde{P}_{ji\sigma}^{kl\Lambda}(\Pi) &= \tilde{\gamma}_p^\Lambda(j\sigma, j+k\sigma; i\sigma, i+l\sigma; \Pi) \\
 &= \delta_{ji}\delta_{kl}U_{jj+k} - \delta_{k,-l}\delta_{(j+k)i}U_{ji} + P_{ji\sigma}^{kl\Lambda}(\Pi) - \delta_{i+l}^L \delta_{j+ki}^L D_{j\sigma}^{(i+l-j)(j+k-i)\Lambda}(0) + \delta_{ij}^L \delta_{j+ki+l}^L D_{j(i+l)\sigma}^{(i-j)(j+k-i-l)\Lambda}(0),
 \end{aligned} \tag{31b}$$

$$\begin{aligned}
 \tilde{X}_{ji}^{kl\Lambda}(\mathbf{X}) &= \tilde{\gamma}_x^\Lambda(j\uparrow, i+l\downarrow; i\uparrow, j+k\downarrow; \mathbf{X}) \\
 &= \delta_{ji}\delta_{kl}U_{jj+k} + X_{ji}^{kl\Lambda}(\mathbf{X}) + \delta_{i+l}^L \delta_{j+ki}^L P_{ji}^{(i+l-j)(j+k-i)\Lambda}(0) + \delta_{ij}^L \delta_{j+ki+l}^L D_{j(j+k)\uparrow\downarrow}^{(i-j)(i+l-j-k)\Lambda}(0),
 \end{aligned} \tag{31c}$$

$$\begin{aligned}
 \tilde{D}_{ji\sigma\sigma'}^{kl\Lambda}(\Delta) &= \tilde{\gamma}_d^\Lambda(j\sigma, i+l\sigma'; j+k\sigma, i\sigma'; \Delta) \\
 &= \delta_{0k}\delta_{0l}U_{ji} - \delta_{\sigma\sigma'}\delta_{ji}\delta_{kl}U_{jj+k} + D_{ji\sigma\sigma'}^{kl\Lambda}(\Delta) + \delta_{i+l}^L \delta_{j+ki}^L P_{j(j+k)\sigma\sigma'}^{(i+l-j)(i-j-k)\Lambda}(0) + \delta_{ij}^L \delta_{j+ki+l}^L X_{j(j+k)\sigma\sigma'}^{(i-j)(i+l-j-k)\Lambda}(0),
 \end{aligned} \tag{31d}$$

which account for the interchannel feedback contained in equation (22). Note that Eq. (31d) is not fully expressed in terms of the definitions (26). This can only be done once σ and σ' are specified explicitly and then leads to three independent equations. W^p , W^x , and W^d each represent a specific bubble, i.e., a product of two propagators summed over an internal frequency:

$$\begin{aligned}
 W_{ij}^{lk, p\Lambda}(\Pi) &= T \sum_n [\mathcal{S}_{ij}^{\uparrow\Lambda}(\omega_n) \mathcal{G}_{i+l, j+k}^{\downarrow\Lambda}(\Pi - \omega_n) \\
 &\quad + \mathcal{S}_{i+l, j+k}^{\downarrow\Lambda}(\omega_n) \mathcal{G}_{ij}^{\uparrow\Lambda}(\Pi - \omega_n)],
 \end{aligned} \tag{32a}$$

$$W_{ij\sigma}^{lk, p\Lambda}(\Pi) = T \sum_n [\mathcal{S}_{ij}^{\sigma\Lambda}(\omega_n) \mathcal{G}_{i+l, j+k}^{\sigma\Lambda}(\Pi - \omega_n)], \tag{32b}$$

$$\begin{aligned}
 W_{ij}^{lk, x\Lambda}(\mathbf{X}) &= T \sum_n [\mathcal{S}_{i+l, j+k}^{\downarrow\Lambda}(\omega_n) \mathcal{G}_{ij}^{\uparrow\Lambda}(\omega_n + \mathbf{X}) \\
 &\quad + \mathcal{G}_{j+ki+l}^{\downarrow\Lambda}(\omega_n) \mathcal{S}_{ij}^{\uparrow\Lambda}(\omega_n + \mathbf{X})],
 \end{aligned} \tag{32c}$$

$$\begin{aligned}
 W_{ij\sigma}^{lk, d\Lambda}(\Delta) &= T \sum_n [\mathcal{S}_{i+l, j+k}^{\sigma\Lambda}(\omega_n) \mathcal{G}_{ij}^{\sigma\Lambda}(\omega_n + \Delta) \\
 &\quad + \mathcal{G}_{i+l, j+k}^{\sigma\Lambda}(\omega_n) \mathcal{S}_{ij}^{\sigma\Lambda}(\omega_n + \Delta)].
 \end{aligned} \tag{32d}$$

D. eCLA versus CLA and the role of $D_{\uparrow\downarrow}$

Let us now recapitulate the similarities and differences between our new eCLA method to the previous CLA method

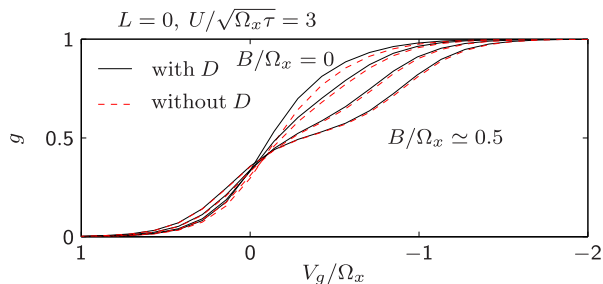


FIG. 1. The linear conductance $g = G/G_Q$ of a QPC as a function of gate voltage, plotted for the cases with and without feedback of $D^{\uparrow\downarrow}$ in an intermediate parameter regime for four equidistant magnetic fields. Note that the difference between the two cases is suppressed with increasing the magnetic field.

used in Ref. [8]. There, only on-site models were considered and the guiding idea for approximations in the fRG flow was to include only those vertex structures that are already generated in second order in the interaction. Therefore it was sufficient to consider only an on-site feedback between the individual channels, i.e., the feedback range was the same as the interaction range. In the development of the eCLA, we followed the same idea, but found it to be advantageous to separate the feedback length L from the actual range of the interaction L_U . To be exact in second order, L has to be chosen at least as large as L_U . However, it can be chosen also larger than L_U , and thus enables us to study the importance of the neglected higher-order terms. If L is chosen exactly equal to L_U , we are in principle back at the original idea to include only vertex structures in the flow which are already generated in second order of the interaction. However, there is one exception to the last statement; for purely on-site interactions ($L_U = 0$), the contributions of $D^{\uparrow\downarrow}$ and $P^{\sigma\sigma}$ to the vertex are of third and fourth order, respectively. In Ref. [8], they were therefore neglected, consistent with the policy of keeping only structures generated in second order. In the present paper, however, our implementation does not explicitly distinguish between $L_U = 0$ and $L_U > 0$ and includes the $D^{\uparrow\downarrow}$ and $P^{\sigma\sigma}$ contributions regardless of the values of L_U and L , even for $L_U = L = 0$. To be specific, for $L_U = L = 0$, our present flow scheme keeps $P^{\sigma\sigma} = 0$ but leads to a finite contribution of $D^{\uparrow\downarrow}$. Consequently, our results for $L_U = L = 0$ differ slightly from those obtained in Refs. [7,8], and the difference is a measure of the magnitude of the third-order $D^{\uparrow\downarrow}$ contribution. In Fig. 1, we compare the dependence of the QPC conductance on the magnetic field for a model with purely on-site interactions (defined in Sec. III below) for both CLA and eCLA with $L = 0$. The difference is most noticeable for $B = 0$ in the region of the 0.7-anomaly, i.e., in the regime where interactions influence the conductance most strongly, but even here the difference is not very big. (Of course, this holds only in intermediate parameter regimes, i.e., in regimes where both the eCLA and the CLA are convergent.)

E. The flow equation of the self-energy

Using the above definitions, the flow equation of the self-energy, Eq. (8), can be written explicitly

as

$$\begin{aligned} \frac{d}{d\Lambda} \Sigma_{ji}^{\sigma\Lambda}(\omega_n) = & -T \sum_{k,\sigma',n'} \left\{ \sum_l S_{i+l,j+k}^{\sigma'\Lambda}(\omega'_n) [U_{i(i+l)} \delta_{lk} \delta_{ji} \right. \\ & - U_{ij} \delta_{k,-l} \delta_{j(i+l)} \delta_{\sigma\sigma'} + P_{j\sigma\sigma'}^{kl\Lambda}(\omega_n + \omega'_n) \\ & + X_{j\sigma\sigma'}^{kl\Lambda}(\omega_n - \omega'_n)] \\ & \left. + \sum_{i_2} S_{i_2,i_2+k}^{\sigma'\Lambda}(\omega'_n) D_{j\sigma\sigma'}^{(i-j)k\Lambda}(0) \right\}, \quad (33) \end{aligned}$$

where the l,k summation is restricted to $|l|, |k| \leq L$, whereas the sum over i_2 runs over the whole interacting region. To summarize, dfRG2 is defined by the flow equations (29) and (33), together with the definitions (9), (18), (26), (31), and (32).

F. Restrictions for actual computations

In our actual computations, we restrict ourselves to the case of zero temperature and use so called static fRG, meaning that we treat the vertices as frequency independent. The zero-temperature limit enables us to transform the summation over discrete Matsubara frequencies into continuous integrals along the imaginary axis, and the Θ_T in Eq. (7) is a sharp step function. Using this, we are able to apply Morris' lemma [23], which enables us to simplify the integral expressions containing the single-scale propagator \mathcal{S} in the flow equations (27): under integration over ω , the following relations hold:

$$\mathcal{S}^\Lambda(i\omega) \stackrel{T=0}{=} \delta(|\omega| - \Lambda) \tilde{\mathcal{G}}^\Lambda(i\omega), \quad (34a)$$

$$\tilde{\mathcal{G}}^\Lambda(i\omega) = [[\mathcal{G}_0(i\omega)]^{-1} - \Sigma^\Lambda(i\omega)]^{-1}, \quad (34b)$$

$$\begin{aligned} \mathcal{S}_{i,j}^\Lambda(i\omega_1) \mathcal{G}_{k,l}^\Lambda(i\omega_2) \stackrel{T=0}{=} & \delta(|\omega_1| - \Lambda) \Theta(|\omega_2| - \Lambda) \\ & \times \tilde{\mathcal{G}}_{i,j}^\Lambda(i\omega_1) \tilde{\mathcal{G}}_{k,l}^\Lambda(i\omega_2). \quad (34c) \end{aligned}$$

The static fRG approximation treats the vertex quantities γ_p^Λ , γ_x^Λ , γ_d^Λ as frequency independent, setting the bosonic frequencies Π , X , and Δ to zero. Via Eq. (8), this automatically implies that the self-energy is frequency independent, too. In the case of QPC models with on-site interaction, this approximation was compared with results of the frequency dependent fRG scheme, the so-called ‘‘dynamic fRG’’ and was seen to yield reasonable results for the zero-frequency Green's function at zero temperature. However, for models with finite-ranged interactions, we find more pronounced static fRG artifacts (described in Sec. IV), which might be improved by the use of the dynamical method. This is a topic for future research. We stress here that it should in principle be straightforward to implement the dynamical method. The main restriction is simply the effort in computation time, which scales like the number of used frequencies, N_f , which in Ref. [7] is typically of the order 10^2 .

G. Numerical implementation

In a numerical implementation, the flow will start at a value Λ_i which is usually chosen as large, but is not infinite. For Λ_i large enough, one can show [5] that the flow of the self-energy

from $\Lambda = \infty$ to $\Lambda = \Lambda_i$ results in a value of $\gamma_1^{\Lambda_i}$ given by

$$\gamma_1^{\Lambda_i}(q'_1, q_1) = -\frac{1}{2} \sum_q v(q, q'_1; q, q_1). \quad (35)$$

This is then used as the initial condition for γ_1 in the numeric fRG flow. The initial condition for the vertex γ_2 , given by Eq. (3), stays the same.

In the case of sfRG2, the vertices and the self-energy only depend on Λ . In order to carry out the resulting integration, we mapped the domain of the flow parameter $\Lambda \in [0, \infty)$ onto the finite domain $x \in [0, 1)$ by using the substitution $\Lambda = \frac{x}{1-x}$, cf. Ref. [8]. To integrate the resulting flow, we followed Dormand-Prince [24], using a fourth-order Runge-Kutta method with adaptive step-size control.

For static fRG, the computationally most expensive step is the block-matrix multiplication of Eq. (29), which scales as $\mathcal{O}(N^3 L^3)$. In dynamic fRG schemes with nonfrequency cutoff (e.g., with hybridisation flow [4]), for intermediate $N \lesssim 10^2$ most of the calculation time is spent on the bubble integrals of Eq. (32), whose calculation time scales as $\mathcal{O}(N^2 L^2 N_f)$, where N_f is the number of bosonic frequencies. Since the numerical cost for this calculation (for the system sizes used in our setup) is comparable to the block-matrix multiplication of Eq. (29), it might be possible to implement the eCLA within those schemes, too.

III. RESULTS: ON-SITE INTERACTIONS

Having derived our eCLA scheme in the last section, we are now able to apply it to the two models of primary interest here, namely the QPC and the QD. In the present section, we study purely on-site models,

$$U_{ij} = \delta_{ij} U, \quad (36)$$

where we treat the strength U of the interaction as a tunable and space-independent parameter, which is suppressed smoothly to zero at the ends of the interacting region. The focus of this section lies on comparing our results to the ones obtained previously by BHD to explore the consequences of the improved feedback for a well-studied example. If not otherwise specified, plots in this section are calculated with $\mu = 0$, i.e., with half-filled leads.

A. Models for QPC and QD

Our interest lies in the low-energy physics of a QPC or a QD. For this reason, we consider only the lowest subband of a QPC, or a QD coupled to one-dimensional leads. We use a one-dimensional model Hamiltonian of the same form as used in Refs. [7,8,19]:

$$\hat{H} = \sum_{j\sigma} [E_j^\sigma \hat{n}_{j\sigma} - \tau (d_{j\sigma}^\dagger d_{j+1\sigma} + \text{H.c.})] + \sum_j U_j \hat{n}_{j\uparrow} \hat{n}_{j\downarrow}. \quad (37)$$

It describes an infinite tight-binding chain with constant lattice spacing a , constant hopping amplitude τ , on-site interaction U_j , and on-site potential energy $E_j^\sigma = V_j - \frac{\sigma B}{2}$. Here, V_j will be used to model the smooth electrostatic QPC or QD potential defined by gates (as described below and illustrated in Fig. 2),

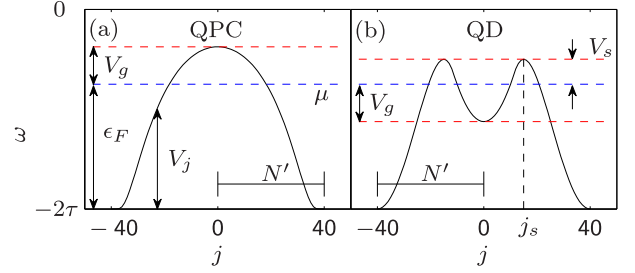


FIG. 2. Typical QPC and QD barrier shapes, controlled via the parameters, ϵ_F , V_g , N' , and, for the QD, V_s and j_s . For these plots, both μ and the barrier top lie were chosen to lie below the center of the bulk band, which we take as reference energy where $\omega = 0$. The case of half-filled leads, used for most of our calculations, corresponds to choosing $\mu = 0$.

and the Zeeman energy B accounts for a uniform external magnetic field parallel to the 2DEG. We take U_j and V_j to be nonzero only within a (single or double) “barrier region” of $N = 2N' + 1$ sites centered around $j = 0$, containing the QPC or QD. The rest of the chain represents two noninteracting leads with bandwidth 4τ , chemical potential μ , bulk Fermi energy $\epsilon_F = 2\tau + \mu$, and effective mass $m^* = \hbar^2/(2\tau a^2)$ (defined as the curvature of the dispersion at the band bottom in the bulk). Adopting the convention in Ref. [8], we choose the center of the bulk band as energy origin. In order to arrive at a discrete QPC potential V_j , we start with a continuous QPC potential

$$V(x) = \begin{cases} (V_g + \epsilon_F) \exp\left(\frac{-\gamma^2(x/L_{\text{bar}})^2}{1-(x/L_{\text{bar}})^2}\right), & |x| \leq L_{\text{bar}}, \\ 0, & |x| > L_{\text{bar}}, \end{cases} \quad (38)$$

where $2L_{\text{bar}}$ is the whole barrier length and V_g controls the barrier height, measured with respect to (w.r.t.) ϵ_F . Near the barrier top, the potential (38) can be expanded as

$$V(x) = V_g + \epsilon_F - \frac{1}{2} \frac{m^*}{\hbar^2} \Omega_x^2 x^2 + \mathcal{O}(x^4), \quad (39)$$

where the curvature parameter Ω_x is given by

$$\Omega_x = \gamma \frac{\hbar}{L_{\text{bar}}} \sqrt{\frac{2(V_g + \epsilon_F)}{m^*}}. \quad (40)$$

It has units of energy and serves as a characteristic energy scale for the QPC. It also defines a characteristic length scale for the QPC barrier top:

$$l_x = \hbar/\sqrt{2m^*\Omega_x} = a\sqrt{\tau/\Omega_x}. \quad (41)$$

The dimensionless parameter γ in the exponent of Eq. (38) can be used to vary the barrier curvature [Eq. (40)] without changing the barrier height. Through most of Sec. III, we will keep $\gamma = 1$ constant and consider only gate-voltages small compared to ϵ_F , such that the curvature can be assumed to be independent of V_g . However, when studying eCLA convergence properties (Fig. 4), and when dealing with longer-ranged interactions in Sec. IV, we will need to choose $\gamma \neq 1$.

We discretize the QPC potential (38) by choosing a number of sites N and setting the lattice spacing $a = 2L_{\text{bar}}/N$, to arrive

at

$$V_j = V(j \cdot a) = \begin{cases} (V_g + \varepsilon_F) e^{-\gamma^2 \frac{(j/N')^2}{1-(j/N')^2}}, & |j| \leq N', \\ 0, & |j| > N'. \end{cases} \quad (42)$$

The resulting barrier shape given by Eq. (42) is plotted in Fig. 2(a). The leading behavior around the maximum at $j = 0$ is quadratic and the same as in Ref. [8]:

$$V_j = V_g + \varepsilon_F - \frac{\Omega_x^2}{4\tau} j^2 + \mathcal{O}(j^4), \quad (43)$$

and the curvature can be expressed through the discrete quantities as $\Omega_x = \gamma \frac{2\sqrt{\tau(\varepsilon_F + V_g)}}{N'}$. For our on-site studies, where V_g is only varied in a small region around $V_g = 0$, we use the approximation $\Omega_x = \gamma \frac{2\sqrt{\tau\varepsilon_F}}{N'}$. In order to avoid discretization artifacts, the discretization length a should be chosen significantly smaller than l_x . In our actual computations for the QPC with on-site interactions, we use a ratio l_x/a varying between approximately 4–10 sites.

To model a QD, we use a potential that can be tuned smoothly from the QPC shape described above to a double-barrier structure, as shown in Fig. 2(b). The discretization procedure is analogous to the QPC and we state here only the resulting discrete dot potential, which is the same as used in Refs. [7,19]:

$$V_j = \begin{cases} 0, & \forall |j| \geq N', \\ (V_s + \varepsilon_F) \left[2 \left(\frac{|j| - N'}{j_s - N'} \right)^2 - \left(\frac{|j| - N'}{j_s - N'} \right)^4 \right], & \forall j_0 \leq |j| \leq N', \\ V_g + \varepsilon_F + \frac{\Omega_x^2 j^2}{4\tau} \operatorname{sgn}(V_s - V_g), & \forall 0 \leq |j| < j_0. \end{cases} \quad (44)$$

We can vary the dot width via j_s , and the depth of the quadratic well in the middle via V_s and V_g . These choices determine the values of j_0 and Ω_x in order to make the potential continuously differentiable. Of course, this is just one convenient way to model the dot structure, and the qualitative behavior of the physical results does not depend on the specific implementation.

For the on-site interaction, we use both for the QPC and the QD the form used by BHD [7]:

$$U_j = U e^{-(j/N')^6 / [1 - (j/N')^2]}. \quad (45)$$

It is almost constant and equal to U in the center of the QPC and drops smoothly to zero at the flanks of the barrier region.

B. Physical behavior of the models

We now briefly summarize the physics of these models, which was already discussed in great detail by BHD in Refs. [7,19]. Our main handle for tuning the QPC potential is the gate voltage V_g , which controls the height of the barrier. If the barrier top lies well above the chemical potential, the QPC is closed. Lowering the barrier, the QPC opens up and the linear conductance g increases smoothly from 0 to 1 in the region of gate voltages $0 \lesssim V_g \lesssim \Omega_x$, where Ω_x is the curvature of the QPC introduced above. Additionally, the width of the conductance step, i.e., the gate-voltage interval in which the conductance increases from zero to one, is also set by Ω_x .

The general shape of the conductance curve for a parabolic barrier in the absence of interactions is a step described by a Fermi function, as was shown by Büttiker in Ref. [15]. If one switches on on-site interactions, the conductance curve becomes asymmetric and flattens increasingly at the top. This effect can be traced back to the fact that when the barrier top drops below the chemical potential as the QPC is being opened up, the maximum in the LDOS just above the barrier top (called van Hove ridge in Ref. [7]) is aligned with the chemical potential, thereby strongly enhancing interaction effects. It turns out that the effective on-site interaction strength is in fact given by

$$U_j^{\text{eff}} = U \cdot \mathcal{A}_j^0(\mu), \quad (46)$$

where

$$\mathcal{A}_j^0(\omega) = -\frac{1}{\pi} \operatorname{Im} \mathcal{G}_{jj}^0(\omega + i0^+) \quad (47)$$

is the noninteracting local density of states per site. Near the barrier center, the resulting U^{eff} scales like $U/\sqrt{\Omega_x \tau}$.

In the QD case, we can vary the width and depth of the middle well, [cf. Figs. 6(d) and 6(e) below]. Typically, we want to study the crossover between QPC and QD, thus we start out with a QPC setup and lower the potential of the central region to change the geometry to a QD model. The characteristic physics of the quantum dot is determined by the structure of the discrete levels of the bound states in the well. This quantization leads to a conductance peak whenever such a level crosses the chemical potential and the dot gets filled by one electron more. In the interacting case, the degenerate levels split on a scale of the interaction strength U . However, there is a further effect: the odd valleys, i.e., the regions between the peaks where the dot contains an odd number of electrons, become conductance plateaus with $G_Q \approx 1$. This behavior reflects the occurrence of the Kondo [25] effect since the singly occupied dot level behaves like a localized spin coupled to a fermionic bath.

In this work, we will apply our eCLA first to the same type of on-site models of QPCs as used by BHD [7,8,19] and analyse the resulting effects. Importantly, we find that in comparison to the CLA used previously, the eCLA yields an improved stability of the fRG flow in the case of large bare LDOS at the chemical potential. This improvement allows us to additionally study the QPC-QD crossover, which involves a very high LDOS due to the flat barrier top that occurs in this transition. Using the CLA, it had not been possible to study this transition when the barrier top lies close to the chemical potential μ , since the CLA equations did not converge. Due to this problem, in the real-space approach chosen by Heyder *et al.* [19], it was not possible to study dots which contain just a few electrons. Since our new feedback scheme significantly ameliorates the convergence problem, we are now able to study the crossover from a QPC to a QD, which is just occupied by a single electron. This will be shown in Sec. III D.

C. Increasing the feedback length

Let us now study the influence of the feedback length L on the zero-temperature linear conductance [26],

$$g = \frac{1}{2} \sum_{\sigma} |2\pi\rho^{\sigma}(\mu + i0^+) \mathcal{G}_{-N',N'}^{\sigma}(\mu + i0^+)|^2. \quad (48)$$

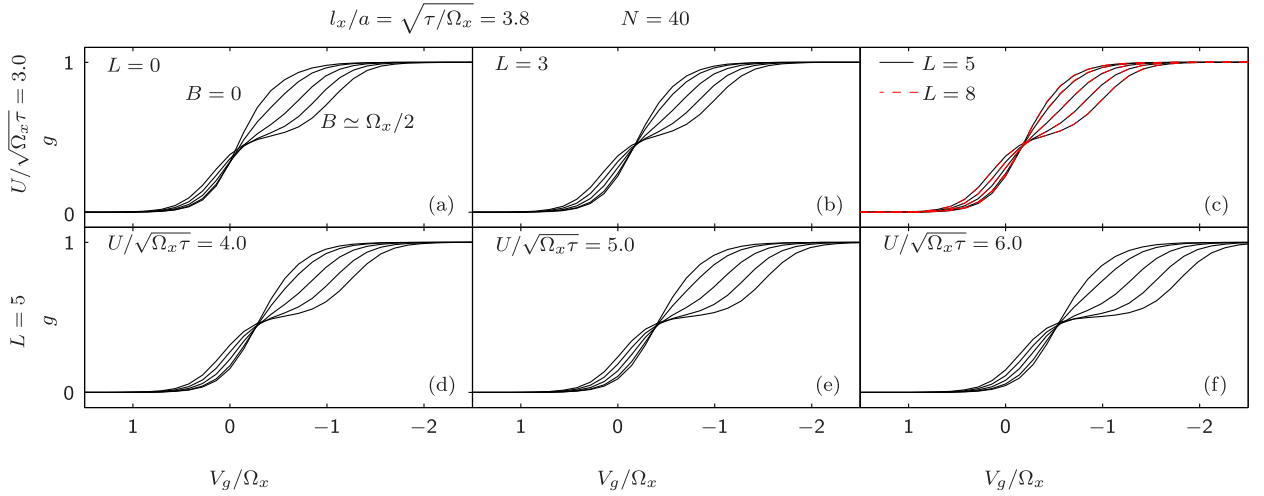


FIG. 3. Linear conductance g calculated using the static eCLA for five equidistantly chosen magnetic fields B between 0 and $\Omega_x/2$. (a)–(c) Conductance at fixed $U/\sqrt{\Omega_x\tau} = 3.0$ and four values of L . (d)–(f) Conductance at fixed $L = 5$, for three values of $U/\sqrt{\Omega_x\tau}$.

Here, $\rho(\omega)$ is the density of states at the boundary of a semi-infinite tight-binding chain; two such chains represent the two one-dimensional noninteracting leads, coupled to the central interacting region. Let us first look at the QPC case. We are interested in the shape of the conductance trace as a function of applied gate voltage and how this shape changes with external parameters, such as an applied magnetic field.

For pure on-site interactions, it is natural to choose the feedback length $L = 0$. This is what has been done in Refs. [7,8,19,27], and the results have been discussed therein in detail. Here, we will allow a nonzero L , although the actual interaction is purely on-site. This implies that a certain class of additional third-order terms will be generated during the RG flow which introduce a better coupling between the channels in the sense of the feedback in Eq. (23). For $L \rightarrow N$, the third-order truncated static fRG scheme is recovered *fully* regarding the spatial structure of the two-particle vertex (but not for its frequency structure, since we are using the static approximation). Figures 3(a) to 3(c) show the conductance G as a function of gate voltage V_g for different values of magnetic field B , calculated at fixed U and different values of feedback parameters L . Increasing the latter from $L = 0$ to $L = 3$, cf. Fig. 3(b), leads to quantitative but not qualitative changes in the shape of the conductance curves—the main effect is that the width of the B -induced subplateau decreases. In this regard, increasing L has a qualitatively similar effect to decreasing U (at $L = 0$), cf. Figs. 3(d) to 3(f). Note, though, that increasing L hardly affects the V_g position of the conductance step, whereas decreasing U does shift the step slightly towards higher V_g values, as expected physically due to the lowering of the Hartree barrier. Increasing the feedback beyond $L = 5$ does not lead to any significant quantitative changes, as can be seen in Fig. 3(c) where $L = 5$ (black line) is directly compared with $L = 8$ (red dashed line). Hence, for the present model, convergence is reached for $L \lesssim 5$. In general, this value depends on the strength of interaction U , and more importantly on the actual shape of the barrier.

In Fig. 4, we study the convergence behavior as function of the feedback length L more thoroughly, for four different values of the geometric length scale l_x/a [Eq. (41)], which is the width of the region where the LDOS is enhanced. To determine the convergence behavior, we first chose a large value L_{large} (here $L_{\text{large}} = 21$) for which $\max_{V_g} |g_{L_{\text{large}}}(V_g) - g_{L_{\text{large}}-1}(V_g)|$ is smaller than 10^{-4} , i.e., for which we can assume that the conductance is converged against its limit. We then plot

$$\Delta g_L := \max_{V_g} |g_L(V_g) - g_{L_{\text{large}}}(V_g)| \quad (49)$$

as a function of L . For our purposes, as for the plots in Fig. 3, we will regard that the conductance as being converged when $\Delta g_L \leq 0.5 \times 10^{-2}$. In Fig. 4, this criterion is indicated by the dashed line. The inset shows the smallest L (named L_C) for which the conductance is converged as a function of l_x/a . We see that for all models under our consideration L_C is comparable to l_x/a . Due to this convergence, the number of vertex components can safely be reduced from $O(N^4)$

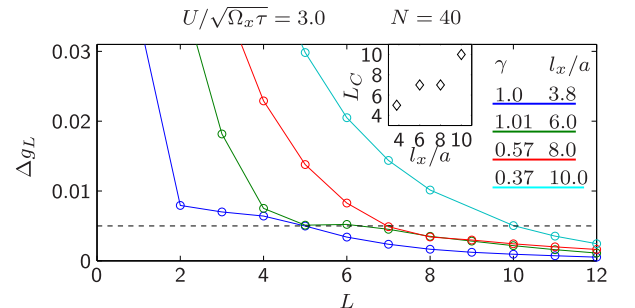


FIG. 4. Convergence behavior of the conductance for different values of l_x/a , where Δg_L is defined in Eq. (49). The parameters for the $l_x/a = 3.8$ data are the same as in Fig. 3. For the larger l_x values the chemical potential was chosen as $\mu = -1.7$ and the parameter γ was varied. The inset shows the dependence of L_C on l_x .

to $\mathcal{O}(N^2L^2)$, where $L \approx l_x/a$. It would be interesting to investigate if this number can be reduced even further, a next possible candidate being $\mathcal{O}(NL^3)$, by studying the structure of the vertex in more detail. This is, however, beyond the scope of this work and we leave this question for further research.

The extended feedback between the channels becomes increasingly important with increasing interaction strength. For $L = 5$, the eCLA yields meaningful, converged results for interaction values for which the $L = 0$ flow obtained by CLA is divergent. This is the case for $U \gtrsim 4\sqrt{\Omega_x\tau}$. Figures 3(d) to 3(f) show the conductance for such large values of interaction and $L = 5$. The qualitative behavior is unchanged w.r.t. smaller values of the interaction, and the quantitative strength of the impact of the interaction increases continuously, in that the width of the spin-split subplateau increases with U .

To shed light on the effect of the enhanced coupling between the channels, we now analyze the resulting two-particle vertex quantitatively, by studying its extremal value

$$\gamma_2^{\text{ext}} = \max_{q'_1 q'_2 q_1 q_2} |\gamma_2(q'_1, q'_2; q_1, q_2)|, \quad (50)$$

where the q 's stand here both for site and spin indices. Furthermore, we identify the two most contributing parts to these value as

$$\begin{aligned} \gamma_x^{\text{ext}} &= \max_{j'_1 j'_2 j_1 j_2} \gamma_x(j'_1 \uparrow, j'_2 \downarrow; j_1 \uparrow, j_2 \downarrow), \\ \gamma_p^{\text{ext}} &= \min_{j'_1 j'_2 j_1 j_2} \gamma_p(j'_1 \uparrow, j'_2 \downarrow; j_1 \uparrow, j_2 \downarrow). \end{aligned} \quad (51)$$

Note that we used the minimum in the definition of γ_p^{ext} , since the γ_p contribution is mainly negative, whereas γ_x is dominated by its positive part. Figure 5 shows these quantities and the conductance as a function of V_g for $L = 0$ and 5. The main message of this figure is that for intermediate interaction strength (solid black curves) the flow converges for both $L = 0$ (left column) and $L = 5$ (right column) and yields qualitatively the same results for the conductance in Figs. 5(a) and 5(b). If, however, one increases the interaction strength further (red solid curves) the flow for $L = 0$ starts to diverge [Figs. 5(c) and 5(e)] and the values of physical observables computed from it become wrong, reflected for example in the kink of the red conductance curve in Fig. 5(a). A good measure for the behavior of the flow is the maximum value of the two-particle vertex, plotted in Figs. 5(c) and 5(d). We see that the kink in the conductance curve corresponds to a very large value of $\gamma_2^{\text{ext}}/U = 58.2$ [lying outside of the range of Fig. 5(c)]. In contrast, for $L = 5$, γ_2^{ext} as well as the conductance stay well behaved and, in fact, the flow converges without problems [Figs. 5(b) and 5(d)]. In order to shed light on this stabilizing effect of the enhanced feedback, we show in Figs. 5(e) and 5(f) the $P^{\uparrow\downarrow}$ and $X^{\uparrow\downarrow}$ part of the channels, which constitute the contributions to γ_2^{ext} with the largest moduli. In the case of intermediate interaction (black curves) the X and P contributions are of the same order of magnitude but differ in their relative sign. If one looks at the completely uncoupled channels, i.e., the pure ladder contributions (cf. the study in Ref. [8]) and increases the interaction strength, the X channel is the first one to diverge. Our interpretation of the stabilizing effect is now as follows. Since the channels are coupled, a slight increase in the modulus of the X channel

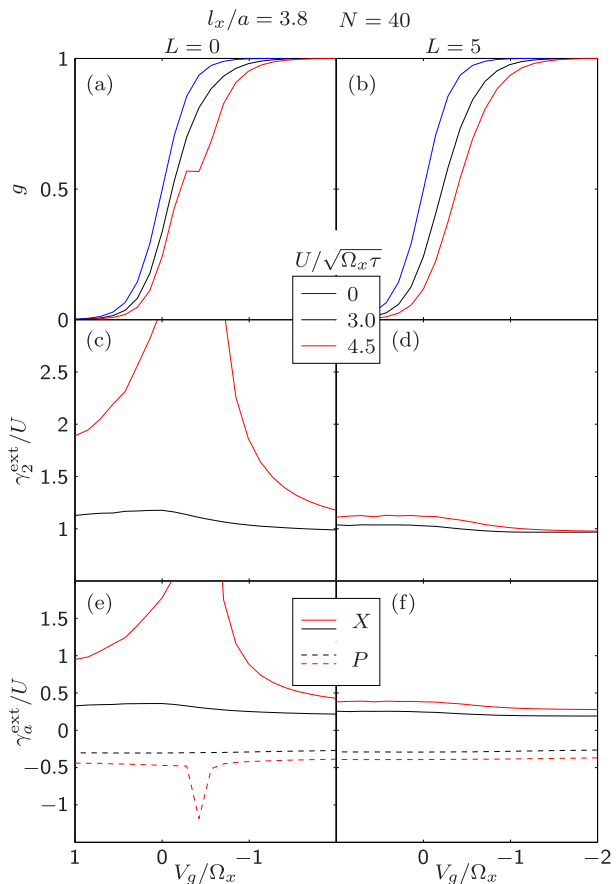


FIG. 5. Conductance and vertex quantities calculated for the two feedback lengths $L = 0$ (left column) and $L = 5$ (right column) with three different effective interaction strengths $U/\sqrt{\Omega_x\tau}$, at zero magnetic field.

leads via the feedback to a slight increase of the modulus of the P channel, and due to their relative sign difference they partially cancel, so that the resulting additional contribution to γ_2 is small. If the effective interaction becomes too strong, this ameliorating effect eventually breaks down and the flow diverges. In the $L = 5$ case, we take much more feedback between the individual channels into account than for $L = 0$ and it is therefore reasonable that the divergence point of the flow is shifted toward larger effective interactions.

D. Crossover between a closed QPC and a QD

As we have seen above, the increase of the feedback length L leads to a more stable fRG flow in regions for high LDOS, corresponding to a large effective interaction strength. This stabilization effect enables us to study parameter regimes that have been hard to treat with previous fRG schemes. We illustrate this below for a situation known to suffer from fRG divergence problems, namely the crossover from a QPC to a QD. In Ref. [19], it was found that when using the CLA (called “fRG2” there), the fRG flow for this transition suffers from divergences if the flat barrier top is too close to the chemical potential. For this reason, it was not possible for fRG2 to smoothly describe how the dot filling increases

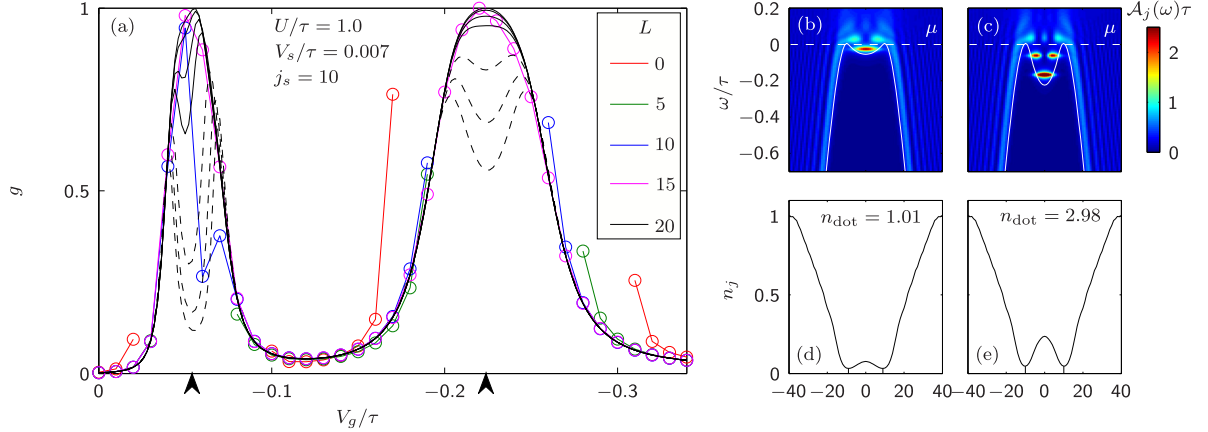


FIG. 6. The crossover from a QPC to a QD. (a) The conductance as a function of gate-voltage V_g , calculated for several magnetic fields (black solid lines: $B = 0, 1, 2, 3 \times 10^{-4}$, black dashed lines: $B = 6, 9, 12 \times 10^{-4}$) with feedback length $L = 20$. Colored symbols indicate the conductance values obtained with smaller feedback lengths. (b) and (c) Noninteracting LDOS (color scale) and barrier shape (solid white curve) for the two gate voltages marked by the left and right vertical arrows in (a), respectively. Horizontal white dashed lines indicate the chemical potential μ . (d), (e) The electron density per site n_j again computed for the two gate voltages indicated in (a). Summing n_j over all sites between the two density minima yields $n_{\text{dot}} = 1.01$ and 2.98.

with decreasing V_g , and the region where no or only a few electrons occupy the dot remained inaccessible within the CLA. The eCLA enables us now to study precisely this interesting region. [In Ref. [19], this regime was treated instead using a simpler fRG scheme without vertex flow (“fRG1”). Although this did qualitatively produce the Kondo physics that is expected if the QD occupancy is odd, Ref. [19] argued that fRG1 is generically less reliable than fRG2. For example, for a QPC geometry, it underestimates the skewing of the zero-temperature conductance step that is characteristic for the 0.7-anomaly. For this reason, the detailed studies of QD-QPC crossovers performed in Ref. [19] were all limited to deep dots, studied using fRG2.]

In Fig. 6(a), we show the conductance curve for the crossover between a closed QPC and a QD, in which the first two bound state levels cross the chemical potential as the dot is made deeper. This level structure is illustrated in Figs. 6(b) and 6(c) where we show the noninteracting LDOS of the dot structure for the two gate voltages indicated by the black markers in Fig. 6(a). Both of these gate voltages lie within regions where the sharp LDOS maximum associated with a bound state near $\omega = \mu$ causes convergence problems if the feedback length L is small, but not if L is chosen sufficiently large, which is possible within the eCLA.

When varying the gate voltage, we can see Kondo plateaus in the conductance arising in the V_g regions where the occupation of the dot is odd. This is illustrated in Figs. 6(d) and 6(e), where we show the site-resolved density, again for the two V_g values indicated in (a). We see that the electrons are localized within the QPC, which here had a width of 20 sites. When the densities within the QPC are integrated, we indeed obtain approximately one electron for the first plateau and three electrons for the second plateau. These Kondo plateaus, caused by Kondo screening of the dot spin, get suppressed with increasing magnetic field since the spin degeneracy is broken. This suppression happens in the first and second Kondo plateau for magnetic fields on the scale $\sim 1 \times 10^{-4}\tau$ (solid black

lines), and $\sim 3 \times 10^{-4}\tau$ (dashed black lines), respectively. A quantitative extraction and analysis of the Kondo scales of the setup is beyond the scope of this paper. Our main purpose here is to illustrate that the finite-ranged feedback of eCLA enables us to treat a parameter regime which was not accessible with previous fRG schemes and produces qualitatively correct Kondo physics. To outline this, we have indicated in Fig. 6(a) how the range of convergence increases with increasing L from 0 to 30. We see that the $L = 0$ method is only convergent in the parameter regimes where the occupancy of the dot is even and hence the conductance is small. By increasing L from 0 over 5 to 10, we see that also the conductance plateaus become more and more visible. At $L = 20$, the whole Kondo plateau is accessible. Upon further increasing the feedback up to $L = 30$ (not shown here), we find that the conductance results for $L = 20$ are already properly converged.

IV. FINITE-RANGED INTERACTIONS

In this section, we consider a model of a QPC with an interaction whose range extends over up to N sites, in contrast to the purely on-site interaction studied in Sec. III. The purpose of this study is to illustrate the potential of the eCLA to deal with finite-ranged interactions in a setting where the screening of a longer-ranged interaction comes into play, and to take a first step towards exploring the physical consequences of screening. We should emphasize, though, that we do *not* aim here to achieve a fully realistic treatment of screening in a QPC. That would require including higher-lying transport modes (we consider just the lowest-lying one), which would go well beyond the scope of the present paper.

Our model is described by the following Hamiltonian:

$$\hat{H} = \sum_{ij\sigma} [E_j^\sigma \hat{n}_{j\sigma} - \tau(d_{j\sigma}^\dagger d_{j+1\sigma} + \text{H.c.})] + \frac{1}{2} \sum_{i,j,\sigma,\sigma'} U_{ij} \hat{n}_{i\sigma} \hat{n}_{j\sigma'} (1 - \delta_{ij} \delta_{\sigma\sigma'}). \quad (52)$$

Here, E_j^σ is chosen as described in Sec. III, and U_{ij} can differ from zero for all sites with separation $|i - j| < L_U$, where L_U determines the bare interaction range. Note that we now also have a bare interaction between electrons with the same spin, which was absent in the on-site case. In the previous section, the interaction strength was controlled by a single value U [cf. Eq. (45)] and treated as a tunable parameter, whose strength was varied by hand. However, now U_{ij} is a matrix with N^2 parameters, and we need to specify its form explicitly. For this, we start with a continuous 3D model of a QPC, and for the Hilbert spaces associated with transverse motion in the y and z directions, we reduce the dimensionality down to one, by taking into account only the ground states of the respective confining potentials, cf. Ref. [28]. In this way, we arrive at a continuous effective theory in 1D for the x direction, which in a last step is discretized using a finite difference method, already applied by BHD in Ref. [8]. We use the resulting model to compute the conductance and the density profile of a QPC, and study their dependence on the screening effects of the long-ranged interaction and the geometric dimensions of the QPC.

A. Derivation of a one-dimensional Hamiltonian

We start from the Hamiltonian $\hat{H} = \hat{H}_0 + \hat{H}_1$ with

$$\begin{aligned}\hat{H}_0 &= \sum_{\sigma} \int d^3r \hat{\Psi}_{\sigma}^{\dagger}(\mathbf{r}) \left(V_{\text{QPC}}(\mathbf{r}) - \frac{\hbar^2}{2m} \nabla^2 \right) \hat{\Psi}_{\sigma}(\mathbf{r}), \\ \hat{H}_1 &= \frac{1}{2} \sum_{\sigma_1, \sigma_2} \int d^3r_1 \int d^3r_2 U(\mathbf{r}_1 - \mathbf{r}_2) \\ &\quad \times \hat{\Psi}_{\sigma_1}^{\dagger}(\mathbf{r}_1) \hat{\Psi}_{\sigma_2}^{\dagger}(\mathbf{r}_2) \hat{\Psi}_{\sigma_2}(\mathbf{r}_2) \hat{\Psi}_{\sigma_1}(\mathbf{r}_1),\end{aligned}\quad (53)$$

where the fermionic field $\hat{\Psi}_{\sigma}^{\dagger}(\mathbf{r})$ creates an electron with spin σ at the continuous position variable \mathbf{r} . The interaction is of screened Coulomb form with screening length l_s and relative dielectric constant κ , which is given in ESU-CGS units by

$$U(\mathbf{r}_1 - \mathbf{r}_2) = \frac{e^2}{\kappa} \left(\frac{1}{|\mathbf{r}_1 - \mathbf{r}_2|} - \frac{1}{\sqrt{|\mathbf{r}_1 - \mathbf{r}_2|^2 + l_s^2}} \right), \quad (54)$$

cf. Hirose *et al.* [29]. This interaction form results from taking image charges on the top gate into account, which is positioned at a distance of $l_s/2$ above the 2DEG. We use a QPC potential given by

$$V_{\text{QPC}}(x, y, z) = \left[\alpha V(x) + m^* \frac{\Omega_y(x)^2 y^2}{\hbar^2} \frac{1}{2} \right] \Delta(z), \quad (55)$$

with $\Omega_y(x) = 2\beta V(x)$, and $m^* = 0.067m_e$ is the effective mass of GaAs. The function $\Delta(z)$ ensures the confinement to the 2DEG and the one-dimensional potential $V(x)$ which enters here is the same as that used in our on-site-model studies, Eq. (38). The QPC potential V_{QPC} has a saddlelike form: it defines a quadratic confinement in y direction with a positive curvature $\Omega_y(x)$ that decreases with increasing $|x|$, whereas the curvature in x direction is negative, with magnitude Ω_x . The confinement in y -direction disappears for $|x| \rightarrow \infty$, where $V(x) = 0$. For the coefficients α and β , we impose the condition $\alpha + \beta = 1$, which turns out to ensure that the effective one-dimensional potential resulting from eliminating the y and z directions is precisely $V(x)$. We

specify the transverse curvature at the center of the QPC to be $\Omega_y = \Omega_y(0)$, thereby fixing the parameter $\beta = \frac{\Omega_y}{2V(0)}$.

We now project onto the ground state subspace for the transverse directions. With this step, taken for the sake of simplicity, we ignore all transport modes except the one contributing to the first conductance step. For a truly realistic description of screening, the higher-lying modes would have to be taken into account, too. This would lead to stronger screening and an effective interaction of shorter range than that obtained below.

Concretely, we thus represent our quantized fields as

$$\hat{\Psi}_{\sigma}(\mathbf{r}) = \phi_x(y) \varphi(z) \hat{\psi}_{\sigma}(x). \quad (56)$$

Here, $\phi_x(y)$ and $\varphi(z)$ are the normalized ground state wave functions of the confining potentials in the y and z directions, respectively,

$$\varphi(z) = \sqrt{\delta(z)}, \quad (57)$$

$$\phi_x(y) = \frac{1}{(2\pi)^{1/4} \sqrt{l_y(x)}} e^{-y^2/(4l_y^2(x))}, \quad (58)$$

and the operator $\hat{\psi}_{\sigma}(x)$ creates an electron in a state with wave function $\delta(x)\phi_x(y)\varphi(z)$. In our 2DEG setup, $\delta(z)$ is a peak of weight one, very narrow compared to the scales in x and y directions, whereas $\phi_x(y)$ is the ground state of a harmonic oscillator with characteristic length

$$l_y(x) = \frac{\hbar}{\sqrt{2m^*\Omega_y(x)}}. \quad (59)$$

With this, we arrive at an effective 1D continuous theory described by the effective 1D Hamiltonian

$$\begin{aligned}\hat{H}_{\text{eff}} &= \sum_{\sigma} \int dx \hat{\psi}_{\sigma}^{\dagger}(x) \left[\frac{\hbar}{2m} \partial_x^2 + (\alpha + \beta)V(x) \right] \hat{\psi}_{\sigma}(x) \\ &\quad + \sum_{\sigma_1, \sigma_2} \int dx_1 dx_2 \frac{U(x_1, x_2)}{2} \hat{\psi}_{\sigma_1}^{\dagger}(x_1) \hat{\psi}_{\sigma_2}^{\dagger}(x_2) \hat{\psi}_{\sigma_2}(x_2) \hat{\psi}_{\sigma_1}(x_1).\end{aligned}\quad (60)$$

We now choose $\alpha + \beta = 1$ as stated above, thus ensuring that the resulting effective one-dimensional potential is indeed given by $V(x)$. The matrix elements of the interaction are given by

$$\begin{aligned}U(x_1, x_2) &= \frac{e^2}{\kappa} \sqrt{\frac{1}{2\pi(l_y^2(x_1) + l_y^2(x_2))}} \\ &\quad \times \left\{ \exp \left[\frac{(x_1 - x_2)^2}{4(l_y^2(x_1) + l_y^2(x_2))} \right] K_0 \left[\frac{(x_1 - x_2)^2}{4(l_y^2(x_1) + l_y^2(x_2))} \right] \right. \\ &\quad \left. - \exp \left[\frac{(x_1 - x_2)^2 + l_s^2}{4(l_y^2(x_1) + l_y^2(x_2))} \right] K_0 \left[\frac{(x_1 - x_2)^2 + l_s^2}{4(l_y^2(x_1) + l_y^2(x_2))} \right] \right\}.\end{aligned}\quad (61)$$

For a typical 2DEG of GaAs-AlGaAs, the relative dielectric constant has the value $\kappa \approx 12.9$. K_0 is the modified Bessel

function of second kind in zeroth order. It diverges logarithmically when its argument approaches zero.

In order to discretize our 1D continuous theory along the x direction, we set $x := a \cdot j$ and replace the continuous field $\hat{\psi}_\sigma(x)$ by the discrete set of operators $d_{j\sigma}$, where a is the lattice spacing and j the site index. This results in a Hamiltonian of the form (52). Treating the second derivative in the kinetic term using a finite difference method, the single-particle part of the Hamiltonian takes the form $H_0 = \sum_{ij\sigma} h_{ij}^\sigma$, with

$$h_{ij}^\sigma = \left(V_i - \frac{\sigma B}{2} \right) \delta_{ij} - \tau (\delta_{i,i+1} + \delta_{i,i-1}), \quad (62)$$

where V_i is just the discretized version of the effective 1D potential, B is the magnetic field, and $\tau = \frac{\hbar^2}{2m^*a^2}$ is the hopping matrix element. We define a discretized form of the interaction by

$$U_{ij} := U(ai, aj), \text{ if } i \neq j; \quad (63)$$

$$U_{ii} := \frac{1}{a^2} \int_{a(i-1/2)}^{a(i+1/2)} dx_1 \int_{a(i-1/2)}^{a(i+1/2)} dx_2 U(x_1, x_2), \quad (64)$$

where we treat the on-site case separately, since $U(x_1, x_2)$ has an integrable singularity as x_1 approaches x_2 . The above treatment presupposes that the transverse wave functions do not change significantly on a scale set by a . If a is much smaller than the characteristic length of the electrostatic potential, the above discretization scheme correctly captures the physical behavior of the continuous theory while regularizing the short distance of the interaction, with $U_{ii} = -\frac{e^2}{\kappa\sqrt{\pi l_s(ai)}} \ln[a/l_s(ai)] + \mathcal{O}(1)$ for $a \rightarrow 0$.

Having arrived at the discretized Hamiltonian (52), let us take a final look at the parameters that characterize our system. From the dimensionful constants \hbar , e^2/κ , and m^* , one can construct an intrinsic length scale $[\frac{\hbar^2}{m^*e^2\kappa}] \approx 10$ nm and intrinsic energy scale $[\frac{m^*e^4}{2\hbar^2\kappa^2}] \approx 5.5$ meV. It is possible to express all our model's length and energy scales in terms of these two dimensionful constants. However, it is often convenient to be able to relate quantities like the gate-voltage dependence of the conductance or the spatial resolution of the density directly to the geometry of the QPC. For this reason, we introduce in our studies below for each QPC a characteristic energy scale $\bar{\Omega}_x$, and a corresponding length scale $\tilde{l}_x = \hbar/\sqrt{2m^*\bar{\Omega}_x}$, which we measure in absolute units and which characterize the mean geometry of the QPC barrier. Concretely, we will take for $\bar{\Omega}_x$ the curvature of the bare barrier at the renormalized conductance pinch-off gate voltage V_g^{po} , where the conductance just begins to increase from zero (and the barrier height is $\varepsilon_F + V_g^{\text{po}}$). All the other geometric quantities are then specified relative to $\bar{\Omega}_x$. To be specific, we will characterize our QPC by the following rescaled dimensionless quantities (denoted by tildes):

$$\begin{aligned} \text{(i)} \quad \tilde{\Omega}_x &= \frac{\bar{\Omega}_x}{\text{meV}}, & \text{(ii)} \quad \tilde{V}_g &= \frac{V_g}{\bar{\Omega}_x}, & \text{(iii)} \quad \tilde{\Omega}_y &= \frac{\bar{\Omega}_y(0)}{\bar{\Omega}_x}, \\ \text{(iv)} \quad \tilde{l}_s &= \frac{l_s}{\tilde{l}_x}, & \text{(v)} \quad \tilde{L}_{\text{bar}} &= \frac{L_{\text{bar}}}{\tilde{l}_x}, & \text{(vi)} \quad \tilde{x} &= \frac{x}{\tilde{l}_x}, \\ \text{(vii)} \quad \tilde{\Omega}_y'' &= \frac{\tilde{l}_x^2}{\bar{\Omega}_x} \left[\frac{\partial}{\partial \tilde{x}} \Omega_y(x) \right]_{x=0}. \end{aligned} \quad (65)$$

$$\begin{aligned} \tilde{\Omega}_x &= 1.05 & \tilde{\Omega}_y &= 1.91 & \tilde{L}_{\text{bar}} &= 6.79 & \tilde{\Omega}_y'' &= -0.060 \\ \tilde{l}_s &: & 2.15 & & 1.72 & & 0.86 \end{aligned}$$

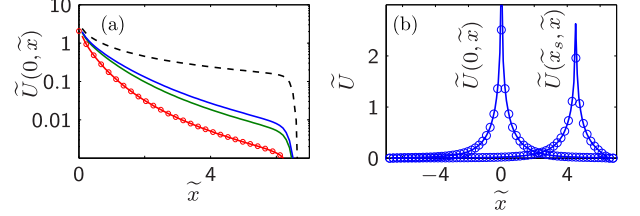


FIG. 7. (a) Distance dependence of the bare interaction $\tilde{U}(0, \tilde{x})$ between an electron located at the QPC center and one at \tilde{x} , plotted on a logarithmic scale, for three values of \tilde{l}_s . The dashed black line shows the limit of $\tilde{l}_s \rightarrow \infty$ and the dots on the lowest curve (red) illustrate the chosen discretization points for the case $N = 61$. (b) $\tilde{U}(0, \tilde{x})$ (central peak) and $\tilde{U}(x_s, \tilde{x})$ (side peak), plotted for $\tilde{l}_s = 2.15$ on a linear scale for both negative and positive \tilde{x} values.

$\tilde{\Omega}_x$ describes the longitudinal barrier curvature in units of meV, \tilde{V}_g the normalized gate voltage, $\tilde{\Omega}_y$ the transverse curvature at the barrier center, \tilde{L}_{bar} the total barrier length which controls the behavior of the flanks, \tilde{x} the longitudinal coordinate, and $\tilde{\Omega}_y''$ the x dependence of the transverse curvature at the barrier center. Note that if one chooses to specify $\tilde{\Omega}_x$, $\tilde{\Omega}_y$, $\tilde{\Omega}_y''$, \tilde{l}_s , and \tilde{L}_{bar} , this implicitly also fixes ε_F : its value has to be chosen in such a way that the resulting curvature at pinchoff has the specified value $\tilde{\Omega}_x$.

It is instructive to express the interaction $U(x_1, x_2)$ of Eq. (61) in terms of the rescaled dimensionless parameters. If we define $U_b = e^2/(\kappa\tilde{l}_x)$, the dimensionless ratio $\tilde{U}(\tilde{x}_1, \tilde{x}_2) = U(x_1, x_2)/U_b$ depends only on the dimensionless parameters (65) (ii)–(vii), but not on $\bar{\Omega}_x$. Thus the dependence of the interaction strength (in absolute units) on the longitudinal curvature $\bar{\Omega}_x$ of the QPC is fully encapsulated in U_b . The corresponding dimensionless parameter

$$\tilde{U}_b = U_b/\bar{\Omega}_x = \frac{\sqrt{2m^*}e^2}{\kappa\hbar} \frac{1}{\sqrt{\bar{\Omega}_x}} \quad (66)$$

characterizes the effective on-site interaction strength at the barrier center for the present long-ranged interaction model, and plays a role analogous to the parameter $U_0^{\text{eff}} = U \cdot \mathcal{A}_0^0(\mu)$ of Eq. (46) (which likewise scales as $1/\sqrt{\bar{\Omega}_x}$) for the on-site interaction model of Sec. III. Evidently, \tilde{U}_b increases with decreasing $\bar{\Omega}_x$, implying that interactions become ever more important the smaller the curvature of the barrier top. Typical values for \tilde{U}_b for the plots below range between 4.2 and 4.9.

The spatial structure of the long-ranged interaction for typical choices for the physical parameters is shown in Fig. 7. In Fig. 7(a), we plotted the dimensionless ratio $\tilde{U}(0, \tilde{x}) = U(0, \tilde{x} \cdot \tilde{l}_x)/U_b$ for three values of the rescaled screening length \tilde{l}_s , as a function of positive $\tilde{x} = x/\tilde{l}_x$. This ratio is independent of $\bar{\Omega}_x$ itself, but increases significantly with increasing screening length. In (b), we again show $\tilde{U}(0, \tilde{x})$ (central peak) and for comparison also $\tilde{U}(x_s, \tilde{x}) = U(x_s \cdot \tilde{l}_x, \tilde{x} \cdot \tilde{l}_x)/U_b$ for fixed $x_s = 4.5$ as a function of \tilde{x} , where the \tilde{x} range contains now the whole QPC. Due to the reflection symmetry of our system about the QPC center, $\tilde{U}(0, \tilde{x})$ is a symmetric

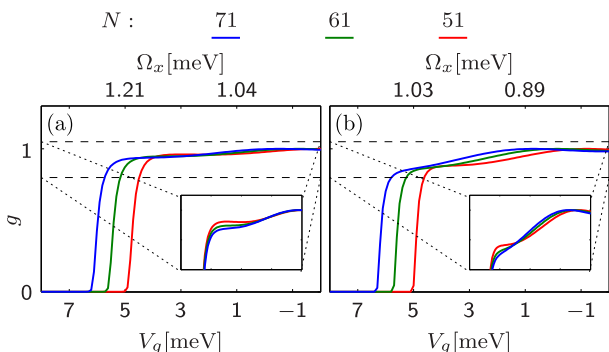


FIG. 8. QPC conductance step shape for three choices of the number of discretization points N (with maximal feedback length $L = N - 1$), for two QPCs with different curvatures. We used the following parameters, in absolute units [cf. Eqs. (38) and (61)]. In (a), $\gamma = 0.85$, $\varepsilon_F = 13.89$ meV, $\Omega_y = 2.35$ meV, $L_{\text{bar}} = 146.11$ nm, and $l_s = 46.17$ nm; and in (b), $\gamma = 0.85$, $\varepsilon_F = 11.00$ meV, $\Omega_y = 2.00$ meV, $L_{\text{bar}} = 158.24$ nm, and $l_s = 50.00$ nm. The insets zoom into the range $g \in [0.8, 1.05]$ and plot g as a function of $V_g - V_g^{\text{po}}$ to align the pinchoffs. When expressed in terms of the dimensionless parameters of Eq. (65), the parameter choices in (a) and (b) differ only in $\tilde{\Omega}_x$. For example, for the middle $N = 61$ curves (green), we obtain for panel (a) $\mathfrak{A} = \{\tilde{\Omega}_x = 1.23, \tilde{\Omega}_y = 1.91, \tilde{L}_{\text{bar}} = 6.79, \tilde{\Omega}_y' = -0.060, \tilde{l}_s = 2.15\}$, and for panel (b), $\mathfrak{B} = \{\tilde{\Omega}_x = 1.05, \tilde{\Omega}_y = 1.91, \tilde{L}_{\text{bar}} = 6.79, \tilde{\Omega}_y' = -0.060, \tilde{l}_s = 2.15\}$.

function of \tilde{x} . In contrast, $\tilde{U}(\tilde{x}_s, \tilde{x})$ is an asymmetric function of \tilde{x} around the point $\tilde{x} = \tilde{x}_s$, decreasing more quickly when $\tilde{x} - \tilde{x}_s$ becomes large positive than large negative, because the transverse potential is wider in the former case. This widening of the transverse potential is also the reason why $\tilde{U}(\tilde{x}_s, \tilde{x})$ as a function of $\tilde{x}_s - \tilde{x}$ with fixed \tilde{x}_s is in general smaller than $\tilde{U}(0, \tilde{x})$ as a function of \tilde{x} .

B. Discretization dependence

We begin our treatment of long-ranged interactions by investigating to what extent our results depend on the number of discretization points N with all other parameters held fixed. Figure 8 shows this dependence for two QPCs whose parameters were chosen to yield somewhat different ranges of Ω_x curvatures. The first point to notice involves the V_g value of the conductance pinchoff: whereas in the absence of interactions it occurs near $V_g = 0$, turning on our long-ranged interactions shifts it towards the left, i.e., towards a larger gate voltage. This behavior is unphysical, since for any fixed V_g at which the density is nonzero, turning on interactions should generate a Hartree barrier that causes the conductance to decrease, not increase. We suspect that this unphysical behavior is an fRG artefact, possibly due to our use of the static approximation. We leave the issue of exploring what will happen when using a dynamic version of our eCLA as a topic for future study. We remark, however, that similar unphysical shift artifacts were encountered in Ref. [8] when comparing various different fRG methods that treated the details of the vertex flow in somewhat different ways. Nevertheless, although the V_g^{po} values of the conductance curves in Ref. [8] depended on methodological details, the overall shape of the

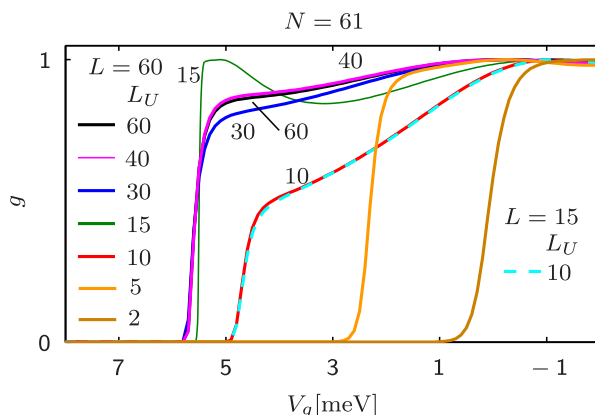


FIG. 9. QPC conductance curves at fixed N , calculated with feedback length $L = N - 1$ for several values of the interaction cutoff L_U (solid lines), and with $L = 15$ for $L_U = 10$ (dashed line). The QPC parameters were chosen as in Fig. 8(b). Note that while convergence in L is rapid, the conductance becomes independent of the cutoff length only for $L_U > 40$. Furthermore, for $L_U \lesssim l_x/a \approx 4.4$, we recover the conductance shape of short-ranged interactions.

conductance steps were essentially the same, i.e., when plotted as functions of $V_g - V_g^{\text{po}}$, they coincided. We find a similar trend here: if we increase N , V_g^{po} increases, because changing N slightly changes the strength and shape of the interaction function U_{ij} , causing corresponding changes in V_g^{po} and Ω_x ; however, the *shape* of the conductance steps in Figs. 8(a) and 8(b) seems at least qualitatively convergent when N increases [cf. insets in (a) and (b)], despite the N dependence of the step's position. For the remainder of this paper we will therefore only address the overall shape of the conductance step.

In Figs. 8(a) and 8(b), we expressed all parameters in terms of absolute units. In most of the remaining plots where physical properties are discussed, we use instead the more convenient dimensionless quantities introduced in Eq. (65) (and denoted by tildes). We have also extracted these dimensionless parameters for Figs. 8(a) and 8(b) and summarized them for further use in the parameter sets \mathfrak{A} and \mathfrak{B} given in the caption of Fig. 8.

In Fig. 8, we used the maximal feedback length $L = N - 1$ to fully take interactions over the whole QPC into account. However, due to numerical costs, this limited the number of sites that could be treated to $N \leq 71$. For this reason, we have also explored using a cutoff length L_U for the interaction range, setting $U_{ij} = 0$ for $|i - j| > L_U$. The resulting conductance curves for different L_U are shown in Fig. 9. We first note that when the cutoff length L_U becomes smaller than the characteristic length $l_x/a \approx 4.4$ of the QPC, we recover the conductance shape for short-ranged interactions. This behavior is analogous to that obtained in Fig. 10 below, when reducing the screening length l_s below l_x . Furthermore, we find rapid convergence when increasing L beyond L_U for a fixed N ; for example, Fig. 9 contains two curves for $L_U = 10$, one computed with $L = 60$ (solid), the other with $L = 15$ (dashed), which essentially coincide. However, the shape of the conductance step becomes independent of L_U only for rather

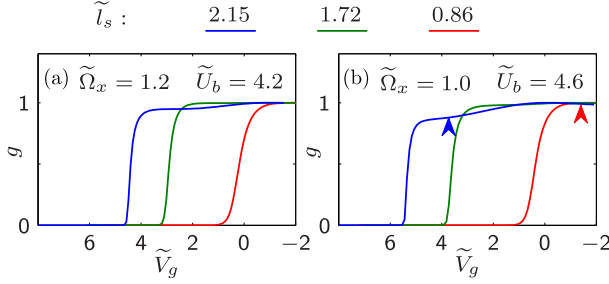


FIG. 10. (a) and (b) The conductance curves corresponding to the interactions depicted in Fig. 7(a), for two different QPC mean curvatures $\tilde{\Omega}_x = 1.2$ and 1.0 , respectively. The arrows at the right (red) $\tilde{l}_s = 0.86$ and the left (blue) $\tilde{l}_s = 2.15$ curve in (b) indicate the gate voltages $\tilde{V}_g = -1.43$ and $\tilde{V}_g = 3.73$ at which the density profiles in Figs. 11(a) and 11(b) were calculated, respectively.

large values of L_U , implying that the tail of the long-ranged interaction actually matters significantly. Therefore, we did not pursue using $L_U < N$ any further and for the remainder of this work show only data obtained without interaction cutoff and with full feedback length, $L = N - 1$.

C. Effects of long-ranged interactions on QPC properties

After these technical considerations, let us now study how the fact that the interaction range is not zero affects the QPC properties. For this, we first briefly discuss the dependence of our finite-ranged interaction on the given physical parameters and then study the resulting consequences on the conductance and the density. As pointed out earlier, this study does not aim to achieve a fully realistic description of screening in a QPC, but rather serves as a first illustration of the potential of the eCLA for treating a model with reasonably long-ranged interactions.

Figures 10(a) and 10(b) show, for two different values of the curvature $\tilde{\Omega}_x$, respectively, three conductance curves corresponding to the three choices of \tilde{l}_s used in Fig. 7(a). For both choices of $\tilde{\Omega}_x$, we obtain an on-site-like conductance step shape when \tilde{l}_s is small. When \tilde{l}_s is increased, i.e., when the amount of screening is reduced, the step shape acquires some additional features, such as the emergence of a “preplateau” at a value of g slightly lower than 1, followed by a much slower increase towards 1 in Fig. 10(a). These features are more pronounced for the longer QPC (i.e., smaller curvature) of Fig. 10(b), where the conductance quickly reaches a preplateau around $g \simeq 0.8$ and thereafter increases much more slowly.

In order to explore the origin of this behavior, we show in Figs. 11(a) and 11(b) two density profiles (thin lines), calculated, respectively, for two fixed parameter choices from Fig. 10(b), indicated in the latter by the right (red) marker for $\tilde{l}_s = 0.86$, $\tilde{V}_g = -1.43$ and the left (blue) marker for $\tilde{l}_s = 2.15$, $\tilde{V}_g = 3.73$. In Fig. 11(b), for which the rescaled screening length \tilde{l}_s is larger, we observe three qualitative changes relative to Fig. 11(a). First, the flanks of the density profile are somewhat steeper. Second, the spatial region in which the density is low has become wider. And third, in this low-density region the density shows some weak density oscillations that are absent in Fig. 11(a).

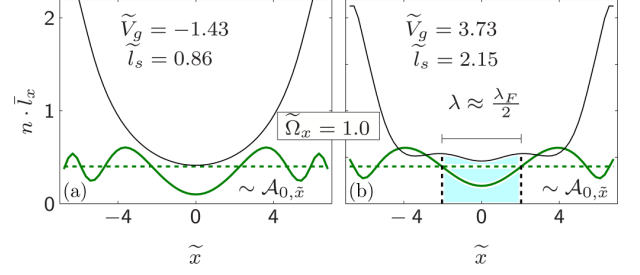


FIG. 11. Density profiles (thin lines) calculated for two fixed parameter choices from Fig. 10, indicated for panels (a) and (b) by the right and left arrows in Fig. 10(b), respectively. For comparison, the thick lines depict (a vertically rescaled version of) the imaginary part of the interacting single-particle propagator at the chemical potential, $\mathcal{A}_{0,\tilde{x}} = -\frac{1}{\pi\tilde{l}_x} \text{Im} G_{0,\tilde{x}}^R(\omega = 0)$. Horizontal dashed lines indicate where $\mathcal{A}_{0,\tilde{x}} = 0$. In (b), the distance between the two density maxima (marked by the dashed vertical lines) is $\lambda = 3.62\tilde{l}_x$. This agrees well with two estimates of $\lambda_F/2$, either from the distance between the two central zeros of $\mathcal{A}_{0,\tilde{x}}$ finding $\lambda_F/2 = 3.82\tilde{l}_x$ or from the mean density \bar{n} in the center of the QPC (shaded region) finding $\lambda_F/2 = 3.55\tilde{l}_x$.

The first two features suggest that the long-range interactions have generated a renormalized barrier whose shape has a flatter top and steeper flanks than the bare parabolic barrier. This flattening occurs because the bare density is larger in the flanks than near the center, hence the upward Hartree-type shift of the barrier potential, which is proportional to the bare density, is larger in the flanks than near the center. The upward renormalization in the flanks becomes stronger the larger the interaction range, because then the upward Hartree-type shift at a given site is determined by a weighted average of the density over a range of nearby sites (whose extent is set by the screening length), and since the bare density profile is convex, the sites in the flanks contribute more strongly.

To shed further light on the third feature, namely the weak density oscillations in the low-density region, we compare their oscillation period with estimates for the “local Fermi wavelength” λ_F at the QPC center, which can be extracted from either the interacting Green’s function or the mean density in the center of the QPC. To illustrate the first method, the thick lines in Figs. 11(a) and 11(b) indicate the oscillatory behavior of $\mathcal{A}_{0,\tilde{x}} = -\frac{1}{\pi\tilde{l}_x} \text{Im} G_{0,\tilde{x}}^R(\omega = 0)$. For a homogeneous system, the Green’s function oscillates with period λ_F , and likewise we can here define an effective $\lambda_F/2$ in the middle of the QPC by taking the distance between the two central zeros of the thick line. For Fig. 11(b), the position of these two zeros is in good agreement with the position of the density maxima of the QPC (indicated by the two dashed vertical lines), whereas the density in Fig. 11(a) shows no features on the scale of λ_F . An alternative way to extract an effective λ_F is to calculate the mean density \bar{n} in the center of the QPC between the two density maxima (shaded region in Fig. 11), and use $\lambda_F = 2\pi/k_F = 4/\bar{n}$. For Fig. 11(b), the first method yields $\lambda_F/2 = 3.82\tilde{l}_x$, and the second $\lambda_F/2 = 3.55\tilde{l}_x$, which are both in reasonable agreement with each other and the distance $\lambda = 3.62\tilde{l}_x$ between the two density maxima. Thus we conclude that the period of the density oscillations observed

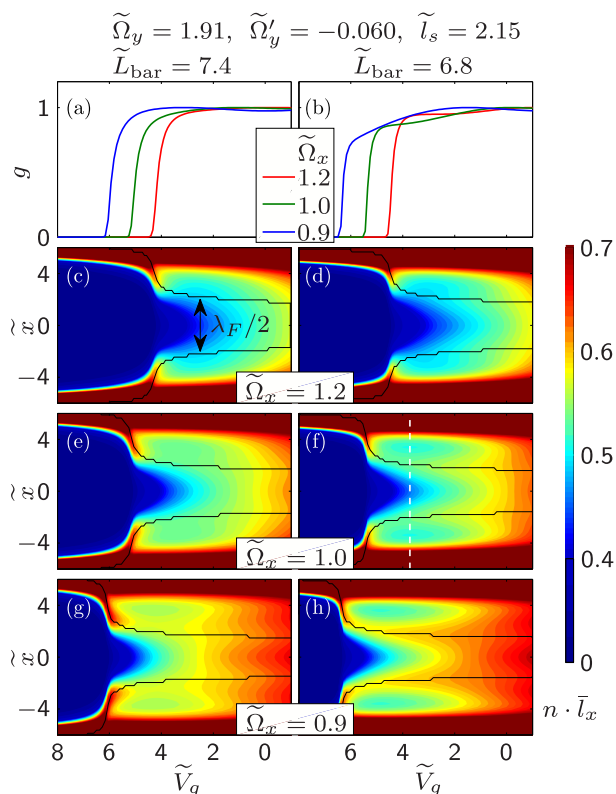


FIG. 12. Study of two QPCs with different \tilde{L}_{bar} , for three choices of $\tilde{\Omega}_x$. The other dimensionless parameters were chosen the same as in \mathfrak{B} [cf. caption of Fig. 8]. (a) and (b) Conductance as function of gate voltage and (c)–(h) density as function of position and gate voltage. While the conductance changes its shape for both QPCs, the shorter one (b) shows stronger features, preeminently a shoulder in the conductance step. In the density, both QPCs show the development of oscillations with approximate wavelength $\lambda_F/2$, which is determined by the Green's function as in Fig. 11 and indicated by the distance between the black lines. In the last plots (g) and (h), the density oscillations transition at smaller gate voltages from two to three maxima. The cut along the dashed white line in (f) is precisely the density profile plotted in Fig. 11(b).

here can be associated with $\lambda_F/2$, or equivalently wave number $2k_F$.

In Fig. 12, we examine this behavior more systematically, using two QPCs having a comparatively long screening length of $\tilde{l}_s = 2.15$, but which differ slightly in \tilde{L}_{bar} , i.e., in their total barrier length. For both QPCs, the conductance step [Figs. 12(a) and 12(b)] changes its shape with decreasing curvature $\tilde{\Omega}_x$ and for the right QPC with smaller \tilde{L}_{bar} develops additional pronounced features in the plateau region. In Figs. 12(c)–12(h), we show the corresponding densities (color scale) as functions of gate voltage and longitudinal position, and find that with decreasing curvature $\tilde{\Omega}_x$ the density develops oscillations. The period of these oscillations is again set by $\lambda_F/2$, which is indicated in Figs. 12(c)–12(h) by the distance between the black lines. While for the right QPC the two density maxima follow very accurately the black lines, in the left QPC they lie slightly further apart than $\lambda_F/2$. The reason

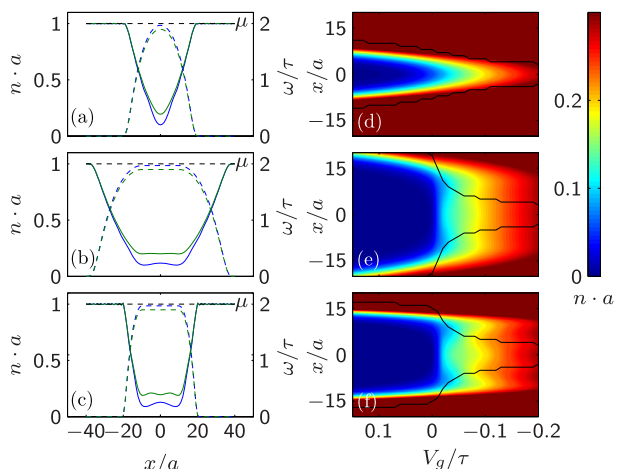


FIG. 13. (a)–(c) Barrier shapes (dashed lines) and corresponding noninteracting densities (solid lines) for almost open QPCs with (a) a parabolic barrier top, (b) a flat barrier top with wide flanks, (c) and a flat barrier top with steep flanks. (d)–(f) Density profiles corresponding to these three barrier shapes, plotted as functions of position and gate voltage. In these plots, $\lambda_F/2$ is again indicated by the distance between the black lines. The flat barrier top with steep flanks of panel (c) yields pronounced Friedel oscillations in the density profile shown in (f), which resemble the density oscillations caused by the long-range interaction in the open regime of the QPCs of Figs. 12(e)–12(h). This suggests that for the latter, the renormalized barriers have a rather flat tops with steep flanks.

for this might be that the left QPC is slightly longer (\tilde{L}_{bar} is larger), giving the electrons in the center more space to form the two repelling density maxima, but not enough space to fit a third density maximum into the available region. In summary, we find that when increasing the geometric proportions of the QPC compared to the scale set by the interactions, i.e., when decreasing $\tilde{\Omega}_x$, the conductance develops additional features in the plateau region, and simultaneously density oscillations arise on a scale set by $\lambda_F/2$.

We interpret the $2k_F$ density oscillations seen in Fig. 11(b) as Friedel oscillations generated by the inhomogeneity induced by the renormalized QPC potential. A similar interpretation was evoked in Iqbal *et al.* [30] where they also found a wavelength $\lambda_F/2$, or equivalently a wave number of $2k_F$, for their spin polarized, emergent localized states (ELS) obtained from SDFT calculations in long QPCs.

To support this interpretation, we show in Figs. 13(a)–13(c) some density profiles (solid lines) obtained for a QPC model of *noninteracting* electrons traversing a QPC, comparing three different barrier shapes (dashed lines): (a) a parabolic top, (b) a flat top with a slow transition to broad flanks, and (c) a flat top with a rather quick transition to steep flanks. For a given gate voltage, the overall shape of the density profile mirrors that of the barrier top for all three cases. Moreover, pronounced additional density oscillations arise for case (c). Panels (d) to (f) show the corresponding evolution of such density profiles with gate voltage. For gate voltages where the QPC is sufficiently open that the density in the center is not very low, the density oscillations seen in Figs. 13(c) and

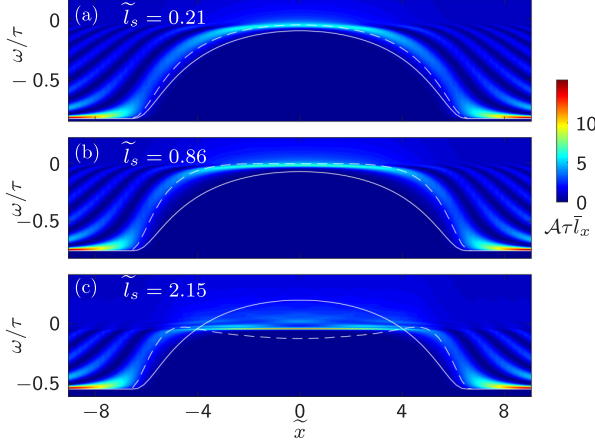


FIG. 14. Interacting LDOS in the static approximation [Eq. (67)], shown as function of position and energy (color scale), for three different values of the screening length \tilde{l}_s . Solid white lines show the bare potential V_j and dashed white lines $V_j + \Sigma_{jj}$, as functions of position. The physical parameters used for this plot correspond to those of Fig. 10(b), with the gate voltage was set to $\tilde{V}_g = -1.91$ in (a), $\tilde{V}_g = -1.43$ in (b), and $\tilde{V}_g = 3.73$ in (c). (The latter two correspond to the red and blue markers in Fig. 10.) The shape of the band bottom reflects that of the renormalized barrier. (The fact that the renormalized barrier top lies *below* the bare barrier top in (c) is due to the artifact of static fRG discussed in Sec. IV B.)

13(f) are reminiscent, respectively, of those seen in Figs. 11(b) and 12(c)–12(h) for QPCs with interactions whose range is longer than the characteristic QPC length (i.e., with $\tilde{l}_s > 1$). This supports the interpretation offered above that such QPCs indeed have renormalized barriers with rather flat tops and steep flanks. However, for higher gate voltages where the QPC is beginning to close off and the density in the center becomes very low, we see a qualitative difference between the density profiles shown in Fig. 13(f) and those of Figs. 12(c)–12(h): the former shows a weak density maximum, whereas the latter do not, because in the regime of very low densities, the Hartree-type renormalization of the barrier shape is not yet strong enough to generate a flattish barrier top.

To further explore our hypothesis concerning the occurrence of a renormalized barrier with a flattened top and steep flanks, we have studied the influence of the screening length, \tilde{l}_s , on the interacting LDOS in the static approximation,

$$\mathcal{A}_j(\omega) = -\frac{1}{\pi} \text{Im} G_{jj}(\omega + i0^+) = -\frac{1}{\pi} \text{Im}[\omega - h^0 - \Sigma]_{jj}^{-1}, \quad (67)$$

where $h_{ij}^0 = \delta_{ij} V_j - \tau[\delta_{i,j+1} + \delta_{i,j-1}]$ is the bare single-particle Hamiltonian, and Σ_{ij} is the static self-energy at the end of the RG flow [31]. Figure 14 shows the LDOS (color scale) as a function of position and energy, for three values of the screening length, \tilde{l}_s . We interpret the shape of the effective band bottom as indicative of the shape of the effective barrier. We observe that with increasing \tilde{l}_s , the effective barrier top indeed does become strikingly flat over an extended region of space centered on the middle of the QPC, ending in rather steep flanks, as anticipated above.

For comparison, solid white lines show the bare potential V_j with its parabolic top. Moreover, dashed white lines show $V_j + \Sigma_{jj}$, to illustrate the contribution of the diagonal elements of the self-energy to the renormalization of the potential barrier. However, while $V_j + \Sigma_{jj}$ does show a trend toward barrier flattening with increasing screening length, for the largest \tilde{l}_s value [Fig. 14(c)], it leads to a shallow local minimum at $\tilde{x} = 0$, reminiscent of a QD-like barrier shape. To correctly capture the shape of the band bottom, which shows no such local minimum, the off-diagonal elements of the self-energy have to be taken into account, too. This is done when computing the LDOS according to Eq. (67), which involves inverting the entire matrix $\omega - h^0 - \Sigma$ before taking diagonal elements. The above results show that long-range interactions can have a rather striking flattening effect on the effective barrier shape, and that long flat barriers lead to interesting density oscillations. It would thus be interesting to study the geometric crossover from a QPC to a homogeneous wire obtained by making the QPC length \tilde{l}_x very long, or by using flat-topped bare barriers of increasing width. In a paper by Schulz [32], concerning Wigner crystal physics in 1D, it was predicted that in a homogeneous 1D model with long-ranged Coulomb interactions in the low-density limit, the density-density correlator $\langle \rho(x)\rho(0) \rangle$ contains both $2k_F$ and $4k_F$ oscillations. The latter decay more slowly with x , and are argued by Schulz to lead to a Wigner crystal in a homogeneous system. During the aforementioned geometric crossover from a QPC to a long wire, well-developed $4k_F$ density oscillations can be expected to emerge, which could be regarded as precursors for the formation of a Wigner crystal. A systematic study of this behavior would be extremely interesting, but falls beyond the scope of this paper and is left for future study. In particular, future work would have to incorporate screening also due to higher transport channels, leading to a shorter-ranged interaction, so that the effects discussed above would likely turn out to be somewhat less pronounced than found here.

V. CONCLUSION AND OUTLOOK

Building on previous works [7,8], we have introduced an improved approximation scheme for third-order truncated fRG. We use an extended coupled ladder approximation (eCLA), splitting the fRG-flow into three channels depending on the internal index structure. When treated independently, each of these channels behaves as in the random phase approximation. The complexity of the eCLA scheme depends on the amount of feedback admitted between the individual channels. For the frequency dependence, we only used static feedback between the channels. In order to control the amount of feedback in the spatial structure, we have introduced the feedback length L . In the case $L = 0$, we get the minimal feedback between the channels, corresponding to the CLA of previous works [8], whereas for $L \rightarrow N - 1$ we recover the full spatial vertex flow in second order.

For actual computations, we restricted ourselves to static fRG, i.e., in addition to using only a static feedback between the channels we also neglected the frequency dependence of the vertices altogether. In this additional approximation, we calculated the zero-temperature Green's function at the

chemical potential, which is the relevant quantity in order to compute the linear conductance of the system.

We first applied our new method to a QPC model with on-site interactions, which has extensively been studied in the past. Here, we observed that the longer-ranged feedback leads to a quantitative but not qualitative change as long as both methods are convergent for the respective parameters. In particular, we observed for barriers with characteristic lengths between 4–10 sites that convergence in L is achieved once L becomes comparable to l_x . Additionally, we observed that the enhanced feedback stabilizes the fRG flow and therefore leads also to convergence in parameter regimes which could not be studied with the $L = 0$ method. To illustrate this increased stability, we studied QPC-QD crossovers analogous to those discussed by Heyder *et al.* in Ref. [19] using the CLA. There, the convergence of the fRG flow suffers especially from the high LDOS at the chemical potential that occurs during the crossover when the barrier top becomes flat in an extended region close to the chemical potential. Our stabilized flow, however, enabled us to study this type of transition. In particular, we succeeded to study regimes of very shallow dots, containing only a few electrons, and observed the Kondo plateau in the conductance expected for such dots.

Finally, in order to test the full potential of our improved feedback, we applied it to a QPC with finite-ranged interactions. The most striking observation was that for a relatively flat QPC in the regime of low density and sufficiently long-ranged interactions, the conductance reaches a preplateau somewhat *below* $g = 1$ (before slowly climbing towards $g = 1$), accompanied by the onset of oscillations in the density. The wavelength of these density oscillations was determined to be approximately $\lambda_F/2$, admitting an interpretation as Friedel oscillations arising from a renormalized barrier shape with a rather flat top and steep flanks. This behavior is consistent with that observed by Iqbal *et al.* [30] in SDFt calculations for their emergent localized states (ELS) in a spin-polarized QPC.

It would be of great interest to explore these type of effects more systematically in the future, within a more realistic model that incorporates the effects of higher transport modes when deriving the effective screened interaction for the lowest-lying transport mode. In particular, the geometric crossover between a QPC potential and a homogeneous quantum wire, expected to show Wigner crystallization, could be explored in this fashion. However, it remains to be seen whether fRG will be able to cope with the truly homogeneous limit; such a study will presumably also have to employ tools more powerful than fRG, such as the density matrix renormalization group.

By way of an outlook to future technical fRG developments, let us remark that it would be desirable to find ways of avoiding an fRG artifact that is present in our results: upon turning on a long-ranged interaction, the position of the conductance step shifts not to smaller gate voltages, as physically expected, but to larger ones. We suspect that this artefact results from our use of static fRG. A next possible step to remedy this problem could be to change from static to dynamic fRG, i.e., to implement the frequency dependence of the vertices. Moreover, it would also be possible to use our enhanced feedback scheme in the context of Keldysh fRG, which is additionally able to treat the temperature dependence and nonequilibrium behavior of QPCs. This would be numerically challenging since the Keldysh scheme in the $L = 0$ implementation is already very costly by itself. However, one might profit from the fact that the most expensive part of the Keldysh calculation scales with $\mathcal{O}(L^2)$, and not with $\mathcal{O}(L^3)$ as in our case. Work in that direction is currently in progress.

ACKNOWLEDGMENTS

We thank Jan Heyder, Volker Meden, Yigal Meir and Dennis Schimmel for very helpful discussions. We acknowledge support from the DFG via SFB-631, SFB-TR12, De730/4-3, and the Cluster of Excellence Nanosystems Initiative Munich.

-
- [1] W. Metzner, M. Salmhofer, C. Honerkamp, V. Meden, and K. Schönhammer, *Rev. Mod. Phys.* **84**, 299 (2012).
 - [2] S. Andergassen, T. Enss, C. Karrasch, and V. Meden, in *Lecture Notes in Physics Vol. 645*, edited by B. Barbara, Y. Imry, G. Sawatzky, and P. C. E. Stamp (Springer-Verlag, Berlin, 2008), p. 1.
 - [3] C. Karrasch, T. Enss, and V. Meden, *Phys. Rev. B* **73**, 235337 (2006).
 - [4] S. G. Jakobs, M. Pletyukhov, and H. Schoeller, *Phys. Rev. B* **81**, 195109 (2010).
 - [5] C. Karrasch, Master's thesis, Georg-August Universität Göttingen (2006); [arXiv:cond-mat/0612329v1](https://arxiv.org/abs/cond-mat/0612329v1).
 - [6] C. Karrasch, *The Functional Renormalization Group for Zero-Dimensional Quantum Systems in and out of Equilibrium*, Ph.D. thesis, RWTH Aachen (2010).
 - [7] F. Bauer, J. Heyder, E. Schubert, D. Borowsky, D. Taubert, B. Bruognolo, D. Schuh, W. Wegscheider, J. von Delft, and S. Ludwig, *Nature (London)* **501**, 73 (2013).
 - [8] F. Bauer, J. Heyder, and J. von Delft, *Phys. Rev. B* **89**, 045128 (2014).
 - [9] C. Karrasch, R. Hedden, R. Peters, T. Pruschke, K. Schnhammer, and V. Meden, *J. Phys.: Condens. Matter* **20**, 345205 (2008).
 - [10] Y. Meir, *J. Phys.: Condens. Matter* **20**, 164208 (2008).
 - [11] C. Sloggett, A. I. Milstein, and O. P. Sushkov, *Eur. Phys. J. B* **61**, 427 (2008).
 - [12] K. Aryanpour and J. E. Han, *Phys. Rev. Lett.* **102**, 056805 (2009).
 - [13] B. J. van Wees, H. van Houten, C. W. J. Beenakker, J. G. Williamson, L. P. Kouwenhoven, D. van der Marel, and C. T. Foxon, *Phys. Rev. Lett.* **60**, 848 (1988).
 - [14] D. A. Wharam, T. J. Thornton, R. Newbury, M. Pepper, H. Ahmed, J. E. F. Frost, D. G. Hasko, D. C. Peacock, D. A. Ritchie, and G. A. C. Jones, *J. Phys. C* **21**, L209 (1988).
 - [15] M. Büttiker, *Phys. Rev. B* **41**, 7906 (1990).
 - [16] K. J. Thomas, J. T. Nicholls, M. Y. Simmons, M. Pepper, D. R. Mace, and D. A. Ritchie, *Phys. Rev. Lett.* **77**, 135 (1996).

- [17] N. J. Appleyard, J. T. Nicholls, M. Pepper, W. R. Tribe, M. Y. Simmons, and D. A. Ritchie, *Phys. Rev. B* **62**, R16275 (2000).
- [18] S. M. Cronenwett, H. J. Lynch, D. Goldhaber-Gordon, L. P. Kouwenhoven, C. M. Marcus, K. Hirose, N. S. Wingreen, and V. Umansky, *Phys. Rev. Lett.* **88**, 226805 (2002).
- [19] J. Heyder, F. Bauer, E. Schubert, D. Borowsky, D. Schuh, W. Wegscheider, J. von Delft, and S. Ludwig, *Phys. Rev. B* **92**, 195401 (2015).
- [20] F. Bauer, *Microscopic Origin of the 0.7 Anomaly in Quantum Point Contacts*, Ph.D. thesis, LMU-München (2014).
- [21] S. G. Jakobs, V. Meden, and H. Schoeller, *Phys. Rev. Lett.* **99**, 150603 (2007).
- [22] C. Husemann and M. Salmhofer, *Phys. Rev. B* **79**, 195125 (2009).
- [23] T. R. Morris, *Int. J. Mod. Phys. A* **09**, 2411 (1994).
- [24] J. Dormand and P. Prince, *J. Comput. Appl. Math.* **6**, 19 (1980).
- [25] J. Kondo, *Prog. Theor. Phys.* **32**, 37 (1964).
- [26] S. Datta, *Electronic Transport in Mesoscopic Systems*, Cambridge Studies in Semiconductor Physics and Microelectronic Engineering (Cambridge University Press, Cambridge, 1997).
- [27] O. Goulko, F. Bauer, J. Heyder, and J. von Delft, *Phys. Rev. Lett.* **113**, 266402 (2014).
- [28] A. M. Lunde, A. D. Martino, A. Schulz, R. Egger, and K. Flensberg, *New J. Phys.* **11**, 023031 (2009).
- [29] K. Hirose, Y. Meir, and N. S. Wingreen, *Phys. Rev. Lett.* **90**, 026804 (2003).
- [30] M. J. Iqbal, R. Levy, E. J. Koop, J. B. Dekker, J. P. de Jong, J. H. M. van der Velde, D. Reuter, A. D. Wieck, R. Aguado, Y. Meir, and C. H. van der Wal, *Nature (London)* **501**, 79 (2013).
- [31] As a technical caveat, we note that *static* fRG is expected to be less reliable than dynamic fRG for quantities computed at $\omega \neq 0$, hence it would be highly desirable to repeat this calculation using Keldysh fRG. Work along these lines is currently in progress.
- [32] H. J. Schulz, *Phys. Rev. Lett.* **71**, 1864 (1993).

4 0.7-analog in quantum point contacts

4.1 Overview

This section contains our publication investigating the 0.7-analog structure appearing at the intersection of the opposite spin components of different subbands at large magnetic fields [GTP⁺03, GTP⁺04]. Similar to the 0.7-anomaly, the 0.7-analog structure has been declared an effect of spontaneous spin polarization [GTP⁺03, GTP⁺04, BJY05]. This claim is based on DFT studies, in a similar way as discussed earlier for the 0.7-anomaly in Sec. 1.3. Here, we instead investigate the 0.7-analog from the viewpoint of the van-Hove ridge scenario developed in [BHS⁺13].

For this, we apply our devised eCLA scheme to a QPC model with two subbands, consisting of two interacting (intra and inter band) tight binding chains with a QPC barrier and an imposed external energy offset. This can be achieved via a simple mapping of the two chain model onto a single chain model (of double length) with modified hopping and interaction terms. Since in our eCLA approach the spatial and the spin structure of the bare interaction can be adjusted freely, this requires no change of the fRG implementation used in Sec. 3.2.

In the results part of this paper, we first consider a setup with magnetic fields comparatively small to the band energy offset. We find that the second conductance step is (i) more symmetric than the first step, indicating that the interactions within the second subband are screened by the first subband, and (ii) broadened due to an increasing Hartree shift from the continued filling of the first subband. This second effect is especially important, since it will be responsible for an asymmetry occurring in the magnetic field dependence of the 0.7 analog.

In the second part, we increase the magnetic field until the opposite spin components of the first and the second subband intersect, and study the magnetic field dependence of the 0.7-analog arising at this intersection. Starting from a simple setup with all interactions (intra and inter band) chosen equally, we work our way to a realistic situation, with an appropriate choice of the relative interaction strengths between and within the subbands. With a realistic choice of the relative interaction strengths, we are able to reproduce the noticeable asymmetry occurring in the experimental magnetic field dependence of the conductance at the 0.7-analog. When approached from higher magnetic fields, the 0.7-structure of the analog is much more pronounced than when approached from lower magnetic fields. Aided by our fRG calculations, we are able to pinpoint the cause of this asymmetry to the different intra and inter band interaction strengths. Based on this insight, we can explain the underlying mechanism of this asymmetry using a simple Hartree picture, revealing that it is based on a similar effect as the broadening in (ii).

4.2 Functional renormalization group treatment of the 0.7 analog in quantum point contacts

by

Lukas Weidinger,¹ Christian Schmauder,¹ Dennis H. Schimmel, and Jan von Delft¹

¹ Physics Department, Arnold Sommerfeld Center for Theoretical Physics and Center for NanoScience, Ludwig-Maximilians-Universität München, 80333 München, Germany

reprinted on pages [103–110](#)

Phys. Rev. B. **98**, 115112 (2018),

DOI: [10.1103/PhysRevB.98.115112](https://doi.org/10.1103/PhysRevB.98.115112).

with permission from

© 2018 American Physical Society

Functional renormalization group treatment of the 0.7 analog in quantum point contacts

Lukas Weidinger, Christian Schmauder, Dennis H. Schimmel, and Jan von Delft
 Arnold Sommerfeld Center for Theoretical Physics and Center for NanoScience,
 Ludwig-Maximilians-Universität München, Theresienstrasse 37, D-80333 München, Germany



(Received 17 May 2018; published 7 September 2018)

We use a recently developed fRG method (extended Coupled-Ladder Approximation) to study the 0.7 analog in quantum point contacts, arising at the crossing of the first and second band at sufficiently high magnetic fields. We reproduce the main features of the experimentally observed magnetic field dependence of the conductance at the 0.7 analog, using a QPC model with two bands and short-range interactions. In particular, we reproduce the fact that this dependence is qualitatively different, depending on whether the analog is approached from higher or lower magnetic fields. We show that this effect can be explained qualitatively within a simple Hartree picture for the influence of the lowest electrons.

DOI: [10.1103/PhysRevB.98.115112](https://doi.org/10.1103/PhysRevB.98.115112)

I. INTRODUCTION

In quasi-one-dimensional structures, such as quantum wires or quantum point contacts (QPCs), an in-plane magnetic field induces a Zeeman splitting of different spin subbands. When this splitting equals the one-dimensional level spacing introduced by the lateral confinement of the structure, one finds crossing features similar to the 0.7 anomaly, as observed at zero magnetic field. Therefore, these features are called 0.7 analogs [1]. The most prominent of these 0.7 characteristics is the development of a shoulderlike structure in the conductance with increasing magnetic fields. In Fig. 1, one can see this shoulder in the original 0.7 regime (dashed ellipse) as well as the similar feature at the 0.7 analog (solid ellipse). The apparent similarities have intertwined the explanation attempts of 0.7 anomaly and 0.7 analogs, prominently featuring spontaneous spin-polarization [2], and quasilocalized states [3].

However, despite observed similarities, there are also features specific to the 0.7 analog that have no counterpart for the 0.7 anomaly. A striking example is the asymmetry in the magnetic field dependence of the conductance, depending on whether the analog is approached from higher or lower fields, see Fig. 1, which is an annotated version of Fig. 1 in Ref. [1]. While the 0.7 analog resembles the 0.7 anomaly at higher magnetic fields (green curve), the conductance curves at lower fields (red curve) are much more symmetric and show no sign of a 0.7 shoulder.

Some years ago, an interpretation of the 0.7 anomaly was introduced in Ref. [4] that traces its origins back to the structure of the noninteracting van Hove ridge in the local density of states. This interpretation has been supported by direct conductance calculations of the QPC via the functional renormalization group (fRG). Following this approach, we use here a recently developed extended coupled-ladder approximation (eCLA) fRG scheme [5] to study the features of the 0.7 analog at the crossing of the $1\uparrow$ and $2\downarrow$ spin subbands of a QPC, working out the similarities and differences between 0.7 analog and 0.7 anomaly.

We argue that the 0.7 analog physics can be explained in a similar manner as the 0.7 anomaly, evoking a smeared van Hove singularity in the local density of states. However, the effects of the electrons in the lowest spin subband are of critical importance. We demonstrate that these electrons cause the above-mentioned asymmetry in the magnetic field dependence of the conductance and study its dependence on the ratio of intra- to interband interaction strength.

II. THEORETICAL MODEL AND METHOD

A. Model

Since our goal is a qualitative understanding of the 0.7 analog physics, we use here the simplest model that should be able to give us the relevant features. We model the lowest two bands of the QPC via one-dimensional spinful tight-binding chains with an intra- and interband short-ranged interaction. The external magnetic field is modeled by a Zeeman term, splitting the energies of spin up and spin down electrons. We point out that, in experiments, one observes additionally to the Zeeman effect also a diamagnetic shift with increasing magnetic field. This shift is understood analytically [6], and is expected not to be relevant for the qualitative physics of interest here [1]. Therefore, we will omit this effect in the present qualitative study, and concentrate on the physics caused by the interactions. Our Hamiltonian will thus be of the form

$$H = -\tau \sum_{i,s,\sigma} [c_{i,s\sigma}^\dagger c_{i+1,s\sigma} + \text{H.c.}] + \sum_{i,s,\sigma} V_{i,s\sigma} n_{i,s\sigma} + \sum_{i,s} U_{i,s}^{\text{intra}} n_{i,s\uparrow} n_{i,s\downarrow} + \sum_{i,\sigma_1,\sigma_2} U_i^{\text{inter}} n_{i1\sigma_1} n_{i2\sigma_2}, \quad (1)$$

where $c_{i,s\sigma}$ annihilates an electron at site i in band s with spin $\sigma \in \{+, -\} = \uparrow, \downarrow$, and $n_{i,s\sigma} = c_{i,s\sigma}^\dagger c_{i,s\sigma}$ is the corresponding number operator. In our calculations, we will use the hopping amplitude τ as unit of energy, i.e., we measure the on-site energy, $V_{i,s\sigma}$, as well as the intraband interaction, $U_{i,s}^{\text{intra}}$, and the interband interaction, U_i^{inter} , in units of τ . Within a

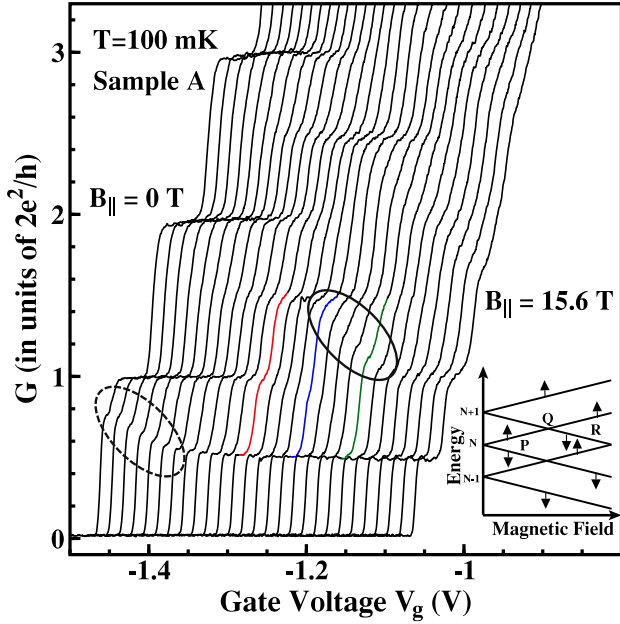


FIG. 1. Figure 1 of Ref. [1] with some additional annotations. As a guide for the eye, we colored three curves: The analog (blue) of the zero-field conductance step as well as two curves at magnetic fields $\Delta B = \pm 2.4 T$ above (green) and below (red) of the analog of the zero-field conductance step. The 0.7 anomaly is indicated by the dashed ellipse, that of its analog by the solid one. Clearly this 0.7-like behavior is only present if the analog is approached from above.

central region, $i \in [-N, N]$, we use the following form for the potential term:

$$V_{is\sigma} = V_g \exp\left[-\frac{(i/N)^2}{1 - (i/N)^2}\right] + V_s^{\text{off}} + \sigma \frac{B}{2}. \quad (2)$$

Here the first summand leads to a quadratic barrier top in the middle of the QPC with curvature $\Omega_x = 2\sqrt{V_g\tau}/N$ and corresponding characteristic length $l_x = a\sqrt{\tau/\Omega_x}$, with a being the lattice constant. The second term constitutes the band offset (we choose $V_1^{\text{off}} = 0$, and therefore use the abbreviation $V^{\text{off}} := V_2^{\text{off}}$) and the third term is the Zeeman splitting. To illustrate these settings, we have plotted the potential structure in Fig. 2.

Analogous to Ref. [4], we take both V_g as well as U_{is}^{intra} , and U_i^{inter} to be zero outside of the central region, where we thus have two noninteracting tight-binding leads with the site independent energy offset

$$V_{is\sigma} = V_s^{\text{off}} + \sigma \frac{B}{2}. \quad (3)$$

Those can be integrated analytically and their contribution absorbed in the self-energy Σ of the central region. Note that this contribution will, however, depend on V_s^{off} , as well as B . The short-ranged interactions U_{is}^{intra} and U_i^{inter} are treated as free parameters, chosen as site independent within the middle of the central region, and reduced smoothly to zero at its edges. All our calculations will be carried out in thermal equilibrium at zero temperature, implying that all states below the chemical potential μ are filled, all states above are empty.

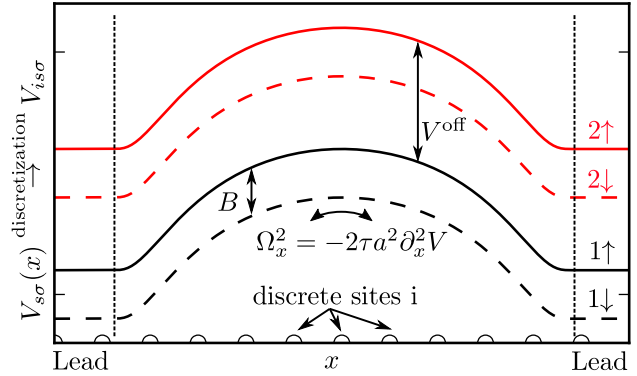


FIG. 2. Schematic illustration of the potential structure for the two spin-split bands, as given by Eq. (2). Note that the curvature of the barrier, Ω_x , is the same for all four subbands.

Our typical observable will be the linear response conductance through the system, and its dependence on the chemical potential μ , as well as on the magnetic field B .

Note that to keep things simple and clear, we have made here several simplifying assumptions. We omit any hopping terms between the two bands, keep the offset between the bands a site independent constant throughout the whole system (in particular the barrier curvature for both bands is the same) and omit any longer-ranged interactions. Furthermore, in all our calculations we will keep V_g constant and vary μ instead. In terms of the Fermi energy on the central site, $\epsilon_F = \mu - V_g$, this is the same as varying V_g with constant μ , but has the advantage that the bare curvature $\Omega_x(V_g)$ of the barrier does not change.

B. Method

To determine the interaction-induced self-energy, Σ , and two-particle vertex, γ , we use the recently introduced eCLA fRG scheme [5] within a static implementation. This scheme was originally designed to treat longer-ranged interactions. It enables the treatment of our two-band model, since it is possible to map the Hamiltonian Eq. (1) onto a one-dimensional chain model with longer-ranged interactions. For this, we simply interleave the different bands, as sketched in Fig. 3, leading to a new effective one-dimensional Hamiltonian, containing interactions between neighboring sites:

$$H_{\text{eff}} = -\tau \sum_{j,\sigma} [c_{j\sigma}^\dagger c_{j+2\sigma} + \text{H.c.}] + \sum_{j,\sigma} \tilde{V}_{j\sigma} n_{j\sigma} + \sum_j \tilde{U}_j^{\text{intra}} n_{j\uparrow} n_{j\downarrow} + \sum_{j,\sigma_1,\sigma_2} \tilde{U}_{2j}^{\text{inter}} n_{2j\sigma_1} n_{2j+1\sigma_2}. \quad (4)$$

Here the new index is given by $j = 2i + s - 1$ ($s = 1$ is band 1, $s = 2$ is band 2), and the coefficients are $\tilde{V}_{j\sigma} = V_{is\sigma}$, $\tilde{U}_j^{\text{intra}} = U_{is}^{\text{intra}}$, and $\tilde{U}_j^{\text{inter}} = U_i^{\text{inter}}$. We will sometimes use $\alpha = (s, \sigma)$ as composite species index.

This Hamiltonian is now in a form suitable for the eCLA approach. Without going into detail, we just point out that this method depends crucially on a dimensionless parameter, L , called the feedback length in Ref. [5], which determines the spatial extent of the renormalized vertex, γ . This L has to

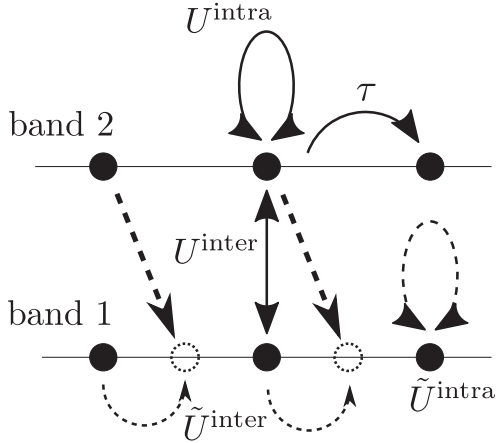


FIG. 3. Schematic procedure of interleaving the two bands. Note that in the effective chain, we get again on-site, as well as anisotropic nearest neighbor interactions.

be chosen large enough to reach convergence, and we will comment on the convergence properties in the beginning of the next section.

Finally, the calculation of the zero-temperature linear response conductance, $g = \frac{\hbar}{2e^2} \frac{\partial I}{\partial V}$, from the self-energy obtained with our fRG method, is carried out via the formula [7–9]

$$g = \frac{1}{2} \sum_{\sigma,s} |2\pi\rho^{\sigma s}(\mu + i0^+) \mathcal{G}_{-NN}^{\sigma s}(\mu + i0^+)|^2, \quad (5)$$

where $\rho^{\sigma s}$ is the density of states on the first lead site for spin σ and band s , and $\mathcal{G}_{-NN}^{\sigma s}$ is the propagator for an electron in band s with spin σ from the leftmost to the rightmost site of the central region.

III. RESULTS

We use the following general settings in this section: The band offset is chosen as $V^{\text{off}} = 0.1\tau$ and $N = 30$, therefore the total number of spatial sites in the central region is $N_{\text{tot}} = 61$ and correspondingly the total number of effective sites in Eq. (4) is $N_{\text{eff-tot}} = 122$. Furthermore, except for Fig. 6, we set $V_g = 0.5\tau$, implying a curvature $\Omega_x \approx 0.05\tau$.

In Fig. 4(a), we show the noninteracting, as well as the fully L -converged conductance for our two-band model, with the simplest nontrivial interaction configuration, $U_{is}^{\text{intra}} = U_i^{\text{inter}} = 0.7\tau$. These values correspond to a typical value for the onsite interactions in a one-band QPC used in Ref. [4]. The main changes caused by the interaction are the slightly more asymmetric shape of the conductance steps, and the shift to larger chemical potentials observed for the second step. Qualitatively, this shift is caused by the additional interaction energy between the electrons of the two bands (Hartree shift).

A. Convergence in L

Before we proceed, let us first discuss the convergence of our method with respect to the feedback length L . For a one-band QPC with onsite interactions, L has to be of the

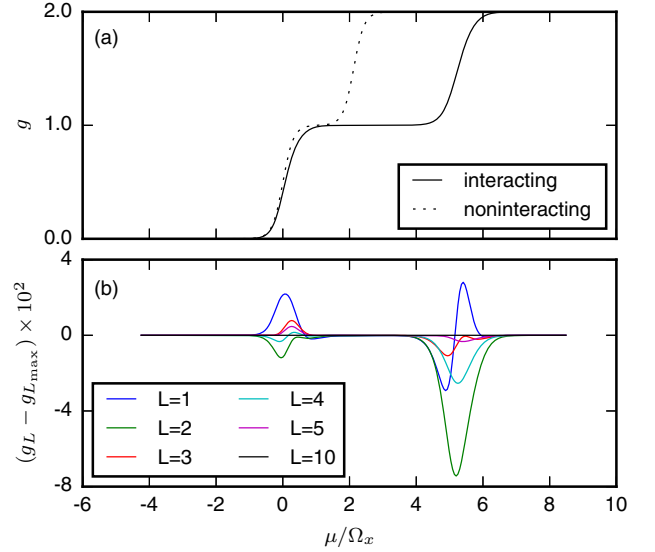


FIG. 4. (a) Conductance g for the non- as well as the interacting system for $L = 10$ as function of μ . (b) Difference between the conductance for several L values to the converged result (at $L = L_{\text{max}} = 10$). We see that convergence is achieved around $L = 5$.

order of the characteristic length of the harmonic barrier top to achieve convergence: $L \approx l_x/a$, with the lattice spacing a . For our interleaved two-band system, we would thus simply expect $L \approx 2l_x/a$, since the effective distance between two points of the same band is doubled and the effect of the now-finite interaction range on the convergence should be negligible, since the introduced nearest-neighbor interaction is still much shorter than l_x . In Fig. 4(b), the convergence behavior in L is shown. We see that the convergence for the two-band model is achieved around $L \approx 5$. Since in our system $l_x \approx 4.6a$, this shows that L can in fact be chosen smaller than the naive guess, $L \approx 2l_x/a$, indicating stabilizing feedback effects between the two bands.

As a side remark, we point out that the finite extent of the renormalized vertex beyond the lowest value (i.e., $L > 1$) is actually important to treat the screening properties between the two bands. This will be seen in the next section when we study the magnetic-field dependence of the conductance.

B. Small magnetic field

Before we look at the 0.7 analog, we want to take a brief look at the properties of the conductance at magnetic fields much smaller than the band spacing, $B \ll V^{\text{off}}$, see Fig. 5, solid curves.

There are two main observations we make here: First, we see that the magnetic-field dependence of the second step is more symmetric, indicating that the interaction of the electrons in the second band is screened by electrons in the first band. Second, we see that the second conductance step is broader than the first one. This feature can be qualitatively understood in a simple Hartree picture: While increasing μ during the second step, electrons are still filling up the lowest band, leading to an increasing Hartree shift for the

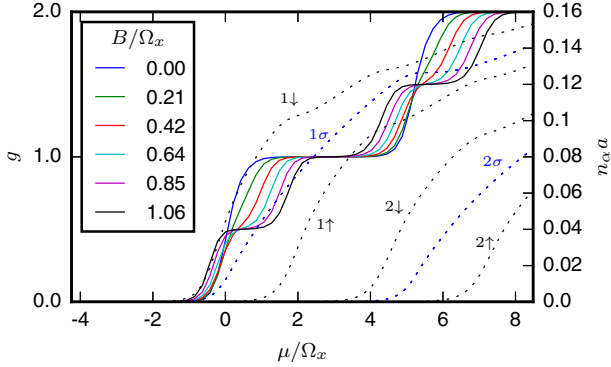


FIG. 5. Solid curves: Conductance at low magnetic fields, i.e., with $B \ll V^{\text{off}} = 0.1\tau \approx 2.12\Omega_x$ and $U^{\text{intra}} = U^{\text{inter}} = 0.7\tau$. The second spin-split double step is more symmetric and broader than the first. Dotted curves: Spin resolved electron densities n_α on the central QPC site for $B/\Omega_x = 0$ (blue) and $B/\Omega_x = 1.06$ (black). Note the damping that appears in n_α whenever a different particle species enters the QPC.

electrons in the higher band. As a result, the second step gets broadened.

To further validate this explanation, we can compute an estimate for the observed broadening via

$$\Delta E = U^{\text{inter}}(\Delta n_{1\downarrow} + \Delta n_{1\uparrow})a, \quad (6)$$

where $\Delta n_{1\sigma}$ is the total change of the first-band spin- σ density at the center of the QPC during the second conductance step. Instead of considering a “pure” Hartree effect where one would use for $n_{1\sigma}$ only the density of a system without interband interaction, we can improve on that by using the actual fully interacting densities that we obtained from our fRG calculation. These densities are given by

$$n_i^\alpha = \int_{-\infty}^{\mu} d\omega \mathcal{A}_i^\alpha(\omega), \quad (7)$$

where the local density of states at site i for particle species α , $\mathcal{A}_i^\alpha(\omega) = -\text{Im} G_{ii}^\alpha(\omega)/\pi$ is given by the imaginary part of the fully interacting retarded electron propagator $G_{ii}^\alpha(\omega)$. It is instructive to take a quick look at these densities themselves: In Fig. 5, we have plotted the density for the different particle species in the center of the QPC, $n_\alpha \equiv n_0^\alpha$ (dotted curves). Each time a new particle species enters the QPC, the increase of any other species n_α is slowed down, or “damped,” due to the corresponding interaction. The damping of $n_{1\sigma}$ during the second conductance step will lead (starting in second order in U^{inter}) to a reduction of the pure Hartree broadening of that step. We see that the damping in $n_{1\sigma}$ is most pronounced at $B = 0$, when both $n_{2\uparrow}$ and $n_{2\downarrow}$ particles enter the QPC at the same time. Correspondingly, the width of the second conductance step is only slightly larger than that of the first. On the other hand, for $B/\Omega_x = 1.06$, the damping in $n_{1\sigma}$ is relatively small, leading to a pronounced broadening of the second conductance step. Using Eq. (6), the effective Hartree broadening can be obtained from the change of the densities $n_{1\sigma}$ during the second conductance step. For example, in the $B/\Omega_x = 1.06$ case, the second conductance step occurs between $\mu/\Omega_x \approx 3.3$, with densities $n_{1\downarrow} \approx 0.12/a$, $n_{1\uparrow} \approx$

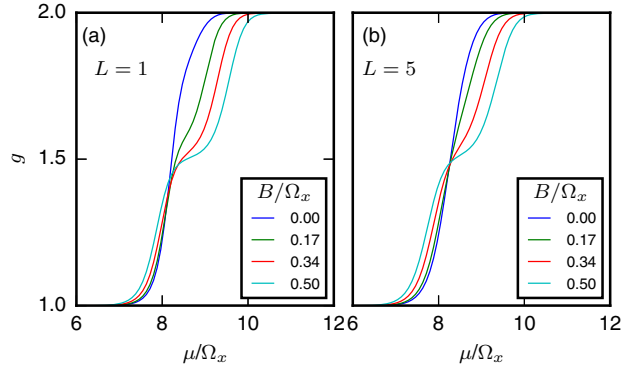


FIG. 6. Magnetic field dependence of the second conductance step. (a) $L = 1$, (b) $L = 5$. We see that the second conductance step is more symmetric in the $L = 5$ case, indicating a better screening of interactions in the second band.

$0.08/a$, and $\mu/\Omega_x \approx 7.8$, with densities $n_{1\downarrow} \approx 0.15/a$, $n_{1\uparrow} \approx 0.13/a$. Therefore, the effective Hartree broadening given by Eq. (6) is

$$\begin{aligned} \Delta E &\approx 0.7\tau \cdot [(0.15 - 0.12) + (0.13 - 0.08)] \\ &= 0.056\tau \approx 1.1\Omega_x. \end{aligned} \quad (8)$$

This result can be compared with the observed broadening of the second conductance step: The widths of the steps are $\Delta\mu_{\text{step 1}} \approx (2.4 - (-1.2))\Omega_x = 3.6\Omega_x$ and $\Delta\mu_{\text{step 2}} \approx (7.8 - 3.3)\Omega_x = 4.5\Omega_x$, leading to a relative broadening of $\Delta\mu_{\text{step 2}} - \Delta\mu_{\text{step 1}} \approx 0.9\Omega_x$, which is in qualitative agreement with Eq. (8). The effect that the electrons in the first band change the form of the second conductance step is quite generic and will be also encountered in the 0.7 analog case.

Here it is also interesting to look at the L -dependence of the conductance with various magnetic fields. Particularly for longer QPCs, where $l_x \gtrsim 5a$, the increase in L has a visible impact, see Fig. 6.

For $L = 1$, the second conductance step is very asymmetric, but becomes more symmetric with increasing L , due to the screening of the interaction in the second band instigated by electrons in the first band. The curvature, $\Omega_x \approx 0.03\tau$ ($V_g = 0.2\tau$), which we used here, is comparable to the one in a previous fRG study [10] of the two-band model. However, in that work, the results were not converged in L , therefore underestimating screening effects.

C. 0.7 analog at large magnetic field

Having studied the properties of the two-band model at low magnetic fields, we are now prepared to tackle the 0.7 analog. This analog appears at the crossing of the $1\uparrow$ and the $2\downarrow$ spin subbands at a magnetic field, $B = B_c$, which is of the order of the energy separation of the two bands V^{off} (determined by the confinement in the lateral direction). This situation resembles the situation given in the 0.7 anomaly, in the sense that two particle species are competing while trying to get through the QPC. Therefore, one might naively expect that the 0.7 analog shows the same features as the 0.7 anomaly. However, this is only partially true. While for

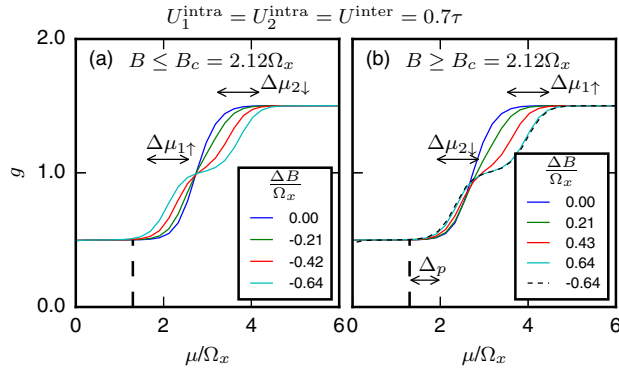


FIG. 7. (a) Conductance curves for $B \leq B_c = 0.1\tau \approx 2.12\Omega_x$ and (b) for $B \geq B_c$ at equal intra- and interband interaction strengths. In (b), the dotted curve is the manually shifted curve, $\Delta B/\Omega_x = -0.64$, from (a). We see that it has exactly the same form as the corresponding curve for $\Delta B/\Omega_x = 0.64$. The quantities $\Delta\mu_{1\uparrow}$, $\Delta\mu_{2\downarrow}$ measure the width of the corresponding half-steps and Δ_p indicates the pinch-off shift between $\Delta B < 0$ and $\Delta B > 0$, see also Fig. 8.

$\Delta B = B - B_c > 0$ the experimentally measured conductance shows the typical feature of 0.7 physics, namely the development of a shoulder with increasing magnetic field, this feature is missing for $\Delta B < 0$.

In trying to understand the underlying physics, we first start with the simplest interaction model, $U_{is}^{\text{intra}} = U_i^{\text{inter}} \equiv U = 0.7\tau$, which we already used in the last sections. Figure 7 shows the resulting conductance.

We make two main observations: First, the curves for $\Delta B < 0$ lie approximately symmetrically around the B_c curve, while the $\Delta B > 0$ curves do not. However, second, the actual shapes of corresponding curves, i.e., for $B = B_c - \Delta B$ and $B = B_c + \Delta B$, are very similar, they are just offset by different amounts.

This behavior can be understood by a similar argument as used for the broadening of the conductance step in the low magnetic field case above. As already mentioned, in a case with only $1\uparrow$ and $2\downarrow$ particles, the situation would be completely symmetric. Therefore the different behavior must stem from the other particles in the system. Since, in the analog case, the $2\uparrow$ spin subband lies much higher than the chemical potential and is therefore empty, the $1\downarrow$ particles must be responsible for the change of situation.

Both of our observations can be explained by taking the effect of the $1\downarrow$ electrons in a simple Hartree argument into account: The Hartree shift on particle species α induced by the $1\downarrow$ particles in the center of the QPC is given by $E_H^\alpha = U_\alpha n_{1\downarrow} a$, where U_α denotes the appropriate interaction (U^{intra} for $\alpha = 1\uparrow$, U^{inter} for $\alpha = 2\downarrow$). Assuming that the chemical potential μ is already far above the $1\downarrow$ van Hove ridge, $\mathcal{A}_{1\downarrow}(\omega) \approx \mathcal{A}_{1\downarrow}$ will be approximately constant, and the Hartree shift will be approximately of the form $E_H^\alpha \approx U_\alpha (n_{1\downarrow}^c + (\mu - b_{1\downarrow}) \mathcal{A}_{1\downarrow}) a$, with a constant $n_{1\downarrow}^c$ and the barrier top of the $1\downarrow$ particles given by $b_{1\downarrow} = V_g - \frac{B}{2}$. Leaving the other interactions aside for a moment, we can readily write down the μ - and B -dependence of the renormalized barrier

tops of the $1\uparrow$ and $2\downarrow$ particles:

$$\begin{aligned} b_{1\uparrow} &= V_g + \frac{B}{2} + E^{1\uparrow H}(B, \mu), \\ b_{2\downarrow} &= V_g + V^{\text{off}} - \frac{B}{2} + E^{2\downarrow H}(B, \mu). \end{aligned} \quad (9)$$

The qualitative behavior of this equations is shown in Fig. 8, and provides a good explanation for the observed phenomena: In contrast to the noninteracting case [Fig. 8(a)], we obtain for $U^{\text{intra}} = U^{\text{inter}}$ a pinch-off asymmetry, Δ_p , between the pinch-offs at magnetic fields above and below the analog, see Fig. 8(b). Taking into account the interaction between $1\uparrow$ and $2\downarrow$ (whose main effect is a broadening of the second half-step), this results in the more symmetric arrangement of the two half-steps around the crossing curve for $\Delta B < 0$, and to a more asymmetric situation in the $\Delta B > 0$ case. However, we see that the shape of corresponding curves is the same since the μ -width of the half-steps, $\Delta\mu_{1\uparrow}$ and $\Delta\mu_{2\downarrow}$, is equal.

If we compare this to experiment [1], we see that this setting reflects only partially the experimental situation: While the half-steps are indeed arranged more symmetrically for $\Delta B < 0$ than for the $\Delta B > 0$ case, also the form of the corresponding curves themselves differs substantially in experiment. For $\Delta B > 0$, the conductance curves are much more asymmetric in the μ behavior, developing a 0.7 analog plateau, while for $\Delta B < 0$ they are not. To analyze this quantitatively in our calculation, we introduce the ‘‘conductance asymmetry’’ $\Delta g(\mu) = g_m(\mu) - g(\mu)$, where $g_m(\mu)$ is the mirror image of $g(\mu)$ around the point $g(\mu)/g_0 = 1.0$ under reflection in both the horizontal and vertical direction. The more asymmetric the conductance curve is in μ , the larger gets the modulus of Δg . This is illustrated in Fig. 9(a). Figure 9(b) shows the dependence of this asymmetry Δg on the magnetic field. We see that contrary to the experiment the asymmetry is equally strong above and below the crossing value B_c .

This indicates that our description up to now lacks an important ingredient. We will argue in the following that this is due to the unphysical choice $U^{\text{intra}} = U^{\text{inter}}$. Generically, one would expect $U^{\text{inter}} < U_2^{\text{intra}} < U_1^{\text{intra}}$. The first statement is due to the smaller overlap of the transversal wave functions between different bands, the second because the transversal wave function in the second band is spread out wider than in the first band. Both effects lead to a weakening of the effective one-dimensional interaction strength. Estimates for the ratios of this different interaction strengths can be obtained in a similar manner as in Ref. [5], see Appendix, and yield $U_2^{\text{intra}}/U_1^{\text{intra}} \approx 0.77$ and $U^{\text{inter}}/U_1^{\text{intra}} \approx 0.36$. Keeping our previous U_1^{intra} fixed, this leads approximately to $U_2^{\text{intra}} = 0.5\tau$ and $U^{\text{inter}} = 0.3\tau$.

To investigate the influence of these differences in interaction strength, we proceed in two steps. In the ideal case where the analog region is well separated from the $2\uparrow$ conductance step, we expect that the influence of U_2^{intra} at the analog is not important, since the barrier for the $2\uparrow$ electrons is way above the chemical potential. Therefore, we will first keep U_2^{intra} equal to $U_1^{\text{intra}} = 0.7\tau$ and investigate the influence of a reduction of $U^{\text{inter}} = 0.3\tau$ alone. In Fig. 10, we show the resulting conductance curves. Again, we encounter a pinch-off shift of the higher spin subband steps; however, due to

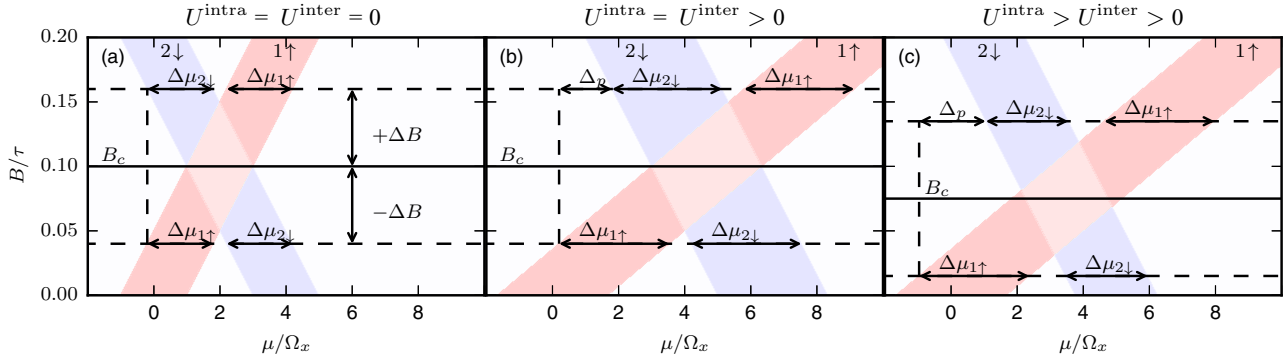


FIG. 8. Schematic behavior of the Hartree renormalized barriers of the $1\uparrow$ (red) and $2\downarrow$ (blue) particles as function of μ and B . The colored regions indicate where $|b_\alpha - \mu| < \Omega_x/2$, i.e., the regions within which the conductance steps occur. (a) Noninteracting case: $B_c = V^{\text{off}}$, no pinch-off asymmetry, no shape asymmetry. (b) $U^{\text{intra}} = U^{\text{inter}}$: $B_c = V^{\text{off}}$, pinch-off asymmetry ($\Delta_p > 0$), no shape asymmetry. (c) $U^{\text{intra}} > U^{\text{inter}}$: $B_c < V^{\text{off}}$, pinch-off asymmetry ($\Delta_p > 0$) and shape asymmetry ($\Delta\mu_{1\uparrow} > \Delta\mu_{2\downarrow}$).

the different interaction strengths, the crossing point B_c is now shifted, too. More importantly, we see that in addition to the pinch-off asymmetry, also the shape of corresponding curves for $\Delta B < 0$ and $\Delta B > 0$ differ, the curves for $\Delta B < 0$ being much more symmetric than the $\Delta B > 0$ curves. This is the behavior also observed in experiment and for further reference, we will call it the “shape asymmetry.”

These features can be readily explained with our Hartree picture for the renormalized barrier positions Eq. (9). Their behavior for $U^{\text{intra}} > U^{\text{inter}}$ (i.e., the Hartree shift for the $2\downarrow$ subband is smaller than for the $1\uparrow$ subband) is shown in Fig. 8(c). We see two immediate effects: (i) The $2\downarrow$ subband is shifted to lower values of μ and therefore the value of the magnetic field B_c , where the two subbands cross is shifted to lower magnetic fields, as encountered in the Fig. 10, and (ii) the width $\Delta\mu_{2\downarrow}$ of the $2\downarrow$ half-step is decreased, therefore yielding the shape asymmetry: For $\Delta B < 0$, the first half-step ($1\uparrow$) is broader than the second half-step ($2\downarrow$), thus counteracting the asymmetry introduced by the interband interaction between the competing particles themselves and leading in

to a more symmetric curve. For $\Delta B > 0$, the effect is reversed, leading to a more asymmetric curve.

Furthermore, Fig. 8(c) exhibits a third interesting, albeit less pronounced feature: Due to the smaller interaction with the lowest electrons, the μ -width of the $2\downarrow$ -strip is smaller than the width of the $1\uparrow$ -strip and therefore the two middle corners of the intersecting diamond [light pink region in

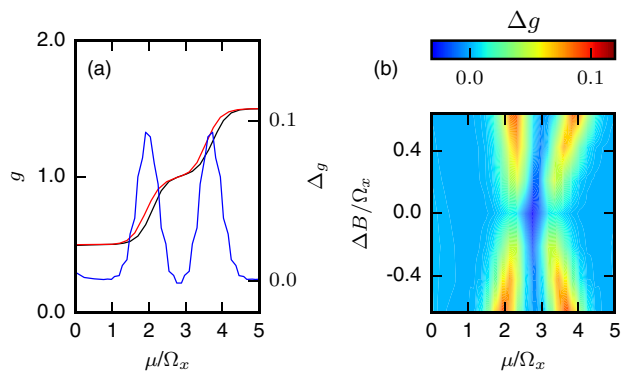


FIG. 9. Illustration of the asymmetry in μ . (a) Conductance curve $\Delta B/\Omega_x = -0.64$ from Fig. 7 (black), together with its mirror image (red) under inversion around the $g = 1.0$ point, and the difference Δg between the two curves (blue). (b) Colorplot of Δg as a function of magnetic field and chemical potential. We see that the strength of the curve asymmetry is symmetric around B_c .

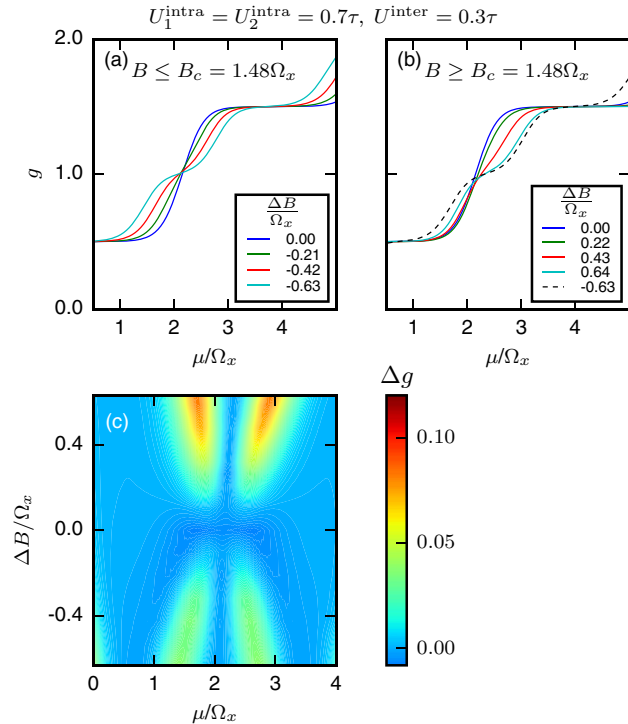


FIG. 10. (a), (b) same plot as in Fig. 7, but for larger intra- than interband interaction ($U_{1,2}^{\text{intra}} = 0.7\tau$, $U^{\text{inter}} = 0.3\tau$), resulting in $B_c \approx 1.48\Omega_x$. In (b), the dashed curve is again the $\Delta B/\Omega_x = -0.63$ curve from (a), manually shifted such that it intersects the corresponding $\Delta B/\Omega_x = 0.64$ curve at the $g/g_0 = 1$ point. However, contrary to Fig. 7(b), the shape of the two curves does not coincide. (c) Colorplot of the shape asymmetry. In contrast to Fig. 9(b), we see that the asymmetry is clearly stronger for $\Delta B > 0$ than for $\Delta B < 0$.

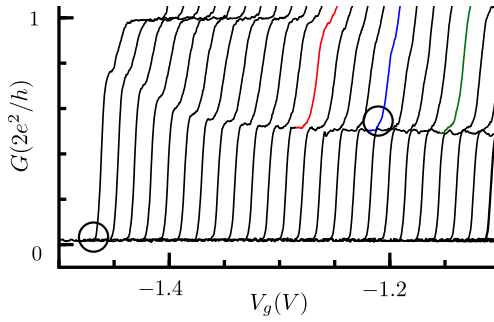


FIG. 11. Zoom of Fig. 1. Note the slight kink that occurs at the onset of the blue 0.7 analog curve compared to the steep onset of the $B = 0$ curve (circled areas).

Fig. 8(c)] do not lie on the B_c line, but are shifted slightly upward or downward from it. Directly at the B_c line, i.e., at the 0.7 analog, the broader $1\uparrow$ and the thinner $2\downarrow$ steps superimpose symmetrically, which leads to a conductance curve with slightly less steep parts at the onset and at the end in μ direction. Since the Hartree picture we use in Fig. 8 takes only the interaction with the $1\downarrow$ electrons and not the interaction between the $1\uparrow$ and $2\downarrow$ electrons themselves into account, we expect this small effect to be most prominent at the onset of the second conductance step. In the experimental data, one might interpret the slight kink that occurs at the onset of the blue 0.7 analog step, compared to the smooth $B = 0$

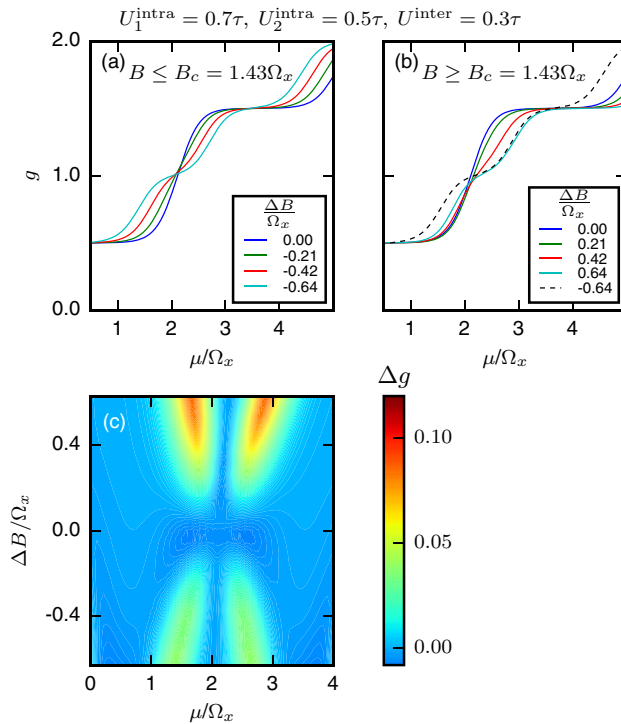


FIG. 12. (a), (b) same plot as in Figs. 7(a) and 7(b) and Figs. 10(a) and 10(b), but for three different interactions: $U_1^{\text{intra}} = 0.7\tau$, $U_2^{\text{intra}} = 0.5\tau$, and $U^{\text{inter}} = 0.3\tau$. In comparison to Fig. 10, the crossing point is slightly reduced to $B_c = 1.43\Omega_x$; however, the asymmetry persists. (c) Colorplot of the shape asymmetry, which stays very similar to Fig. 10(c).

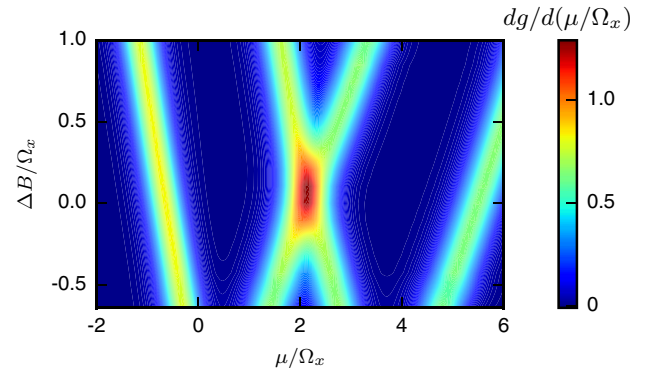


FIG. 13. Colorplot of the transconductance as function of B and μ . Note the more pronounced asymmetry at the $\Delta B > 0$ than the $\Delta B < 0$ part of the crossing region.

curve, as a result of the described effect, compare circled onsets in Fig. 11. However, this feature is quite weak and could also be caused by other causes, e.g., a gate-dependent deformation of the QPC potential. Furthermore, we do not observe any visible effect of this kind in our fRG calculations, see Fig. 10.

As a last step, we finally also reduce $U_2^{\text{intra}} = 0.5\tau < U_1^{\text{intra}}$. The results are shown in Fig. 12. We see that the reduction of U_2^{intra} slightly shifts the crossing point B_c to lower values of the magnetic field; however, the shape asymmetry introduced by the lowering of U^{inter} stays intact. Thus, in terms of Fig. 8, the net effect of the reduction of U_2^{intra} is simply a slight shift of the blue $2\downarrow$ barrier top position stripe to the left, i.e., to lower values of μ , without changing its slope.

D. Limitations

A limitation of our static zero temperature calculation is that we have no access to inelastic processes. We suspect that this leads to a main difference between our results and experimental observations, namely that we do not see a pronounced finite temperature plateau in the conductance. This can be clearly seen by comparing the transconductances $dg/d\mu$, see Fig. 13, where we do not observe the “gap” at $\Delta B > 0$ as in the experimental data, cf. Fig. 2(a) in Ref. [1] or Fig. 1(b) in Ref. [11]. However, we also see in the transconductance, that for $\Delta B > 0$ the broadening of the conductance curve in the second half-step is more pronounced than for $\Delta B < 0$, where the half-steps are more symmetric in position as well as slope.

IV. CONCLUSION

We have studied the 0.7 analog in QPCs using a two-band model with intra- and interband onsite interactions and found that we could qualitatively reproduce the magnetic field dependence of the conductance around the analog. In particular, we could reproduce the asymmetry in the conductance, depending on whether the analog is approached from higher or lower magnetic fields.

Due to our use of a static fRG scheme, we were not able to investigate finite temperature properties of the analog, which is an interesting direction for further research.

ACKNOWLEDGMENTS

We thank Prof. Dr. D. A. Ritchie for letting us use Fig. 1 from their publication [1]. Furthermore, we gratefully acknowledge support from the Cluster of Excellence Nanosystems Initiative Munich.

APPENDIX: ESTIMATE OF THE QPC INTERACTION STRENGTHS

Following the approach of Ref. [12], we calculated in Ref. [5] the intraband interaction for a QPC with a single band

that resulted from a screened Coulomb interaction. This was done by taking only the ground state ϕ_1 of the transversal y direction (in the two-dimensional electron gas plane) into account. Since the confinement in y direction can be approximated by a harmonic potential, ϕ_1 is simply the ground state of a harmonic oscillator. In a QPC with two bands, we additionally also take the first excited state of the harmonic y confinement into account. The computation of the resulting matrix elements for the interaction between two effective one-dimensional states at x_0 and x_1 can be done analogously to the one-dimensional case and yields in terms of integrals over the relative coordinate r in the transversal direction:

$$U_1^{\text{intra}}(x_0, x_1) = (l_y^2(x_0) + l_y^2(x_1))^{-\frac{1}{2}} \int dr g(r), \quad (\text{A1})$$

$$U_2^{\text{intra}}(x_0, x_1) = (l_y^2(x_0) + l_y^2(x_1))^{-\frac{9}{2}} \int dr g(r) [3l_y^2(x_0)l_y^2(x_1)(l_y^2(x_0) + l_y^2(x_1))^2 + (l_y^2(x_0) + l_y^2(x_1)) \times (l_y^4(x_0) - 4l_y^2(x_0)l_y^2(x_1) + l_y^4(x_1))r^2 + l_y^2(x_0)l_y^2(x_1)r^4)], \quad (\text{A2})$$

$$U^{\text{inter}}(x_0, x_1) = (l_y^2(x_0) + l_y^2(x_1))^{-\frac{5}{2}} \int dr g(r) [l_y^4(x_1) + l_y^2(x_0)(l_y^2(x_1) + r^2)], \quad (\text{A3})$$

where $l_y(x)$ is the (x dependent) characteristic length in y direction, e the electron charge, κ the dielectric constant, and $g(r)$ (which consists of the screened Coulomb interaction, as well as the lateral confinement) is given by

$$g(r) = \frac{e^2}{\kappa} \left[\frac{1}{\sqrt{(x_0 - x_1)^2 + r^2}} - \frac{1}{\sqrt{(x_0 - x_1)^2 + r^2 + l_s^2}} \right] e^{-r^2/(2(l_y^2(x_0) + l_y^2(x_1)))}, \quad (\text{A4})$$

where l_s is the screening length. All these contributions are logarithmically divergent for $x_0 \rightarrow x_1$. In this work, we make the simplest approximation and ignore the position dependence of the U 's, by setting them to their value in the QPC center. Then we obtain for the ratios of the different effective interaction strengths used in Sec. III C:

$$\frac{U_2^{\text{intra}}}{U_1^{\text{intra}}} = \lim_{x_1 \rightarrow 0} \frac{U_2^{\text{intra}}(0, x_1)}{U_1^{\text{intra}}(0, x_1)} \approx 0.77, \quad (\text{A5})$$

$$\frac{U^{\text{inter}}}{U_1^{\text{intra}}} = \lim_{x_1 \rightarrow 0} \frac{U^{\text{inter}}(0, x_1)}{U_1^{\text{intra}}(0, x_1)} \approx 0.36, \quad (\text{A6})$$

where in the last step we used a ratio $l_s/l_y(0) = 3$, which could, for example, be realized in a QPC with $l_s = 50$ nm and $l_y = 17$ nm, which corresponds in a GaAs 2DEG to a curvature $\Omega_y = 2$ meV.

-
- [1] A. C. Graham, K. J. Thomas, M. Pepper, N. R. Cooper, M. Y. Simmons, and D. A. Ritchie, *Phys. Rev. Lett.* **91**, 136404 (2003).
- [2] K.-F. Berggren, P. Jaksch, and I. Yakimenko, *Phys. Rev. B* **71**, 115303 (2005).
- [3] Y. Meir, *J. Phys.: Condens. Matter* **20**, 164208 (2008).
- [4] F. Bauer, J. Heyder, E. Schubert, D. Borowsky, D. Taubert, B. Bruognolo, D. Schuh, W. Wegscheider, J. von Delft, and S. Ludwig, *Nature* **501**, 73 (2013).
- [5] L. Weidinger, F. Bauer, and J. von Delft, *Phys. Rev. B* **95**, 035122 (2017).
- [6] F. Stern, *Phys. Rev. Lett.* **21**, 1687 (1968).
- [7] S. Datta, *Electronic Transport in Mesoscopic Systems*, Cambridge Studies in Semiconductor Physics (Cambridge University Press, Cambridge, 1997).
- [8] A. Oguri, *J. Phys. Soc. Jpn.* **70**, 2666 (2001).
- [9] D. Schimmel, Transport through Inhomogeneous Interacting Low-Dimensional Systems, Ph.D. thesis, Ludwig-Maximilians-Universität, München, 2017.
- [10] K. Eissing, Functional Renormalization Group Applied to a Multimode Quantum Point Contact, Master's thesis, LMU München, 2013.
- [11] A. C. Graham, D. L. Sawkey, M. Pepper, M. Y. Simmons, and D. A. Ritchie, *Phys. Rev. B* **75**, 035331 (2007).
- [12] A. M. Lunde, A. D. Martino, A. Schulz, R. Egger, and K. Flensberg, *New J. Phys.* **11**, 023031 (2009).

5 Keldysh fRG treatment of finite-ranged interactions in quantum point contacts

5.1 Overview

This section contains our publication investigating the temperature dependence of the conductance of a quantum point contact (QPC) with finite-ranged interactions. The inclusion of a finite interaction range at finite temperature is a major step, since it tremendously increases the number of possible interaction processes, possibly yielding effects that were missed out using only an onsite interaction model like in [SBvD17]. Furthermore, a reasonable treatment of finite interaction range is also a necessary requirement in order to study the transition of (comparatively short) QPCs to longer quantum wires (c.f. the discussion in the Introduction of this thesis).

In order to achieve the goal stated above, we develop a (semi-) dynamic Keldysh version of the extended Coupled Ladder Approximation (eCLA) introduced in our previous publication in Sec. 3.2. For this, we proceed analogously to previous works on Keldysh fRG [Jak09, SBvD17, Sch17]. In particular, we use a hybridization flow by introducing artificial leads (as opposed to a frequency cutoff as in Sec. 3.2), keeping the flow parameter dependent action physical during the flow. Therefore, important relations like fluctuation dissipation theorems are manifestly fulfilled for this flow.

The introduction of the feedback length L for the spatially extended feedback of the eCLA requires special care in the dynamic case. Due to numerical costs, it is not possible to include the extended spatial feedback for all frequencies. Therefore, we introduce the concept of a dynamical feedback length $L(\Omega)$, keeping the extended spatial feedback only around the feedback frequencies of the respective vertex channels, which constitute the most important frequencies. Although we are not able to reach full convergence w.r.t. $L(\Omega)$, we can still see a very interesting trend from our results for the QPC conductance.

While, for a model with onsite interactions, the conductance always retains a qualitatively similar shape when temperature is increased, this changes for models with finite-ranged interactions. When the interaction range is comparable to the characteristic length of the QPC, we find that the conductance develops a pronounced 0.7-shoulder with increasing temperature. This constitutes the main result of this paper.

Unfortunately, this finding is somewhat spoiled by methodological problems and therefore we can not claim it as the whole truth. Besides the above mentioned convergence issues (c.f. Sec. 3.2), our method also suffers from the violation of Ward identities. This violation makes the conductance computation ambiguous, i.e. formally equivalent expressions for the conductance in terms of the vertex quantities and the self-energy yield different results. We treat this problem here by a somewhat ad hoc method, based on the artificial restoration of Ward consistency between self-energy and vertex. A truly reliable method should of course fulfill this Ward consistency on its own. A possible candidate for such an improved method could be a future multiloop fRG (mfRG) implementation of the eCLA. This recently developed fRG method [KvD18a, KvD18b, KvD18c] goes beyond second order truncation fRG and is conserving on a one-particle level. Work in this direction is currently in progress.

5.2 Keldysh Functional Renormalization Group Treatment of Finite-Ranged Interactions in Quantum Point Contacts

by

Lukas Weidinger,¹ and Jan von Delft¹

¹ Physics Department, Arnold Sommerfeld Center for Theoretical Physics and Center for NanoScience, Ludwig-Maximilians-Universität München, 80333 München, Germany

reprinted on pages [113–137](#)

[arXiv:1912.02700](#).

Keldysh Functional Renormalization Group Treatment of Finite-Ranged Interactions in Quantum Point Contacts

Lukas Weidinger¹ and Jan von Delft¹

¹*Arnold Sommerfeld Center for Theoretical Physics and Center for NanoScience, Ludwig-Maximilians-Universität München, Theresienstrasse 37, D-80333 München, Germany*

(Dated: November 20, 2020)

We combine two recently established methods, the extended Coupled-Ladder Approximation (eCLA) [Phys. Rev. B **95**, 035122 (2017)] and a dynamic Keldysh functional Renormalization Group (fRG) approach for inhomogeneous systems [Phys. Rev. Lett. **119**, 196401 (2017)] to tackle the problem of finite-ranged interactions in quantum point contacts (QPCs) at finite temperature. Working in the Keldysh formalism, we develop an eCLA framework, proceeding from a static to a fully dynamic description. Finally, we apply our new Keldysh eCLA method to a QPC model with finite-ranged interactions and show evidence that an interaction range comparable to the length of the QPC might be an essential ingredient for the development of a pronounced 0.7-shoulder in the linear conductance. We also discuss problems arising from a violation of a Ward identity in second-order fRG.

I. INTRODUCTION

In a previous work [1], we have devised an extended Coupled-Ladder Approximation (eCLA), an approximation scheme within the second-order truncated functional Renormalization Group (fRG) approach. The eCLA is capable of a controlled incorporation of the spatial extent of the one-particle irreducible two-particle vertex (hereafter simply called "vertex") into a channel-decomposed [2–4] fRG flow. Using a static Matsubara implementation, we showed that this scheme improves the convergence of the fRG flow by increasing the feedback between the separate channels of the vertex flow. Furthermore, by design, this scheme includes a correct treatment of finite-ranged interactions up to second order in the interaction. Applying the eCLA scheme to a quantum point contact (QPC), we observed that with an increasing interaction range, the effective QPC barrier flattens and additional features in the linear conductance (hereafter simply called "conductance") arise, caused by corresponding Friedel oscillations.

The eCLA has recently also been used in [5] to study phase transitions in an one-dimensional spinless tight-binding chain with nearest and next nearest neighbor interaction. Furthermore, in [6] a set of second order flow-equations was derived for a one-dimensional system of spinless fermions, which can be obtained as a special case of the spin-1/2 eCLA equations.

In this paper, we build on our previous QPC studies, now focusing on the following question: how does the temperature dependence of the QPC conductance change when the interaction range is increased from 0 up to the scale of the characteristic QPC length? In this regime, our previous zero-temperature static Matsubara approach indicated only a slight broadening of the conductance step. However, it is very interesting to study the behavior in this regime at finite temperature, since – contrary to experimental findings, see e.g. [4, 7, 8] – an earlier study [9], utilizing only onsite interactions, found no pronounced 0.7-shoulder in the conductance. In order to be able to treat finite temperatures, we here present an implementation of the eCLA in a dynamic

Keldysh setup, as devised in [10, 11] and extended and successfully applied to QPCs with short-range interactions in [9]. Since a full treatment of both the spatial as well as the frequency structure of the vertex is numerically not possible, we introduce an additional approximation scheme that allows us to take the extended spatial structure of the vertex for successively more frequencies into account. Although the numerical costs did not permit us to reach full convergence w.r.t. the used frequency range, the qualitative behavior at large ranges remained stable. Furthermore, we analytically argue that we are indeed able to capture the most important vertex contributions to the conductance within the covered frequency range.

Finally, we apply this new method to a QPC at finite temperature and show evidence that a finite interaction range on the scale of the length of the QPC likely is an essential factor for the development of a pronounced 0.7-shoulder in the conductance (see Fig. 7 below).

We also discuss problems arising from a violation of a Ward identity in second-order fRG. We suggest a simple correction factor for ameliorating these problems, but conclude that a truly reliable cure will require going beyond second-order fRG.

This paper is structured as follows. Sec. II defines the model used to describe a QPC. Sec. III describes methodological details, in particular regarding our parametrization of the vertex. (Problems arising from a Ward identity violation are addressed in Sec. III C, see Fig. 3 below). Sec. IV presents our results for the temperature dependence of the QPC conductance and Sec. V our conclusions. Three appendices deal with further technical details, such as vertex symmetries (App. B), the importance of a dynamic treatment of vertex feedback (App. E), and the consequences of violating Ward identities (App. F).

II. MODEL

We consider a Hamiltonian consisting of a one-dimensional tight-binding chain with finite-ranged inter-

actions:

$$H = - \sum_{i\sigma} \tau_i [c_{i\sigma}^\dagger c_{i+1\sigma} + h.c.] + \sum_{i\sigma} \sigma \frac{B}{2} n_{i\sigma} + \frac{1}{2} \sum_{ij\sigma\sigma'} U_{ij} (1 - \delta_{ij} \delta_{\sigma\sigma'}) n_{i\sigma} n_{j\sigma'}, \quad (1)$$

where $c_{i\sigma}$ annihilates an electron at site $i \in \mathbb{Z}$ with spin σ and $n_{i\sigma} = c_{i\sigma}^\dagger c_{i\sigma}$ is the number operator. Instead of a quadratic onsite potential as used in [1], we use a quadratic modulation in the hopping, $\tau_i = \tau - \Delta\tau_i$, to model the QPC barrier. This approach was also used in [9]. It causes a constriction of the tight-binding band, leading to a density of states which, close to the lower band edge, is equivalent to the one generated by a quadratic onsite potential. Moreover, at the upper band edge this method avoids the formation of sharp bound states which are difficult to treat numerically and lead to problems with e.g. the normalization of the density of states.

The hopping modulation and the interactions are both taken to be finite only within a central region with $2N+1$ sites, i.e. $U(i, j) = 0$, if i or $j \notin [-N, N]$ and $\Delta\tau_i = 0$ if $i \notin [-N, N-1]$. Note that the central region contains one hopping element less than onsite terms. Within this region the hopping and interaction takes the form

$$\Delta\tau_i = \frac{1}{2} V_g e^{-x_i^2/(1-x_i^2)}, \quad x_i = \frac{2i+1}{2N}, \quad (2)$$

$$U_{ij} = \left[\delta_{ij} U_0 + (1 - \delta_{ij}) U_1 \frac{e^{-|i-j|/\chi}}{|i-j|} \right] f(i, j), \quad (3)$$

where $i \in [-N, N-1]$ for $\Delta\tau_i$ and $i, j \in [-N, N]$ for U_{ij} . The hopping variation $\Delta\tau_i$ is characterized by V_g , the effective barrier height in the center of the QPC, as well as an exponential factor $\exp[-x_i^2/(1-x_i^2)]$ governing the form of the barrier: In the QPC center a quadratic barrier top dominates, while in the QPC flanks the barrier goes smoothly to zero. The interaction consists of an onsite term $\delta_{ij} U_0$ as well as a Yukawa-like offsite term governed by interaction strength U_1 and exponential decay rate χ . We chose the Yukawa-like form of the interaction strength in order to fit two demands: (i) The interaction should not only be onsite anymore (as it was in [9]), but also have a finite extent comparable to the characteristic QPC length. (ii) It still has to decay quickly enough, i.e. not develop an algebraic long-range tail, in order to be numerically treatable at finite temperature within a dynamic Keldysh setup. The situation of weaker screening, introducing only an algebraic decay in the interaction strength, requires a very large spatial extent of the vertex. For this situation, a dynamic treatment within the eCLA approach is therefore not feasible. However, for zero temperature, this case can be studied approximately within a static fRG approach that requires considerably lesser numerical resources [1]. The function $f(i, j)$ is inserted for numerical purposes and consists of two factors

$$f(i, j) = \exp\left(-\frac{z(i, j)^6}{1 - z(i, j)^2}\right) \times \theta(L_U - |i - j|), \quad (4)$$

with $z(i, j) = \max\left(\frac{|i|}{N}, \frac{|j|}{N}\right)$. The exponential factor suppresses the interaction at the edges of the central region and thus assures a smooth transition from finite interaction strength to zero interaction in the leads. Note that instead of the quadratic power that appears in the numerator of the exponential factor in the hopping variation (2), we used in (4) a power of $z(i, j)^6$ in the exponential term. This ensures that the interaction strength around the barrier top stays almost constant and only drops off, smoothly, relatively close to the edges of the central region. The θ factor introduces a cutoff in the interaction range, i.e. the interaction is only finite for ranges $|i - j| \leq L_U$. Since in this work we will focus only on qualitative predictions, we will in fact use only L_U to vary the range of the interaction, while keeping χ fixed on the scale of the QPC length. Concretely, if not specified otherwise, we will use the following parameters throughout: Spatial discretization $N = 30$, i.e. we have a total number of $2N + 1 = 61$ sites; barrier height $V_g = 0.5\tau$, i.e. the lower edge of the noninteracting band in the QPC center lies at $\omega_b = -2\tau + V_g = -1.5\tau$, c.f. Fig. 1(a); screening length $\chi = 5$. This is on the scale of the characteristic length of our QPC, see below; magnetic field $B = 0$.

The curvature of the central barrier, which sets the characteristic energy scale of the QPC, is then given by $\Omega_x = 2\sqrt{V_g\tau}/N \approx 0.05\tau$. Likewise, the characteristic QPC length scale is given by $l_x = a\sqrt{\tau/\Omega_x} \approx 5a$, where a denotes the lattice constant of our discretization. Moreover, if not otherwise specified, we will use the following set of interaction parameters. Onsite interaction: $L_U = 0$, $U \equiv U_0 = 0.7\tau = 3.2\sqrt{\Omega_x\tau}$. These values were also used in [9]. We remark that this onsite interaction strength is close to its maximal value that can be used before the fRG flow breaks down. Finite-ranged interaction: $L_U = 3$, $U_0 = 0.5\tau = 2.3\sqrt{\Omega_x\tau}$, $U_1 = 0.3\tau = 1.4\sqrt{\Omega_x\tau}$. These parameters are chosen in such a way that (i) $L_U > l_x/(2a)$ i.e. a particle on the top of the QPC barrier can interact with a particle outside of the QPC center, whose width is set by the characteristic length l_x . (ii) The strength of the onsite term $U_0 = 0.5$ in (3) is chosen to be slightly smaller than that for the pure onsite interaction with $U = 0.7$, in order to compensate for the finite extent of the interaction. The strength of the offsite interaction is chosen in an ad hoc fashion as $U_1 = 0.3$ which, as we will see, is large enough to lead to a noticeable impact on the conductance behavior. In the end of Sec. III B 4 we take a very brief look on how the conductance changes with (i) increasing interaction range L_U and (ii) when varying the overall interaction strength while keeping the ration U_0/U_1 fixed. A systematic study of the conductance dependence on the detailed form of the interaction is, however, beyond the scope of this paper. The resulting barrier and interaction forms for this choice of parameters are shown in Fig. 1.

Primarily, we are interested in the form of the first conductance step that occurs when the QPC opens up, right after pinch-off. To vary the effective barrier height, we vary the chemical potential μ instead of the gate voltage V_g , as done in experiments. This has the advantage that

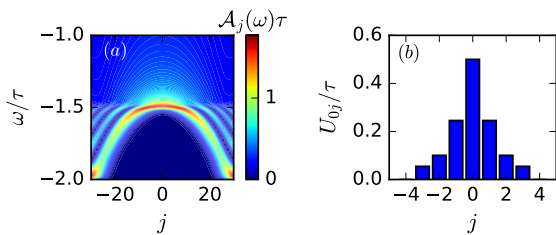


Figure 1. (a) Colorplot of the non-interacting LDOS $\mathcal{A}_j(\omega)$ for the chosen QPC model. (b) Interaction profile U_{0j} in the center of the QPC as function of site j .

the curvature Ω_x of the central barrier does not change during the conductance step. All observed changes during the step therefore depend only on the energetic distance of the chemical potential to the barrier top, i.e. on the Fermi energy at the central site, $\epsilon_F = \mu - \omega_b$.

III. METHOD

In order to compute the conductance from the described model, we use a second-order truncated Keldysh fRG (in a similar fashion as described in [9]). However, in order to treat finite-ranged interactions we extend the scheme used there, applying an eCLA-approximation, as described in [1].

This section is divided into three parts. Sec. III A summarizes the general Keldysh fRG approach to the QPC model (1). Since this general approach is the same as in [9], we provide only a brief description and just state the most important relations. In Sec. III B, we describe the combination of Keldysh- and eCLA fRG in detail, discuss the resulting flow equations and comment on symmetries of the involved quantities. Finally, in Sec. III C we discuss how to obtain the conductance from our fRG data, using the approach presented in [12].

A. Keldysh fRG setup

1. Propagators

We implement our fRG flow as hybridization flow [3, 9], by introducing a flow parameter Λ into the retarded bare propagator which nominally acts as coupling strength between the system sites (including the leads) and an artificial source of dissipation

$$G_{0,\Lambda}^R(\omega) = \frac{1}{\omega - H_0 + \frac{i}{2}\Lambda}, \quad (5)$$

where H_0 denotes the single-particle part of the Hamiltonian (1). Via the relations (9a) and (10), the Λ dependency will also enter the advanced and the Keldysh component of the bare propagator. In the limit $\Lambda \rightarrow \infty$ which serves as a starting point of the flow, the artificial dissipation renders the model trivial, whereas for $\Lambda \rightarrow 0$ we recover the full bare propagator.

As usual, before carrying out any numerical calculations, the non-interacting leads can be integrated out analytically [2–4] and their effect is absorbed into a self-energy contribution Σ_{lead} for the central region given by sites $[-N, \dots, N]$. This contribution is located at the two ends of the central region and its retarded component is given by [9]

$$\Sigma_{\text{lead}ij}^{R\sigma\Lambda}(\omega) = \frac{1}{2}(\delta_{i,-N}\delta_{j,-N} + \delta_{i,N}\delta_{j,N}) \times \left(\omega_\sigma + i\frac{\Lambda}{2} - i\sqrt{4\tau^2 - \left(\omega_\sigma + i\frac{\Lambda}{2}\right)^2} \right), \quad (6)$$

with $\omega_\sigma = \omega - \frac{\sigma}{2}B$. Using this quantity, the retarded bare propagator $G_{0,\Lambda ij}^R(\omega)$ with i, j within the central region can be expressed as

$$G_{0,\Lambda ij}^R(\omega) = \left[\frac{1}{\omega - H_0^C - \Sigma_{\text{lead}}^{R\sigma\Lambda} + \frac{i}{2}\Lambda} \right]_{ij}, \quad (7)$$

where H_0^C is the part of the single-particle Hamiltonian that lives entirely within the central region.

Using the Λ dependent bare propagator (7), the retarded component of the single-scale propagator can be obtained by

$$S^R(\omega) = (GG_0^{-1}\partial_\Lambda G_0 G_0^{-1}G_\Lambda^R(\omega)) = G_\Lambda^R(\omega) \left(-\frac{i}{2} + \partial_\Lambda \Sigma_{\text{lead}}^{R\Lambda}(\omega) \right) G_\Lambda^R(\omega). \quad (8)$$

In order to simplify notation, we will suppress the index Λ in the following.

For all propagators and the self-energy, the advanced component is the hermitian conjugate of the retarded component and the Keldysh component is its own negative hermitian conjugate, i.e. for all $\xi \in \{G_0, G, S, \Sigma\}$ we have

$$\xi^A = (\xi^R)^\dagger, \quad (9a)$$

$$\xi^K = -(\xi^K)^\dagger. \quad (9b)$$

Additionally, due to our equilibrium setup, these quantities also fulfill a fluctuation-dissipation theorem (FDT)

$$\xi^K(\omega) = (1 - 2f(\omega))(\xi^R(\omega) - \xi^A(\omega)). \quad (10)$$

Here, $f(\omega) = (1 + e^{(\omega-\mu)/T})^{-1}$ denotes the Fermi distribution with chemical potential μ and temperature T (Boltzmann constant $k_B = 1$ by convention).

For further use, we also note that using Keldysh indices $\in \{1, 2\}$ we have

$$G^R = G^{21}, \quad G^A = G^{12}, \quad G^K = G^{22}. \quad (11)$$

Here and in the following sections, we use the common notation, where “2” indicates the classical and “1” the quantum component, c.f. [10, 11].

2. Keldysh and frequency structure of the vertex

We arrange the Keldysh structure of the two-particle vertex according to the convention [10, 11]

$$\gamma^{\alpha\beta|\gamma\delta} = \begin{pmatrix} (11|11) & (11|21) & (11|12) & (11|22) \\ (21|11) & (21|21) & (21|12) & (21|22) \\ (12|11) & (12|21) & (12|12) & (12|22) \\ (22|11) & (22|21) & (22|12) & (22|22) \end{pmatrix}, \quad (12)$$

where $\alpha, \beta, \gamma, \delta \in \{1, 2\}$ denote Keldysh indices.

Furthermore, we use a channel decomposition,

$$\gamma(\omega'_1, \omega'_2|\omega_1, \omega_2) \approx \bar{v} + \varphi^P(\Pi) + \varphi^X(X) + \varphi^D(\Delta), \quad (13)$$

with the bosonic frequencies given by

$$\Pi = \omega_1 + \omega_2 = \omega'_1 + \omega'_2, \quad (14a)$$

$$X = \omega_2 - \omega'_1 = \omega'_2 - \omega_1, \quad (14b)$$

$$\Delta = \omega_2 - \omega'_2 = \omega'_1 - \omega_1. \quad (14c)$$

The quantity \bar{v} denotes the bare vertex whose Keldysh structure reads [3]

$$\bar{v}^{\alpha'_1\alpha'_2|\alpha_1\alpha_2} = \frac{1}{2}\bar{v} \begin{pmatrix} 0 & 1 & 1 & 0 \\ 1 & 0 & 0 & 1 \\ 1 & 0 & 0 & 1 \\ 0 & 1 & 0 & 1 \end{pmatrix}. \quad (15)$$

The spin and spatial dependence of the antisymmetrized quantity \bar{v} is given by

$$\begin{aligned} \bar{v}_{j'_1j'_2|j_1j_2}^{\sigma'_1\sigma'_2|\sigma_1\sigma_2} &= \delta_{j'_1j_1}\delta_{j'_2j_2}\delta_{\sigma'_1\sigma_1}\delta_{\sigma'_2\sigma_2}U_{j_1j_2}^{\sigma_1\sigma_2} \\ &\quad - \delta_{j'_1j_2}\delta_{j'_2j_1}\delta_{\sigma'_1\sigma_2}\delta_{\sigma'_2\sigma_1}U_{j_1j_2}^{\sigma_1\sigma_2}, \end{aligned} \quad (16)$$

with

$$U_{j_1j_2}^{\sigma_1\sigma_2} = \begin{cases} 0, & \text{if } j_1 = j_2 \text{ and } \sigma_1 = \sigma_2 \\ U_{j_1j_2}, & \text{else.} \end{cases} \quad (17)$$

The quantities $\varphi^P(\Pi)$, $\varphi^X(X)$, $\varphi^D(\Delta)$ denote the contributions of the respective channels. Using general symmetries of the vertex, as well as additional (approximate) symmetries introduced by our chosen approximation of the fRG equations, it can be shown that [3, 9] the form of the resulting Keldysh structure depends on the individual channel and is given by

$$\varphi^P(\Pi) = \begin{pmatrix} 0 & d^P & d^P & 0 \\ a^P & b^P & b^P & a^P \\ a^P & b^P & b^P & a^P \\ 0 & d^P & d^P & 0 \end{pmatrix}(\Pi), \quad (18a)$$

$$\varphi^X(X) = \begin{pmatrix} 0 & d^X & a^X & b^X \\ a^X & b^X & 0 & d^X \\ d^X & 0 & b^X & a^X \\ b^X & a^X & d^X & 0 \end{pmatrix}(X), \quad (18b)$$

and

$$\varphi^D(\Delta) = \begin{pmatrix} 0 & a^D & d^D & b^D \\ a^D & 0 & b^D & d^D \\ d^D & b^D & 0 & a^D \\ b^D & d^D & a^D & 0 \end{pmatrix}(\Delta). \quad (18c)$$

Furthermore, including frequency, spin and spatial structure one finds that these components are not all independent but fulfill additional symmetry relations (see App. B). In thermal equilibrium, it is possible to express all d -components via the complex conjugate of a -components, see (B13). Additionally, the components of the vertex fulfill a FDT [10, 11],

$$b^P = 2i \operatorname{Im}(a^P) \coth\left(\left(\frac{\Pi}{2} - \mu\right)/T\right), \quad (19a)$$

$$b^X = -2i \operatorname{Im}(a^X) \coth\left(\frac{X}{2T}\right), \quad (19b)$$

$$b^D = 2i \operatorname{Im}(a^D) \coth\left(\frac{\Delta}{2T}\right), \quad (19c)$$

leaving the a -components as the only independent part of the Keldysh structure. As a final remark, we emphasize that in the chosen convention $a^P(\Pi)$ and $a^D(\Delta)$ are both retarded, whereas $a^X(X)$ is advanced [10, 11].

3. Frequency parametrization

We now briefly explain the nature of our chosen frequency parametrization and introduce some notations that will be useful in the subsequent sections. Here again, we closely follow the method described in [9], therefore we refer the interested reader to its extensive supplement material. Since we are working in the Keldysh formalism, both the fermionic frequencies in the propagators and self-energy as well as the bosonic frequencies of the vertices are continuous real numbers and one cannot formally distinguish them (as one does in the finite temperature Matsubara formalism). For our numerical treatment, we use two different frequency parametrizations.

The first one discretizes the state of the system, i.e. self-energy and vertices, with N_{freq} underlying frequency points. Since both computation time and allocated memory depend crucially on N_{freq} , this number should be chosen with care. For the explicit implementation of the grid, we proceed then as follows. Within the energy window $[-4\tau, 4\tau]$, corresponding to twice the band width introduced through our tight-binding leads, we choose a linear discretization, outside of this window we use an exponentially-spaced discretization scheme. Of the number N_{freq} of total frequency points, we use roughly 2/3 of them within and 1/3 outside of the linear window. In addition to this underlying grid, we add a number of extra frequencies, which depend upon whether we want to use the grid for the self-energy, the P-channel, or the XD-channel contribution of the vertex. The idea here is that for each of those cases there is a frequency window of special physical interest. For the self-energy, this window is around the chemical potential, and for the vertex channels around the so-called feedback frequency, which equals 2μ in the P- and 0 in the X-channel. In each of these cases we add one extra frequency point at each of these special frequencies. Additionally, in the case of finite temperature, N_T frequencies are added to resolve a frequency window $[-5T, 5T]$ of width $10T$ around the special frequencies. We use $N_{\text{freq}} \sim 1490$ and $N_T = 10$

and have verified that our results are converged w.r.t. these two parameters. While the number of base grid frequencies $N_{\text{freq}} \sim 1490$ was already used in [9], the chosen number of additional frequencies (~ 100) to resolve the temperature window in [9] was much higher than our $N_T = 10$. Our comparatively low choice of this number is due to the fact, that for our study N_T affects the numerical cost much more than for [9], due to the inclusion of the long-range part of the vertex around the feedback frequencies, see Sec. III B 4. However, even with the choice $N_T = 10$, our data is still reasonably converged w.r.t. N_T , see App. G. We use the following notation for the frequency parametrization: We denote the total number of frequency points by N_f for the fermionic grid, and by N_A with $A \in \{P, X\}$, for the bosonic P-, and XD-channel grid. We denote the respective frequency grids by $\omega_f = \{\omega_n\}_{0 \leq n \leq N_f}$ and $\Omega^A = \{\Omega_n^A\}_{0 \leq n \leq N_A}$. We introduce the notation Ω_f^A for the feedback frequency of the bosonic channels, i.e. $\Omega_f^P = 2\mu$ and $\Omega_f^X = 0$. Moreover, we denote the index of the feedback frequency by n_A . Thus, we have $\Omega_{n_P}^P = 2\mu$ and $\Omega_{n_X}^X = 0$.

A second frequency parametrization is utilized to discretize the propagators G and S . In a precomputation step, taking place before the evaluation of the r.h.s. of the FRG flow equations, we evaluate G and S on a very fine grid of approximately $N_{\text{pre}} \sim 30000$ frequency points, using linear interpolation of the self-energy. Whenever a propagator within the r.h.s. of the flow has to be evaluated at a given arbitrary frequency (not necessarily a grid frequency) we use its linearly interpolated value obtained from this fine frequency grid. Concretely, this evaluation always occurs as part of a frequency integration over an internal fermionic frequency ω , see (22), (26) below. Due to the matrix inversion involved in the computation of a propagator from the self-energy, the precomputation method is much faster than computing the propagators separately for each internal frequency occurring in the frequency integration. Compared to the time the actual evaluation of the r.h.s. takes, the time spent for this precomputation is negligible. In order to facilitate the integration, we employ a frequency substitution (see discussion in Sec. III B 5). In all our computations, the fine propagator grid was chosen as a uniform grid in this substituted frequency space.

At the end of this subsection, we summarize the introduced parameters for our frequency grids in Tab. I. The specified values for the number of frequencies will be used for all subsequent calculations, except in App. G, where we discuss the convergence behavior w.r.t. N_T .

B. Extended Coupled Ladder Approximation

1. Spatial short indices and simple eCLA

Having summarized the general Keldysh setup in the previous subsection, we are now in the position to formulate the FRG flow equations using a variation of the eCLA-Method [1]. For this, we first introduce spatial “short” indices l, k and “long” indices j, i , parameteriz-

Table I. Summary of parameters for frequency grids.

Parameter	Description
$N_{\text{freq}} \sim 1490$	Number of basic grid frequencies for self-energy and vertices.
$N_T = 10$	Additional frequencies in the temperature window $[-5T, 5T]$ around the feedback frequencies for the respective vertex channels and the chemical potential for the self-energy.
Ω^A	Resulting frequency grid for channel $A \in \{P, X\}$.
$N_A \sim 1500$	Total number of frequencies in Ω^A .
Ω_f^A	Feedback frequency of channel A : $\Omega_f^P = 2\mu, \Omega_f^X = 0$.
n_A	Index of the feedback frequency of channel A : $\Omega_{n_P}^P = 2\mu, \Omega_{n_X}^X = 0$.
ω_f	Resulting frequency grid for self-energy.
$N_f \sim 1500$	Total number of frequencies in ω_f .
$N_{\text{pre}} \sim 30000$	Total number of frequencies in the fine propagator grid.

ing the spatial structure of the vertices, as:

$$(a^P)_{ji}^{lk}(\Pi) = a_{j(j+l)|i(i+k)}^P(\Pi), \quad (20a)$$

$$(a^X)_{ji}^{lk}(\mathbf{X}) = a_{j(i+k)|i(j+l)}^X(\mathbf{X}), \quad (20b)$$

$$(a^D)_{ji}^{lk}(\Delta) = a_{j(i+k)|(j+l)i}^D(\Delta). \quad (20c)$$

Since the treatment of the full spatial structure of the vertex is numerically too costly, the eCLA scheme restricts the range of the short indices l, k by introducing the feedback-length L , with $|l|, |k| \leq L$. The range of the corresponding long indices j, i is dependent on l, k , respectively, since we require that both j, i and $j+l, i+k$ lie within the central region, i.e.

$$\max(-N, -N-l) \leq j \leq \min(N, N-l) \quad (21a)$$

$$\max(-N, -N-k) \leq i \leq \min(N, N-k). \quad (21b)$$

Generically, the feedback length L should be chosen at least as great as the range of the bare interaction L_U ($L \geq L_U$), such that the spatial structure of all vertex components generated in second-order of the bare interaction can be represented. In practical applications, we view L as an internal numerical parameter in which convergence should be reached. For example, in case of a QPC with onsite-interactions [1] and a static implementation of the eCLA, convergence in the conductance was achieved for $L \approx l_x/a$, where l_x is the characteristic length of the QPC.

However, in this form the eCLA is still too costly to be implemented in a dynamic Keldysh setup, due to the large number of frequencies needed to resolve sharp structures on the real frequency axis: A straightforward parameterization with $N_P = N_X \sim 1500$ bosonic frequencies, as was chosen in [9], is numerically not possible if we want to take a feedback length L into account that

is at least of the order of the characteristic QPC length $L \approx l_x/a \sim 5$, where a is the lattice spacing of the spatial discretization. For this reason, we have to further refine our eCLA scheme, see Sec. III B 4 below. However, to do this efficiently, we first take a look at the structure of the Keldysh-fRG flow equations.

2. Flow equations

In this subsection, we state the general form of the flow equations for self-energy and two-particle vertex. In order to get a feeling for their general structure, we will not write down their full index dependencies, but rather focus on the important aspects. In App. D the flow equations are then given with their full index structure.

Due to the equilibrium symmetries of self-energy and vertex (a thorough discussion of these is included in App. B), we only have to compute the flow of Σ^R and the a components of the vertex. In our presentation here, we will first present the Keldysh and frequency structure and suppress spin and spatial indices. For the self-energy this flow takes the following form

$$\begin{aligned} \partial_\Lambda \Sigma^R(\omega) \hat{=} & \int d\omega' \left\{ S^R(\omega') \left[b^X(\omega' - \omega) + b^D(0) \right] \right. \\ & + S^A(\omega') \left[b^P(\omega' + \omega) + b^D(0) \right] \\ & \left. + S^K(\omega') \left[\frac{1}{2}\bar{v} + a^P(\omega' + \omega) + a^X(\omega' - \omega) + a^D(0) \right] \right\}, \end{aligned} \quad (22)$$

where we have written “ $\hat{=}$ ” instead of “ $=$ ” in order to indicate that we suppressed a (non trivial) spin and spatial structure. Via the relations (9a,10), S^A and S^K can be expressed through S^R and the b components can

be expressed through the a components using the vertex FDTs (19). Therefore, the flow of the retarded self-energy can be expressed solely through S^R and the a components of the vertex. By splitting (22) into a static and a dynamic part, its spatial structure can be expressed using only two pairs of short-long indices (j, l) and (i, k) , see App. D. For each combination of those one has to compute an internal frequency integral. Therefore the computational effort for the self-energy scales like $(2N + 1)^2(2L + 1)^2$.

The flow of the a components of the vertex is of the general structure

$$\partial_\Lambda a^A(\Omega) \hat{=} \tilde{a}^A(\Omega) I^A(\Omega) \tilde{a}^A(\Omega), \quad (23)$$

with $A \in \{P, X, D\}$ and correspondingly $\Omega \in \{\Pi, X, \Delta\}$. Again we have suppressed spatial and spin indices, for details see App. D. In (23), the tilded quantities are given by

$$\tilde{a} \hat{=} \frac{1}{2}\bar{v} + a^A + \phi^B + \phi^C, \quad (24)$$

where ϕ^B, ϕ^C denotes the static feedback from the other two channels, which is chosen as in [9–11], namely $\phi^P = a^P(2\mu)$, $\phi^X = a^X(0)$, $\phi^D = a^D(0)$. The main effort in the vertex flow goes into the computation of the bubble quantities $I^A(\Omega)$, which contain the internal frequency integration. Suppressing spatial and spin structure, these bubbles are of the form

$$I^P = (\tilde{I}^{pp})^{22|21} + (\tilde{I}^{pp})^{22|12} \quad (25a)$$

$$I^X = (\tilde{I}^{ph})^{22|12} + (\tilde{I}^{ph})^{21|22} \quad (25b)$$

$$I^D = -\left[(\tilde{I}^{ph})^{22|21} + (\tilde{I}^{ph})^{12|22} \right], \quad (25c)$$

with

$$(\tilde{I}^{pp})^{\alpha'_1 \alpha'_2 | \alpha_1 \alpha_2}(\Pi) \hat{=} \frac{i}{2\pi} \int d\omega \left[S^{\alpha'_1 \alpha_1}(\omega) G^{\alpha'_2 \alpha_2}(\Pi - \omega) + [S \leftrightarrow G] \right], \quad (26a)$$

$$(\tilde{I}^{ph})^{\alpha'_1 \alpha'_2 | \alpha_1 \alpha_2}(X) \hat{=} \frac{i}{2\pi} \int d\omega \left[S^{\alpha'_1 \alpha_1}(\omega) G^{\alpha'_2 \alpha_2}(\omega + X) + [S \leftrightarrow G] \right], \quad (26b)$$

and the Keldysh convention (11).

Let us now take a look at the spatial structure of (23). We have already seen in (20) that $(a^A)_{ji}^{lk}$ has a blockmatrix structure in position space, with two pairs of short and long indices (l, j) and (k, i) . The same is true for the bubble quantities $(I^A)_{ji}^{lk}$. If we introduce the blockmatrix multiplication in spacial indices

$$[A \cdot B]_{ji}^{lk} = A_{ji_1}^{lk_1} B_{i_1 i}^{k_1 k}, \quad (27)$$

the multiplications appearing between the different factors in (23) are all of this blockmatrix type, although for the D-channel some factors are to be transposed. For details see App. D. In our regime of parameters, the bottleneck in computation time is not the blockmatrix mul-

tiplications in (23) but rather the computation of the bubbles (26). Therefore, as for the self-energy, the leading contribution to computation time for the r.h.s. of the vertex flow scales as $(2N + 1)^2(2L + 1)^2$.

After having specified the flow-equations, the last piece missing to determine the flow completely are the initial conditions. For a finite but large Λ_{ini} (in practice $\Lambda_{\text{ini}} = 10^5 \tau$) they are given by [10, 11]

$$\Sigma_{ij}^{R\sigma\Lambda_{\text{ini}}}(\omega) = \frac{1}{2} \sum_{k\tau} \tilde{v}_{ik|jk}^{\sigma\tau|\sigma\tau}, \quad (28)$$

$$a^{P\Lambda_{\text{ini}}} = a^{X\Lambda_{\text{ini}}} = a^{D\Lambda_{\text{ini}}} = 0. \quad (29)$$

3. Bubble symmetries

Since the evaluation of the bubble integrals in (26) will be the most expensive part of the fRG flow, we briefly comment on simplifications occurring due to symmetry relations of the bubbles. While we refer the interested reader again to App. D for details, it turns out that we only need to compute two Keldysh components of the bubbles (26), namely

$$I^{pp} = (\tilde{I}^{pp})^{22|21}, \quad (30a)$$

$$I^{ph} = (\tilde{I}^{ph})^{22|12}. \quad (30b)$$

Thus generically, we have to compute 8 integrals of the type given in (26), namely $(I^{pp})^{\sigma\tau}$ and $(I^{ph})^{\sigma\tau}$ for all possible spin combinations of $\sigma, \tau = \pm \uparrow, \downarrow$. In thermal equilibrium, the propagators G and S for our system are symmetric in position space (see discussion in App. A), i.e.

$$G_{ji}^{\sigma}(\omega) = G_{ij}^{\sigma}(\omega) \quad (31a)$$

$$S_{ji}^{\sigma}(\omega) = S_{ij}^{\sigma}(\omega). \quad (31b)$$

Due to this property, the bubbles satisfy

$$I_{ji}^{lk} = I_{ij}^{kl}. \quad (32)$$

This implies that we only have to compute the components of the bubble with $k \geq l$, and for $l = k$ only the components with $i \geq j$.

A further great simplification occurs in the case of zero magnetic field: Here we only need to compute the two integrals $(I^{pp})^{\uparrow\uparrow}$ and $(I^{ph})^{\downarrow\downarrow}$.

4. Dynamic feedback length

Now that we have obtained the fRG equations, we can proceed to tackle the problem identified in Sec. III B 1: the huge numerical cost arising from the combination of high frequency resolution in the vertex ($N_A \sim 1500$) with a finite feedback length on the scale of the QPC length $L \sim l_x/a \sim 5$ sites. Our Ansatz to overcome this challenge is to introduce for each channel A two individual feedback lengths, a static one, L_s^A , and a dynamic one, $L^A(\Omega)$, which depends on the bosonic frequency Ω of the respective channel and decreases with increasing difference between Ω and the feedback frequency Ω_f^A . We choose these feedback lengths in such a way that $L^A(\Omega) \leq L_s^A$ for all Ω and that at the feedback frequency $L^A(\Omega_f^A) = L_s^A$ holds. Our strategy is now the following: For each dynamic block-matrix quantity $M^A \in \{a^A, I^A\}$, we compute the components $M_{ji}^{Alk}(\Omega)$ (we suppress spin indices in this subsection) only for the spatial and frequency grid points for which $|l|, |k| \leq L^A(\Omega)$ holds. Thus, using the dynamic feedback length, we can restrict the numerical effort to obtain and store the spatial structure of these quantities for each frequency individually. On the other hand, if we have to evaluate M^A in a computation for a short-index $|l|$ or $|k|$ greater than $L^A(\Omega)$, we

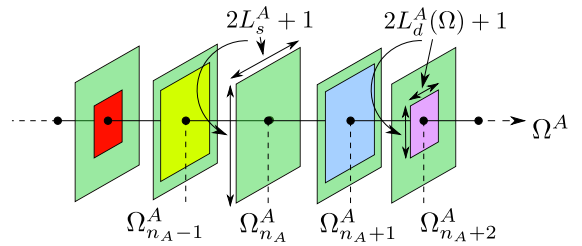


Figure 2. Illustration of the dynamic feedback length $L^A(\Omega)$. The vertex contribution at the feedback frequency is depicted in green, contributions at other frequencies are shown in different colors. Note that for frequencies $\Omega \neq \Omega_{n_A}^A$, vertex contributions beyond the dynamic feedback length $L^A(\Omega)$ but within the static feedback length L_s^A are replaced by the green feedback contributions.

apply the following rule:

$$M_{ji}^{Alk}(\Omega) = \begin{cases} 0, & \text{if } |l| > L_s^A \text{ or } |k| > L_s^A \\ M_{ji}^{Alk}(\Omega_f^A), & \text{else.} \end{cases} \quad (33)$$

Thus, if we do not have the dynamic value for a combination of short indices (l, k) available, we replace it, if possible, by the corresponding value at the feedback frequency. Otherwise we have to set it to zero. A schematic illustration of this procedure is given in Fig. 2. In the special case $L^A(\Omega) = L$ for all Ω and $A \in \{P, X\}$, we recover the simple eCLA scheme described in III B 1.

Using this extended scheme, we are able to include a long-range contribution at physically important frequencies, namely the ones around the feedback frequencies $\Pi = 2\mu$ in the P- and $X = 0$ in the XD-channel. Those frequencies can be shown to have the biggest contribution to low-energy observables like the linear conductance. A short argument for this can be found in App. E. For all other frequencies we can treat the long-range feedback in a static manner, similar to the treatment in [1]: Everytime, we have to evaluate the long-range contribution at one of those frequencies, we will simply replace it by its value at the feedback frequency of the respective channel.

This approximation is admittedly quite crude. However, note that many previous treatments that were even cruder, e.g. treating the vertex only statically altogether, still led to reasonable results. In this sense, our semi-static treatment should be understood as the next step on the way to a more quantitatively reliable method. The approximation could be improved by not using the values at the feedback frequency, but the values at the edge of the region that was parametrized in detail when going beyond that region. However, in our view, such a more refined treatment would only be warranted if at the same time one also refrained from making the channel decomposition of the vertex. Recall that the channel decomposition tracks only a single frequency argument per channel and evaluates the contributions from the other two channels only at the feedback frequency. The errors incurred in this manner seem to be comparable to the ones incurred by the approximation of Eq. (33). A more sophisticated parametrization of the frequency dependence

is left for future work.

The remaining question is how to choose the frequency dependence of the dynamic feedback length $L^A(\Omega)$. Note that generically, for this scheme to be formally exact in second-order in the bare interaction, $L^A(\Omega)$ would have to be chosen greater than L_U for all frequencies in the grid. However, this is exactly the situation we want to avoid with this construction: The hope is that the relevant (low energy) physics can already be captured with a (much) smaller dynamic feedback length when evaluating quantities away from their respective feedback frequencies. Thus our goal is to choose a sequence of parameterizations $L_n^A(\Omega)$ that (a) formally converges pointwise to $2N$ (the maximal value of the feedback length): $\lim_{n \rightarrow \infty} L_n^A(\Omega) = 2N$, and (b) achieves a much quicker convergence than the formal one in low-energy observables, yielding an efficient low-energy description. In principle, one is free to choose such a sequence in any way one likes. In this work, we use a very simple treatment, with a parameterization $L^A(\Omega)$ characterized by only two numerical integer parameters, $L \geq 0$ and $N_L \geq 0$, where $2N_L + 1$ sets the window of frequencies around Ω_f^A within which we treat the long-ranged part of the vertex dynamically. In fact, we here choose these two parameters channel independent and refer to L as *the* feedback length and N_L as the number of long-range frequencies. Physically, the contributions around the feedback frequency Ω_f^A are most important, i.e. there it is important to resolve the long-range structure in frequency. We call this frequency range Θ_A^f and choose it in a symmetric fashion around the feedback frequency via $\Theta_A^f = [\Omega_{n_A - N_L}^A, \Omega_{n_A + N_L}^A]$. Therefore we set $L^A(\Omega) = L$ for all $\Omega \in \Theta_A^f$. Away from the feedback frequency, we expect a static treatment of the long-range structure to be acceptable, therefore we set the dynamic feedback length $L^A(\Omega) = 0$ for all $\Omega \notin \Theta_A^f$. In the limit of large L and N_L , we recover the full channel decomposed description of the vertex as given in (13).

Note that for a fixed finite $L > 0$, and for all observables that depend only on the low energy properties of the system (like e.g. the linear conductance) this method interpolates between two extreme cases: As discussed above, for a large number of long-range frequencies N_L , the results of this method converge to the results obtained without static long-range feedback. On the other hand, for $N_L = 0$ (i.e. the only long-range contributions live at the feedback frequencies) this method still already incorporates the spatial structure of the long-range feedback L , even though only statically. Loosely speaking, this $N_L = 0$ case results from the simplest possible combination of the previous dynamic work on Keldysh-fRG [9] and the static eCLA implementation in [1]. By further increasing N_L , we can deepen the combination between those approaches and create more reliable dynamic results.

At the end of this subsection, we summarized the introduced numerical parameters for the dynamic feedback length in Tab. II.

Table II. Summary of parameters for dynamic feedback length

Parameter	Description
$L^A(\Omega)$	Dynamic feedback length. Controls the spatial extent of the vertex that is taken into account at frequency Ω .
L_s^A	Static feedback length, $L_s^A = L^A(\Omega_{n_A}^A)$. For all other frequencies Ω we have $L^A(\Omega) \leq L_s^A$.
Θ_A^f	Frequency range around the feedback frequency, for which $L^A(\Omega)$ is non-vanishing. Concretely, $L^A(\Omega) = L$ for $\Omega \in \Theta_A^f$ and zero otherwise.
N_L	$2N_L + 1$ is the number of frequencies in Θ_A^f . Concretely, $\Theta_A^f = [\Omega_{n_A - N_L}^A, \Omega_{n_A + N_L}^A]$.

5. Further implementational details

The coupled system of flow equations (D2,D3) and (D10) was solved with a standard fourth-order Runge-Kutta ODE solver. The integration over frequencies on the r.h.s. of the flow equations was carried out using Gaussian quadrature with Patterson sets [13]. In order to facilitate the computation, we used a substitution of the real frequency axis to the interval $(-7, 7)$, which transforms the integrand in such a way that (integrable) poles are avoided and the integrand becomes finite on the whole interval $(-7, 7)$. This substitution is a slightly modified version of the one used in [9], see [14] for details. The most time-consuming part of the calculation is the evaluation of the r.h.s. of the flow equations, especially the computation of the bubble integrals in the vertex- (D4) and self-energy flow (D2,D3). In order to speed up computation time, we used a hybrid MPI + OMP implementation, parallelizing the computation of the self-energy bubble in external frequencies ω and the vertex bubbles $I^{lk}(\Omega)$ both in external frequency Ω and additionally in the short-indices l, k . Furthermore, we also parallelized the block-matrix multiplication appearing on the r.h.s. of the flow in the short-indices l, k .

C. Conductance Computation

The main observable of interest for us is the linear conductance g . In order to compute it, we use a formula first derived by Oguri [15]. We employ its convenient Keldysh formulation developed in [12], whose notational conventions we have also adopted in this work. Within this formulation the conductance g can be expressed as

$$g = g_1 + g_2, \quad (34)$$

with the one-particle contribution

$$g_1 = -\frac{e^2}{h} \int_{-\infty}^{\infty} d\epsilon f'(\epsilon) \text{Tr}\{\Gamma^l(\epsilon)G^R(\epsilon)\Gamma^r(\epsilon)G^A(\epsilon)\} \quad (35)$$

and the two-particle contribution $g_2 = g_{2\Sigma} + g_{2\Phi}$, with

$$g_{2\Sigma} = \frac{2e^2}{h} \int d\epsilon f'(\epsilon) \text{Tr} \{ \Gamma^l(\epsilon) G^R(\epsilon) \text{Im} \Sigma^R(\epsilon) G^A(\epsilon) \}, \quad (36a)$$

$$g_{2\Phi} = \frac{e^2}{h} \int d\epsilon f'(\epsilon) \text{Tr} \{ \Gamma^l(\epsilon) G^A(\epsilon) \tilde{\Phi}^l(\epsilon) G^R(\epsilon) \}. \quad (36b)$$

Here, f' denotes the derivative of the Fermi distribution w.r.t. energy ϵ , $\Gamma^r(\epsilon)_{ij} = \delta_{iN} \delta_{jN} \Gamma(\epsilon)$, $\Gamma^l(\epsilon)_{ij} = \delta_{-N_i} \delta_{-N_j} \Gamma(\epsilon)$, with $\Gamma(\epsilon) = \theta(2\tau - |\epsilon|) \sqrt{4\tau^2 - \epsilon^2}$, are the hybridization functions for the right/left lead, $2 \text{Im} \Sigma^R = -i(\Sigma^R - \Sigma^A)$ and $\tilde{\Phi}^r(\epsilon)$ is the vertex correction term.

This term encodes the direct contribution of the two-particle vertex to the conductance. It is given by (c.f. [12], Eq. (20))

$$\begin{aligned} (\tilde{\Phi}^{l/r})_{j_2' j_2}^{\sigma_2}(\epsilon) &= \frac{1}{2\pi i} \int d\epsilon' \sum_{j_1', j_1} \left[G^A(\epsilon') \Gamma^{l/r}(\epsilon') G^R(\epsilon') \right]_{j_1 j_1'}^{\sigma_1} \\ &\times K_{j_1' j_2' | j_1 j_2}^{\sigma_1 \sigma_2 | \sigma_1 \sigma_2}(\epsilon, \epsilon', 0). \end{aligned} \quad (37)$$

The vertex response part $K_{j_1' j_2' | j_1 j_2}^{\sigma_1 \sigma_2 | \sigma_1 \sigma_2}(\epsilon, \epsilon', 0)$ can be brought into the form (using the vertex FDTs (19))

$$K_{j_1' j_2' | j_1 j_2}^{\sigma \sigma | \sigma \sigma}(\epsilon, \epsilon', 0) = 2i \left[\text{Im}(a^p)_{j_1' j_1}^{\sigma \sigma (j_2' - j_1') (j_2 - j_1)}(\epsilon' + \epsilon) f^p(\epsilon, \epsilon') - \text{Im}(a^d)_{j_1' j_1}^{\sigma \sigma (j_2 - j_1') (j_2' - j_1)}(\epsilon' - \epsilon) f^x(\epsilon, \epsilon') \right] \quad (38a)$$

$$K_{j_1' j_2' | j_1 j_2}^{\sigma \sigma | \bar{\sigma} \bar{\sigma}}(\epsilon, \epsilon', 0) = 2i \left[\text{Im}(a^p)_{j_2' j_2}^{(j_1' - j_2') (j_1 - j_2) \sigma \bar{\sigma}}(\epsilon' + \epsilon) f^p(\epsilon, \epsilon') - \text{Im}(a^x)_{j_2' j_2}^{(j_1' - j_2') (j_1 - j_2) \sigma \bar{\sigma}}(\epsilon' - \epsilon) f^x(\epsilon, \epsilon') \right] \quad (38b)$$

$$K_{j_1' j_2' | j_1 j_2}^{\sigma \bar{\sigma} | \sigma \bar{\sigma}}(\epsilon, \epsilon', 0) = 2i \left[\text{Im}(a^p)_{j_1' j_1}^{(j_2' - j_1') (j_2 - j_1) \sigma \bar{\sigma}}(\epsilon' + \epsilon) f^p(\epsilon, \epsilon') + \text{Im}(a^x)_{j_1' j_1}^{(j_2 - j_1') (j_2' - j_1) \sigma \bar{\sigma}}(\epsilon - \epsilon') f^x(\epsilon, \epsilon') \right], \quad (38c)$$

with the functions $f^p(\epsilon, \epsilon') = 2f(\epsilon') + 2b(\epsilon' + \epsilon - \mu)$ and $f^x(\epsilon, \epsilon') = 2f(\epsilon') + 2b(\epsilon' - \epsilon + \mu)$. Here $b(\epsilon) = 1/(e^{\beta(\epsilon - \mu)} - 1)$ denotes the Bose distribution.

Fig. 3 shows the resulting conductance for a generic set of parameters. Fig. 3(a) depicts the two-particle contributions g_2 , $g_{2\Sigma}$, and $g_{2\Phi}$. In particular, note that for small values of the chemical potential μ , the total two-particle contribution becomes negative. This carries over to the total conductance, see Fig. 3(b): At pinch-off, the one particle-contribution g_1 vanishes and thus the negative two-particle part g_2 leads to a negative conductance g . This behavior is clearly unphysical, as the total conductance should vanish below pinch-off. The cause of this problem has to stem from the two major approximations that we applied: The channel decomposition (13) and the general second-order fRG truncation. Especially the latter is known to lead to a violation of the law of current conservation and Ward identities (see App. F for a more detailed discussion). In particular, the Ward identity

$$\tilde{\Phi}^l(\epsilon) + \tilde{\Phi}^r(\epsilon) = -2 \text{Im} \Sigma^R(\epsilon), \quad (39)$$

derived in [12], is violated in our approximation scheme, leading to unphysical results for transport quantities [14]. To ameliorate this problem, we replace the vertex contributions $\tilde{\Phi}^{l/r}$ by ‘‘Ward-corrected’’ versions,

$$\tilde{\Phi}_{ij}^{l/r, W}(\epsilon) = \tilde{\Phi}_{ij}^{l/r}(\epsilon) F_{ij}(\epsilon), \quad F_{ij}(\epsilon) = \frac{-2 \text{Im} \Sigma_{ij}^R(\epsilon)}{(\tilde{\Phi}^r + \tilde{\Phi}^l)_{ij}(\epsilon)}. \quad (40)$$

The multiplicative factor F_{ij} nominally equals 1 if $\tilde{\Phi}^{l,r}$ satisfy the Ward identity (39) with $\text{Im} \Sigma^R$. If they do not, it by construction ensures that $\tilde{\Phi}^{l/r, W}$ do,

$$\tilde{\Phi}^{l, W}(\epsilon) + \tilde{\Phi}^{r, W}(\epsilon) = -2 \text{Im} \Sigma^R(\epsilon), \quad (41)$$

thereby compensating the adverse consequences of the second-order truncation scheme. (To avoid numerical errors arising from division by very small numbers, we set $F_{ij}(\epsilon) = 1$ whenever its denominator becomes smaller than 10^{-8} ; the results are not sensitive to the value of this bound.) The sum of (36a) and (36b), with $\tilde{\Phi}^l$ replaced by $\tilde{\Phi}^{l, W}$ in the latter, yields

$$g_2^W = -\frac{e^2}{h} \int_{-\infty}^{\infty} d\epsilon f'(\epsilon) \text{Tr} \{ \Gamma^l(\epsilon) G^A(\epsilon) \tilde{\Phi}^{r, W}(\epsilon) G^R(\epsilon) \}. \quad (42)$$

Note that the integrand is proportional to $\tilde{\Phi}^r$. This property ensures that the conductance vanishes at pinch-off, as can be seen by the following argument. Assume that the QPC is closed, i.e. the chemical potential μ is below the QPC barrier. Then in the integral (42) only frequencies ϵ below the QPC barrier contribute, implying that the propagators $G_{ij}^{R/A}(\epsilon)$ are only non-vanishing for spatial indices i, j on the same side of the barrier. Therefore, since the hybridization function $\Gamma^l(\epsilon)$ lives on the left side of the system, only contributions of $\tilde{\Phi}_{ij}^r(\epsilon)$ contribute where i, j are on the left side of the barrier. However, applying the same logic in the definition of $\tilde{\Phi}^r(\epsilon)$ (37), we see that $\tilde{\Phi}_{ij}^r(\epsilon)$ is only non-vanishing for i, j on the right side of the barrier. Therefore, the two-particle part of the conductance vanishes at pinch-off. Indeed, this is confirmed by the violet curves in Fig.3(c,d), computed using Eq. (42) for g_2^W .

All conductance results shown in the subsequent sections are obtained using the Ward-corrected two-particle contribution (42).

Note that if one evokes the Ward identity (39) without replacing $\tilde{\Phi}^{l/r}$ by $\tilde{\Phi}^{l/r, W}$, the sum of (36a) and (36b)

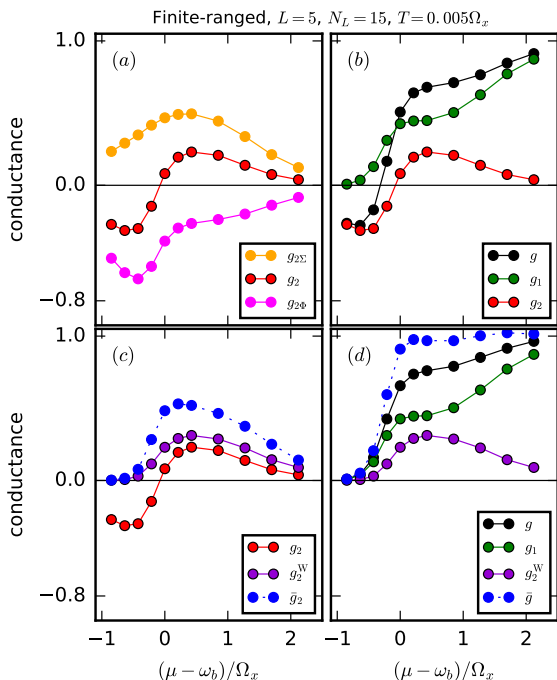


Figure 3. Conductance obtained via straightforward application of formulas (35-36). (a) Two-particle contributions $g_2 = g_{2\Sigma} + g_{2\Phi}$ [Eq. (36)]. (b) Single- and two-particle contributions to the total conductance $g = g_1 + g_2$ [Eq. (34-36)]. Note that both g_2 and g are negative at pinch-off. (c) Comparison of g_2 to g_2^W and \tilde{g}_2 ; the latter two go to zero at pinch-off. (d) Single-particle and Ward-corrected two-particle contributions to the total conductance $g = g_1 + g_2^W$. For comparison we also show $\tilde{g} = g_1 + \tilde{g}_2$.

yields an expression for g_2 similar to (42), but containing $\tilde{\Phi}^r$ instead of $\tilde{\Phi}^{r,W}$. This expression \tilde{g}_2 , which corresponds to the second term in Eq. (23) of [12], also vanishes at pinch-off, see Fig. 3(c,d). However, we believe it to be unreliable when used in conjunction with second-order-truncated fRG, since the latter, as mentioned above, yields results for $\tilde{\Phi}^{l,r}$ which (in contrast to $\tilde{\Phi}^{l/r,W}$) violate the Ward identity used for its derivation.

IV. RESULTS

In this section, we investigate the features one obtains for a QPC with a finite-ranged interaction of the type described in Sec. II. The section is divided into two parts. In the first part, we present results obtained with a dynamic treatment of the short-range part and a static treatment of the long-range part of the vertex. In the second part, both short-range and long-range contributions of the vertex are treated dynamically.

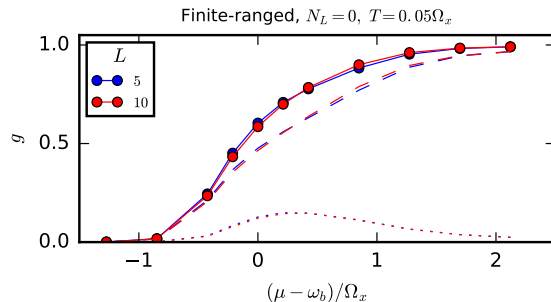


Figure 4. Conductance for large feedback lengths $L = 5, 10$ (solid curves), computed using a static treatment of the long-range part of the vertex, i.e. using $N_L = 0$. Dashed and dotted curves indicate the one- and two-particle contribution, respectively. As in the static Matsubara case, we see that $L = 5$ is sufficient to achieve convergence.

A. Static long-range part

The results of this first subsection are obtained using $N_L = 0$, i.e. by a direct combination of the dynamic treatment of the short-range part [9] and the static treatment of long-range part of the vertex [1]. As discussed in Sec. III B, introducing a finite-ranged interaction necessitates the introduction of the feedback length L , measuring the range over which the vertex develops structure during the RG flow. In [1], we have shown that in the static Matsubara setup convergence in L was reached for $L \sim l_x/a$ and $L > L_U$, where l_x is the characteristic QPC length and L_U the range of the interaction. In our new Keldysh formulation, this statement remains true. As an example, Fig. 4 shows a typical conductance curve for our generic finite-ranged interaction from Sec. II, computed at a finite temperature $T = 0.05\Omega_x$. We see that convergence is reached around $L = 5 \approx l_x/a$. In the rest of this work, we always use $L = 5$ if not explicitly stated otherwise.

Having assured the convergence w.r.t. the feedback length, we can now compare the implication of finite-ranged interactions on the conductance within a *static* long-range feedback description. For this, we compare a typical onsite-interaction model (here we use the same parameters as used in [9], in particular onsite $U = 0.7\tau$) with a model with finite-ranged interactions. The form of the interaction is here chosen as introduced in Sec. II, i.e. with a onsite interaction strength $U = 0.5\tau$ and exponentially screened offsite components, reaching an interaction range of $L_U = 3$. Therefore, a particle in the center of the QPC can directly interact with a particle outside the center, being half the characteristic QPC length away. The resulting conductances are shown in Fig. 5. Fig. 5(a) displays the conductance of the onsite model, which is qualitatively very similar to the one obtained in [9], even though we here use a finite feedback length L . It is important to mention that in [9] this onsite interaction strength was chosen as large as possible without causing a

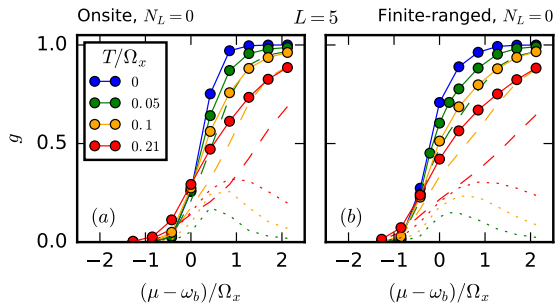


Figure 5. Temperature dependence of the conductance (solid curves) for a model with (a) onsite interactions and (b) finite-ranged interactions ($L_U = 3$), computed using a feedback length $L = 5$ and static long-range part $N_L = 0$. Dashed and dotted curves indicate the one- and two-particle contributions, respectively. In the finite-ranged case (b) the conductance shows a slightly stronger flattening in the 0.7 region than in the onsite case (a). However, the form of the curves is still quite similar.

failure of convergence for the RG flow. However, even in this maximal interaction strength case, no development of a pronounced 0.7-shoulder with increasing temperature was observed. In Fig. 5(b) we use a finite-ranged interaction. The only difference compared to part (a) is that the conductance curves are slightly more asymmetric, indicating that due to its finite range, the amount of interaction that can be taken into account with fRG is larger. However, there is still no pronounced shoulder in the conductance. In the next subsection, we will see that this changes when taking a dynamic contribution of the long-range part into account.

B. Dynamic long range part

In this section, we will extend our study by treating the long-range part of the vertex dynamically within a certain window of frequencies. As explained in Sec. III B, this window is controlled numerically by the number, N_L , of frequency points around the feedback frequencies for which the long-range part is taken into account. However, there is a caveat: Our frequency parametrization is not strictly uniformly spaced, especially around the feedback frequencies we have to distinguish two scales, c.f. Sec. III A 3. The smaller scale is set by temperature, and we use $N_T = 10$ frequencies distributed on that scale around the feedback frequency to resolve the temperature dependence. The other relevant scale is set by the curvature Ω_x , which is resolved by our underlying equally spaced general frequency grid, introduced in Sec. III A 3. Therefore, when we increase N_L up to ~ 5 we take only the vertex contribution in a frequency range set by temperature into account. A further increase of N_L then begins also to resolve the Ω_x scale, which sets the scale of the characteristic width of the conductance step.

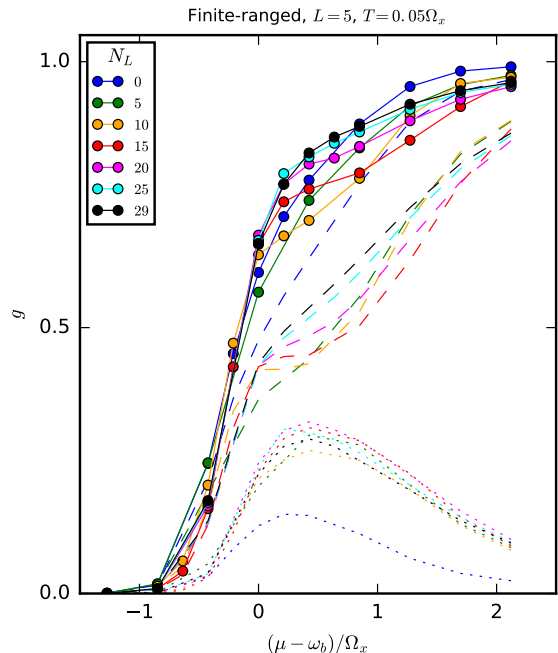


Figure 6. Dependence of the conductance on increasing N_L , which controls the width of the frequency window within which the long-ranged part of the vertex is treated dynamically, at finite $L = 5$. While, within our numerical resources, convergence in N_L could not be fully reached, finite values of N_L seem to lead to a more prominent 0.7-feature than in the onsite case: This is most pronounced for medium $N_L = 10, 15$ and still noticeable at large $N_L = 25, 29$.

Concretely, the half-width of the frequency range of the long-range vertex is given by $\Delta\omega = 0.8\Omega_x$ for $N_L = 10$ and increases roughly by $0.8\Omega_x$ per additional increase of 5 in N_L . Thus, the biggest value $N_L = 29$ corresponds to a maximal frequency range of $\Delta\omega = 3.8\Omega_x$. Furthermore, one can show that the leading frequency contribution to the conductance at the chemical potential μ lies around the feedback frequencies in a range determined by $\epsilon_F = \mu - V_b$ (c.f. App. E), i.e. it is on a scale set by Ω_x . Between $N_L = 10$ and $N_L = 15$, $\Delta\omega$ becomes bigger than Ω_x . Thus, starting from $N_L = 15$, we take all leading frequency contributions into account for values of the chemical potential reaching the shoulder region, c.f. Fig. 6.

The dependence of the resulting conductance on N_L for a typical set of parameters is shown in Fig. 6. Although, we were not able to reach completely converged results at our maximal value $N_L = 29$ (after which we hit the memory bound of our computational resources), there seems to be a persistent feature for large N_L : Going from $N_L = 0$ (the static long-range result from last section) up to finite $N_L = 29$, we observe a qualitative difference in the conductance. In the second half of the conductance step a shoulder-like structure emerges, resembling the 0.7-anomaly observed at finite temperature in var-

ious experiments [4, 7, 8, 16–18]. This feature is most pronounced for $N_L = 10 - 15$, when just the leading frequency contribution is taken into account and relaxes somewhat for larger N_L . However, as we will show below, even for $N_L = 29$ the 0.7-feature is still much more prominent than in the onsite case.

When decomposing the conductance in one- and two-particle contributions (dashed and dotted lines in Fig. 6), we see that this 0.7-feature comes from two effects: (i) In the shoulder region, the one-particle part itself exhibits a kink at a conductance value around $g \sim 0.4$. This feature is very strongly pronounced for $N_L = 10$ and seems to weaken somewhat for larger N_L . Note here that near pinch-off the differences between curves with different N_L are small and become larger starting when μ reaches the shoulder region. This behavior is consistent with our discussion in App. E. (ii) The two-particle contribution increases steeply from pinch-off towards its maximum in the shoulder region and decreases after that. This feature seems to be almost equally pronounced for all large $N_L = 15 - 29$. Both of these effects lead to the development of a shoulder-like structure in the conductance.

Concluding this discussion, we point out another interesting effect. Even if the one- and two-particle parts themselves are still subject to changes in N_L , these changes seem to mostly cancel out each other. The resulting conductance seems to be much lesser dependent on N_L : Comparing the magenta ($N_L = 20$), cyan ($N_L = 25$), and black lines ($N_L = 29$) in Fig. 6, the $N_L = 29$ data seem almost converged in the shoulder region. In fact, apart from the precise position of the shoulder, the qualitative shape of all three curves is already very similar. Intuitively this effect makes sense: If a particle traverses the QPC and contributes directly to the conductance via the one-particle contribution it is less likely to have given energy to create particle-hole excitations which might contribute to the two-particle part of the conductance and vice versa.

In the following, we study the dependence of the 0.7-feature on temperature, interaction range and interaction strength. For this, we will always compare the onsite interaction result with the finite-ranged results for both the leading frequency case at $N_L = 15$, where the 0.7-structure is most pronounced, as well as for the full $N_L = 29$ result.

Above we have established the development of a 0.7-shoulder in the finite-ranged interaction model when treating the long-range contributions of the vertex dynamically. In Fig. 7, we study how finite-ranged interactions affect the temperature dependence of the conductance. We see that the form of the onsite-conductance in Fig. 7(a) is still the same as in Fig. 5(a,b). However, in Fig. 7(b,c), we see that for finite-ranged interactions increasing temperatures lead to a more and more pronounced 0.7-plateau. As above, we see that in the $N_L = 15$ case the 0.7-feature is most pronounced, however also for $N_L = 29$ it is much stronger than in the onsite case. In addition to having a different shape, the

conductance also depends much more strongly on temperature itself. We see that finite-ranged interactions, if treated dynamically, have the potential to introduce major changes compared to onsite interactions and are likely to be essential ingredients in the development of a pronounced 0.7-plateau. This finding constitutes the main result of this paper.

While we believe that the qualitative behavior of the conductance is captured correctly within our approach, we still want to comment on two inaccuracies: In the $N_L = 29$ case, the $T = 0.1\Omega_x$ curve exhibits a slight kink in the 0.7-structure, which can be traced back to a peak in the two-particle contribution. This is probably an artifact of our method, indicating that for this parameter regime an improvement of the vertex description is in order: While it could be that simply a larger value of N_L is needed to converge to a smooth result, it might also be possible that for a more accurate description one would have to improve the vertex treatment altogether. We comment on one possible way to do this below. Another problem that we can observe in Fig. 7(b,c) is a (slight) pinch-off shift to lower chemical potentials, i.e. the QPC with finite-ranged interactions opens up earlier than the one with onsite interactions or even the one without interactions. This unphysical behavior, an artifact of our method, was also encountered in our earlier work in the Matsubara context [1]. It will be interesting to see, whether further improvements of the vertex treatment succeed in eliminating this unphysical shift.

Further insight can be gained by looking at the resulting local density of states (LDOS) of the interacting system. First of all, this yields an intrinsic consistency check, by inspecting how well the LDOS satisfies the normalization condition $\int d\omega \mathcal{A}_i(\omega) = 1$, see Fig. 8. Note that the normalization condition is relatively well satisfied in the center of the QPC (where the relevant physics for transport happens) and is off in the flanks of the QPC. This is somewhat to be expected, since we utilized our numerical resources in such a manner as to best resolve the position and frequency dependence in the center region, i.e. for frequencies close to barrier top and chemical potential. For up to site $15 \approx 3l_x/a$ the LDOS normalization is fulfilled well, which is exactly the region of the renormalized flat barrier top, as we will see below. Beyond that most of the LDOS contribution sits deeper in the flanks of the QPC away from the barrier top and the region of good resolution. Within the region of the barrier top itself, the leading frequency contribution $N_L = 15$ seems to be yielding the best results.

Having checked the LDOS normalization, we next discuss the frequency resolved LDOS structure. Fig. 9 shows the LDOS $\mathcal{A}_i(\omega)$ as a colorplot depending on frequency and site index of the effective QPC barrier. Comparing the onsite result (a) to the finite-ranged results (b,c) shows that the latter exhibit a stronger flattening. This behavior is qualitatively consistent with our static Matsubara treatment, which also suggested a flatter barrier top for finite-ranged interactions. Just as the conductance earlier, this indicates again that here more interaction processes are taken into account. Comparing the

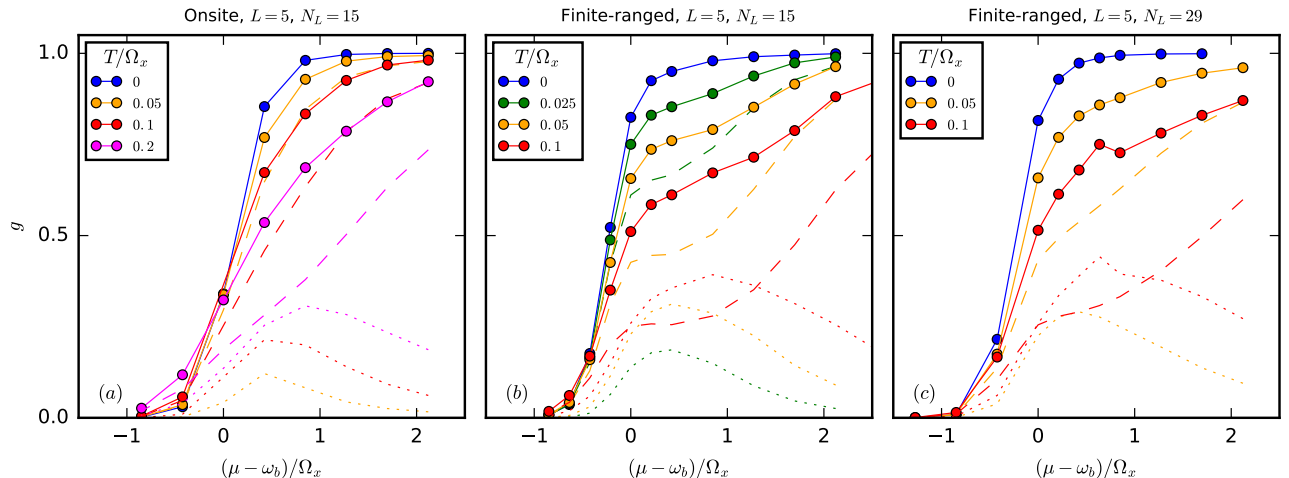


Figure 7. Temperature dependence of the conductance for (a) onsite and (b) finite-ranged interactions with $N_L = 15$ and (c) $N_L = 29$. In contrast to the onsite case, the finite-ranged conductance shows a much more pronounced 0.7-feature: While for $N_L = 15$ in (b) an actual shoulder emerges, the full $N_L = 29$ result in (c) is still much more asymmetric than the onsite-case.

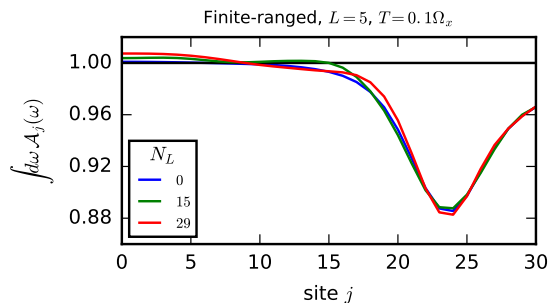


Figure 8. LDOS normalization in the plateau region ($\mu - \omega_b$)/ $T = 0.4$ for finite interaction range for different parameters N_L . In the QPC center the normalization condition $\int d\omega \mathcal{A}_j(\omega) = 1$, is satisfied much better than in the flanks.

two finite-ranged results, the $N_L = 15$ result exhibits a stronger van Hove ridge peak than the $N_L = 29$ result. Applying the rationale developed in [4], this is consistent with the more pronounced 0.7-structure in the conductance in Fig. 7.

Aside from the form of the renormalized barrier in the 0.7-regime of the conductance step, one can also look at the development of this barrier when varying the chemical potential. For this we plot in Fig. 10 the LDOS on the middle site $\mathcal{A}_0(\omega)$ as function of frequency and chemical potential, analogously to Fig. (5) of [9]. We see that when the chemical potential (black line) crosses the barrier top ω_b , the van Hove ridge of the interacting LDOS increases with it. This pinning is much more pronounced for the finite-ranged case [Fig. 10(b,c)] than for the onsite-case [Fig. 10(a)]. Again, this indicates the presence of more

interaction processes in the case of finite-ranged interactions.

Up to now, we always used the same finite-ranged interaction with an interaction range on the scale of the characteristic length of the QPC and a strength that had been chosen ad hoc. A systematic study of how these properties affect the QPC conductance is beyond the scope of this work. However, in the very last part of this subsection, we will take a first brief look what happens when these parameters are changed. Fig. 11 shows the influence of a variation in the interaction range. With increasing interaction cutoff L_U , the conductance changes from the onsite $L_U = 0$ to the $L_U = 3$ results discussed earlier. We see that the 0.7-feature becomes more pronounced, while at the same time the unphysical pinch-off shift mentioned above occurs.

Fig. 12, instead shows the dependence of the conductance on increasing interaction strength with fixed range $L_U = 3$. Here, we keep the ratio of onsite- and offsite-interaction strength $U_0/U_1 = 5/3$ fixed and increase U_0 from 0.3τ beyond our usual value 0.5τ to the large value 0.7τ . With increasing interaction strength, the form of the conductance becomes more asymmetric and the 0.7-structure eventually develops a oscillatory feature. Similar to the observations discussed above, this is very pronounced for the leading frequency contribution ($N_L = 15$) and less visible for $N_L = 29$. Again the unphysical pinch-off shift in the chemical potential is clearly visible.

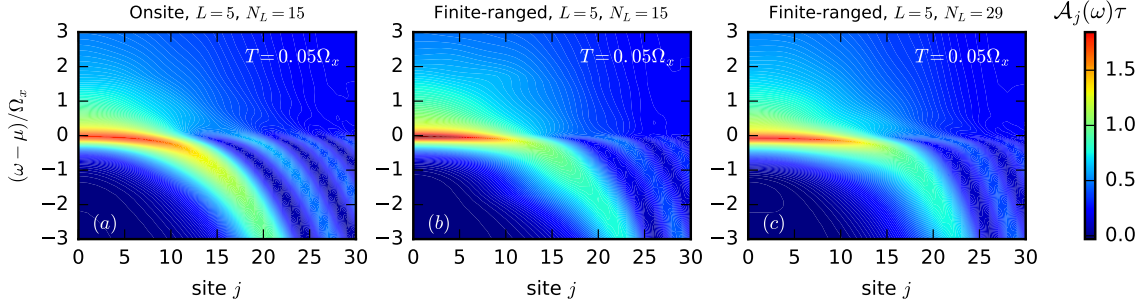


Figure 9. QPC LDOS as function of site and frequency for (a) onsite-, and finite-ranged interactions with (b) $N_L = 15$ and (c) $N_L = 29$. Note that in (b) and (c) the renormalized barrier top is much flatter than in the onsite case. For the $N_L = 15$ case in (b), the LDOS peak in the middle of the QPC is slightly more pronounced than in the $N_L = 29$ case (c).

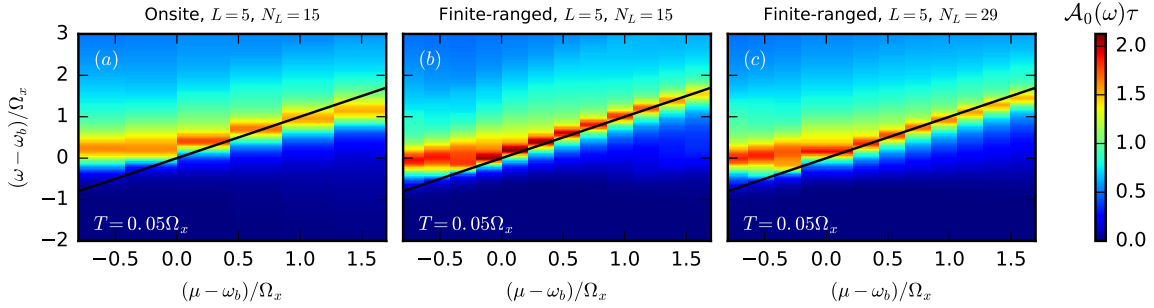


Figure 10. Central QPC LDOS $\mathcal{A}_0(\omega)$ as function of chemical potential and frequency for (a) onsite-, and finite-ranged interactions with (b) $N_L = 15$ and (c) $N_L = 29$. For finite-ranged interactions the pinning of the van Hove ridge to the chemical potential is much stronger than in the onsite case. Note that in the leading contribution case $N_L = 15$, the LDOS is more pronounced than in the full $N_L = 29$ result.

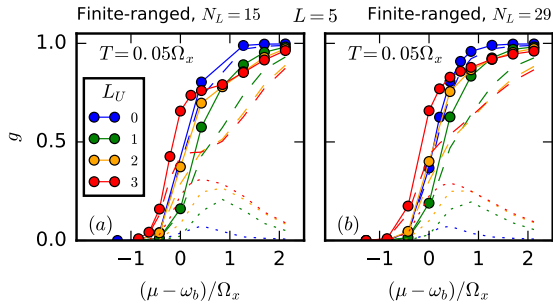


Figure 11. Dependence of the conductance on the interaction range for (a) $N_L = 15$ and (b) $N_L = 29$. With increasing interaction range the 0.7-feature develops in the conductance step. Note that with increasing L_U the pinch-off of the conductance is shifted to smaller chemical potentials

C. Further challenges

In the data of the previous subsection, we have noticed that for finite-ranged interactions an unphysical shift in the conductance occurs: The pinch-off is shifted to lower chemical potentials, seeming to imply that the effective QPC barrier gets somehow reduced by finite-ranged interactions. This effect was also found to a varying extent in previous fRG work on QPCs [1, 4, 9, 12, 19] and is an artefact of our method, presumably our truncation scheme. Together with the other inconsistencies, namely the violation of the Ward identity (39) and the associated issue that the two-particle contribution to the conductance is negative unless the Ward-correction (40) is used, this implies that in order to obtain quantitatively reliable results for the conductance one will have to go beyond the channel decomposition (13), and in general also beyond second-order truncated fRG. In particular, a more refined description and treatment of the vertex is required, using not only one but all three independent frequencies. A possible approach for meeting the latter challenge within the Matsubara formalism is detailed in [20]. A general improvement of our method

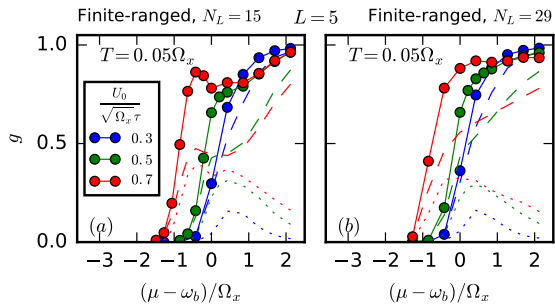


Figure 12. Dependence of the conductance on the interaction strength (a) for the leading frequency contribution $N_L = 15$, as well as (b) the full $N_L = 29$ contribution. For large interaction strength the 0.7-structure develops an oscillatory feature, more pronounced in (a) but also visible in (b). Note again the unphysical shift to smaller chemical potentials occurring for larger interaction strength.

could be to combine this efficient vertex treatment with the recently developed multiloop fRG (mfRG) method [21–23] which provides a natural strategy for going beyond second-order truncated fRG. Work in this direction is currently in progress.

V. CONCLUSIONS

The work reported here had two goals. The first was methodological – advancing fRG methodology by combining long-range feedback (eCLA) with the Keldysh formalism. The second goal was phenomenological – investigating the effect of finite-ranged interactions on the temperature dependence of the 0.7-anomaly in QPCs.

Regarding our second goal, the conclusions are encouraging: we find clear indications that finite-ranged interactions strengthen the 0.7-shoulder in the conductance step at finite temperature. However, we were unable to fully achieve our first goal: the approximations used (1-loop truncation, channel decomposition of the vertex) are too crude to obtain a fully converged and truly satisfactory fRG treatment of long-range interactions in the Keldysh formalism. Moreover, we encountered problems arising from the violation of Ward identities.

Thus, we conclude that finite-ranged interactions merit further study in the context of the 0.7-anomaly, but more sophisticated methodology is needed to describe them satisfactorily. A promising candidate for further studies in this direction would be multi-loop Keldysh-fRG [21–23]. Work in this direction is currently in progress.

ACKNOWLEDGMENTS

We thank Dennis Schimmel, Jan Winkelmann and Edoardo di Napoli for helpful discussions.

Furthermore, we gratefully acknowledge support from

the Deutsche Forschungsgemeinschaft through the Cluster of Excellence *Nanosystems Initiative Munich* and Germany’s Excellence Strategy-EXC-2111-390814868.

Finally, we gratefully acknowledge the Gauss Centre for Supercomputing e.V. (www.gauss-centre.eu) for supporting this project by providing computing time through the John von Neumann Institute for Computing (NIC) on the GCS Supercomputer JUWELS at Jülich Supercomputing Centre (JSC).

APPENDIX

In this appendix, we discuss some more technical aspects of our model and method. We begin with summarizing the general symmetries of our system in App. A. These symmetries are exact and do not depend on the channel decomposition or our fRG approximations. In App. B, we discuss the implications of these general symmetries on the components (18) of the channel decomposition and count the number of independent components. In particular, we use in App. B a more general form of the multiparticle FDTS (19,B13) in the channel decomposition than in previous works [9–11]. For the interested reader, we have included a derivation of this more general form in App. C. In App. D, we show the explicit form of the flow equations from Sec. III B 2, including the full index structure. In App. E, we discuss the importance of the feedback frequencies for the conductance, and give a justification for our frequency approximation within Sec. III B 4 while developing the dynamic feedback length. In App. F, we explicitly show the violation of the Ward identity (39) for increasing interaction strength. Finally, in App. G, we discuss the convergence of our results w.r.t. the number of frequencies N_T for which we take a long-range structure of the vertex into account, c.f. Sec. III B 4.

Appendix A: General symmetries

In this section, we list the general symmetries that our system introduced in Sec. II obeys. The derivation of these symmetry relations can be found in great detail in [10]. Note that all the symmetries discussed in this section are exact. In particular they do *not* depend on the channel decomposition (13), or any fRG approximations.

1. Particle permutation. For any permutation P of $(1, \dots, n)$ with sign $(-1)^P$ holds (c.f. Eq. (3.18) in [10])

$$\xi_{Pm'|m} = \xi_{m'|Pm} = (-1)^P \xi_{m'|m}, \quad (\text{A1})$$

where $\xi \in \{G, \gamma\}$ is either a multi-particle Green’s or vertex function and $m = (m_1, \dots, m_n)$ is a multi-particle index, with $m_k = (\omega_k, \alpha_k, q_k)$ consisting of frequency ω_k , Keldysh index α_k , and site and spin index $q_k = (i_k, \sigma_k)$.

2. Complex conjugation. For $\xi \in \{G, \gamma\}$ holds (c.f.

Eq. (3.24) in [10])

$$\xi_{q'|q}^{\alpha'|\alpha}(\omega'|\omega)^* = (-1)^{z_\xi + \sum_k(\alpha'_k + \alpha_k)} \xi_{q|q'}^{\alpha|\alpha'}(\omega|\omega'), \quad (\text{A2})$$

with $z_G = n$ and $z_\gamma = 1$. For further reference, we also state the equivalent relation of (A2) on the double time contour (i.e. before rotating to Keldysh space)

$$\xi_{q'|q}^{j'|j}(t'|t)^* = (-1)^{z_\xi} \xi_{q|q'}^{\bar{j}|\bar{j}'}(t, t'), \quad (\text{A3})$$

where $j, j' \in \{+, -\}^n$ are multi-particle indices on the double time contour (+: forward branch, -: backward branch), and $\bar{j} = -j$.

3. Thermal equilibrium and time reversal. In thermal equilibrium, our system obeys the general Kubo-Martin-Schwinger (KMS) condition [24–26], which leads to the relation (c.f. Eq. (3.52) in [10])

$$e^{\beta\Delta^{j'|\bar{j}'}}(\omega|\omega') G_{q|q'}^{\bar{j}|\bar{j}'}(\omega|\omega') = (-1)^{m^{j'|\bar{j}'}} \tilde{G}_{q|q'}^{\bar{j}|\bar{j}'}(\omega|\omega'), \quad (\text{A4})$$

with

$$m^{j'|\bar{j}'} = \sum_{k:j_k=+} 1 - \sum_{k:j_k=-} 1, \quad (\text{A5})$$

and

$$\Delta^{j'|\bar{j}'}(\omega'|\omega) = \sum_{k:j_k=+} (\omega_k - \mu) - \sum_{k:j_k=-} (\omega'_k - \mu). \quad (\text{A6})$$

The tilded Green's function \tilde{G} in (A4) is defined as the normal Green's function G , however with anti-time ordering on the forward- and time ordering on the backward branch, see Eq. (3.16) in [10]. In the single-particle case, \tilde{G} can be expressed simply in terms of G via the relation (c.f. Eq. (3.17) in [10])

$$\tilde{G}_{q'|q}^{j'|\bar{j}'}(\omega'|\omega) = G_{q'|q}^{\bar{j}|\bar{j}'}(\omega'|\omega). \quad (\text{A7})$$

Combining (A4) with (A7) and rotating to Keldysh space (we follow the convention in [10], see (A15)) yields the single-particle FDTs (10).

Additionally to the KMS conditions, thermal equilibrium also implies the following time reversal behavior for multi-particle Green's functions (c.f. Eq. (3.71) in [10])

$$\tilde{G}_{q|q'}^{j|\bar{j}'}(\omega|\omega') = G_{q'|q}^{\bar{j}|\bar{j}'}(\omega'|\omega) \Big|_{\tilde{H}}. \quad (\text{A8})$$

Here, $\tilde{q} = \Theta q$ denote the time reversed basis states, where Θ is the anti-unitary time reversal operator

$$\Theta|i, \sigma\rangle = e^{i\frac{\pi}{2} \sum_k \sigma_k} |i, \bar{\sigma}\rangle, \quad (\text{A9})$$

with $\bar{\sigma}$ denoting the opposite spin of $\sigma \in \{+, -\}^n$. Note that the propagator on the r.h.s. of (A8) has to be evaluated using the time reversed Hamiltonian $\tilde{H} = \Theta H \Theta^\dagger$.

The Eqs. (A4) (relating G and \tilde{G}) and (A10) (relating \tilde{G} and $G|_{\tilde{H}}$) are general equilibrium properties. Our specific system exhibits additionally a special form of time-reversal symmetry, that will allow us to relate G and \tilde{G} : For the components of the propagators evaluated in the basis $\{|q\rangle\}$ with $|q\rangle = |i, \sigma\rangle$ holds (see Eq. (3.80) in [10])

$$G_{q'q}^{j'|\bar{j}'}(t, t') = G_{\tilde{q}'\tilde{q}}^{j'|\bar{j}'}(t, t') \Big|_{\tilde{H}}. \quad (\text{A10})$$

Although our system is more general than the ones considered in [10], the proof that (A10) holds for our specific choice of the basis $\{|q\rangle\}$ can be done completely analogously to the one in [10], pp. 60–61. For details, see [27]. We remark that for (A10) to hold, the Hamiltonian (1) does *not* have to be time reversal invariant itself, in particular (A10) also holds for finite magnetic field.

Using (A10), we can obtain two more important symmetry relations. In the single-particle case, combining (A10) with (A8) and (A7) yields

$$G_{q'q}^{j'|\bar{j}'}(\omega'|\omega) = G_{q|q'}^{\bar{j}|\bar{j}'}(\omega|\omega'). \quad (\text{A11})$$

Since, in our system, G is diagonal in spin and frequency, this implies that the spatial transposition symmetry (31a) and by extension also (31b).

In the multiparticle case, one can combine (A10) with (A8) and (A4) to obtain after transformation to Keldysh space a FDT for G . An analog relation holds for the vertex γ , making it possible to express this multi-particle FDTs for $\xi \in \{G, \gamma\}$ in the compact form (see Eqs. (3.104, 3.106) in [10])

$$\text{Re} \xi_{\epsilon \epsilon'}^{j'|\bar{j}'}(\omega'|\omega) = - \left[1 - 2f \left(\Delta^{j'|\bar{j}'}(\omega'|\omega) + \mu \right) \right] \text{Re} \xi_{-\epsilon \epsilon'}^{j'|\bar{j}'}(\omega'|\omega), \quad (\text{A12a})$$

$$\text{Im} \xi_{-\epsilon \epsilon'}^{j'|\bar{j}'}(\omega'|\omega) = - \left[1 - 2f \left(\Delta^{j'|\bar{j}'}(\omega'|\omega) + \mu \right) \right] \text{Im} \xi_{\epsilon \epsilon'}^{j'|\bar{j}'}(\omega'|\omega), \quad (\text{A12b})$$

where

$$\epsilon_\xi^{j'|j} = (-1)^{1+n_\xi+m^{j'|j}}, \quad (\text{A13})$$

and for given $\epsilon = \pm 1$

$$\gamma_\epsilon^{j'|j} = \sum_{(-1)^{\sum_k(\alpha'_k+\alpha_k)}=\epsilon} D^{j'|\alpha'} \gamma^{\alpha'|\alpha} (D^{-1})^{\alpha|j}, \quad (\text{A14})$$

with the Keldysh rotation

$$D^{-|1} = D^{\pm|2} = \frac{1}{\sqrt{2}}, \quad (\text{A15a})$$

$$D^{+|1} = -\frac{1}{\sqrt{2}}. \quad (\text{A15b})$$

Appendix B: Symmetries of vertex components

In this section, we discuss the symmetries of the vertex components φ^P , φ^X , φ^D of Eq. (18). These symmetries arise from the general vertex symmetries discussed in App. A. We first take a look at the general (i.e. not necessarily equilibrium) symmetries in App. B1, and discuss special equilibrium properties in more detail in App. B2, where we also comment on additional symmetries arising in the case of zero magnetic field or a parity-symmetric model.

1. General case

Using general vertex properties and the channel decomposition of 2nd-order truncated fRG, one obtains various relations for the vertex components in (18) (c.f. e.g. [10, 11]). Fig. 13(a,b) depicts how those symmetries relate the different components. We use the notation:

- P_i : Exchange of incoming particles:
 $\varphi_{\beta'_1\beta'_2|\beta_1\beta_2} \xrightarrow{P_i} -\varphi_{\beta'_1\beta'_2|\beta_1\beta_2},$
- P_o : Exchange of outgoing particles:
 $\varphi_{\beta'_1\beta'_2|\beta_1\beta_2} \xrightarrow{P_o} -\varphi_{\beta'_2\beta'_1|\beta_1\beta_2},$
- C : Vertex conjugation:
 $\varphi_{\beta'_1\beta'_2|\beta_1\beta_2} \xrightarrow{C} (-1)^{1+\sum_k \alpha'_k+\alpha_k} \varphi_{\beta_1\beta_2|\beta'_1\beta'_2}^*.$

Here $\beta = (\alpha, \omega, j, \sigma)$ are composite-indices, comprised of Keldysh index, frequency, spatial site and spin. Each of these three symmetries is depicted by an arrow, connecting related vertex components. Therefore each of the components is connected via three solid arrows to other components or itself. The symmetries obey the general relations

$$\begin{aligned} P_i^2 &= P_o^2 = C^2 = 1, \\ [P_o, P_i] &= 0, \\ CP_i &= P_oC. \end{aligned} \quad (\text{B1})$$

This implies that not all the relations between the various vertex components are independent, i.e. that they can not be expressed via each other. However, one can always find an independent subset of relations. In Fig. 13, an example for such an independent subset is given by the relations colored red. Expressed as equations, this independent subset takes the form

$$(a^P)_{j'_1j'_2|j_1j_2}^{\sigma'_1\sigma'_2|\sigma_1\sigma_2}(\text{II}) \stackrel{P_o}{=} -(a^P)_{j'_2j'_1|j_1j_2}^{\sigma'_2\sigma'_1|\sigma_1\sigma_2}(\text{II}), \quad (\text{B2})$$

$$\stackrel{P_i}{=} -(a^P)_{j'_1j'_2|j_2j_1}^{\sigma'_1\sigma'_2|\sigma_2\sigma_1}(\text{II}), \quad (\text{B3})$$

$$\stackrel{C}{=} (d^{P*})_{j_1j_2|j'_1j'_2}^{\sigma_1\sigma_2|\sigma'_1\sigma'_2}(\text{II}). \quad (\text{B4})$$

$$(b^P)_{j'_1j'_2|j_1j_2}^{\sigma'_1\sigma'_2|\sigma_1\sigma_2}(\text{II}) \stackrel{P_o}{=} -(b^P)_{j'_2j'_1|j_1j_2}^{\sigma'_2\sigma'_1|\sigma_1\sigma_2}(\text{II}), \quad (\text{B5})$$

$$\stackrel{C}{=} -(b^{P*})_{j_1j_2|j'_1j'_2}^{\sigma_1\sigma_2|\sigma'_1\sigma'_2}(\text{II}). \quad (\text{B6})$$

$$(a^X)_{j'_1j'_2|j_1j_2}^{\sigma'_1\sigma'_2|\sigma_1\sigma_2}(\text{X}) \stackrel{P_o}{=} -(d^D)_{j'_2j'_1|j_1j_2}^{\sigma'_2\sigma'_1|\sigma_1\sigma_2}(\text{X}), \quad (\text{B7})$$

$$\stackrel{P_i}{=} -(a^D)_{j'_1j'_2|j_2j_1}^{\sigma'_1\sigma'_2|\sigma_2\sigma_1}(-\text{X}), \quad (\text{B8})$$

$$\stackrel{C}{=} (d^{X*})_{j_1j_2|j'_1j'_2}^{\sigma_1\sigma_2|\sigma'_1\sigma'_2}(\text{X}). \quad (\text{B9})$$

$$(b^X)_{j'_1j'_2|j_1j_2}^{\sigma'_1\sigma'_2|\sigma_1\sigma_2}(\text{X}) \stackrel{P_i}{=} -(b^D)_{j'_1j'_2|j_2j_1}^{\sigma'_1\sigma'_2|\sigma_2\sigma_1}(-\text{X}), \quad (\text{B10})$$

$$\stackrel{C}{=} -(b^{X*})_{j_1j_2|j'_1j'_2}^{\sigma_1\sigma_2|\sigma'_1\sigma'_2}(\text{X}). \quad (\text{B11})$$

$$(a^D)_{j'_1j'_2|j_1j_2}^{\sigma'_1\sigma'_2|\sigma_1\sigma_2}(\Delta) \stackrel{C}{=} (a^{D*})_{j_1j_2|j'_1j'_2}^{\sigma_1\sigma_2|\sigma'_1\sigma'_2}(-\Delta). \quad (\text{B12})$$

2. Equilibrium case

Besides the generic single-particle FDTs (10), which are a generic property of any equilibrium system, the multiparticle relation (A12) holds due to the special form of time-reversal symmetry (A10) that our system obeys. Applying this multi-particle relation to our channel decomposition, we obtain two properties for our vertex quantities, namely (ii) the vertex FDTs from (19), as well as (iii) the relation

$$a^* = d, \quad (\text{B13})$$

which holds for all channels. Since especially the relations (19c) and (B13) have (to our knowledge) not been stated in this generality before, we give a short derivation for the interested reader in App C.

In Fig. 13, the symmetries containing the additional equilibrium symmetry relations are depicted in panels (c,d). In the following, we will restrict our discussion to this equilibrium case. Then, for finite magnetic field, we have 7 independent components in spin space:

$$(a^P)^{\sigma\sigma} := (a^P)^{\sigma\sigma|\sigma\sigma}, \quad \sigma = \uparrow, \downarrow, \quad (\text{B14a})$$

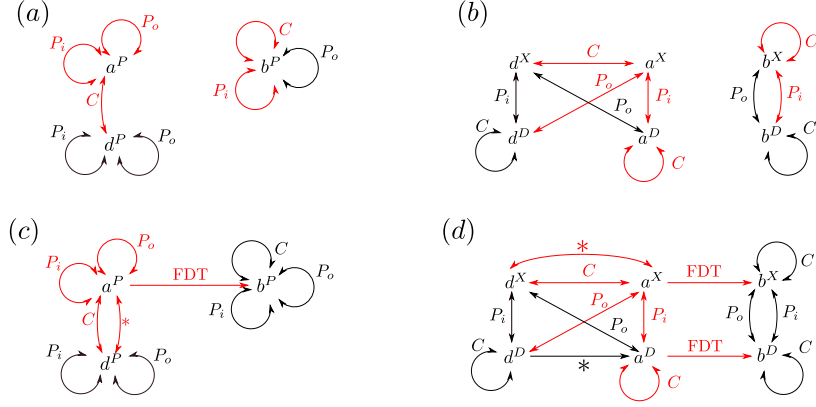


Figure 13. Graphical representation of the symmetry relations for the P-channel (a,c) and XD-channel (b,d). The first row (a,b) depicts the general symmetries for the non-equilibrium case, the second row (c,d) depicts the symmetries for the special case of thermal equilibrium. For each subfigure, the red colored symmetries are an example for an independent subset.

$$(a^P)^{\uparrow\downarrow} := (a^P)^{\uparrow\downarrow\downarrow\uparrow}, \quad (\text{B14b})$$

$$(a^X)^{\uparrow\downarrow} := (a^X)^{\uparrow\downarrow\downarrow\uparrow}, \quad (\text{B14c})$$

$$(a^D)^{\sigma\sigma} := (a^D)^{\sigma\sigma|\sigma\sigma}, \quad \sigma = \uparrow, \downarrow, \quad (\text{B14d})$$

$$(a^D)^{\uparrow\downarrow} := (a^D)^{\uparrow\downarrow\downarrow\uparrow}. \quad (\text{B14e})$$

The remaining task is to determine the symmetries of these quantities in position and frequency space and to identify the independent components. This process can be illustrated again via the symmetry diagrams shown in Fig. 13. We are now looking for a complete subset of independent symmetry operations that do not change the channel or spin configuration, i.e. that do not mix the quantities introduced in (B14). This can be done in the following way: Start from one component and form all possible closed paths with the solid arrows starting and ending at the same component. Then discard those loops that change the spin structure. The remaining paths form the desired complete set of remaining symmetries. This leads to the following symmetry counts: $a^{P\sigma\sigma}$: 3, $a^{P\uparrow\downarrow}$: 1, $a^{X\uparrow\downarrow}$: 1, $a^{D\sigma\sigma}$: 2, $a^{D\uparrow\downarrow}$: 1.

In order to classify these symmetries, we use the short-index notation introduced in (20), i.e. we encode the spatial structure in a (frequency dependent) block-matrix $A(\Omega) = \{A_{ji}^{lk}(\Omega)\}$, with a bosonic frequency Ω . To simplify notation, let us define the following generic independent transformations in position and frequency space:

$$[A^{I_1}]_{ji}^{lk}(\Omega) = -A_{(j+l)i}^{(-l)k}(\Omega), \quad (\text{B15a})$$

$$[A^{I_2}]_{ji}^{lk}(\Omega) = -A_{j(i+k)}^{l(-k)}(\Omega), \quad (\text{B15b})$$

$$[A^T]_{ji}^{lk}(\Omega) = A_{ij}^{kl}(\Omega), \quad (\text{B15c})$$

$$[A^Z]_{ji}^{lk}(\Omega) = A_{(j+l)(i+k)}^{*(-l)(-k)}(-\Omega). \quad (\text{B15d})$$

With this, we can classify the symmetries in position and

Table III. Symmetries of vertex components in position and frequency space.

	$a^{P\sigma\sigma}$	$a^{P\uparrow\downarrow}$	$a^{X\uparrow\downarrow}$	$a^{D\sigma\sigma}$	$a^{D\uparrow\downarrow}$
I_1	✓	–	–	–	–
I_2	✓	–	–	–	–
T	✓	✓	✓	✓	–
Z	–	–	–	✓	✓

frequency as in Table III. The invariance under transposition T implies that for all vertex components in (B14) except $a^{D\uparrow\downarrow}$, the spatial block-matrix is symmetric, i.e. we only need to compute components with

$$k \geq l, \quad (\text{B16})$$

and for $k = l$ it suffices to compute components with $i \geq j$. The additional symmetries I_1, I_2 in $a^{P\sigma\sigma}$ imply that there we only need to consider $l > 0$. Finally, for both the D -channel contributions $a^{D\sigma\sigma}$ and $a^{D\uparrow\downarrow}$ we need to only compute the contributions for the frequencies $\Delta \geq 0$.

Zero magnetic field

In our work, we do not consider a finite magnetic field. This directly implies that we only need to compute one spin component of $a^{P\sigma\sigma}$ and $a^{D\sigma\sigma}$ (e.g. $\sigma = \uparrow$). Furthermore, applying the same method as described above, we find that each of the mixed spin components now has one symmetry more, changing the symmetry counts to $a^{P\sigma\sigma}$: 3, $a^{P\uparrow\downarrow}$: 2, $a^{X\uparrow\downarrow}$: 2, $a^{D\sigma\sigma}$: 2, $a^{D\uparrow\downarrow}$: 2.

Again we can classify the symmetries, see Table IV. In terms of independent vertex components this implies

Table IV. Same as in Table III but for zero magnetic field.

	$a^{P\uparrow\uparrow}$	$a^{P\uparrow\downarrow}$	$a^{X\uparrow\downarrow}$	$a^{D\uparrow\uparrow}$	$a^{D\uparrow\downarrow}$
I_1	✓	—	—	—	—
I_2	✓	—	—	—	—
$I \equiv I_1 \circ I_2$	✓	✓	—	—	—
T	✓	✓	✓	✓	✓
Z	—	—	✓	✓	✓

that now we have to compute only the components with non-negative frequencies in the X -channel and that the spatial block structure of $a^{D\uparrow\downarrow}$ is now symmetric. Furthermore, additionally to the symmetric condition (B16), now one only needs to compute the components with $l \leq 0$ in $a^{P\uparrow\downarrow}$. (Note that, in agreement with our choice of sign in (B16), this is a weaker statement than the condition $l > 0$ that is encountered for $a^{P\uparrow\uparrow}$, which is symmetric under I_1 and I_2 independently).

Parity

Finally, in the equilibrium context, the setup studied in this work is parity symmetric, due to the parity symmetry of the Hamiltonian. In our notation, the parity transformation can be expressed as

$$[A^M]_{ji}^{lk}(\Omega) = A_{(-j)(-i)}^{(-l)(-k)}(\Omega). \quad (\text{B17})$$

$$\text{Re} \left[\nu_{\epsilon_1^{j'lj}}^{j'lj} + \sum_A (\varphi_{\epsilon_1^{j'lj}}^A)^{j'lj}(\Omega^A) \right] = - \left[1 - 2f(\Delta^{j'lj}(\Pi, X, \Delta) + \mu) \right] \text{Re} \left[\nu_{-\epsilon_1^{j'lj}}^{j'lj} + \sum_A (\varphi_{-\epsilon_1^{j'lj}}^A)^{j'lj}(\Omega^A) \right], \quad (\text{C1a})$$

$$\text{Im} \left[\nu_{-\epsilon_1^{j'lj}}^{j'lj} + \sum_A (\varphi_{-\epsilon_1^{j'lj}}^A)^{j'lj}(\Omega^A) \right] = - \left[1 - 2f(\Delta^{j'lj}(\Pi, X, \Delta) + \mu) \right] \text{Im} \left[\nu_{\epsilon_1^{j'lj}}^{j'lj} + \sum_A (\varphi_{\epsilon_1^{j'lj}}^A)^{j'lj}(\Omega^A) \right], \quad (\text{C1b})$$

where $A \in \{P, X, D\}$ and correspondingly $\Omega^A \in \{\Pi, X, \Delta\}$, and where we applied an analogous definition of (A14) to the φ 's and ν . Using (14), we obtain for $\Delta^{j'lj}(\omega'|\omega)$

$$\Delta^{-+--}(\omega'|\omega) = 0, \quad (\text{C2a})$$

$$\Delta^{++--}(\omega'|\omega) = 2\mu - (\omega'_1 + \omega'_2) = 2\mu - \Pi, \quad (\text{C2b})$$

$$\Delta^{-++-}(\omega'|\omega) = \omega_1 - \omega'_2 = -X, \quad (\text{C2c})$$

$$\Delta^{-++-}(\omega'|\omega) = \omega_2 - \omega'_2 = \Delta. \quad (\text{C2d})$$

Furthermore, combining (A14) and (15) yields the bare vertex expressions

$$\nu_+^{j'lj} = 0, \quad (\text{C3a})$$

$$\nu_-^{j'_1 j'_2 | j_1 j_2} = \nu^{j'_1 j'_2 | j_1 j_2} \sim \delta(j'_1 = j'_2 = j_1 = j_2). \quad (\text{C3b})$$

Analogously, a combination of (A14) with the Keldysh

In our work this relation is then a symmetry for all vertex components.

Summary

Each of the above-mentioned symmetries reduces the independent components of the vertex by roughly a factor of 1/2. Since in our work the computation of the bubbles (30) takes the most time, our implementation does not make explicit use of the vertex symmetries in Table IV. However, they are useful tools for checking an implementation for possible mistakes.

Appendix C: Derivation of vertex FDTs

In this section, we give a brief derivation of the vertex FDTs (19) and the relation (B13). As starting point, we use the general statement (A12) for the exact two-particle vertex in contour space, derived in [10], Eq. (3.106). We remark that the spin and spatial structure of (A12) is trivial. For this reason, we will not display any spin or spatial indices in this section.

Inserting the channel decomposition (13) in (A12) yields

structure of the vertices (18) leads i.a. to the relations

$$(\varphi_-^A)^{-+--} = a^A + d^A, \quad (\text{C4a})$$

$$(\varphi_+^A)^{-+--} = b^A, \quad (\text{C4b})$$

for all $A \in \{P, X, D\}$, as well as

$$(\varphi_-^P)^{+++-} = -a^P + d^P, \quad (\text{C4c})$$

$$(\varphi_+^P)^{+++-} = -b^P, \quad (\text{C4d})$$

$$(\varphi_{\pm}^P)^{-+--} = (\varphi_{\pm}^P)^{-+--} = 0, \quad (\text{C4e})$$

$$(\varphi_-^X)^{-+--} = a^X - d^X, \quad (\text{C4f})$$

$$(\varphi_+^X)^{-+--} = -b^X, \quad (\text{C4g})$$

$$(\varphi_{\pm}^X)^{+++-} = (\varphi_{\pm}^X)^{-+--} = 0, \quad (\text{C4h})$$

and

$$(\varphi_-^D)^{-+|+-} = a^D - d^D, \quad (\text{C4i})$$

$$(\varphi_+^D)^{-+|+-} = -b^D, \quad (\text{C4j})$$

$$(\varphi_{\pm}^D)^{++|+-} = (\varphi_{\pm}^D)^{-+|+-} = 0. \quad (\text{C4k})$$

If we insert (C2), (C3) and (C4) into (C1a), we obtain

$$\sum_A \text{Re} [b^A(\Omega^A)] = 0, \quad (\text{C5a})$$

$$\text{Re} [-b^P(\Pi)] = -[1 - 2f(3\mu - \Pi)] \text{Re} [-a^P + d^P](\Pi), \quad (\text{C5b})$$

$$\text{Re} [-b^X(X)] = -[1 - 2f(\mu - X)] \text{Re} [a^X - d^X](X), \quad (\text{C5c})$$

$$\text{Re} [-b^D(\Delta)] = -[1 - 2f(\mu + \Delta)] \text{Re} [a^D - d^D](\Delta). \quad (\text{C5d})$$

If we insert (C2), (C3) and (C4) into (C1b), we obtain

$$\sum_A \text{Im} [a^A(\Omega^A) + d^A(\Omega^A)] = 0, \quad (\text{C6a})$$

$$\text{Im} [-a^P + d^P](\Pi) = -[1 - 2f(3\mu - \Pi)] \text{Im} [-b^P(\Pi)], \quad (\text{C6b})$$

$$\text{Im} [a^X - d^X](X) = -[1 - 2f(\mu - X)] \text{Im} [-b^X(X)], \quad (\text{C6c})$$

$$\text{Im} [a^D - d^D](\Delta) = -[1 - 2f(\mu + \Delta)] \text{Im} [-b^D](\Delta). \quad (\text{C6d})$$

Using (C5) and (C6a) together with the continuity of the vertex components as well as their high frequency asymptotic $\lim_{|\Omega| \rightarrow \infty} \varphi^A(\Omega) = 0$ yields relation (B13). If we additionally also use the relations (C6b-C6d) and the identity

$$\frac{1}{1 - 2f(\mu + \Omega)} = \coth\left(\frac{\Omega}{2T}\right), \quad (\text{C7})$$

we obtain the vertex FDTs (19).

Appendix D: Explicit flow equations

In this section, we give the full form of the flow equations discussed in Sec. III B 2, including all spin- and spatial indices. For the notation of the latter, we use the general short-index notation introduced in (20). Using the symmetries of the vertex for the equilibrium case (as discussed in App. B), the general fRG-flow equations in the channel decomposition (see e.g. [10, 11]) can be formulated as shown below.

In order to facilitate the representation of the self-energy flow, it is convenient to split the self-energy into a static and a dynamic contribution $\Sigma = \Sigma_s + \Sigma_d$. Furthermore, we introduce first the following auxiliary quantities, identified by a tilde:

$$\partial_{\Lambda}(\tilde{\Sigma}_s)^{R\sigma}_{j(j+l)}(\omega) = -\frac{i}{2\pi} \int d\omega' \left[\frac{1}{2} \bar{v}_{j(i+k)|(j+l)i}^{\sigma\sigma|\sigma\sigma} + (a^D)_{ji}^{\sigma\sigma lk}(0) \right] S_{i(i+k)}^{K\sigma}(\omega'), \quad (\text{D1a})$$

$$\begin{aligned} \partial_{\Lambda}(\tilde{\Sigma}_d)^{R\sigma}_{ji}(\omega) = & \frac{i}{2\pi} \int d\omega' \left\{ (b^D)_{ji}^{\sigma\sigma lk}(\omega - \omega') S_{(j+l)(i+k)}^{R\sigma}(\omega') - (b^P)_{ji}^{\sigma\sigma lk}(\omega' + \omega) S_{(i+k)(j+l)}^{A\sigma}(\omega') \right. \\ & \left. + [(a^D)_{ji}^{\sigma\sigma lk}(\omega - \omega') - (a^P)_{ji}^{\sigma\sigma lk}(\omega' + \omega)] S_{(j+l)(i+k)}^{K\sigma}(\omega') \right\}. \end{aligned} \quad (\text{D1b})$$

Then the flow of the self-energy is given by:

$$\begin{aligned} \partial_{\Lambda}(\Sigma_s)^{R\uparrow}_{j(j+l)}(\omega) = & \partial_{\Lambda}(\tilde{\Sigma}_s)^{R\uparrow}_{j(j+l)}(\omega) \\ & - \frac{i}{2\pi} \int d\omega' \left[\frac{1}{2} \bar{v}_{j(i+k)|(j+l)i}^{\uparrow\downarrow\uparrow\downarrow} + (a^D)_{ji}^{\uparrow\downarrow lk}(0) \right] S_{i(i+k)}^{K\downarrow}(\omega'), \end{aligned} \quad (\text{D2a})$$

$$\begin{aligned} \partial_{\Lambda}(\Sigma_d)^{R\uparrow}_{ji}(\omega) = & \partial_{\Lambda}(\tilde{\Sigma}_d)^{R\uparrow}_{ji}(\omega) \\ & - \frac{i}{2\pi} \int d\omega' \left\{ (b^X)_{ji}^{\uparrow\downarrow lk}(\omega' - \omega) S_{(j+l)(i+k)}^{R\downarrow}(\omega') + (b^P)_{ji}^{\uparrow\downarrow lk}(\omega' + \omega) S_{(i+k)(j+l)}^{A\downarrow}(\omega') \right. \\ & \left. + [(a^X)_{ji}^{\uparrow\downarrow lk}(\omega' - \omega) + (a^P)_{ji}^{\uparrow\downarrow lk}(\omega' + \omega)] S_{(j+l)(i+k)}^{K\downarrow}(\omega') \right\}, \end{aligned} \quad (\text{D2b})$$

and

$$\partial_{\Lambda}(\Sigma_s)^{R\downarrow}_{j(j+l)}(\omega) = \partial_{\Lambda}(\tilde{\Sigma}_s)^{R\downarrow}_{j(j+l)}(\omega)$$

$$-\frac{i}{2\pi} \int d\omega' \left[\frac{1}{2} \bar{v}_{i(j+l)|i+k}^{\uparrow\downarrow\uparrow\downarrow} + (a^D)_{ij}^{\uparrow\downarrow kl} (0) \right] S_{i(i+k)}^{K\uparrow}(\omega'). \quad (\text{D3a})$$

$$\begin{aligned} \partial_\Lambda (\Sigma_d)_{ji}^{R\downarrow}(\omega) &= \partial_\Lambda (\tilde{\Sigma}_d)_{ji}^{R\downarrow}(\omega) \\ &= -\frac{i}{2\pi} \int d\omega' \left\{ (b^X)_{(j+l)(i+k)}^{\uparrow\downarrow(-l)(-k)}(\omega - \omega') S_{(j+l)(i+k)}^{R\uparrow}(\omega') + (b^P)_{(j+l)(i+k)}^{\uparrow\downarrow(-l)(-k)}(\omega' + \omega) S_{(i+k)(j+l)}^{A\uparrow}(\omega') \right. \\ &\quad \left. + \left[(a^{X*})_{(j+l)(i+k)}^{\uparrow\downarrow(-l)(-k)}(\omega - \omega') + (a^P)_{(j+l)(i+k)}^{\uparrow\downarrow(-l)(-k)}(\omega' + \omega) \right] S_{(j+l)(i+k)}^{K\uparrow}(\omega') \right\}. \end{aligned} \quad (\text{D3b})$$

Before we proceed to write down the flow of the two-particle vertex, let us take a look at the bubble terms (26). Displaying the full spin and spatial structure, (26) reads

$$\left[(\tilde{I}^{pp})^{\alpha'_1 \alpha'_2 | \alpha_1 \alpha_2} \right]_{ji}^{\sigma\tau lk}(\Pi) = \frac{i}{2\pi} \int d\omega \left[(S^{\alpha'_1 \alpha_1})_{ji}^\sigma(\omega) (G^{\alpha'_2 \alpha_2})_{(j+l)(i+k)}^\tau(\Pi - \omega) + [S \leftrightarrow G] \right], \quad (\text{D4a})$$

$$\left[(\tilde{I}^{ph})^{\alpha'_1 \alpha'_2 | \alpha_1 \alpha_2} \right]_{ji}^{\sigma\tau lk}(X) = \frac{i}{2\pi} \int d\omega \left[(S^{\alpha'_1 \alpha_1})_{ji}^\sigma(\omega) (G^{\alpha'_2 \alpha_2})_{(i+k)(j+l)}^\tau(\omega + X) + [S \leftrightarrow G] \right]. \quad (\text{D4b})$$

The symmetrical appearance of G and S in definition (D4) implies a corresponding symmetry for the whole bubbles. Using the notation introduced in (B15) with $I \equiv I_1 \circ I_2$, the implied $[G \leftrightarrow S]$ symmetry of the bubble reads

$$\left[(\tilde{I}^{pp})^{\alpha'_1 \alpha'_2 | \alpha_1 \alpha_2} \right]^{\sigma\tau}(\Pi) = \left[(\tilde{I}^{pp})^{\alpha'_2 \alpha'_1 | \alpha_2 \alpha_1} \right]^{I\tau\sigma}(\Pi), \quad (\text{D5a})$$

$$\left[(\tilde{I}^{ph})^{\alpha'_1 \alpha'_2 | \alpha_1 \alpha_2} \right]^{\sigma\tau}(X) = \left[(\tilde{I}^{ph})^{\alpha'_2 \alpha'_1 | \alpha_2 \alpha_1} \right]^{I\tau\sigma}(-X). \quad (\text{D5b})$$

These symmetries immediately follow from definition (D4). Additionally, by complex conjugation, we have for $\zeta \in \{I^{pp}, I^{ph}\}$

$$\zeta^{\alpha'_1 \alpha'_2 | \alpha_1 \alpha_2} = (-1)^{1+\alpha'_1+\alpha'_2+\alpha_1+\alpha_2} \left[\zeta^{\alpha_1 \alpha_2 | \alpha'_1 \alpha'_2} \right]^*, \quad (\text{D6})$$

which follows from (D4) and (9). In terms of the components in Keldysh space (30), and with properly treated spin and spatial structure, the bubbles I^A with $A \in \{P, X, D\}$ from (25) take the form

$$(I^P)^{\sigma\tau}(\Pi) = \left[(\tilde{I}^{pp})^{22|21} + (\tilde{I}^{pp})^{22|12} \right]^{\sigma\tau}(\Pi) = \left[(I^{pp})^{\sigma\tau} + (I^{pp})^{I\tau\sigma} \right](\Pi), \quad (\text{D7a})$$

$$(I^X)^{\sigma\tau}(X) = \left[(\tilde{I}^{ph})^{22|12} + (\tilde{I}^{ph})^{21|22} \right]^{\sigma\tau}(X) = \left[(I^{ph})^{\sigma\tau}(X) + (I^{ph})^{I*\tau\sigma}(-X) \right], \quad (\text{D7b})$$

$$(I^D)^{\sigma\tau}(\Delta) = -\left[(\tilde{I}^{ph})^{22|21} + (\tilde{I}^{ph})^{12|22} \right]^{I\sigma\tau}(\Delta) = -(I^X)^{\tau\sigma}(-\Delta). \quad (\text{D7c})$$

Furthermore, using the propagator FDTs (10), together with the general relation

$$1 - 2f(\mu - \omega) = -\left[1 - 2f(\mu + \omega) \right], \quad (\text{D8})$$

one can straightforwardly show (c.f. [10], pp. 166-167) that the bubbles (D7) are real at their feedback frequencies, i.e. $I^P(2\mu)$ and $I^X(0)$, $I^D(0)$ are real.

For the flow of the vertex we define:

$$(\tilde{a}^P)_{ji}^{\sigma\sigma lk}(\Pi) = \frac{1}{2} \bar{v}_{j(j+l)|i+k}^{\sigma\sigma|\sigma\sigma} + (a^P)_{ji}^{\sigma\sigma lk}(\Pi) - (\phi^D)_{ji}^{\sigma\sigma(i+k-j)(j+l-i)} + (\phi^D)_{j(i+k)}^{\sigma\sigma(i-j)(j+l-i-k)}, \quad (\text{D9a})$$

$$(\tilde{a}^P)_{ji}^{\uparrow\downarrow lk}(\Pi) = \frac{1}{2} \bar{v}_{j(j+l)|i+k}^{\uparrow\downarrow|\uparrow\downarrow} + (a^P)_{ji}^{\uparrow\downarrow lk}(\Pi) + (\phi^X)_{ji}^{\uparrow\downarrow(i+k-j)(j+l-i)} + (\phi^D)_{j(i+k)}^{\uparrow\downarrow(i-j)(j+l-i-k)}, \quad (\text{D9b})$$

$$(\tilde{a}^X)_{ji}^{\uparrow\downarrow lk}(X) = \frac{1}{2} \bar{v}_{j(i+k)|i(j+l)}^{\uparrow\downarrow|\uparrow\downarrow} + (a^X)_{ji}^{\uparrow\downarrow lk}(X) + (\phi^P)_{ji}^{\uparrow\downarrow(i+k-j)(j+l-i)} + (\phi^D)_{j(j+l)}^{\uparrow\downarrow(i-j)(i+k-j-l)}, \quad (\text{D9c})$$

$$(\tilde{a}^D)_{ji}^{\sigma\sigma lk}(\Delta) = \frac{1}{2} \bar{v}_{j(i+k)|(j+l)i}^{\sigma\sigma|\sigma\sigma} + (a^D)_{ji}^{\sigma\sigma lk}(\Delta) + (\phi^P)_{j(j+l)}^{\sigma\sigma(i+k-j)(i-j-l)} - (\phi^D)_{j(j+l)}^{\sigma\sigma(i-j)(i+k-j-l)}, \quad (\text{D9d})$$

$$(\tilde{a}^D)_{ji}^{\uparrow\downarrow lk}(\Delta) = \frac{1}{2} \bar{v}_{j(i+k)|(j+l)i}^{\uparrow\downarrow|\uparrow\downarrow} + (a^D)_{ji}^{\uparrow\downarrow lk}(\Delta) + (\phi^P)_{j(j+l)}^{\uparrow\downarrow(i+k-j)(i-j-l)} + (\phi^X)_{j(j+l)}^{\uparrow\downarrow(i-j)(i+k-j-l)}. \quad (\text{D9e})$$

The static interchannel feedback is chosen as in [9–11] $\phi^P = a^P(2\mu)$, $\phi^X = a^X(0)$, $\phi^D = a^D(0)$. Note that since the bubbles (D7) are real valued at the respective feedback frequencies, the ϕ are also real and furthermore (due to the vertex FDTs (19) and (B13)) they have the same Keldysh structure as the bare vertex (15).

If we use the definition of block-matrix multiplication in spacial indices (27), the flow of the vertex can be written

in the simple form:

$$(\tilde{a}^P)^{\sigma\sigma}(\Pi) = \frac{1}{2} (\tilde{a}^P)^{\sigma\sigma}(\Pi) \cdot (I^P)^{\sigma\sigma}(\Pi) \cdot (\tilde{a}^P)^{\sigma\sigma}(\Pi) \quad (\text{D10a})$$

$$(\dot{a}^P)^{\uparrow\downarrow}(\Pi) = (\tilde{a}^P)^{\uparrow\downarrow}(\Pi) \cdot (I^P)^{\uparrow\downarrow}(\Pi) \cdot (\tilde{a}^P)^{\uparrow\downarrow}(\Pi) \quad (\text{D10b})$$

$$(\dot{a}^X)^{\uparrow\downarrow}(\text{X}) = (\tilde{a}^X)^{\uparrow\downarrow}(\text{X}) \cdot (I^X)^{\uparrow\downarrow}(\text{X}) \cdot (\tilde{a}^X)^{\uparrow\downarrow}(\text{X}) \quad (\text{D10c})$$

$$(\dot{a}^D)^{\uparrow\uparrow}(\Delta) = -(\tilde{a}^D)^{\uparrow\uparrow}(\Delta) \cdot (I^X)^{\uparrow\uparrow}(-\Delta) \cdot (\tilde{a}^D)^{\uparrow\uparrow}(\Delta) \\ - (\tilde{a}^D)^{\uparrow\downarrow}(\Delta) \cdot (I^X)^{\downarrow\downarrow}(-\Delta) \cdot (\tilde{a}^D)^{T\uparrow\downarrow}(\Delta) \quad (\text{D10d})$$

$$(\dot{a}^D)^{\downarrow\downarrow}(\Delta) = -(\tilde{a}^D)^{\downarrow\downarrow}(\Delta) \cdot (I^X)^{\downarrow\downarrow}(-\Delta) \cdot (\tilde{a}^D)^{\downarrow\downarrow}(\Delta) \\ - (\tilde{a}^D)^{T\uparrow\downarrow}(\Delta) \cdot (I^X)^{\uparrow\uparrow}(-\Delta) \cdot (\tilde{a}^D)^{\uparrow\downarrow}(\Delta) \quad (\text{D10e})$$

$$(\dot{a}^D)^{\uparrow\downarrow}(\Delta) = -(\tilde{a}^D)^{\uparrow\downarrow}(\Delta) \cdot (I^X)^{\downarrow\downarrow}(-\Delta) \cdot (\tilde{a}^D)^{\downarrow\downarrow}(\Delta) \\ - (\tilde{a}^D)^{\uparrow\uparrow} \cdot (I^X)^{\uparrow\uparrow}(-\Delta) \cdot (\tilde{a}^D)^{\uparrow\downarrow}. \quad (\text{D10f})$$

energy observables. In particular, we use the linear response conductance g of Eq. (34) as an example. In order to illustrate the underlying mechanism, we first focus on the system at $T = 0$. In this case, the conductance consists only of the one-particle contribution (35), i.e. it is completely determined by the knowledge of $\Sigma(\mu)$. We obtain $\Sigma(\mu)$ via our fRG flow, i.e. in order to understand the influence of our treatment of the two-particle vertex on the conductance, we have to take a look at the flow equations formulated in Sec. III B 2. In case of the static part $\partial_\Lambda(\Sigma_s)^R$, this is easy: The vertex contribution a^D is only evaluated directly at the feedback frequency $\Delta = 0$. For the dynamic contribution $\partial_\Lambda(\Sigma_d)^R$, we have to look a little closer. In the $T = 0$ case, we can prove here two exact statements (E4a, E4b). By using the FDTS (19) and performing the limit $T \rightarrow 0$, we obtain

Appendix E: Importance of feedback frequencies

In this section, we discuss the importance of the feedback frequencies in the vertex (c.f. Sec. III B 4) for low-

$$\partial_\Lambda(\tilde{\Sigma}_d)^{R\sigma}_{ji}(\mu) = \frac{1}{\pi} \int d\omega' \left(2\theta(\omega' - \mu) - 1 \right) \text{Im} \left[\left((a^P)_{ji}^{\sigma\sigma lk}(\mu + \omega') - (a^{D*})_{ji}^{\sigma\sigma lk}(\mu - \omega') \right) S_{(j+l)(i+k)}^{R\sigma}(\omega') \right]. \quad (\text{E1})$$

Since both a^P and a^D are retarded and approach constants and $S^R(\omega) \sim \frac{1}{\omega^2}$ for large frequency arguments ω , we have furthermore:

$$\int d\omega' \left((a^P)_{ji}^{\sigma\sigma lk}(\mu + \omega') - (a^{D*})_{ji}^{\sigma\sigma lk}(\mu - \omega') \right) S_{(j+l)(i+k)}^{R\sigma}(\omega') = 0. \quad (\text{E2})$$

With this, we can rewrite (E1) and obtain

$$\partial_\Lambda(\tilde{\Sigma}_d)^{R\sigma}_{ji}(\mu) = -\frac{2}{\pi} \int_{-\infty}^{\mu} d\omega' \text{Im} \left[\left((a^P)_{ji}^{\sigma\sigma lk}(\mu + \omega') - (a^{D*})_{ji}^{\sigma\sigma lk}(\mu - \omega') \right) S_{(j+l)(i+k)}^{R\sigma}(\omega') \right]. \quad (\text{E3})$$

Proceeding analogously, we can obtain for the complete dynamic self-energy

$$\partial_\Lambda(\Sigma_d)^{R\uparrow}_{ji}(\mu) = \partial_\Lambda(\tilde{\Sigma}_d)^{R\uparrow}_{ji}(\mu) - \frac{2}{\pi} \int_{-\infty}^{\mu} d\omega' \text{Im} \left[\left\{ (a^P)_{ji}^{\uparrow\downarrow lk}(\mu + \omega') + (a^{X*})_{ji}^{\uparrow\downarrow lk}(\omega' - \mu) \right\} S_{(j+l)(i+k)}^{R\downarrow}(\omega') \right], \quad (\text{E4a})$$

$$\partial_\Lambda(\Sigma_d)^{R\downarrow}_{ji}(\mu) = \partial_\Lambda(\tilde{\Sigma}_d)^{R\downarrow}_{ji}(\mu) - \frac{2}{\pi} \int_{-\infty}^{\mu} d\omega' \text{Im} \left[\left\{ (a^P)_{(j+l)(i+k)}^{\uparrow\downarrow(-l)(-k)}(\mu + \omega') + (a^X)_{(j+l)(i+k)}^{\uparrow\downarrow(-l)(-k)}(\mu - \omega') \right\} S_{(j+l)(i+k)}^{R\uparrow}(\omega') \right]. \quad (\text{E4b})$$

In the one-particle part of the conductance (35), we have to evaluate $G_{-NN}^{R\sigma}(\mu)$ at opposite ends of the chain.

In order for a self-energy component $(\Sigma_d)_{ji}^R(\mu)$ to yield a substantial contribution to this propagator, the spatial indices j, i have to fulfill at least one of the following two criteria: (i) The spatial indices lie on different sides of the QPC barrier. In this case, $\Sigma_{ji}^R(\mu)$ yields a direct hopping contribution to $G_{-NN}^{R\sigma}(\mu)$. (ii) At least one spatial index lies in the region of the barrier top. In this case, one either obtains a still significant hopping contribution (if the other index does not lie in the region of the barrier

top) or a renormalization of the barrier top (if both indices lie in the region of the barrier top). The remaining case, where both indices lie away from the barrier top on the same side of the QPC barrier, does not yield any significant contributions to the conductance. In this case, both spatial indices j, i lie in a connected spatial region where the lower band edge is way below the chemical potential (c.f. Fig. 1(a)), i.e. in this region the movement of electrons is not impaired anyway. Therefore, we will assume in the following that j, i fulfill at least one of the two criteria (i), (ii).

In this case, we can approximately change the lower bound of the integration in (E1-E4b) from $-\infty$ to $\omega_b = -2\tau + V_g$, the energy of the barrier top in the middle of the QPC: For small l, k the propagator $S_{(i+k)(j+l)}^{R\sigma}(\omega')$ gets suppressed exponentially by the barrier once $\omega' < \omega_b$. For large l or k , the vertex contributions $(a^A)^{lk}(\omega')$ will be small, since the interaction range of the bare interaction is finite and much shorter than the length of the entire system (including the QPC flanks). Therefore, in the flow of the self-energy components $\Sigma_{j,i}^R(\mu)$ where i, j fulfill at least one of the conditions (i) or (ii), only vertex components within the frequency range $[2\mu - (\mu - \omega_b), 2\mu]$ are important for the P-contribution, and in the range $[-(\mu - \omega_b), (\mu - \omega_b)]$ for the X- and D-channel contribu-

tions. Since we are especially interested in the behavior during the first conductance step, i.e. when $(\mu - \omega_b) \sim \Omega_x$, the leading frequency contribution of the vertex components lies in the frequency range $\Omega^f \pm \Omega_x$, where Ω^f are the feedback frequencies 2μ and 0 , defined in Sec. III A 3.

At finite temperatures, for the one-particle contribution of the conductance, the same argument holds in essence. It is just slightly more technical due to keeping track of the temperature smearing of Fermi steps. Instead of evaluating Σ only at μ , we now need it in an interval $[\mu - \Delta_T, \mu + \Delta_T]$, where the scale of $\Delta_T \sim 5T$ is set by temperature, c.f. (35). In analogy to (E1), the flow of $\Sigma(\mu + \Delta\omega)$, with $\Delta\omega \in [-\Delta_T, \Delta_T]$ can be rewritten using

$$\begin{aligned} \partial_\Lambda(\tilde{\Sigma}_d)^{R\sigma}_{ji}(\mu + \Delta\omega) = & -\frac{2}{\pi} \int_{-\infty}^{\mu} d\omega' \operatorname{Im} \left[\left((a^P)_{ji}^{\sigma\sigma lk}(\mu + \Delta\omega + \omega') - (a^{D*})_{ji}^{\sigma\sigma lk}(\mu + \Delta\omega - \omega') \right) S_{(i+k)(j+l)}^{R\sigma}(\omega') \right] \\ & + \frac{1}{\pi} \int d\omega' \left[\left\{ \coth\left(\frac{\omega' - \mu + \Delta\omega}{2T}\right) - [2\theta(\omega' - \mu) - 1] \right\} \operatorname{Im}(a^P)_{ji}^{\sigma\sigma lk}(\mu + \Delta\omega + \omega') S_{(i+k)(j+l)}^{R\sigma*}(\omega') \right. \\ & + \left\{ (1 - 2n_F(\omega')) - [2\theta(\omega' - \mu) - 1] \right\} (a^P)_{ji}^{\sigma\sigma lk}(\mu + \Delta\omega + \omega') \operatorname{Im} S_{(i+k)(j+l)}^{R\sigma}(\omega') \\ & - \left\{ \coth\left(\frac{\mu + \Delta\omega - \omega'}{2T}\right) - [2\theta(\mu - \omega') - 1] \right\} \operatorname{Im}(a^D)_{ji}^{\sigma\sigma lk}(\mu + \Delta\omega - \omega') S_{(i+k)(j+l)}^{R\sigma}(\omega') \\ & \left. - \left\{ (1 - 2n_F(\omega')) - [2\theta(\omega' - \mu) - 1] \right\} (a^D)_{ji}^{\sigma\sigma lk}(\mu + \Delta\omega - \omega') \operatorname{Im} S_{(i+k)(j+l)}^{R\sigma}(\omega') \right]. \quad (\text{E5}) \end{aligned}$$

Note that in (E5) all four terms in curly brackets $\{\dots\}$ decay exponentially in ω' on the scale of temperature T for ω' outside a small interval around μ . Following the same line of argument as above, one finds that the vertex components are suppressed outside of an interval around the feedback frequency which is widened on the order of temperature: The important frequencies effectively lie in the intervals $[2\mu - (\mu - \omega_b) - \Delta_T, 2\mu + \Delta_T]$ for the P-channel and $[-(\mu - \omega_b) - \Delta_T, (\mu - \omega_b) + \Delta_T]$ for the X- and D-channel, where $\Delta_T \sim 2\Delta_T$ lies again on the scale of temperature. Analogous arguments hold for the complete self-energy.

For finite temperature there is also a two-particle contribution (42) to the conductance, directly containing a vertex contribution. This vertex contribution is effectively only needed in an interval of width set by temperature around the feedback frequencies. This can be seen from (42) together with (37) and (38), since the functions

$$f^p(\mu + \Delta_T, \epsilon') = \coth\left[\frac{\epsilon' - \mu + \Delta_T}{2T}\right] - \tanh\left[\frac{\epsilon' - \mu}{2T}\right], \quad (\text{E6})$$

$$f^x(\mu + \Delta_T, \epsilon') = \coth\left[\frac{\epsilon' - \mu - \Delta_T}{2T}\right] - \tanh\left[\frac{\epsilon' - \mu}{2T}\right] \quad (\text{E7})$$

decay exponentially with increasing $|\epsilon' - \mu|$, on a scale set by temperature. Furthermore, the input argument Δ_T is analogous to the one appearing in (E5) and lives again

on the scale of temperature. That the leading frequency contribution for the two-particle contribution of the conductance is determined on the scale of temperature can also be nicely seen in Fig. 6. The main contribution to g_2 is collected by going from $N_L = 0$ to $N_L = 5$, i.e. while resolving the temperature scale (c.f. the discussion in Sec. IV B). Further increase in $N_L > 5$ only slightly changes the two-particle contribution.

Appendix F: Violation of Ward Identities

In Sec. III C, we have seen that the conductance computation suffers from a violation of the Ward identity (39). Here, we will elaborate on this violation and show how it depends on external and numerical parameters. One of the main influences on the severity of this violation are the interaction parameters employed. For an onsite interaction model our fRG treatment is exact to second order in the interaction, even in the case of the feedback length $L = 0$. Therefore, for small enough interaction strengths, the violation of the Ward identity (39) scales like $\sim U^3$, i.e. in this weak interaction regime we expect (39) to be well satisfied. This can indeed be seen in Fig. 14(a,b).

However, for an interaction strength suitable to observe 0.7-physics, the Ward identity is severely violated,

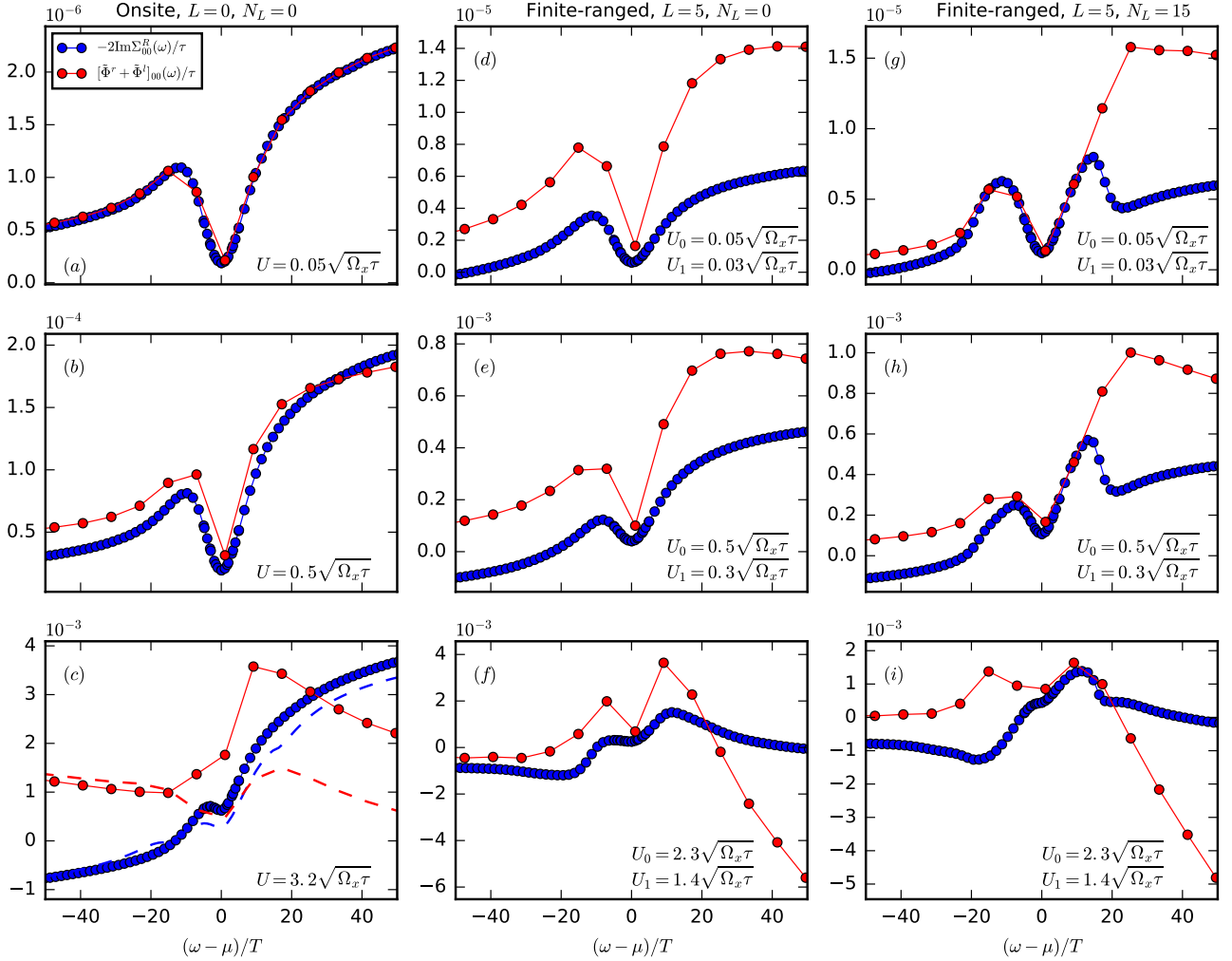


Figure 14. Violation of the Ward identity (39) at temperature $T = 0.1\Omega_x$ for onsite interactions (first column), and finite-ranged interactions with $N_L = 0$ (second column) and $N_L = 15$ (third column). The power of 10 indicated above each panel is a scale factor for the vertical axis. Within each column the interaction strength is increased from very small in the first row, up to the realistic strength in the last row. In (c), the dashed lines (blue for $-2\text{Im}\Sigma_{00}^R$ and red for $(\tilde{\Phi}^l + \tilde{\Phi}^r)_{00}$), show the onsite interaction results computed using $L = 5$, $N_L = 15$. Note that with these choices the violation in the region around the chemical potential μ is reduced compared to the $N_L = 0$ result, even in the case of onsite interactions.

see Fig. 14(c). For this reason, the best way to obtain the conductance from the results of our current fRG method, is the Ward-corrected treatment described in Sec. III C, which restores the Ward consistency between the two-particle part and the self-energy.

Note that the situation is somewhat remedied by using our eCLA scheme with finite L and finite N_L already for the onsite interaction, see the dashed lines in Fig. 14(c). In the static Matsubara case [1], we saw that the eCLA scheme stabilizes the fRG flow by coupling the individual channels better together, extending the accessible physical parameter regime. Now we also see that it increases the internal consistency of the results between the one- and two particle level.

In the case of the model with finite-ranged interactions the situation is qualitatively similar. However, with our approximate treatment of the frequency dependence of the long-ranged part of the vertex, described in Sec. III B 4, we generally already make a mistake in second (i.e. the leading order) in the Ward identity. This is due to the fact that it is numerically not possible to incorporate the effect of long-range feedback at all frequencies. We take long-range contributions only into account in a certain frequency range around the feedback-frequencies [c.f. (33)]. Following the logic of App. E, we therefore expect the Ward identity (39) to hold only in this frequency range around the chemical potential, even at small interaction strengths. This effect can indeed be seen by com-

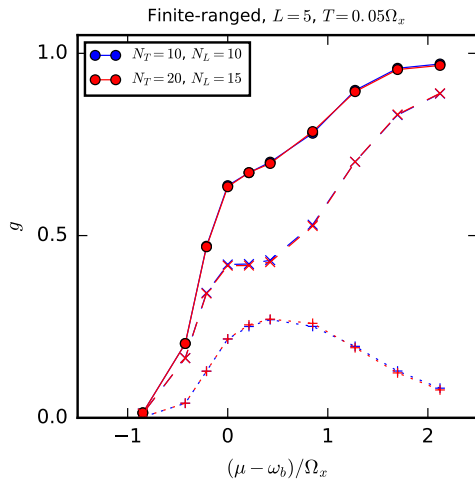


Figure 15. Conductance curves for $N_T = 10$ (blue) and $N_T = 20$ (red). As before, solid lines indicate the whole conductance g , while dashed lines indicate the one-particle and dotted lines the two-particle contributions. The resulting curves almost perfectly agree.

paring Figs. 14(d,e) to Figs. 14(g,h). At large interaction strengths the violation then becomes much more severe, as for the onsite interaction model. This necessitates introducing the Ward-correction strategy of Eq. (40).

Appendix G: Convergence w.r.t. N_T

In our whole work, we used $N_T = 10$ additional frequencies in the temperature window $[-5T, 5T]$ around the chemical potential / feedback frequencies in order to resolve the finite temperature behavior of the self-energy / two-particle vertex. Despite $N_T = 10$ being much lesser than the comfortable ~ 100 additional frequencies used in Ref. [9] for the same purpose, our results are still converged w.r.t. N_T , see Fig. 15. Here we compare the results for the finite-ranged interaction model with $N_T = 10$ (blue curves) and $N_T = 20$ (red curves). Note that in order to not change the frequency range θ_A^f , for the respective channels $A \in \{P, X, D\}$, we also had to increase the number of long range frequencies N_L accordingly. Both curves lie almost perfectly on top of each other, indicating that a further increase of N_T beyond 10 is not necessary.

-
- [1] L. Weidinger, F. Bauer, and J. von Delft, *Phys. Rev. B* **95**, 035122 (2017).
 - [2] C. Karrasch, R. Hedden, R. Peters, T. Pruschke, K. Schönhammer, and V. Meden, *Journal of Physics: Condensed Matter* **20**, 345205 (2008).
 - [3] S. G. Jakobs, M. Pletyukhov, and H. Schoeller, *Phys. Rev. B* **81**, 195109 (2010).
 - [4] F. Bauer, J. Heyder, E. Schubert, D. Borowsky, D. Taubert, B. Bruognolo, D. Schuh, W. Wegscheider, J. von Delft, and S. Ludwig, *Nature* **501**, 73 (2013).
 - [5] L. Markhof, B. Sbierski, V. Meden, and C. Karrasch, *Phys. Rev. B* **97**, 235126 (2018).
 - [6] B. Sbierski and C. Karrasch, *Phys. Rev. B* **96**, 235122 (2017).
 - [7] K. J. Thomas, J. T. Nicholls, M. Y. Simmons, M. Pepper, D. R. Mace, and D. A. Ritchie, *Phys. Rev. Lett.* **77**, 135 (1996).
 - [8] M. J. Iqbal, R. Levy, E. J. Koop, J. B. Dekker, J. P. de Jong, J. H. M. van der Velde, D. Reuter, A. D. Wieck, R. Aguado, Y. Meir, and C. H. van der Wal, *Nature* **501**, 79 (2013).
 - [9] D. H. Schimmel, B. Bruognolo, and J. von Delft, *Phys. Rev. Lett.* **119**, 196401 (2017).
 - [10] S. Jakobs, Phd-Thesis, RWTH Aachen (2009).
 - [11] S. G. Jakobs, M. Pletyukhov, and H. Schoeller, *Journal of Physics A: Mathematical and Theoretical* **43**, 103001 (2010).
 - [12] J. Heyder, F. Bauer, D. Schimmel, and J. von Delft, *Phys. Rev. B* **96**, 125141 (2017).
 - [13] T. N. L. Patterson, *Mathematics of Computation* **22**, 847 (1968).
 - [14] D. Schimmel, Phd-Thesis, Ludwigs-Maximilians-Universität München (2017).
 - [15] A. Oguri, *Journal of the Physical Society of Japan* **70**, 2666 (2001), <https://doi.org/10.1143/JPSJ.70.2666>.
 - [16] N. J. Appleyard, J. T. Nicholls, M. Pepper, W. R. Tribe, M. Y. Simmons, and D. A. Ritchie, *Phys. Rev. B* **62**, R16275 (2000).
 - [17] S. M. Cronenwett, H. J. Lynch, D. Goldhaber-Gordon, L. P. Kouwenhoven, C. M. Marcus, K. Hirose, N. S. Wingreen, and V. Umansky, *Phys. Rev. Lett.* **88**, 226805 (2002).
 - [18] A. P. Micolich, *Journal of Physics: Condensed Matter* **23**, 443201 (2011).
 - [19] F. Bauer, J. Heyder, and J. von Delft, *Phys. Rev. B* **89**, 045128 (2014).
 - [20] N. Wentzell, G. Li, A. Tagliavini, C. Taranto, G. Rohringer, K. Held, A. Toschi, and S. Andergassen, ArXiv e-prints (2016), [arXiv:1610.06520](https://arxiv.org/abs/1610.06520) [cond-mat.str-el].
 - [21] F. B. Kugler and J. von Delft, *Phys. Rev. B* **97**, 035162 (2018).
 - [22] F. B. Kugler and J. von Delft, *Phys. Rev. Lett.* **120**, 057403 (2018).
 - [23] F. B. Kugler and J. von Delft, *New Journal of Physics* **20**, 123029 (2018).
 - [24] R. Kubo, *Journal of the Physical Society of Japan* **12**, 570 (1957), <https://doi.org/10.1143/JPSJ.12.570>.
 - [25] P. C. Martin and J. Schwinger, *Phys. Rev.* **115**, 1342 (1959).
 - [26] R. Kubo, *Reports on Progress in Physics* **29**, 255 (1966).
 - [27] L. Weidinger, *Finite-ranged interactions and multiband effects in quantum point contacts*, Ph.D. thesis, Ludwigs-Maximilians-Universität München (2020, TBP).

5.3 A technical comment

Here and in the following, equations references that refer to our publication in Sec. 5.2 above are marked with the prefix ‘‘P3:’’.

In this section, we comment briefly on how the approximation of the dynamic feedback length affects the ladder structure of the vertex flow. For this, we take a look at the vertex flow resulting from the flow equations P3:(D10), when using our extended eCLA scheme as described in Sec. P3:III B4. In particular, we take a look at the structure that results from decoupling the different channels by setting the interchannel feedback $\phi^P = \phi^X = \phi^D = 0$ in Eqs. P3:(D9) and the self-energy to zero throughout the flow. For convenience we introduce the quantities

$$[\nu^{P\sigma\tau}]_{ji}^{lk} = \frac{1}{2} \bar{\nu}_{j(j+l)|i(i+k)}^{\sigma\tau} \quad (5.1)$$

$$[\nu^{X\sigma\tau}]_{ji}^{lk} = \frac{1}{2} \bar{\nu}_{j(i+k)|i(j+l)}^{\sigma\tau} \quad (5.2)$$

$$[\nu^{D\sigma\tau}]_{ji}^{lk} = \frac{1}{2} \bar{\nu}_{j(i+k)|(j+l)i}^{\sigma\tau}. \quad (5.3)$$

Let us now first consider the case where we do not make any static approximations in P3:(D10). It is well known that in this case the channel-decoupled fRG-flow yields a RPA-like ladder structure for each channel. Explicitly, one obtains for $A \in \{P, X\}$

$$(a^P)^{\sigma\sigma} = \left(1 - \nu^{A\sigma\sigma} \frac{1}{4} (J^A)^{\sigma\sigma}\right)^{-1} \nu^{A\sigma\sigma} - \nu^{A\sigma\sigma}, \quad (5.4)$$

$$(a^A)^{\uparrow\downarrow} = \left(1 - \nu^{A\sigma\tau} \frac{1}{2} (J^A)^{\sigma\tau}\right)^{-1} \nu^{A\sigma\tau} - \nu^{A\sigma\tau}, \quad (5.5)$$

where the RPA-Bubble J^A is defined in the same way as I^A in P3:(26), just by replacing S with G . For the D-channel we obtain the structure

$$(a^D)^{\sigma\tau} = \left[\left(1 + \nu^D \frac{1}{2} J^D\right)^{-1} \nu^D - \nu^D\right]^{\sigma\tau}, \quad (5.6)$$

that includes internal summation over spin and where J^D is given by

$$(J^D)^{\sigma\tau} = \delta_{\sigma\tau} \left(\delta_{\sigma\uparrow} J^{X\uparrow\uparrow} + \delta_{\sigma\downarrow} J^{X\downarrow\downarrow}\right). \quad (5.7)$$

The question is, what happens when we make the static approximation for bubble and vertex components with $|l|$ or $|k|$ bigger than the dynamic feedback length $L^A(\Omega)$, see P3:(33). In general, the fRG-flow described above will then not have a simple resumable ladder structure. However, if one modifies the used approximation of the vertex slightly (beyond second-order), one can get modified flow equations that are ladder resumable and in fact again yield the relations (5.4-5.6), with J^A evaluated according to our rule P3:(33). For this, we have to change the way we treat vertex elements on the right-hand side with one short-index, say $|l| \leq L^A(\Omega)$ and the other one greater than $L^A(\Omega)$. In this situation, our method described above makes the replacement

$$(a^A)_{ji}^{lk}(\Omega) \rightarrow (a^A)_{ji}^{lk}(\Omega_f^A). \quad (5.8)$$

This looks like the obvious choice, considering that the vertex bubble is treated in the same way. However, for the vertex itself this is, in a sense, not optimally using the bubble information provided through approximation P3:(33). Loosely speaking, in a ladder construction of the

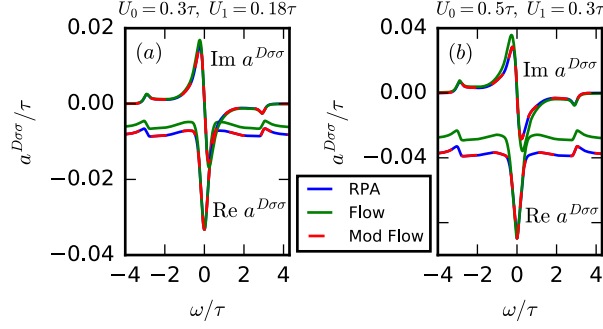


Figure 5.1 Comparison between the RPA, the standard and the modified vertex flow result for the vertex component $a^{D\sigma\sigma}(\Omega)$. We used a small system with $N = 5$, i.e. 11 sites and a finite-ranged interaction ($L_U = 3$) with (a) a smaller and (b) a bigger interaction strength. Case (b) is close to the divergence of the RPA and the differences between the RPA/modified flow and the standard flow become apparent.

vertex given by bare vertices and bubbles, we should not replace Ω with Ω_f^A in all *internal* bubble terms just because the *external* short-index k is greater than $L^A(\Omega)$. At least in a part of the ladder, the bubbles can be evaluated at the actual value of Ω . It turns out that this is the reason why replacement (5.8) prevents the flow to be ladder resumable. However, we can resolve this problem by replacing (5.8) with

$$(a^A)_{ji}^{lk}(\Omega) \rightarrow (a^A)_{jj_1}^{ll_1}(\Omega) \left[(a^A)(\Omega_f^A)^{-1} \right]_{j_1 j_2}^{l_1 l_2} (a^A)_{j_2 i}^{l_2 k}(\Omega_f^A), \quad (5.9)$$

where l_1 runs only in the dynamic range $|l_1| \leq L^P(\Omega)$ and l_2 runs only in the static range $L^P(\Omega) < |l_2| \leq L_s$. The external l appears now only on a quantity with both short-indices in the dynamic range, i.e. one can use the contribution of the actual frequency Ω instead of Ω_f^A . Using this, one can show that the flow sums up again to the RPA-like relations (5.4-5.6), see Appendix A.5.

Since there is no fundamental reason to choose (5.9) over (5.8) beyond the ladder-resumability in the case of decoupled flow equations, we used for all our numerical challenging QPC calculations the simpler form (5.8). However, we tested in small systems ($N = 5$) that the decoupled flow fulfills indeed the relations (5.4-5.6) when the modification (5.9) is used, see Fig. 5.1.

6 Application of Keldysh fRG to disordered systems

In this chapter, we check whether a real frequency Keldysh fRG approach can be used to capture the predicted MBL transition [BAA06] in a one-dimensional system comprised of interacting electrons in a random potential. In this preliminary investigation, we focus on the temperature dependence of some observables aiming to identify the transition temperature, T_c . While a comprehensive analysis of any disordered system would require a disorder averaging, we use here a simplified approach. We explore the properties of the system at certain physical parameters only for *one* typical given realization of disorder and in a vicinity of the chemical potential.

One possible observable for identifying the MBL transition is the linear conductance, which has also been the prime observable in the rest of this thesis. The temperature dependence of the dc conductance is expected [BAA06] to be equal to zero at $T < T_c$ and to grow as a power law with increasing T above T_c . Unfortunately, the present version of the fRG method violates particle conservation laws (see also the discussion in Sec. 5.2), i.e. even in a steady state (of a system of finite size) the conductance is spatially not constant. While we expect the results obtained for a finite (i.e. well bigger than zero) conductance to be still qualitatively correct, the necessary quantitative accuracy to distinguish between exact zero and a power law going to zero around the MBL transition is not possible. We anticipate that this difficulty might be overcome during potential future work on this project, in particular by the usage of multiloop fRG as developed in [KvD18b, KvD18c, KvD18a].

A second possible observable is provided by the fact that the functional order parameter of the localization transition is predicted to be the distribution function of the imaginary part of the single-particle self-energy, $\text{Im } \Sigma$. In the following, we study the temperature and interaction dependence of this quantity, both as function of frequency as well as at selected energies, see Sec. 6.4.1.

A third possibility is closely related to the second one. By studying the number and form of the peaks in the LDOS with increasing interaction strength, one can make a prediction of how strongly the initially non-interacting, localized puddles start to interact with each other. This provides a measure to directly observe the developing delocalization with increasing interaction, see Sec. 6.4.2.

6.1 Setup

We study a one-dimensional spinfull electron system with uniformly distributed onsite disorder and onsite interactions. The system consists of a central region in which disorder and interactions are present, as well as two tight binding leads (without disorder and without interactions) which are coupled to the ends of the central region. The Hamiltonian of this system for a given disorder realization is given by:

$$H = -\tau \sum_{i,\sigma} (c_{i\sigma}^\dagger c_{i+1\sigma} + c_{i+1\sigma}^\dagger c_{i\sigma}) + \sum_i V_i c_{i\sigma}^\dagger c_{i\sigma} + \sum_i U_i n_{i\uparrow} n_{i\downarrow}, \quad (6.1)$$

where i and σ are the lattice site and spin indices, $V_i(\omega) \in [-V_d, V_d]$ is a uniformly distributed random variable and V_d/τ is the (dimensionless) disorder strength. The onsite interaction is

denoted by U_i and is chosen in such a way that $U_i = U$ in the middle of the central system and gets suppressed at the boundary, see Fig. 6.1.

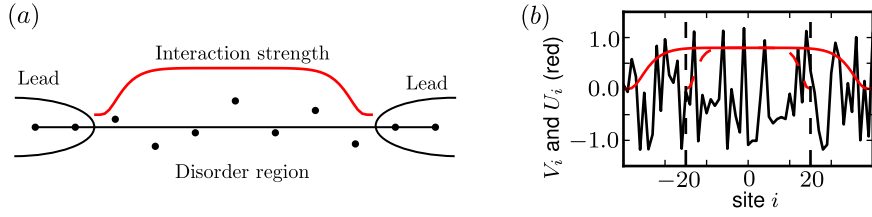


Figure 6.1 (a) Schematic plot of the system with two non-interacting tight-binding leads as well as a disordered, interacting central region. (b) Random potential V_i (black) and interaction U_i for one disorder realization and system size $N = 61$ sites with $V_d = 1.2\tau$ and $U = 0.8\tau$. Dotted lines illustrate properties of a smaller system. Note that the interaction is suppressed at the boundary of the central region.

In the following, we study the dependence of the one-particle self-energy and the LDOS on frequency and temperature. For this, we later on transform the one-particle basis for the central region from real space to the energy eigenspace.

6.2 Choice of parameters

In order to observe the MBL transition, we have to adjust the external parameters such that it is the dominating effect among three competing ones:

- Thermal dephasing with the typical temperature T_{deph}
- Finite bandwidth (4τ) introduced due to the discrete description of our model; we should only consider temperatures $T \ll 4\tau$.
- MBL transition at the critical temperature T_c .

The temperatures T_{deph} and T_c can be estimated as (see [GMP05] and [BAA06]):

$$T_{\text{deph}} \sim \frac{\delta_\xi}{\lambda^2} \quad (6.2)$$

$$T_c \sim \frac{\delta_\xi}{\lambda \ln(1/\lambda)}, \quad (6.3)$$

where λ is the dimensionless interaction strength, and δ_ξ the energy spacing in the localization volume set by the localization length ξ . In Fig. 6.2 these two functions are plotted for $\delta_\xi = 0.2\tau$ (which is a reasonable value for the energy spacing, as we will show below). In total, we require:

1. $T_c \ll T_{\text{deph}}$
2. $T_c \ll \text{Bandwidth} = 4\tau$
3. $\xi \ll \text{System size} = L$

In order to fulfill condition (1), we want λ to be small. However, we also have to keep T_c smaller than the bandwidth (condition (2)), thus we want to make the localization length ξ as large as possible in order to decrease δ_ξ . Due to numerical restrictions, we use a system

with size up to $60a$, where a denotes the lattice spacing. In order to keep ξ (much) smaller than L_{\max} (condition 3) but as big as possible, we adjust the disorder strength V_d such that $\xi_{\max} \approx 20a$. In our model this holds true at $V_d = 1.2\tau$. The energy level spacing is then given by:

$$\delta_\xi = \frac{1}{\nu\xi} = \frac{1}{\frac{1}{4\tau a} 20a} = \frac{1}{5}\tau, \quad (6.4)$$

where we have assumed the density of states ν to be constant, which is reasonable in the middle of the band. Now we can adjust the dimensionless interaction strength λ such that the above conditions (1, 2) are fulfilled, see Fig.6.2. This approximately yields $\lambda = 0.2$, which

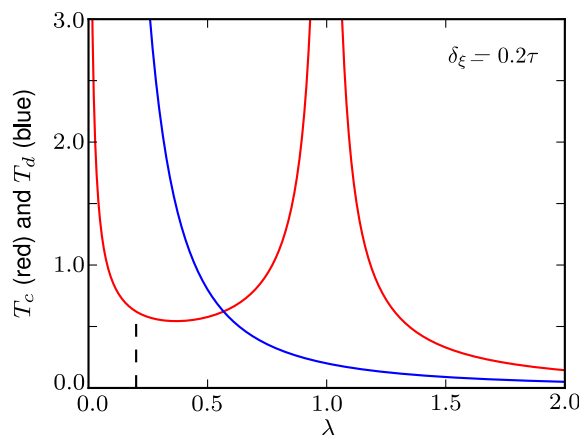


Figure 6.2 The typical dephasing temperature, T_{deph} , (blue) and the MBL-transition temperature, T_c (red), depending on the dimensionless interaction strength λ .

can be transformed to the dimensionfull interaction strength U as:

$$U = \frac{\lambda}{\nu} \frac{1}{a} = \frac{1/5}{1/(4\tau a)} \frac{1}{a} = 0.8\tau. \quad (6.5)$$

To summarize this section, we will look for the MBL-transition in the parameter regime:

- number of disorder sites $N = 61a$
- disorder strength $V_d = 1.2\tau$
- interaction strength $U = 0.8\tau$.

6.3 Data acquisition

Since this project took place before our fully fledged eCLA code was ready, all the data shown here were obtained with the simpler CLA-Code Keldysh code provided by Dennis Schimmel [SBvD17, Sch17]. Furthermore, our used code assumes thermal equilibrium from the start. Formally, this is for a finite system always the case. However, since in the disordered regime the equilibration time diverges in the limit of an infinite system, the stability of the obtained data should also be checked with an explicit non-equilibrium implementation of the code. This has not been done yet and we leave it for a future continuation of this investigation.

6.4 Data analysis

The data analysis is performed as follows. We work in the eigenbasis of the non-interacting part of the Hamiltonian (H_0). If our system is long enough and boundary effects are not important, we can just ignore the leads and diagonalize the single-particle Hamiltonian of the central region given by:

$$H_c = -\tau \sum_{i \in [-N, N]} \left(c_i^\dagger c_{i+1} + c_{i+1}^\dagger c_i + V_i c_i^\dagger c_i \right). \quad (6.6)$$

$$D = V^T H_c V, \quad V^T V = 1, \quad D = \text{diag}(\zeta_1, \dots, \zeta_n). \quad (6.7)$$

In the following, we label the eigenstates of H_c with greek letters α, \dots while we use roman letters i, \dots for the spatial indices. Having obtained the eigenbasis of H_c , we can analyse the behavior of the interaction induced, one-particle-irreducible self-energy $\Sigma_{\alpha\alpha}^\sigma(\omega)$, defined by

$$G_{\alpha\beta}^{-1\sigma}(\omega) = G_0^{-1\sigma}(\omega) - \Sigma_{\alpha\beta}^\sigma(\omega). \quad (6.8)$$

Here G and G_0 denote the full interacting as well as the bare one-particle propagator, α, β are eigenstates of H_0 , and σ and ω are the indices for spin and frequency, which are both conserved in our system. Thus, the self-energy is a matrix valued function, depending on frequency and temperature.

We will also use the density of states (DOS), both as the LDOS

$$\mathcal{A}_i^\sigma(\omega) = -\frac{1}{\pi} \text{Im} G_{ii}^\sigma(\omega), \quad (6.9)$$

i.e. expressed in spatial indices i , as well as in the eigenbasis of the non-interacting Hamiltonian ¹:

$$\mathcal{A}_\alpha^\sigma(\omega) = -\frac{1}{\pi} \text{Im} G_{\alpha\alpha}^\sigma(\omega), \quad (6.10)$$

where G is the full interacting one-particle propagator in the respective basis. This quantity reflects the position (either in real space for $\mathcal{A}_i^\sigma(\omega)$, or in energy for $\mathcal{A}_\alpha^\sigma(\omega)$) and the broadening of the single particle levels in the interacting system.

Consider now the system at a finite temperature $T = 0.1\tau$. For this temperature, the imaginary part of the self-energy is finite, and its frequency structure can be seen clearly. In Fig. 6.3, the frequency dependence of the quasiparticle decay rate $\text{Im} \Sigma_\alpha(\omega)$ and the DOS $\mathcal{A}_\alpha^\sigma(\omega)$ is shown for 6 eigenvalues α in the middle of the spectrum. As we can see, the DOS and the self-energy are closely related. At the position of the levels also the imaginary part of the self-energy has a peak.

6.4.1 Quasiparticle decay rate close to the chemical potential

Let us now focus on the behavior of the occupied level closest to the chemical potential $\mu = 0$, i.e. the blue curve in Fig. 6.3. If we vary the temperature, we get the characteristic behavior of the DOS and $\text{Im} \Sigma$ shown in Fig. 6.4. For increasing temperature, the DOS gets smaller and broader, while $\text{Im} \Sigma$ develops a peak at the level position. If we take a cut at the

¹ For simplicity, we use the same symbol \mathcal{A} . Which quantity is used will always be clear by whether the indexing is in Greek or Roman letters

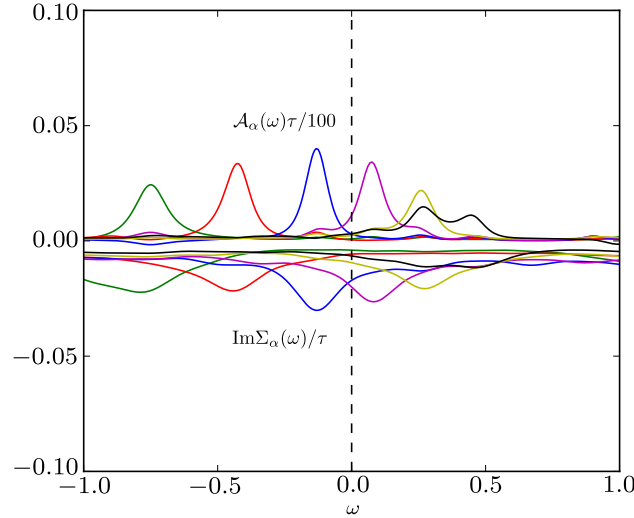


Figure 6.3 DOS $\mathcal{A}_\alpha(\omega)$ (positiv) and corresponding $\text{Im}\Sigma(\omega)$ (negativ) for six different α in the middle of the spectrum. The dashed line denotes the value of the chemical potential. Note that the values of the DOS have been divided by 10^2 .

frequency of the DOS peak at $T = 0$, we can plot for this particular frequency the dependence of the imaginary part of the self-energy on temperature.

With this method, we can extract the temperature dependence of the self-energy for various system sizes and interactions. The results are shown in Fig. 6.5. We see that $\text{Im}\Sigma$ drops quickly for small temperatures, then develops a slight plateau-like region, and then drops off again at a faster rate. The problematic parameter regime for our code are the small temperatures T , where we could not create enough data points due to fRG convergence issues. It is to be expected that for small temperatures the system is harder to treat, since the particles become more localized and corresponding peaks in the LDOS become sharper and are finally missed in our discretization scheme with fixed frequency values. In a future implementation, it would be highly desirable to somehow track the energy levels in frequency space, making sure that sharp levels are better integrated during the fRG flow. On the other hand, we expect that the delocalized levels, i.e. the part of the system that is responsible for a non-vanishing conductance, is still treated fairly well, even in our simple approach. Thus, even if we miss out on some localized levels, the influence of those levels should be negligible, since their interaction with other levels is very small.

In order to analyse the delocalized regime of the system further, we have plotted the three conductance curves of Fig. 6.3 also in a log-log plot, see Fig. 6.6. We can distinguish three different temperature regimes. Starting from small temperatures, the quasi-particle decay rate $-\text{Im}\Sigma$ increases quickly until $T \approx 0.1\tau$. Between $0.1\tau \lesssim T \lesssim 0.3\tau$ the increase slows down and seems to follow a power law with exponent α_1 . After $0.3 \lesssim T$, the increase gets again larger, and seems to follow a power law with exponent α_2 . We illustrate this power law behaviors by fitting lines to the blue $N = 31$ data points before (blue dashed line) and after the kink at $T = 0.3\tau$ (blue solid line). Extracting the exponents as the slopes of these lines yields $\alpha_1 = 0.49$ and $\alpha_2 = 0.80$. Both these exponents are still far from the ergodic metallic case (the expected delocalized phase [BAA06]) where one would expect a power law with exponent $\alpha = 1$.

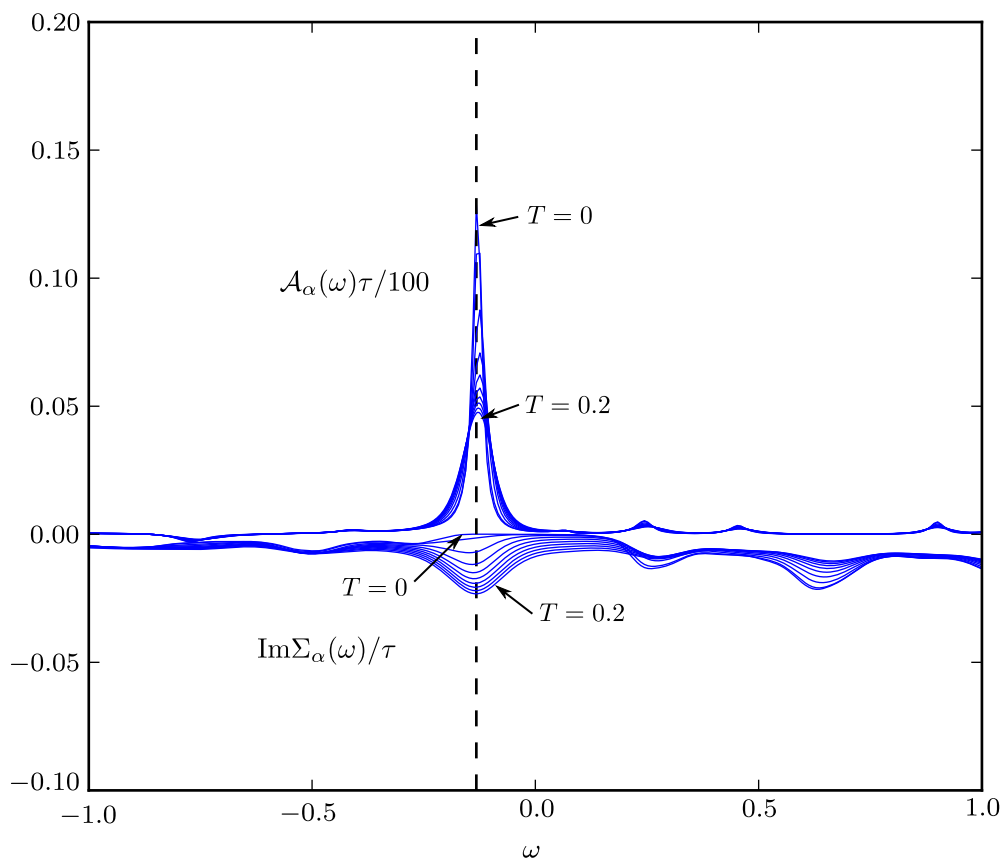


Figure 6.4 Same setting as in Fig. 6.3, but we plot only the DOS and the self-energy for the occupied level closest to the chemical potential (the blue curves from Fig. 6.3) for equally spaced temperatures $T = 0.0, 0.02, \dots, 0.2$. The dashed line indicates the DOS maximum for $T = 0$.

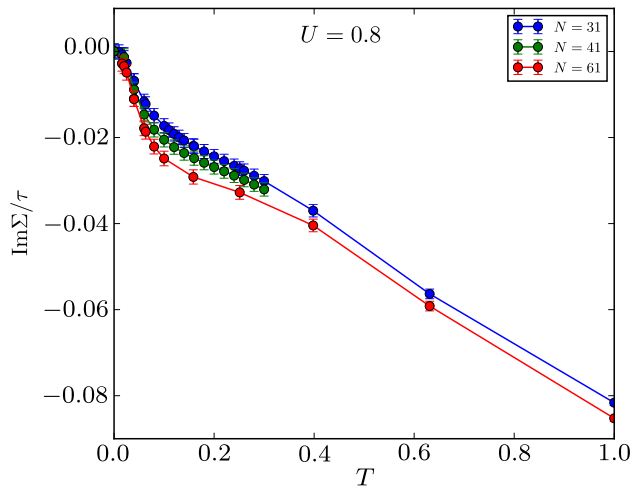


Figure 6.5 Dependence of $\text{Im}\Sigma$ on T , extracted with the method described above. We have plotted here data for three different system sizes $N = 31$ (blue), $N = 41$ (green) and $N = 61$ (red). The bars at the datapoints are not errorbars in a classical sense but indicate the magnitude of the two-particle vertex, and thus serve as a internal sanity check for our FRG approximation.

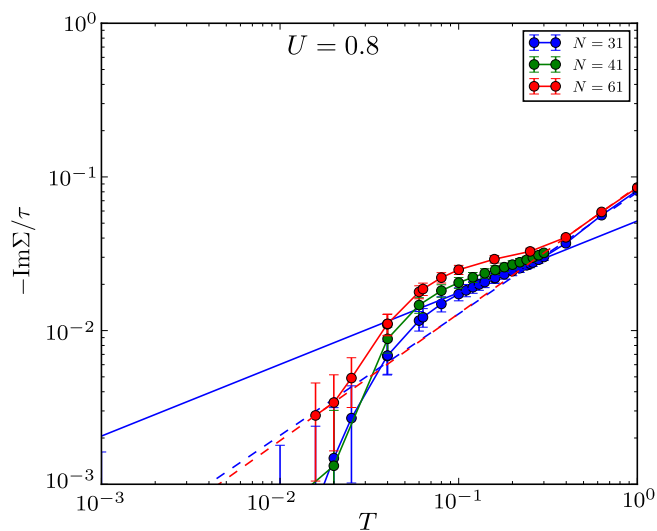


Figure 6.6 Same plot as in Fig. 6.5 but using a log-log scale. Straight lines have been fitted to the linear part of the plots (only shown for the $N = 31$ case, c.f. blue solid and dashed lines) and were used to extract powerlaw exponents.

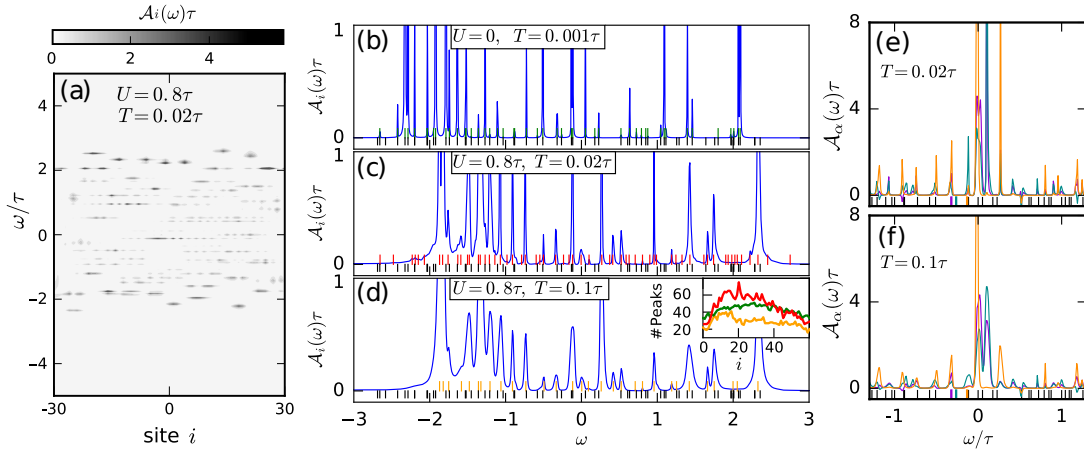


Figure 6.7 (a) Grayscale plot of the interacting LDOS $\mathcal{A}_i^\sigma(\omega)$ as function of site and frequency. (b-d) LDOS at site $i = -5$ in the non-interacting case (b) and in the interacting case (c-d) for different temperatures. Black markers indicate the non-interacting eigenenergies, colored markers the detected peaks in the LDOS. The inset in (d) shows the number of these peaks per site. (e-f) show the DOS in energy space for three different eigenenergies (colored markers) for two different temperatures. Black markers indicate again the non-interacting eigenenergies.

6.4.2 Analysis of DOS and LDOS peaks

In the preceding subsection, we focused on the quasi-particle decay rate as indicator of a possible delocalization transition. In this subsection, we instead study directly the density of states, either in real space (LDOS) or in energy space (DOS). In order to simplify the system, we omit in this part the leads and just work with an isolated central region. We focus on the occurrence and development of LDOS/DOS peaks, both in number and in form, when physical parameters like temperature and interaction strength are changed. Let us start with a look at the LDOS which already provides a nice insight into the occurring delocalization. To get an intuition of the system, we first plot the interacting LDOS $\mathcal{A}_i^\sigma(\omega)$ in Fig. 6.7(a) in a grayscale plot as a function of site i and frequency ω . All states lie roughly in the energy band $[-2\tau, 2\tau]$ set by the hopping, which is somewhat extended by the finite disorder strength V_d . In Fig. 6.7(b-d) we show cuts for $i = -5$ (this choice is in principle arbitrary, as long as it is far enough away from the edges of the system). Here, we choose $i = -5$ since for this value a LDOS peak lies close in energy to the chemical potential (see Fig. 6.7(a)), therefore relating somewhat to the blue DOS level studied in Fig. 6.3 in Sec. 6.4.1. The main observation when going from the non-interacting system in Fig. 6.7(b) to the interacting system in Fig. 6.7(c) is that the position of the LDOS peaks shifts in energy and (more importantly) their number noticeably increases (compare also the green and red curve in the inset of Fig. 6.7(d)). This increase in the peak number reflects the emergence of multi-particle excitations. Increasing the temperature in Fig. 6.7(d) smears these multi-particle excitations into a broader peaks, creating a whole spectrum of possible excitations. The increase in the excitation spectrum can also be beautifully seen in the DOS in energy space, see Fig. 6.7(e). Black markers indicate the non-interacting level positions, and the interacting DOS is plotted for the three non-interacting colored energies. Via interactions, these states develop an overlap with multiple other non-interacting levels, creating many small subpeaks at the corresponding non-interacting eigenenergies. Increasing the temperature in Fig. 6.7(f) leads again to a broadening of the peaks and (around $\omega = 0$) to the development of a whole spectrum of excitations.

6.5 Conclusion of the disorder study

While we could not – within this preliminary study – identify the MBL transition in the investigated one-dimensional disordered system, our method gives us access to quantities like the quasiparticle decay rate, as well as the frequency resolved (L)DOS which can be used to analyse the underlying MBL mechanism. The main problem is that we could not reach small enough temperatures to clearly identify the localization - delocalization point. Furthermore, the violation of conservation laws within our fRG scheme is problematic. Ultimately, it would be nice to directly compute the conductance of the system, with which an experiment would distinguish between localization or delocalization. Unfortunately, due to the violation of Ward identities, the computation of a quantitative conductance is hardly possible with our current second order truncated fRG schemes (compare also the discussion in Sec. 5.2). A way to tackle the conservation problems could be to use a multiloop fRG scheme as developed in [KvD18a, KvD18b, KvD18c], which has been shown to increase the conservation of Ward identities (at least on a one-particle level).

7 Conclusion and Outlook

The main goal of this thesis was to study finite-ranged interactions in QPCs, and in particular their influence on the 0.7-anomaly. In order to achieve that goal, we developed an extended Coupled Ladder Approximation (eCLA) feedback scheme for second order truncated fRG.

This eCLA scheme enabled a static, zero-temperature Matsubara treatment of long-ranged interactions (extending over the whole system, including the QPC flanks), and a semi-dynamic finite-temperature Keldysh treatment of finite-ranged interactions with ranges on the scale of the characteristic QPC length. In the former case, we observed that long-range interactions result in a strong flattening of the QPC barrier, leading to oscillatory features in the conductance via the resulting Friedel-oscillations. In the latter case, we found indications that finite-ranged interactions may play an important role in the development of a more pronounced 0.7-shoulder in the finite temperature conductance of QPCs.

During the development of the improved eCLA scheme, we also applied it to several side applications. In particular, we found that its extended feedback stabilizes the fRG flow, enabling the treatment of larger physical parameter regimes. This could most impressively be seen in the Kondo regime of small quantum dots containing only a few electrons. Furthermore, through a simple mapping, the eCLA scheme enabled us to treat QPCs with several subbands. We used this to study the 0.7-analog at the intersection of magnetically spin-split subbands, enabling us to give an explanation of an asymmetry occurring in the magnetic dependence of the experimentally observed conductance.

While our method suffered from second order artifacts, most prominently a violation of Ward identities and correspondingly an ambiguity in the conductance, we consider it an important step on the way to a more refined treatment. In particular, the recently developed multiloop fRG scheme [KvD18b, KvD18c, KvD18a] offers a natural way to expand our eCLA method beyond second order and improves upon the fulfillment of conservation laws. Work in this direction is currently in progress.

Further open questions which could be investigated with such a refined method are the continuation of our work on disordered systems, the transition from QPCs to quantum wires (here, spin polarization is experimentally expected to play an important role [YKT⁺18]), and also an experimentally observed even-odd effect in the finite temperature transconductance at large magnetic fields, see [CGP⁺09].

A Appendix

A.1 The Keldysh vertex bubbles at the feedback frequencies

Here we show that the vertex bubbles (2.223) are real at their respective feedback frequencies (2.146) in thermal equilibrium. For this, we use the general relation

$$1 - 2n_F(\mu + \omega) = -[1 - 2n_F(\mu - \omega)]. \quad (\text{A.1})$$

Let us first look at the P-bubble W^P . Using Eqs. (2.222) and (2.219) we have

$$\begin{aligned} (I^P)_{ji}^{\sigma\sigma'lk}(\Pi) &= \frac{i}{4\pi} \int d\omega \left[S_{ji}^{K\sigma}(\omega) G_{(j+l)(i+k)}^{R\sigma'}(\Pi - \omega) + [S \leftrightarrow G] \right] \\ &= -\frac{1}{2\pi} \int d\omega (1 - 2n_F(\omega)) \left[\text{Im} S_{ji}^{R\sigma}(\omega) G_{(j+l)(i+k)}^{R\sigma'}(\Pi - \omega) + [S \leftrightarrow G] \right]. \end{aligned} \quad (\text{A.2})$$

Inserting this in Eq. (2.223) we obtain

$$\begin{aligned} (W^P)_{ji}^{\sigma\sigma'lk}(\Pi) &= -\frac{1}{2\pi} \int d\omega (1 - 2n_F(\omega)) \left[\left\{ \text{Im} S_{ji}^{R\sigma}(\omega) G_{(j+l)(i+k)}^{R\sigma'}(\Pi - \omega) \right. \right. \\ &\quad \left. \left. + \text{Im} S_{(j+l)(i+k)}^{R\sigma'}(\omega) G_{ji}^{R\sigma}(\Pi - \omega) \right\} + [S \leftrightarrow G] \right] \\ &= -\frac{1}{2\pi} \int d\omega \left[\left\{ (1 - 2n_F(\omega)) \left(\text{Im} S_{ji}^{R\sigma}(\omega) \text{Re} G_{(j+l)(i+k)}^{R\sigma'}(\Pi - \omega) \right. \right. \right. \\ &\quad \left. \left. + \text{Im} S_{(j+l)(i+k)}^{R\sigma'}(\omega) \text{Re} G_{ji}^{R\sigma}(\Pi - \omega) \right) \right. \\ &\quad \left. \left. + i \text{Im} S_{ji}^{R\sigma}(\omega) \text{Im} G_{(j+l)(i+k)}^{R\sigma'}(\Pi - \omega) \left((1 - 2n_F(\omega)) + (1 - 2n_F(\Pi - \omega)) \right) \right\} + [G \leftrightarrow S] \right]. \end{aligned} \quad (\text{A.3})$$

Using (A.3) together with (A.1), we obtain that $W^P(2\mu)$ is real.

For the XD-bubble W^X we can proceed analogously. We have

$$\begin{aligned} (I^X)_{ji}^{\sigma\sigma'lk}(X) &= \frac{i}{2\pi} \int d\omega \left[S_{ji}^{R\sigma}(\omega) G_{(i+k)(j+l)}^{K\sigma'}(X + \omega) + [S \leftrightarrow G] \right] \\ &= -\frac{1}{\pi} \int d\omega (1 - 2n_F(\omega + X)) \left[S_{ji}^{R\sigma}(\omega) \text{Im} G_{(i+k)(j+l)}^{R\sigma'}(X + \omega) + [S \leftrightarrow G] \right]. \end{aligned} \quad (\text{A.4})$$

Inserting this in Eq. 2.223 and shifting the integration frequency we obtain

$$\begin{aligned}
(W^X)_{ji}^{\sigma\sigma'lk}(X) &= -\frac{1}{\pi} \int d\omega (1 - 2n_F(\omega)) \left[S_{ji}^{R\sigma}(\omega - X) \text{Im} G_{(i+k)(j+l)}^{R\sigma'}(\omega) \right. \\
&\quad \left. + S_{(j+l)(i+k)}^{R\sigma'}(\omega + X) \text{Im} G_{ij}^{R\sigma}(\omega) + [S \leftrightarrow G] \right] \\
&= -\frac{1}{\pi} \int d\omega (1 - 2n_F(\omega)) \left[\left(\text{Re} S_{ji}^{R\sigma}(\omega - X) \text{Im} G_{(i+k)(j+l)}^{R\sigma'}(\omega) \right) \right. \\
&\quad \left. + \text{Re} S_{(j+l)(i+k)}^{R\sigma'}(\omega + X) \text{Im} G_{ij}^{R\sigma}(\omega) \right. \\
&\quad \left. + i \text{Im} S_{ji}^{R\sigma}(\omega - X) \text{Im} G_{(i+k)(j+l)}^{R\sigma'}(\omega) \right. \\
&\quad \left. - i \text{Im} S_{(j+l)(i+k)}^{R\sigma'}(\omega + X) \text{Im} G_{ij}^{R\sigma}(\omega) \right] + [S \leftrightarrow G]. \tag{A.5}
\end{aligned}$$

For $X = 0$, the imaginary part of (A.5) is zero and therefore $W^X(0)$ is real.

A.2 Dependent channel components

Here we list how the dependent channel components are given in terms of the kept components.

A.2.1 Matsubara

In the Matsubara case, we have

$$P^{\downarrow\uparrow} = P^{I\downarrow}, \tag{A.6a}$$

$$P^{\uparrow\downarrow\downarrow\uparrow} = -P^{I_2\uparrow\downarrow}, \tag{A.6b}$$

$$P^{\downarrow\uparrow\uparrow\downarrow} = -P^{I_1\uparrow\downarrow}, \tag{A.6c}$$

$$X^{\downarrow\uparrow}(X) = X^{I\downarrow}(-X) \tag{A.6d}$$

$$X^{\uparrow\downarrow\downarrow\uparrow}(X) = -D^{\uparrow\downarrow}(-X) \tag{A.6e}$$

$$X^{\downarrow\uparrow\uparrow\downarrow}(X) = -D^{T\uparrow\downarrow}(-X) \tag{A.6f}$$

$$D^{\downarrow\uparrow} = D^{T\uparrow\downarrow}, \tag{A.6g}$$

$$D^{\uparrow\downarrow\downarrow\uparrow}(\Delta) = -X^{\uparrow\downarrow}(-\Delta), \tag{A.6h}$$

$$D^{\downarrow\uparrow\uparrow\downarrow}(\Delta) = -X^{I\uparrow\downarrow}(\Delta). \tag{A.6i}$$

A.2.2 Keldysh

In the Keldysh formalism, we have for the generic (i.e. not necessarily equilibrium) case for the P-channel

$$(a^P)^{\downarrow\uparrow} = (a^P)^{I\uparrow\downarrow}, \tag{A.7a} \quad (b^P)^{\downarrow\uparrow} = (b^P)^{I\uparrow\downarrow}, \tag{A.7d}$$

$$(a^P)^{\uparrow\downarrow\downarrow\uparrow} = -(a^P)^{I_2\uparrow\downarrow}, \tag{A.7b} \quad (b^P)^{\uparrow\downarrow\downarrow\uparrow} = -(b^P)^{I_2\uparrow\downarrow}, \tag{A.7e}$$

$$(a^P)^{\downarrow\uparrow\uparrow\downarrow} = -(a^P)^{I_1\uparrow\downarrow}, \tag{A.7c} \quad (b^P)^{\downarrow\uparrow\uparrow\downarrow} = -(b^P)^{I_1\uparrow\downarrow}, \tag{A.7f}$$

$$(d^P)^{\sigma\sigma'} = (a^P)^{T\sigma\sigma'*}, \tag{A.7g} \quad (d^P)^{\uparrow\downarrow\downarrow\uparrow} = -(a^P)^{TI_2\uparrow\downarrow*}, \tag{A.7i}$$

$$= (a^P)^{TI\sigma'\sigma*}, \tag{A.7h} \quad (d^P)^{\downarrow\uparrow\uparrow\downarrow} = -(a^P)^{TI_1\uparrow\downarrow*}, \tag{A.7j}$$

for the X-channel

$$(a^X)^{\sigma\sigma}(X) = -(a^D)^{\sigma\sigma}(-X), \quad (\text{A.8a}) \quad (b^X)^{\sigma\sigma}(X) = -(b^D)^{\sigma\sigma}(-X), \quad (\text{A.8e})$$

$$(a^X)^{\downarrow\uparrow}(X) = (a^X)^{I\uparrow\downarrow*}(-X), \quad (\text{A.8b}) \quad (b^X)^{\downarrow\uparrow}(X) = (b^X)^{TI\uparrow\downarrow}(-X), \quad (\text{A.8f})$$

$$(a^X)^{\uparrow\downarrow\downarrow\uparrow} = -(a^D)^{\uparrow\downarrow}(-X), \quad (\text{A.8c}) \quad (b^X)^{\uparrow\downarrow\downarrow\uparrow} = -(b^D)^{\uparrow\downarrow}(-X), \quad (\text{A.8g})$$

$$(a^X)^{\downarrow\uparrow\uparrow\downarrow} = -(a^D)^{TI\uparrow\downarrow}, \quad (\text{A.8d}) \quad (b^X)^{\downarrow\uparrow\uparrow\downarrow} = -(b^D)^{TI\uparrow\downarrow}, \quad (\text{A.8h})$$

$$(d^X)^{\sigma\sigma} = -(a^D)^{TI\sigma\sigma}, \quad (\text{A.8i})$$

$$(d^X)^{\sigma\bar{\sigma}}(X) = (a^X)^{T\sigma\bar{\sigma}*}(X), \quad (\text{A.8j})$$

$$= (a^X)^{TI\bar{\sigma}\sigma}(-X), \quad (\text{A.8k})$$

$$(d^X)^{\uparrow\downarrow\downarrow\uparrow} = -(d^D)^{\uparrow\downarrow}(-X), \quad (\text{A.8l})$$

$$(d^X)^{\downarrow\uparrow\uparrow\downarrow} = -(a^D)^{TI\uparrow\downarrow}, \quad (\text{A.8m})$$

and for the D-channel

$$(a^D)^{TI\sigma\sigma'}(-\Delta) = (d^D)^{\sigma'\sigma}(\Delta), \quad (\text{A.9a}) \quad (b^D)^{\downarrow\uparrow}(\Delta) = (b^D)^{TI\uparrow\downarrow}(-\Delta), \quad (\text{A.9d})$$

$$(a^D)^{\uparrow\downarrow\downarrow\uparrow} = -(a^X)^{\uparrow\downarrow}(-\Delta), \quad (\text{A.9b}) \quad (b^D)^{\uparrow\downarrow\downarrow\uparrow}(\Delta) = -(b^X)^{\uparrow\downarrow}(-\Delta), \quad (\text{A.9e})$$

$$(a^D)^{\downarrow\uparrow\uparrow\downarrow} = -(a^X)^{I\uparrow\downarrow*}, \quad (\text{A.9c}) \quad (b^D)^{\downarrow\uparrow\uparrow\downarrow} = -(b^X)^{TI\uparrow\downarrow}, \quad (\text{A.9f})$$

$$(d^D)^{\uparrow\downarrow\downarrow\uparrow}(\Delta) = -(a^X)^{T\uparrow\downarrow*}(-\Delta), \quad (\text{A.9g}) \quad (d^D)^{\downarrow\uparrow\uparrow\downarrow} = -(a^X)^{TI\uparrow\downarrow}. \quad (\text{A.9h})$$

In thermal equilibrium this relations are simplified by the FDTs, in particular the relations (2.236) and (2.237) hold.

A.3 Flow equations for the Keldysh self-energy and the b -components of the vertex

For the flow of the Keldysh component of the self-energy, one obtains analogous to (2.212) for the static part

$$\begin{aligned} \frac{\partial}{\partial\Lambda}(\Sigma_s)_{j(j+l)}^{K\uparrow}(\omega) = & -i \sum_{\omega'} \left\{ \left[S + S^{T*} \right]_{i(i+k)}^{\uparrow R}(\omega') \left[\bar{v} + (d^D)(0) \right]_{ji}^{\uparrow\uparrow lk} \right. \\ & \left. + \left[S + S^{T*} \right]_{i(i+k)}^{\downarrow R}(\omega') \left[\bar{v} + (d^D)(0) \right]_{ji}^{\uparrow\downarrow lk} \right\}, \end{aligned} \quad (\text{A.10})$$

and

$$\begin{aligned} \frac{\partial}{\partial\Lambda}(\Sigma_s)_{j(j+l)}^{K\downarrow}(\omega) = & -i \sum_{\omega'} \left\{ \left[S + S^{T*} \right]_{i(i+k)}^{R\uparrow}(\omega') \left[\bar{v} + (a^D)(0) \right]_{ji}^{TI\uparrow\downarrow lk} \right. \\ & \left. + \left[S + S^{T*} \right]_{i(i+k)}^{R\downarrow}(\omega') \left[\bar{v} + (d^D)(0) \right]_{ji}^{\downarrow\downarrow lk} \right\}. \end{aligned} \quad (\text{A.11})$$

For the dynamic part we get

$$\begin{aligned}
\frac{\partial}{\partial \Lambda} (\Sigma_d)_{ji}^{K\uparrow}(\omega) = & -i \sum_{\omega'} \left\{ S_{(i+k)(j+l)}^{A\uparrow}(\omega') (a^P)_{ji}^{\uparrow\uparrow lk}(\omega' + \omega) - S_{(j+l)(i+k)}^{A\uparrow}(\omega') (a^D)_{ji}^{TI\uparrow\uparrow lk}(\omega' - \omega) \right. \\
& + S_{(i+k)(j+l)}^{R\uparrow}(\omega') (d^P)_{ji}^{\uparrow\uparrow lk}(\omega' + \omega) - S_{(j+l)(i+k)}^{R\uparrow}(\omega') (d^D)_{ji}^{TI\uparrow\uparrow lk}(\omega' - \omega) \\
& + S_{(i+k)(j+l)}^{K\uparrow}(\omega') (b^P)_{ji}^{\uparrow\uparrow lk}(\omega' + \omega) - S_{(j+l)(i+k)}^{K\uparrow}(\omega') (b^D)_{ji}^{TI\uparrow\uparrow lk}(\omega' - \omega) \\
& + S_{(i+k)(j+l)}^{A\downarrow}(\omega') (a^P)_{ji}^{\uparrow\downarrow lk}(\omega' + \omega) + S_{(j+l)(i+k)}^{A\downarrow}(\omega') (d^X)_{ji}^{\uparrow\downarrow lk}(\omega' - \omega) \\
& + S_{(i+k)(j+l)}^{R\downarrow}(\omega') (d^P)_{ji}^{\uparrow\downarrow lk}(\omega' + \omega) + S_{(j+l)(i+k)}^{R\downarrow}(\omega') (a^X)_{ji}^{\uparrow\downarrow lk}(\omega' - \omega) \\
& \left. + S_{(i+k)(j+l)}^{K\downarrow}(\omega') (b^P)_{ji}^{\uparrow\downarrow lk}(\omega' + \omega) + S_{(j+l)(i+k)}^{K\downarrow}(\omega') (b^X)_{ji}^{\uparrow\downarrow lk}(\omega' - \omega) \right\}
\end{aligned} \tag{A.12}$$

and

$$\begin{aligned}
\frac{\partial}{\partial \Lambda} (\Sigma_d)_{ji}^{K\downarrow}(\omega) = & -i \sum_{\omega'} \left\{ S_{(i+k)(j+l)}^{A\uparrow}(\omega') (a^P)_{ji}^{I\uparrow\downarrow lk}(\omega' + \omega) + S_{(j+l)(i+k)}^{A\uparrow}(\omega') (a^X)_{ji}^{TI\uparrow\downarrow lk}(\omega - \omega') \right. \\
& + S_{(i+k)(j+l)}^{R\uparrow}(\omega') (d^P)_{ji}^{I\uparrow\downarrow lk}(\omega' + \omega) + S_{(j+l)(i+k)}^{R\uparrow}(\omega') (d^X)_{ji}^{TI\uparrow\downarrow lk}(\omega - \omega') \\
& + S_{(i+k)(j+l)}^{K\uparrow}(\omega') (b^P)_{ji}^{I\uparrow\downarrow lk}(\omega' + \omega) + S_{(j+l)(i+k)}^{K\uparrow}(\omega') (b^X)_{ji}^{TI\uparrow\downarrow lk}(\omega - \omega') \\
& + S_{(i+k)(j+l)}^{A\downarrow}(\omega') (a^P)_{ji}^{\downarrow\downarrow lk}(\omega' + \omega) - S_{(j+l)(i+k)}^{A\downarrow}(\omega') (a^D)_{ji}^{TI\downarrow\downarrow lk}(\omega' - \omega) \\
& + S_{(i+k)(j+l)}^{R\downarrow}(\omega') (d^P)_{ji}^{\downarrow\downarrow lk}(\omega' + \omega) - S_{(j+l)(i+k)}^{R\downarrow}(\omega') (d^D)_{ji}^{TI\downarrow\downarrow lk}(\omega' - \omega) \\
& \left. + S_{(i+k)(j+l)}^{K\downarrow}(\omega') (b^P)_{ji}^{\downarrow\downarrow lk}(\omega' + \omega) - S_{(j+l)(i+k)}^{K\downarrow}(\omega') (b^D)_{ji}^{TI\downarrow\downarrow lk}(\omega' - \omega) \right\}.
\end{aligned} \tag{A.13}$$

Using the symmetry relations (2.207) - (2.208) and the compact notation introduced in (2.170), we can write this in the simpler form

$$\begin{aligned}
\frac{\partial}{\partial \Lambda} (\Sigma_s)^{K\uparrow}(\omega) = & -i \sum_{\omega'} \left\{ \left[\bar{v} + (a^D)^{TI}(0) \right]^{\uparrow\uparrow} \cdot \left[S + S^{T*} \right]^{\uparrow R}(\omega') \right. \\
& \left. + \left[\bar{v} + (d^D)(0) \right]^{\uparrow\downarrow} \left[S + S^{T*} \right]^{\downarrow R}(\omega') \right\},
\end{aligned} \tag{A.14a}$$

and

$$\begin{aligned}
\frac{\partial}{\partial \Lambda} (\Sigma_s)^{K\downarrow}(\omega) = & -i \sum_{\omega'} \left\{ \left[\bar{v} + (a^D)(0) \right]^{TI\uparrow\downarrow} \left[S + S^{T*} \right]^{R\uparrow}(\omega') \right. \\
& \left. + \left[\bar{v} + (a^D)^{TI}(0) \right]^{\downarrow\downarrow} \left[S + S^{T*} \right]^{R\downarrow}(\omega') \right\},
\end{aligned} \tag{A.14b}$$

and for the dynamic part

$$\begin{aligned}
\frac{\partial}{\partial \Lambda} (\Sigma_d)^{K\uparrow}(\omega) = -i \sum_{\omega'} \{ & \\
& \text{Tr} \left[(a^P)^{\uparrow\uparrow}(\omega' + \omega) \times (S^R)^{T\uparrow}(\omega')^* \right] - \text{Tr} \left[(a^D)^{TI\uparrow\uparrow}(\omega' - \omega) \times (S^R)^{\uparrow}(\omega')^* \right] \\
& + \text{Tr} \left[(a^P)^{TI\uparrow\uparrow}(\omega' + \omega)^* \times S^{R\uparrow}(\omega') \right] - \text{Tr} \left[(a^D)^{\uparrow\uparrow}(\omega - \omega') \times (S^R)^{T\uparrow}(\omega') \right] \\
& + \text{Tr} \left[(b^P)^{\uparrow\uparrow}(\omega' + \omega) \times S^{K\uparrow}(\omega') \right] - \text{Tr} \left[(b^D)^{TI\uparrow\uparrow}(\omega' - \omega) \times (S^K)^{T\uparrow}(\omega') \right] \\
& + \text{Tr} \left[(a^P)^{\uparrow\downarrow}(\omega' + \omega) \times (S^R)^{T\downarrow}(\omega')^* \right] + \text{Tr} \left[(a^X)^{T\uparrow\downarrow}(\omega' - \omega)^* \times (S^R)^{\downarrow*}(\omega') \right] \\
& + \text{Tr} \left[(a^P)^{T\uparrow\downarrow}(\omega' + \omega)^* \times S^{R\downarrow}(\omega') \right] + \text{Tr} \left[(a^X)^{\uparrow\downarrow}(\omega' - \omega) \times (S^R)^{T\downarrow}(\omega') \right] \\
& + \text{Tr} \left[(b^P)^{\uparrow\downarrow}(\omega' + \omega) \times S^{K\downarrow}(\omega') \right] + \text{Tr} \left[(b^X)^{\uparrow\downarrow}(\omega' - \omega) \times (S^K)^{T\downarrow}(\omega') \right] \} \quad (\text{A.15a})
\end{aligned}$$

and

$$\begin{aligned}
\frac{\partial}{\partial \Lambda} (\Sigma_d)^{K\downarrow}(\omega) = -i \sum_{\omega'} \{ & \\
& \text{Tr} \left[(a^P)^{I\uparrow\downarrow}(\omega' + \omega) \times (S^R)^{T\uparrow}(\omega')^* \right] + \text{Tr} \left[(a^X)^{TI\uparrow\downarrow}(\omega - \omega') \times (S^R)^{\uparrow}(\omega')^* \right] \\
& + \text{Tr} \left[(a^P)^{TI\uparrow\downarrow}(\omega' + \omega)^* \times S^{R\uparrow}(\omega') \right] + \text{Tr} \left[(a^X)^{I\uparrow\downarrow}(\omega - \omega')^* \times (S^R)^{T\uparrow}(\omega') \right] \\
& + \text{Tr} \left[(b^P)^{I\uparrow\downarrow}(\omega' + \omega) \times S^{K\uparrow}(\omega') \right] + \text{Tr} \left[(b^X)^{TI\uparrow\downarrow}(\omega - \omega') \times (S^K)^{T\uparrow}(\omega') \right] \\
& + \text{Tr} \left[(a^P)^{\downarrow\downarrow}(\omega' + \omega) \times (S^R)^{T\downarrow}(\omega')^* \right] - \text{Tr} \left[(a^D)^{TI\downarrow\downarrow}(\omega' - \omega) \times (S^R)^{\downarrow}(\omega')^* \right] \\
& + \text{Tr} \left[(a^P)^{T\downarrow\downarrow}(\omega' + \omega)^* \times S^{R\downarrow}(\omega') \right] - \text{Tr} \left[(a^D)^{\downarrow\downarrow}(\omega - \omega') \times (S^R)^{T\downarrow}(\omega') \right] \\
& + \text{Tr} \left[(b^P)^{\downarrow\downarrow}(\omega' + \omega) \times S^{K\downarrow}(\omega') \right] - \text{Tr} \left[(b^D)^{\downarrow\downarrow}(\omega - \omega') \times (S^K)^{T\downarrow}(\omega') \right] \}. \quad (\text{A.15b})
\end{aligned}$$

For the vertex, one obtains for b^P and b^X (correspondingly to Eq. (2.231))

$$\begin{aligned}
\frac{\partial}{\partial \Lambda} (b^P)^{\sigma\sigma}(\Pi) = (\tilde{a}^P)^{\sigma\sigma}(\Pi) \cdot \left[(I^{ph})^{11|22} + (I^{ph})^{22|22} + (I^{ph})^{22|11} \right](\Pi) \cdot (\tilde{d}^P)^{\sigma\sigma}(\Pi) \\
+ (\tilde{a}^P)^{\sigma\sigma}(\Pi) \cdot \left[(I^{ph})^{22|12} + (I^{ph})^{22|21} \right](\Pi) \cdot (b^P)^{\sigma\sigma}(\Pi) \\
+ (b^P)^{\sigma\sigma}(\Pi) \cdot \left[(I^{ph})^{21|22} + (I^{ph})^{12|22} \right](\Pi) \cdot (\tilde{d}^P)^{\sigma\sigma}(\Pi), \quad (\text{A.16})
\end{aligned}$$

$$\begin{aligned}
\frac{\partial}{\partial \Lambda} (b^P)^{\uparrow\downarrow}(\Pi) = 2(\tilde{a}^P)^{\uparrow\downarrow}(\Pi) \cdot \left[(I^{ph})^{11|22} + (I^{ph})^{22|22} + (I^{ph})^{22|11} \right](\Pi) \cdot (\tilde{d}^P)^{\uparrow\downarrow}(\Pi) \\
+ 2(\tilde{a}^P)^{\uparrow\downarrow}(\Pi) \cdot \left[(I^{ph})^{22|12} + (I^{ph})^{22|21} \right](\Pi) \cdot (b^P)^{\uparrow\downarrow}(\Pi) \\
+ 2(b^P)^{\uparrow\downarrow}(\Pi) \cdot \left[(I^{ph})^{21|22} + (I^{ph})^{12|22} \right](\Pi) \cdot (\tilde{d}^P)^{\uparrow\downarrow}(\Pi), \quad (\text{A.17})
\end{aligned}$$

$$\begin{aligned}
\frac{\partial}{\partial \Lambda} (b^X)^{\uparrow\downarrow}(X) = (\tilde{a}^X)^{\uparrow\downarrow}(X) \cdot \left[(I^{ph})^{21|12} + (I^{ph})^{12|21} + (I^{ph})^{22|22} \right](X) \cdot (\tilde{d}^X)^{\uparrow\downarrow}(X) \\
+ (\tilde{a}^X)^{\uparrow\downarrow}(X) \cdot \left[(I^{ph})^{21|22} + (I^{ph})^{22|12} \right](X) \cdot (b^X)^{\uparrow\downarrow}(X) \\
+ (b^X)^{\uparrow\downarrow}(X) \cdot \left[(I^{ph})^{22|21} + (I^{ph})^{12|22} \right](X) \cdot (\tilde{d}^X)^{\uparrow\downarrow}(X). \quad (\text{A.18})
\end{aligned}$$

Using the symmetries (2.207) – (2.208) this can be written as

$$\begin{aligned}
\frac{\partial}{\partial \Lambda} (b^P)^{\sigma\sigma}(\Pi) &= (\tilde{a}^P)^{\sigma\sigma}(\Pi) \cdot \left[(I^{ph})^{11|22} + (I^{ph})^{22|22} + (I^{ph})^{22|11} \right](\Pi) \cdot (\tilde{a}^P)^{T\sigma\sigma^*}(\Pi) \\
&+ (\tilde{a}^P)^{\sigma\sigma}(\Pi) \cdot \left[(I^{ph})^{22|12} + (I^{ph})^{22|21} \right](\Pi) \cdot (b^P)^{\sigma\sigma}(\Pi) \\
&+ (b^P)^{\sigma\sigma}(\Pi) \cdot \left[(I^{ph})^{21|22} + (I^{ph})^{12|22} \right](\Pi) \cdot (\tilde{a}^P)^{T\sigma\sigma^*}(\Pi), \quad (\text{A.19a})
\end{aligned}$$

$$\begin{aligned}
\frac{\partial}{\partial \Lambda} (b^P)^{\uparrow\downarrow}(\Pi) &= 2(\tilde{a}^P)^{\uparrow\downarrow}(\Pi) \cdot \left[(I^{ph})^{11|22} + (I^{ph})^{22|22} + (I^{ph})^{22|11} \right](\Pi) \cdot (\tilde{a}^P)^{T\uparrow\downarrow^*}(\Pi) \\
&+ 2(\tilde{a}^P)^{\uparrow\downarrow}(\Pi) \cdot \left[(I^{ph})^{22|12} + (I^{ph})^{22|21} \right](\Pi) \cdot (b^P)^{\uparrow\downarrow}(\Pi) \\
&+ 2(b^P)^{\uparrow\downarrow}(\Pi) \cdot \left[(I^{ph})^{21|22} + (I^{ph})^{12|22} \right](\Pi) \cdot (\tilde{a}^P)^{T\uparrow\downarrow^*}(\Pi), \quad (\text{A.19b})
\end{aligned}$$

$$\begin{aligned}
\frac{\partial}{\partial \Lambda} (b^X)^{\uparrow\downarrow}(X) &= (\tilde{a}^X)^{\uparrow\downarrow}(X) \cdot \left[(I^{ph})^{21|12} + (I^{ph})^{12|21} + (I^{ph})^{22|22} \right](X) \cdot (\tilde{a}^X)^{T\uparrow\downarrow^*}(X) \\
&+ (\tilde{a}^X)^{\uparrow\downarrow}(X) \cdot \left[(I^{ph})^{21|22} + (I^{ph})^{22|12} \right](X) \cdot (b^X)^{\uparrow\downarrow}(X) \\
&+ (b^X)^{\uparrow\downarrow}(X) \cdot \left[(I^{ph})^{22|21} + (I^{ph})^{12|22} \right](X) \cdot (\tilde{a}^X)^{T\uparrow\downarrow^*}(X). \quad (\text{A.19c})
\end{aligned}$$

Analogously, we obtain for the flow of b^D

$$\begin{aligned}
\frac{\partial}{\partial \Lambda} (b^D)^{\uparrow\uparrow}(\Delta) &= -\left\{ (\tilde{a}^D)^{\uparrow\uparrow}(\Delta) \cdot \left[(I^{ph})^{21|12} + (I^{ph})^{22|22} + (I^{ph})^{12|21} \right]^{TI\uparrow\uparrow}(\Delta) \cdot (\tilde{d}^D)^{\uparrow\uparrow}(\Delta) \right. \\
&+ (b^D)^{\uparrow\uparrow}(\Delta) \cdot \left[(I^{ph})^{21|22} + (I^{ph})^{22|12} \right]^{TI\uparrow\uparrow}(\Delta) \cdot (\tilde{d}^D)^{\uparrow\uparrow}(\Delta) \\
&+ (\tilde{a}^D)^{\uparrow\uparrow}(\Delta) \cdot \left[(I^{ph})^{12|22} + (I^{ph})^{22|21} \right]^{TI\uparrow\uparrow}(\Delta) \cdot (b^D)^{\uparrow\uparrow}(\Delta) \\
&+ (\tilde{a}^D)^{\uparrow\downarrow}(\Delta) \cdot \left[(I^{ph})^{21|12} + (I^{ph})^{22|22} + (I^{ph})^{12|21} \right]^{TI\downarrow\downarrow}(\Delta) \cdot (\tilde{a}^D)^{TI\uparrow\downarrow}(-\Delta) \\
&+ (b^D)^{\uparrow\downarrow}(\Delta) \cdot \left[(I^{ph})^{21|22} + (I^{ph})^{22|12} \right]^{TI\downarrow\downarrow}(\Delta) \cdot (\tilde{a}^D)^{TI\uparrow\downarrow}(-\Delta) \\
&\left. + (\tilde{a}^D)^{\uparrow\downarrow}(\Delta) \cdot \left[(I^{ph})^{12|22} + (I^{ph})^{22|21} \right]^{TI\downarrow\downarrow}(\Delta) \cdot (\tilde{b}^D)^{TI\uparrow\downarrow}(-\Delta) \right\}, \quad (\text{A.20})
\end{aligned}$$

$$\begin{aligned}
\frac{\partial}{\partial \Lambda} (b^D)^{\downarrow\downarrow}(\Delta) &= -\left\{ (\tilde{a}^D)^{\downarrow\downarrow}(\Delta) \cdot \left[(I^{ph})^{21|12} + (I^{ph})^{22|22} + (I^{ph})^{12|21} \right]^{TI\downarrow\downarrow}(\Delta) \cdot (\tilde{d}^D)^{\downarrow\downarrow}(\Delta) \right. \\
&+ (b^D)^{\downarrow\downarrow}(\Delta) \cdot \left[(I^{ph})^{21|22} + (I^{ph})^{22|12} \right]^{TI\downarrow\downarrow}(\Delta) \cdot (\tilde{d}^D)^{\downarrow\downarrow}(\Delta) \\
&+ (\tilde{a}^D)^{\downarrow\downarrow}(\Delta) \cdot \left[(I^{ph})^{12|22} + (I^{ph})^{22|21} \right]^{TI\downarrow\downarrow}(\Delta) \cdot (b^D)^{\downarrow\downarrow}(\Delta) \\
&+ (\tilde{d}^D)^{TI\uparrow\downarrow}(-\Delta) \cdot \left[(I^{ph})^{21|12} + (I^{ph})^{22|22} + (I^{ph})^{12|21} \right]^{TI\uparrow\uparrow}(\Delta) \cdot (\tilde{d}^D)^{\uparrow\downarrow}(\Delta) \\
&+ (b^D)^{TI\uparrow\downarrow}(-\Delta) \cdot \left[(I^{ph})^{21|22} + (I^{ph})^{22|12} \right]^{TI\uparrow\uparrow}(\Delta) \cdot (\tilde{d}^D)^{\uparrow\downarrow}(\Delta) \\
&\left. + (\tilde{d}^D)^{TI\uparrow\downarrow}(-\Delta) \cdot \left[(I^{ph})^{12|22} + (I^{ph})^{22|21} \right]^{TI\uparrow\uparrow}(\Delta) \cdot (\tilde{b}^D)^{\uparrow\downarrow}(\Delta) \right\}, \quad (\text{A.21})
\end{aligned}$$

and

$$\begin{aligned}
\frac{\partial}{\partial \Lambda} (b^D)^{\uparrow\downarrow}(\Delta) = & -\left\{ (\tilde{a}^D)^{\uparrow\uparrow}(\Delta) \cdot \left[(I^{ph})^{21|12} + (I^{ph})^{22|22} + (I^{ph})^{12|21} \right]^{TI\uparrow\uparrow}(\Delta) \cdot (\tilde{d}^D)^{\uparrow\downarrow}(\Delta) \right. \\
& + (b^D)^{\uparrow\uparrow}(\Delta) \cdot \left[(I^{ph})^{21|22} + (I^{ph})^{22|12} \right]^{TI\uparrow\uparrow}(\Delta) \cdot (\tilde{d}^D)^{\uparrow\downarrow}(\Delta) \\
& + (\tilde{a}^D)^{\uparrow\uparrow}(\Delta) \cdot \left[(I^{ph})^{12|22} + (I^{ph})^{22|21} \right]^{TI\uparrow\uparrow}(\Delta) \cdot (b^D)^{\uparrow\downarrow}(\Delta) \\
& + (\tilde{a}^D)^{\uparrow\downarrow}(\Delta) \cdot \left[(I^{ph})^{21|12} + (I^{ph})^{22|22} + (I^{ph})^{12|21} \right]^{TI\downarrow\downarrow}(\Delta) \cdot (\tilde{d}^D)^{\downarrow\downarrow}(\Delta) \\
& + (b^D)^{\uparrow\downarrow}(\Delta) \cdot \left[(I^{ph})^{21|22} + (I^{ph})^{22|12} \right]^{TI\downarrow\downarrow}(\Delta) \cdot (\tilde{d}^D)^{\downarrow\downarrow}(\Delta) \\
& \left. + (\tilde{a}^D)^{\uparrow\downarrow}(\Delta) \cdot \left[(I^{ph})^{12|22} + (I^{ph})^{22|21} \right]^{TI\downarrow\downarrow}(\Delta) \cdot (b^D)^{\downarrow\downarrow}(\Delta) \right\}. \quad (\text{A.22})
\end{aligned}$$

Using the symmetries (2.207) - (2.208) as well as the bubble symmetries (2.221), this can be written as

$$\begin{aligned}
\frac{\partial}{\partial \Lambda} (b^D)^{\uparrow\uparrow}(\Delta) = & -\left\{ (\tilde{a}^D)^{\uparrow\uparrow}(\Delta) \cdot \left[(I^{ph})^{12|21} + (I^{ph})^{22|22} + (I^{ph})^{21|12} \right]^{\uparrow\uparrow}(-\Delta) \cdot (\tilde{a}^D)^{T\uparrow\uparrow*}(\Delta) \right. \\
& + (b^D)^{\uparrow\uparrow}(\Delta) \cdot \left[(I^{ph})^{12|22} + (I^{ph})^{22|21} \right]^{\uparrow\uparrow}(-\Delta) \cdot (\tilde{a}^D)^{T\uparrow\uparrow*}(\Delta) \\
& + (\tilde{a}^D)^{\uparrow\uparrow}(\Delta) \cdot \left[(I^{ph})^{21|22} + (I^{ph})^{22|12} \right]^{\uparrow\uparrow}(-\Delta) \cdot (b^D)^{\uparrow\uparrow}(\Delta) \\
& + (\tilde{a}^D)^{\uparrow\downarrow}(\Delta) \cdot \left[(I^{ph})^{12|21} + (I^{ph})^{22|22} + (I^{ph})^{21|12} \right]^{\downarrow\downarrow}(-\Delta) \cdot (\tilde{a}^D)^{T\uparrow\downarrow*}(\Delta) \\
& + (b^D)^{\uparrow\downarrow}(\Delta) \cdot \left[(I^{ph})^{12|22} + (I^{ph})^{22|21} \right]^{\downarrow\downarrow}(-\Delta) \cdot (\tilde{a}^D)^{T\uparrow\downarrow*}(\Delta) \\
& \left. - (\tilde{a}^D)^{\uparrow\downarrow}(\Delta) \cdot \left[(I^{ph})^{21|22} + (I^{ph})^{22|12} \right]^{\downarrow\downarrow}(-\Delta) \cdot (\tilde{b}^D)^{T\uparrow\downarrow*}(\Delta) \right\}, \quad (\text{A.23a})
\end{aligned}$$

$$\begin{aligned}
\frac{\partial}{\partial \Lambda} (b^D)^{\downarrow\downarrow}(\Delta) = & -\left\{ (\tilde{a}^D)^{\downarrow\downarrow}(\Delta) \cdot \left[(I^{ph})^{12|21} + (I^{ph})^{22|22} + (I^{ph})^{21|12} \right]^{\downarrow\downarrow}(-\Delta) \cdot (\tilde{a}^D)^{T\downarrow\downarrow*}(\Delta) \right. \\
& + (b^D)^{\downarrow\downarrow}(\Delta) \cdot \left[(I^{ph})^{12|22} + (I^{ph})^{22|21} \right]^{\downarrow\downarrow}(-\Delta) \cdot (\tilde{a}^D)^{T\downarrow\downarrow*}(\Delta) \\
& + (\tilde{a}^D)^{\downarrow\downarrow}(\Delta) \cdot \left[(I^{ph})^{21|22} + (I^{ph})^{22|12} \right]^{\downarrow\downarrow}(-\Delta) \cdot (b^D)^{\downarrow\downarrow}(\Delta) \\
& + (\tilde{d}^D)^{T\uparrow\downarrow*}(\Delta) \cdot \left[(I^{ph})^{12|21} + (I^{ph})^{22|22} + (I^{ph})^{21|12} \right]^{\uparrow\uparrow}(-\Delta) \cdot (\tilde{d}^D)^{\uparrow\downarrow}(\Delta) \\
& - (b^D)^{T\uparrow\downarrow*}(\Delta) \cdot \left[(I^{ph})^{12|22} + (I^{ph})^{22|21} \right]^{\uparrow\uparrow}(-\Delta) \cdot (\tilde{d}^D)^{\uparrow\downarrow}(\Delta) \\
& \left. + (\tilde{d}^D)^{T\uparrow\downarrow*}(\Delta) \cdot \left[(I^{ph})^{21|22} + (I^{ph})^{22|12} \right]^{\uparrow\uparrow}(-\Delta) \cdot (\tilde{b}^D)^{\uparrow\downarrow}(\Delta) \right\}, \quad (\text{A.23b})
\end{aligned}$$

and

$$\begin{aligned}
\frac{\partial}{\partial \Lambda} (b^D)^{\uparrow\downarrow}(\Delta) = & -\left\{ (\tilde{a}^D)^{\uparrow\uparrow}(\Delta) \cdot \left[(I^{ph})^{12|21} + (I^{ph})^{22|22} + (I^{ph})^{21|12} \right]^{\uparrow\uparrow}(-\Delta) \cdot (\tilde{d}^D)^{\uparrow\downarrow}(\Delta) \right. \\
& + (b^D)^{\uparrow\uparrow}(\Delta) \cdot \left[(I^{ph})^{12|22} + (I^{ph})^{22|21} \right]^{\uparrow\uparrow}(-\Delta) \cdot (\tilde{d}^D)^{\uparrow\downarrow}(\Delta) \\
& + (\tilde{a}^D)^{\uparrow\uparrow}(\Delta) \cdot \left[(I^{ph})^{21|22} + (I^{ph})^{22|12} \right]^{\uparrow\uparrow}(-\Delta) \cdot (b^D)^{\uparrow\downarrow}(\Delta) \\
& + (\tilde{a}^D)^{\uparrow\downarrow}(\Delta) \cdot \left[(I^{ph})^{12|21} + (I^{ph})^{22|22} + (I^{ph})^{21|12} \right]^{\downarrow\downarrow}(-\Delta) \cdot (\tilde{a}^D)^{T\downarrow\downarrow*}(\Delta) \\
& + (b^D)^{\uparrow\downarrow}(\Delta) \cdot \left[(I^{ph})^{12|22} + (I^{ph})^{22|21} \right]^{\downarrow\downarrow}(-\Delta) \cdot (\tilde{a}^D)^{T\downarrow\downarrow*}(\Delta) \\
& \left. + (\tilde{a}^D)^{\uparrow\downarrow}(\Delta) \cdot \left[(I^{ph})^{21|22} + (I^{ph})^{22|12} \right]^{\downarrow\downarrow}(-\Delta) \cdot (b^D)^{\downarrow\downarrow}(\Delta) \right\}. \tag{A.23c}
\end{aligned}$$

A.4 Consistency check of symmetries with flow equations

In this section, we check the consistency of the various symmetry relations for the channel decomposition (Matsubara: (2.177) – (2.179) and (A.6i), Keldysh: (2.207) – (2.208) and (A.7) – (A.9)) that we inferred from the exact symmetries discussed in Sec. 2.2, with the fRG flow.

Due to the symmetries of the bare interaction (2.5) (and since we choose the feedback ϕ to have the same symmetries), one easily sees that $\tilde{\gamma}^A$ has the same symmetries as φ^A for all channels $A \in \{P, X, D\}$.

A.4.1 Permutation of particles

Since we used this symmetry to eliminate redundant spin components, we take a look at the most general flow equations (2.138) that still describe the flow of all spin components. One obtains then straightforwardly

$$\begin{aligned}
\frac{\partial}{\partial \Lambda} (\varphi^P)_{k'_1 k'_2 | k_1 k_2}^\Lambda(\Pi) &= (\tilde{\gamma}^P)_{k'_1 k'_2 | k_3 k_4}^\Lambda(\Pi) (\hat{I}^{pp})_{k_3 k_4 | k'_3 k'_4}^\Lambda(\Pi) (\tilde{\gamma}^P)_{k'_3 k'_4 | k_1 k_2}^\Lambda(\Pi) \\
&= -(\tilde{\gamma}^P)_{k'_2 k'_1 | k_3 k_4}^\Lambda(\Pi) (\hat{I}^{pp})_{k_3 k_4 | k'_3 k'_4}^\Lambda(\Pi) (\tilde{\gamma}^P)_{k'_3 k'_4 | k_1 k_2}^\Lambda(\Pi) \\
&= -\frac{\partial}{\partial \Lambda} (\varphi^P)_{k'_2 k'_1 | k_1 k_2}^\Lambda(\Pi), \tag{A.24}
\end{aligned}$$

$$\begin{aligned}
\frac{\partial}{\partial \Lambda} (\varphi^P)_{k'_1 k'_2 | k_1 k_2}^\Lambda(\Pi) &= (\tilde{\gamma}^P)_{k'_1 k'_2 | k_3 k_4}^\Lambda(\Pi) (\hat{I}^{pp})_{k_3 k_4 | k'_3 k'_4}^\Lambda(\Pi) (\tilde{\gamma}^P)_{k'_3 k'_4 | k_1 k_2}^\Lambda(\Pi) \\
&= -(\tilde{\gamma}^P)_{k'_1 k'_2 | k_3 k_4}^\Lambda(\Pi) (\hat{I}^{pp})_{k_3 k_4 | k'_3 k'_4}^\Lambda(\Pi) (\tilde{\gamma}^P)_{k'_3 k'_4 | k_2 k_1}^\Lambda(\Pi) \\
&= -\frac{\partial}{\partial \Lambda} (\varphi^P)_{k'_2 k'_1 | k_2 k_1}^\Lambda(\Pi), \tag{A.25}
\end{aligned}$$

$$\begin{aligned}
\frac{\partial}{\partial \Lambda} (\varphi^X)_{k'_1 k'_2 | k_1 k_2}^\Lambda(X) &= (\tilde{\gamma}^X)_{k'_1 k'_4 | k_3 k_2}^\Lambda(X) (I^{ph})_{k_3 k_4 | k'_3 k'_4}^\Lambda(X) (\tilde{\gamma}^X)_{k'_3 k'_2 | k_1 k_4}^\Lambda(X) \\
&= (\tilde{\gamma}^D)_{k'_4 k'_1 | k_3 k_2}^\Lambda(X) (I^{ph})_{k_3 k_4 | k'_3 k'_4}^\Lambda(X) (\tilde{\gamma}^D)_{k'_2 k'_3 | k_1 k_4}^\Lambda(X) \\
&= -\frac{\partial}{\partial \Lambda} (\varphi^D)_{k'_2 k'_1 | k_1 k_2}^\Lambda(X), \tag{A.26}
\end{aligned}$$

$$\begin{aligned}
\frac{\partial}{\partial \Lambda} (\varphi^X)_{k'_1 k'_2 | k_1 k_2}^\Lambda(X) &= (\tilde{\gamma}^X)_{k'_1 k'_4 | k_3 k_2}^\Lambda(X) (I^{ph})_{k_3 k_4 | k'_3 k'_4}^\Lambda(X) (\tilde{\gamma}^X)_{k'_3 k'_2 | k_1 k_4}^\Lambda(X) \\
&= (\tilde{\gamma}^D)_{k'_1 k'_4 | k_2 k_3}^\Lambda(-X) (I^{ph})_{k_3 k_4 | k'_3 k'_4}^\Lambda(X) (\tilde{\gamma}^D)_{k'_3 k'_2 | k_4 k_1}^\Lambda(-X) \\
&= (\tilde{\gamma}^D)_{k'_1 k'_4 | k_2 k_3}^\Lambda(-X) (I^{ph})_{k_4 k_3 | k'_4 k'_3}^\Lambda(-X) (\tilde{\gamma}^D)_{k'_3 k'_2 | k_4 k_1}^\Lambda(-X) \\
&= -\frac{\partial}{\partial \Lambda} (\varphi^D)_{k'_1 k'_2 | k_2 k_1}^\Lambda(-X), \tag{A.27}
\end{aligned}$$

where in the second to last line of (A.27), we used the general bubble symmetry

$$(I^{ph})_{k_3 k_4 | k'_3 k'_4}(X) = (I^{ph})_{k_4 k_3 | k'_4 k'_3}(-X), \tag{A.28}$$

which immediately follows from the definition (2.139). Therefore, the permutation of particles symmetry is conserved under the fRG flow.

A.4.2 Complex conjugation

Let us first look at the Matsubara case. Since we have shown the validity of the particle permutation symmetry (2.142) – (2.143), i.e. the replacement of the redundant spin components, we can now use the spatial index free flow equations (2.188) instead of the general equations (2.138). We then obtain the relations for the two-particle vertex contributions

$$\begin{aligned}
\frac{\partial}{\partial \Lambda} A^{\sigma\sigma'}(\Omega)^* &= \alpha^{A\sigma\sigma'} \tilde{A}^{\sigma\sigma'}(\Omega)^* \cdot (W^A)^{\sigma\sigma'}(\Omega)^* \tilde{A}^{\sigma\sigma'}(\Omega)^* \\
&= \alpha^{A\sigma\sigma'} \tilde{A}^{T\sigma\sigma'}(-\Omega) \cdot (W^A)^{T\sigma\sigma'}(-\Omega) \cdot \tilde{A}^{T\sigma\sigma'}(-\Omega) \\
&= \left[\alpha^{A\sigma\sigma'} \tilde{A} \cdot W^A \cdot \tilde{A} \right]^{T\sigma\sigma'}(-\Omega) = \frac{\partial}{\partial \Lambda} A^{T\sigma\sigma'}(-\Omega), \tag{A.29}
\end{aligned}$$

for $A \in \{P, X\}$ and

$$\alpha^{A\sigma\sigma'} = \begin{cases} 2, & \text{for } A=P \text{ and } \sigma \neq \sigma' \\ 1, & \text{else.} \end{cases} \tag{A.30}$$

Furthermore, one obtains for the D -channel (using the flow equations (2.190) and relation (2.180b))

$$\begin{aligned}
\frac{\partial}{\partial \Lambda} D^{\sigma\sigma'}(\Delta)^* &= -\sum_{\tau} \left[D^{\sigma\tau}(\Delta)^* \cdot (W^X)^{\tau\tau}(-\Delta)^* \cdot \tilde{D}^{\tau\sigma}(\Delta)^* \right] \\
&= -\sum_{\tau} \left[D^{I\sigma\tau}(\Delta) \cdot (W^X)^{I\tau\tau}(-\Delta) \cdot \tilde{D}^{I\tau\sigma}(\Delta) \right] \\
&= -\sum_{\tau} \left[D^{\sigma\tau}(\Delta) \cdot (W^X)^{\tau\tau}(-\Delta) \cdot \tilde{D}^{\tau\sigma}(\Delta) \right]^I = \frac{\partial}{\partial \Lambda} D^{I\sigma\sigma'}(\Delta). \tag{A.31}
\end{aligned}$$

In the Keldysh case we have to go back once more to the general flow Eq. (2.138) since in our final (non-equilibrium) flow equations we have used complex conjugation to eliminate the

redundant d -components in the P - and X -channel. We have then for the individual channels

$$\begin{aligned}
\frac{\partial}{\partial \Lambda} (\varphi^P)^{\alpha'|\alpha} (\Pi)^* &= (\tilde{\gamma}^P)^{\alpha'|\beta} (\Pi)^* (I^{pp})^{\beta|\beta'} (\Pi)^* (\tilde{\gamma}^P)^{\beta'|\alpha} (\Pi)^* \\
&= (-1)^{\alpha'|\beta} (\tilde{\gamma}^P)^{\beta|\alpha'} (\Pi)^* (-1)^{\beta|\beta'} (I^{pp})^{\beta'|\beta} (\Pi)^* (-1)^{\beta'|\alpha} (\tilde{\gamma}^P)^{\alpha|\beta'} (\Pi)^* \\
&= (-1)^{\alpha'|\alpha} (\tilde{\gamma}^P)^{\alpha|\beta'} (\Pi)^* (I^{pp})^{\beta'|\beta} (\Pi)^* (\tilde{\gamma}^P)^{\beta|\alpha'} (\Pi)^* \\
&= (-1)^{\alpha'|\alpha} \frac{\partial}{\partial \Lambda} (\varphi^P)^{\alpha|\alpha'} (\Pi), \tag{A.32}
\end{aligned}$$

$$\begin{aligned}
\frac{\partial}{\partial \Lambda} (\varphi^X)^{\alpha'_1 \alpha'_2 |\alpha_1 \alpha_2} (X)^* &= (\tilde{\gamma}^X)^{\alpha'_1 \alpha'_4 |\alpha_3 \alpha_2} (X)^* (I^{ph})^{\alpha_3 \alpha_4 |\alpha'_3 \alpha'_4} (X)^* (\tilde{\gamma}^X)^{\alpha'_3 \alpha'_2 |\alpha_1 \alpha_4} (X)^* \\
&= (-1)^{1+\alpha'_1+\alpha'_4+\alpha_3+\alpha_2} (\tilde{\gamma}^X)^{\alpha_3 \alpha_2 |\alpha'_1 \alpha'_4} (X) \\
&\times (-1)^{1+\alpha_3+\alpha_4+\alpha'_3+\alpha'_4} (I^{ph})^{\alpha'_3 \alpha'_4 |\alpha_3 \alpha_4} (X) \\
&\times (-1)^{1+\alpha'_3+\alpha'_2+\alpha_1+\alpha_4} (\tilde{\gamma}^X)^{\alpha_1 \alpha_4 |\alpha'_3 \alpha'_2} (X) \\
&= (-1)^{\alpha' \alpha} \frac{\partial}{\partial \Lambda} (\varphi^X)^{\alpha_1 \alpha_2 |\alpha'_1 \alpha'_2} (X), \tag{A.33}
\end{aligned}$$

and

$$\begin{aligned}
\frac{\partial}{\partial \Lambda} (\varphi^D)^{\alpha'_1 \alpha'_2 |\alpha_1 \alpha_2} (\Delta)^* &= -(\tilde{\gamma}^D)^{\alpha'_1 \alpha'_3 |\alpha_1 \alpha_4} (\Delta)^* (I^{ph})^{\alpha_3 \alpha_4 |\alpha'_3 \alpha'_4} (\Delta)^* (\tilde{\gamma}^D)^{\alpha'_4 \alpha'_2 |\alpha_3 \alpha_2} (\Delta)^* \\
&= -(-1)^{\alpha'_1+\alpha'_3+\alpha_1+\alpha_4} (\tilde{\gamma}^D)^{\alpha_1 \alpha_4 |\alpha'_1 \alpha'_3} (-\Delta) \\
&\times (-1)^{1+\alpha_3+\alpha_4+\alpha'_3+\alpha'_4} (I^{ph})^{\alpha'_3 \alpha'_4 |\alpha_3 \alpha_4} (\Delta) \\
&\times (-1)^{1+\alpha'_4+\alpha'_2+\alpha_3+\alpha_2} (\tilde{\gamma}^D)^{\alpha_3 \alpha_2 |\alpha'_4 \alpha'_2} (-\Delta) \\
&= -(-1)^{\alpha' \alpha} (\tilde{\gamma}^D)^{\alpha_1 \alpha'_3 |\alpha'_1 \alpha_4} (-\Delta) (I^{ph})^{\alpha_3 \alpha_4 |\alpha'_3 \alpha'_4} (-\Delta) (\tilde{\gamma}^D)^{\alpha'_4 \alpha_2 |\alpha_3 \alpha'_2} (-\Delta) \\
&= (-1)^{\alpha' \alpha} \frac{\partial}{\partial \Lambda} (\varphi^D)^{\alpha \alpha'} (-\Delta). \tag{A.34}
\end{aligned}$$

Therefore, the complex conjugation symmetries (2.205) are conserved under the fRG flow.

A.4.3 Time reversal

In the Matsubara case, the time-reversal symmetries (2.179) are consistent with the flow (2.184), (2.186), (2.188), and (2.190). We have

$$\frac{\partial}{\partial \Lambda} \Sigma_s^{T\sigma} = \frac{\partial}{\partial \Lambda} \Sigma_s^{I\sigma} = -\left\{ [\bar{v} + D(0)]^{\uparrow\sigma} \cdot \hat{S}^\uparrow + [\bar{v} + D(0)]^{\sigma\downarrow} \cdot \hat{S}^\downarrow \right\}^I \tag{A.35}$$

$$= -\left\{ [\bar{v} + D(0)]^{I\uparrow\sigma} \cdot \hat{S}^{I\uparrow} + [\bar{v} + D(0)]^{I\sigma\downarrow} \cdot \hat{S}^{I\downarrow} \right\}^I \tag{A.36}$$

$$= \frac{\partial}{\partial \Lambda} \Sigma_s^\sigma, \tag{A.37}$$

where we used the property (2.179) for the D -channel and the bare vertex (for the bare vertex this property results immediately from (2.5b)) and the fact that $D(0)$ is real. Furthermore,

using Eqs. (2.177) and (2.179) we have

$$\begin{aligned} \frac{\partial}{\partial \Lambda} \Sigma_d^{T\uparrow}(\omega) &= -T \sum_n \left\{ \text{Tr} \left[\left(P^{T\uparrow\uparrow}(\omega_n + \omega) - D^{T\uparrow\uparrow}(\omega - \omega_n) \right) \times S^{T\uparrow}(\omega_n) \right] \right. \\ &\quad \left. + \text{Tr} \left[\left(P^{T\uparrow\downarrow}(\omega_n + \omega) + X^{T\uparrow\downarrow}(\omega_n - \omega) \right) \times S^{T\downarrow}(\omega_n) \right] \right\}, \end{aligned} \quad (\text{A.38})$$

$$\begin{aligned} &= -T \sum_n \left\{ \text{Tr} \left[\left(P^{\uparrow\uparrow}(\omega_n + \omega) - D^{\uparrow\uparrow}(\omega - \omega_n) \right) \times S^{\uparrow}(\omega_n) \right] \right. \\ &\quad \left. + \text{Tr} \left[\left(P^{\uparrow\downarrow}(\omega_n + \omega) + X^{\uparrow\downarrow}(\omega_n - \omega) \right) \times S^{\downarrow}(\omega_n) \right] \right\}, \end{aligned} \quad (\text{A.39})$$

$$= \frac{\partial}{\partial \Lambda} \Sigma_d^{\uparrow}(\omega). \quad (\text{A.40})$$

Therefore the symmetry $\Sigma^T = \Sigma$ is consistent with the flow.

For the P - and X -channel we have using Eqs. (2.179) – (2.180)

$$\frac{\partial}{\partial \Lambda} A^{T\sigma\sigma'}(\Omega) = \alpha^{\sigma\sigma'} \tilde{A}^{T\sigma\sigma'}(\Omega) (W^A)^{T\sigma\sigma'}(\Omega) \tilde{A}^{T\sigma\sigma'}(\Omega) \quad (\text{A.41})$$

$$= \alpha^{\sigma\sigma'} \tilde{A}^{\sigma\sigma'}(\Omega) (W^A)^{\sigma\sigma'}(\Omega) \tilde{A}^{\sigma\sigma'}(\Omega) \quad (\text{A.42})$$

$$= \frac{\partial}{\partial \Lambda} A^{\sigma\sigma'}(\Omega), \quad (\text{A.43})$$

with $A^{\sigma\sigma'} \in \{P^{\uparrow\uparrow}, P^{\downarrow\downarrow}, P^{\uparrow\downarrow}, X^{\uparrow\downarrow}\}$, and $\alpha^{\sigma\sigma} = 1/2$, $\alpha^{\uparrow\downarrow} = 1$. Therefore, the symmetries $P = P^T$ and $X = X^T$ are consistent with the flow.

For the D -channel we have

$$\frac{\partial}{\partial \Lambda} D^{I\sigma\sigma'}(\Delta) = - \sum_{\tau} \left[\tilde{D}^{\sigma\tau}(\Delta) (W^X)^{\tau\tau}(-\Delta) \tilde{D}^{\tau\sigma'}(\Delta) \right]^I \quad (\text{A.44})$$

$$= - \sum_{\tau} \left[\tilde{D}^{I\sigma\tau}(\Delta) (W^X)^{I\tau\tau}(-\Delta) \tilde{D}^{I\tau\sigma'}(\Delta) \right]^I \quad (\text{A.45})$$

$$= - \sum_{\tau} \left[\tilde{D}^{\sigma\tau}(-\Delta) (W^X)^{\tau\tau}(+\Delta) \tilde{D}^{\tau\sigma'}(-\Delta) \right]^I \quad (\text{A.46})$$

$$= \frac{\partial}{\partial \Lambda} D^{\sigma\sigma'}(-\Delta). \quad (\text{A.47})$$

Therefore the symmetry $D^{\sigma\sigma'}(\Delta) = D^{I\sigma\sigma'}(-\Delta)$ is consistent with the flow.

A.4.4 FDTs

We first consider the relation $a^* = d$, stated in (2.236).

For the P - and X -channel we know already from complex conjugation (2.206)

$$\frac{\partial}{\partial \Lambda} d_{q'q}^A(\Omega) = \frac{\partial}{\partial \Lambda} a_{qq'}^A(\Omega)^*, \quad (\text{A.48})$$

with $A \in \{P, X\}$. Therefore, it is enough to show

$$\frac{\partial}{\partial \Lambda} (a^A)_{qq'} = \frac{\partial}{\partial \Lambda} (a^A)_{q'q}. \quad (\text{A.49})$$

Using Eqs. (2.179) – (2.180) yields for $(a^A)^{\sigma\sigma'} \in \{(a^P)^{\uparrow\uparrow}, (a^P)^{\downarrow\downarrow}, (a^P)^{\uparrow\downarrow}, (a^X)^{\uparrow\downarrow}\}$

$$\frac{\partial}{\partial\Lambda}(a^A)^{\sigma\sigma'} = \alpha^{\sigma\sigma'}(\tilde{a}^A)^{\sigma\sigma'} \cdot (W^A)^{\sigma\sigma'} \cdot (\tilde{a}^A)^{\sigma\sigma'} \quad (\text{A.50})$$

$$= \alpha^{\sigma\sigma'}(\tilde{a}^A)^{T\sigma\sigma'} \cdot (W^A)^{T\sigma\sigma'} \cdot (\tilde{a}^A)^{T\sigma\sigma'} \quad (\text{A.51})$$

$$= \alpha^{\sigma\sigma'} \left[(\tilde{a}^A)^{T\sigma\sigma'} \cdot (W^A)^{T\sigma\sigma'} \cdot (\tilde{a}^A)^{T\sigma\sigma'} \right]^T \quad (\text{A.52})$$

$$= \frac{\partial}{\partial\Lambda}(a^A)^{T\sigma\sigma'}. \quad (\text{A.53})$$

Therefore, $(a^A)^* = d^A$ holds for the P - and X -channel.

For the equal spin part of the D -channel we already know from particle exchange (2.208) and complex conjugation (2.207) that

$$\frac{\partial}{\partial\Lambda}(a^D)^{\sigma\sigma}(\Delta) \stackrel{(2.208)}{=} \frac{\partial}{\partial\Lambda}(d^D)^{TI\sigma\sigma}(-\Delta) \stackrel{(2.207)}{=} \frac{\partial}{\partial\Lambda}(d^D)^{T\sigma\sigma}(\Delta)^*. \quad (\text{A.54})$$

Therefore it suffices to show

$$\frac{\partial}{\partial\Lambda}(a^D)^{T\sigma\sigma} = \frac{\partial}{\partial\Lambda}(a^D)^{\sigma\sigma}. \quad (\text{A.55})$$

We have

$$\frac{\partial}{\partial\Lambda}(a^D)^{\sigma\sigma}(\Delta) = -(\tilde{a}^D)^{\sigma\tau}(\Delta)(W^X)^{\tau\tau}(-\Delta)(\tilde{a}^D)^{\tau\sigma}(\Delta) \quad (\text{A.56})$$

$$= -(\tilde{a}^D)^{T\tau\sigma}(\Delta)(W^X)^{T\tau\tau}(-\Delta)(\tilde{a}^D)^{T\sigma\tau}(\Delta) \quad (\text{A.57})$$

$$= -\left[(\tilde{a}^D)^{T\sigma\tau}(\Delta)(W^X)^{T\tau\tau}(-\Delta)(\tilde{a}^D)^{T\tau\sigma}(\Delta) \right]^T \quad (\text{A.58})$$

$$= \frac{\partial}{\partial\Lambda}(a^D)^{T\sigma\sigma}(\Delta). \quad (\text{A.59})$$

Furthermore, using the general bubble symmetry

$$(W^X)^{I\sigma\sigma'}(X) = (W^X)^{\sigma'\sigma}(-X)^*, \quad (\text{A.60})$$

which can be seen immediately from definition (2.223), we have for the $(d^D)^{\uparrow\downarrow}$ component

$$\frac{\partial}{\partial\Lambda}(d^D)^{\uparrow\downarrow}(\Delta) = -\left\{ (\tilde{d}^D)^{\uparrow\uparrow}(\Delta) \cdot (W^X)^{TI\uparrow\uparrow}(\Delta) \cdot (\tilde{d}^D)^{\uparrow\uparrow}(\Delta) \right. \quad (\text{A.61})$$

$$\left. + (\tilde{d}^D)^{\uparrow\downarrow}(\Delta) \cdot (W^X)^{TI\downarrow\downarrow}(\Delta) \cdot (\tilde{d}^D)^{\downarrow\downarrow}(\Delta) \right\} \quad (\text{A.62})$$

$$= -\left\{ (\tilde{a}^D)^{\uparrow\uparrow}(\Delta)^* \cdot (W^X)^{\uparrow\uparrow}(-\Delta)^* \cdot (\tilde{a}^D)^{\uparrow\uparrow}(\Delta)^* \right. \quad (\text{A.63})$$

$$\left. + (\tilde{a}^D)^{\uparrow\downarrow}(\Delta)^* \cdot (W^X)^{\downarrow\downarrow}(-\Delta)^* \cdot (\tilde{a}^D)^{\downarrow\downarrow}(\Delta)^* \right\} \quad (\text{A.64})$$

$$= \frac{\partial}{\partial\Lambda}(a^D)^{\uparrow\downarrow}(\Delta)^* \quad (\text{A.65})$$

Therefore, the relation $(a^A)^* = d^A$ is for all three channels $A \in \{P, X, D\}$ consistent with the flow equations.

Now we can check the consistency of vertex FDTs (2.237) with the flow equations (2.231) and (2.233). In order to shorten notation, we simply write I instead of I^{pp} in the P - and I^{ph} in the X -channel.

For the P -channel we have in thermal equilibrium

$$\begin{aligned}
2i \frac{\partial}{\partial \Lambda} \text{Im}(a^P)^{\sigma\sigma'} &= \alpha^{\sigma\sigma'} \left[(\tilde{a}^P)^{\sigma\sigma'} \left[I^{22|12} + I^{22|21} \right]^{\sigma\sigma'} (\tilde{a}^R)^{\sigma\sigma'} - (\tilde{a}^P)^{\sigma\sigma'*} \left[I^{22|12} + I^{22|21} \right]^* (\tilde{a}^P)^{\sigma\sigma'*} \right] \\
&= \alpha^{\sigma\sigma'} \left[(\tilde{a}^P)^{\sigma\sigma'} \left[I^{22|12} + I^{22|21} \right] 2i \text{Im}(a^P)^{\sigma\sigma'} + 2i \text{Im}(a^P)^{\sigma\sigma'} \left[I^{12|22} + I^{21|22} \right]^{\sigma\sigma'} (\tilde{a}^P)^{\sigma\sigma'*} \right. \\
&\quad \left. + (\tilde{a}^P)^{\sigma\sigma'} \left[I^{22|12} + I^{22|21} \right]^{\sigma\sigma'} (\tilde{a}^P)^{\sigma\sigma'*} - (\tilde{a}^P)^{\sigma\sigma'} \left[I^{12|22} + I^{21|22} \right]^{\sigma\sigma'} (\tilde{a}^P)^{\sigma\sigma'*} \right], \tag{A.66}
\end{aligned}$$

where we used the flow equation (A.19) and the symmetry relations (2.221c) and $I = I^T$ (analogous to (2.235)). Comparing this to the flow of b^P in (A.19), it suffices to show that

$$-\coth\left(\frac{\Pi - 2\mu}{2T}\right) \left[I^{22|12} + I^{22|21} - I^{12|22} - I^{21|22} \right]^{\sigma\sigma'} = \left[I^{11|22} + I^{22|11} + I^{22|22} \right]^{\sigma\sigma'}. \tag{A.67}$$

We have

$$\left[I^{22|12} + I^{22|21} - I^{12|22} - I^{21|22} \right]^{\sigma\sigma'} \tag{A.68}$$

$$= \alpha^{\sigma\sigma'} \frac{i}{4\pi} \int d\omega \left[S^{R\uparrow}(\omega) G^{K\downarrow}(\Pi - \omega) + S^{K\uparrow}(\omega) G^{R\downarrow}(\Pi - \omega) \right] \tag{A.69}$$

$$- S^{A\uparrow}(\omega) G^{K\downarrow}(\Pi - \omega) - S^{K\uparrow}(\omega) G^{A\downarrow}(\Pi - \omega) + [S \leftrightarrow G] \tag{A.70}$$

$$= -\alpha^{\sigma\sigma'} \frac{2i}{\pi} \text{Im} S^{R\sigma}(\omega) \text{Im} G^{R\sigma'}(\Pi - \omega) \left(1 - n_F(X + \omega) - n_F(\omega) \right) + [S \leftrightarrow G]. \tag{A.71}$$

Furthermore,

$$\left[I^{21|12} + I^{12|21} + I^{22|22} \right]^{\sigma\sigma'}(X) \tag{A.72}$$

$$= \alpha^{\sigma\sigma'} \frac{i}{4\pi} \int d\omega \left[S^{A\sigma}(\omega) G^{A\sigma'}(\Pi - \omega) + S^{R\sigma}(\omega) G^{R\sigma'}(\Pi - \omega) \right] \tag{A.73}$$

$$+ S^{K\sigma}(\omega) G^{K\sigma'}(\Pi - \omega) + [S \leftrightarrow G] \tag{A.74}$$

$$= \alpha^{\sigma\sigma'} \frac{i}{4\pi} \int d\omega \left[S^{R\sigma}(\omega) G^{R\sigma'}(\Pi - \omega) + S^{R\sigma}(\omega)^* G^{R\sigma'}(\Pi - \omega)^* \right] \tag{A.75}$$

$$+ (2i)^2 (1 - 2n_F(\omega))(1 - 2n_F(\Pi - \omega)) \text{Im} S^{R\sigma}(\omega) \text{Im} G^{R\sigma'}(\Pi - \omega) + [S \leftrightarrow G] \tag{A.76}$$

$$= \alpha^{\sigma\sigma'} \frac{i}{4\pi} \int d\omega \left[S^{R\sigma}(\omega) G^{R\sigma'}(\Pi - \omega) + S^{R\sigma}(\omega)^* G^{R\sigma'}(\Pi - \omega)^* \right] \tag{A.77}$$

$$- S^{R\sigma}(\omega) G^{R\sigma'}(\Pi - \omega)^* - S^{R\sigma}(\omega)^* G^{R\sigma'}(\Pi - \omega) \tag{A.78}$$

$$+ (2i)^2 (1 - 2n_F(\omega))(1 - 2n_F(\Pi - \omega)) \text{Im} S^{R\sigma}(\omega) \text{Im} G^{R\sigma'}(\Pi - \omega) + [S \leftrightarrow G] \tag{A.79}$$

$$= -\alpha^{\sigma\sigma'} \frac{2i}{\pi} \text{Im} S^{R\sigma}(\omega) \text{Im} G^{R\sigma'}(\Pi - \omega) \left[1 - n_F(\omega) - n_F(\Pi - \omega) + 2n_F(\omega)n_F(\Pi - \omega) + [S \leftrightarrow G] \right] \tag{A.80}$$

Comparing (A.80) with (A.71), it suffices to show the identity

$$\coth\left(\left(\frac{\Pi}{2} - \mu\right)/T\right) \left[1 - n_F(\omega) - n_F(\Pi - \omega) \right] = 1 - n_F(\omega) - n_F(\Pi - \omega) + 2n_F(\omega)n_F(\Pi - \omega), \tag{A.81}$$

which can be done by a straightforward computation, using the explicit form of the Fermi function n_F (2.106). Therefore we have

$$2i \coth\left(\left(\frac{\Pi}{2} - \mu\right)/T\right) \frac{\partial}{\partial \Lambda} \text{Im}(a^P)^{\sigma\sigma'} = \frac{\partial}{\partial \Lambda} (b^P)^{\sigma\sigma'}, \quad (\text{A.82})$$

i.e. the vertex FDT for the P -channel (2.237a) is conserved under the flow.

For the X -channel we have

$$\begin{aligned} 2i \frac{\partial}{\partial \Lambda} \text{Im}(a^X)^{\uparrow\downarrow} &= (\tilde{a}^X)^{\uparrow\downarrow} [I^{22|12} + I^{21|22}] (\tilde{a}^X)^{\uparrow\downarrow} - (\tilde{a}^X)^{\uparrow\downarrow*} [I^{22|12} + I^{21|22}]^* (\tilde{a}^X)^{\uparrow\downarrow*} \\ &= (\tilde{a}^X)^{\uparrow\downarrow} [I^{22|12} + I^{21|22}] 2i \text{Im}(a^X)^{\uparrow\downarrow} + 2i \text{Im}(a^X)^{\uparrow\downarrow} [I^{12|22} + I^{22|21}] (\tilde{a}^X)^{\uparrow\downarrow*} \\ &\quad + (\tilde{a}^X)^{\uparrow\downarrow} [I^{22|12} + I^{21|22}] (\tilde{a}^X)^{\uparrow\downarrow*} - (\tilde{a}^X)^{\uparrow\downarrow} [I^{12|22} + I^{22|21}] (\tilde{a}^X)^{\uparrow\downarrow*}. \end{aligned} \quad (\text{A.83})$$

Comparing this to the flow of b^X in (A.19), it suffices to show that

$$-\coth\left(\frac{X}{2T}\right) [I^{22|12} + I^{21|22} - I^{12|22} - I^{22|21}]^{\uparrow\downarrow}(X) = [I^{21|12} + I^{12|21} + I^{22|22}]^{\uparrow\downarrow}(X) \quad (\text{A.84})$$

We have

$$[I^{22|12} + I^{21|22} - I^{12|22} - I^{22|21}]^{\uparrow\downarrow}(X) \quad (\text{A.85})$$

$$= \frac{i}{2\pi} \int d\omega [S^{R\uparrow}(\omega) G^{K\downarrow}(X + \omega) + S^{K\uparrow}(\omega) G^{A\downarrow}(X + \omega)] \quad (\text{A.86})$$

$$- S^{A\uparrow}(\omega) G^{K\downarrow}(X + \omega) - S^{K\uparrow}(\omega) G^{R\downarrow}(X + \omega) + [S \leftrightarrow G] \quad (\text{A.87})$$

$$= \frac{4i}{\pi} \text{Im} S^{R\uparrow}(\omega) \text{Im} G^{R\downarrow}(X + \omega) (n_F(X + \omega) - n_F(\omega)) + [S \leftrightarrow G]. \quad (\text{A.88})$$

Furthermore,

$$[I^{21|12} + I^{12|21} + I^{22|22}]^{\uparrow\downarrow}(X) \quad (\text{A.89})$$

$$= \frac{i}{2\pi} \int d\omega [S^{R\uparrow}(\omega) G^{A\downarrow}(X + \omega) + S^{A\uparrow}(\omega) G^{R\downarrow}(X + \omega)] \quad (\text{A.90})$$

$$+ S^{K\uparrow}(\omega) G^{K\downarrow}(X + \omega) + [S \leftrightarrow G] \quad (\text{A.91})$$

$$= \frac{i}{2\pi} \int d\omega [S^{R\uparrow}(\omega) G^{R\downarrow}(X + \omega)^* + S^{R\uparrow}(\omega)^* G^{R\downarrow}(X + \omega)] \quad (\text{A.92})$$

$$+ (2i)^2 (1 - 2n_F(\omega))(1 - 2n_F(X + \omega)) + [S \leftrightarrow G] \quad (\text{A.93})$$

$$= \frac{i}{2\pi} \int d\omega [S^{R\uparrow}(\omega) G^{R\downarrow}(X + \omega)^* + S^{R\uparrow}(\omega)^* G^{R\downarrow}(X + \omega)] \quad (\text{A.94})$$

$$- S^{R\uparrow}(\omega) G^{R\downarrow}(X + \omega) - S^{R\uparrow}(\omega)^* G^{R\downarrow}(X + \omega)^* \quad (\text{A.95})$$

$$+ (2i)^2 (1 - 2n_F(\omega))(1 - 2n_F(X + \omega)) + [S \leftrightarrow G] \quad (\text{A.96})$$

$$= \frac{4i}{\pi} \text{Im} S^{R\uparrow}(\omega) \text{Im} G^{R\downarrow}(X + \omega) (n_F(\omega) + n_F(\omega + X) - 2n_F(\omega)n_F(X + \omega)) + [S \leftrightarrow G] \quad (\text{A.97})$$

Comparing (A.97) with (A.88), it suffices to show the identity

$$-\coth\left(\frac{X}{2T}\right)\left[n_F(X+\omega)-n_F(\omega)\right]=n_F(X+\omega)+n_F(\omega)-2n_F(\omega)n_F(X+\omega), \quad (\text{A.98})$$

which again can be done by straightforward computation. Therefore we have

$$-2i\coth\left(\frac{X}{2T}\right)\frac{\partial}{\partial\Lambda}\text{Im}(a^X)^{\uparrow\downarrow}=\frac{\partial}{\partial\Lambda}(b^X)^{\uparrow\downarrow}, \quad (\text{A.99})$$

i.e. the vertex FDT for the X -channel (2.237b) is conserved under the flow.

For the D -channel, we have

$$2i\frac{\partial}{\partial\Lambda}\text{Im}(a^D)^{\sigma\sigma'}(\Delta)=-\left\{(\tilde{a}^D)^{\sigma\tau}(\Delta)\cdot\left[I^{22|21}+I^{12|22}\right]^{I\tau\tau}(\Delta)\cdot(\tilde{a}^D)^{\tau\sigma'}(\Delta)\right. \quad (\text{A.100})$$

$$\left.-(\tilde{a}^D)^{\sigma\tau}(\Delta)^*\cdot\left[I^{22|21}+I^{12|22}\right]^{I\tau\tau*}(\Delta)\cdot(\tilde{a}^D)^{\tau\sigma'*}(\Delta)\right\} \quad (\text{A.101})$$

$$=-\left\{(\tilde{a}^D)^{\sigma\tau}(\Delta)\cdot\left[I^{22|21}+I^{12|22}\right]^{I\tau\tau}(\Delta)\cdot 2i\text{Im}(a^D)^{\tau\sigma'}(\Delta)\right. \quad (\text{A.102})$$

$$\left.+2i\text{Im}(a^D)^{\sigma\tau}(\Delta)\cdot\left[I^{21|22}+I^{22|12}\right]^{I\tau\tau}(\Delta)\cdot(\tilde{a}^D)^{\tau\sigma'}(\Delta)\right. \quad (\text{A.103})$$

$$\left.+(\tilde{a}^D)^{\sigma\tau}(\Delta)\cdot\left[I^{22|21}+I^{12|22}\right]^{I\tau\tau}(\Delta)\cdot(\tilde{a}^D)^{\tau\sigma'}(\Delta)^*\right. \quad (\text{A.104})$$

$$\left.-(\tilde{a}^D)^{\sigma\tau}(\Delta)\cdot\left[I^{21|22}+I^{22|12}\right]^{I\tau\tau}(\Delta)\cdot(\tilde{a}^D)^{\tau\sigma'}(\Delta)^*\right\} \quad (\text{A.105})$$

Comparing expression (A.105) to the flow of the b^D -components (A.23), it suffices to show

$$\coth\left(\frac{\Delta}{2T}\right)\left[I^{22|21}+I^{12|22}-I^{21|22}-I^{22|12}\right]^{\sigma\sigma'}(\Delta)=\left[I^{21|12}+I^{12|21}+I^{22|22}\right]^{\sigma\sigma'}(\Delta), \quad (\text{A.106})$$

which is equivalent to Eq. (A.84). Therefore we have

$$2i\coth\left(\frac{\Delta}{2T}\right)\frac{\partial}{\partial\Lambda}\text{Im}(a^D)^{\sigma\sigma'}=\frac{\partial}{\partial\Lambda}(b^D)^{\sigma\sigma'}, \quad (\text{A.107})$$

i.e. the vertex FDT for the D -channel (2.237c) is conserved under the flow.

A.5 Ladder resumable flow

Equations references in this section that refer to our publication in Sec. 5.2 above are marked with the prefix ‘‘P3:’’.

In this section, we discuss in which sense our approximation P3:(33) leads in the case of decoupled channel flow equations to a resumable RPA-like structure. We focus here on the equal spin contribution of the P-channel, the other contributions can be treated analogously. With this in mind, we suppress the channel and spin labels in the following calculation in order to facilitate notation. The strategy for our calculation is simple. Let us start from (5.4)

and take the derivative w.r.t. the flow-parameter Λ :

$$\frac{\partial}{\partial \Lambda} a_{ji}^{lk}(\Pi) = \left[\left(1 - \nu \frac{1}{4} J(\Pi)\right)^{-1} \nu \right]_{jj_1}^{ll_1} \left[\frac{\partial}{\partial \Lambda} J(\Pi) \right]_{j_1 j_2}^{l_1 l_2} \left[\left(1 - \nu \frac{1}{4} J(\Pi)\right)^{-1} \nu \right]_{j_2 i}^{l_2 k} \quad (\text{A.108})$$

$$\begin{aligned} &= \sum_{|l_1|, |l_2| \leq L_d(\Pi)} \left[a_{jj_1}^{ll_1}(\Pi) + \nu_{jj_1}^{ll_1} \right] \left[\frac{\partial}{\partial \Lambda} J(\Pi) \right]_{j_1 j_2}^{l_1 l_2} \left[a_{j_2 i}^{l_2 k}(\Pi) + \nu_{j_2 i}^{l_2 k} \right] \\ &+ \sum_{|l_1| \leq L_d(\Pi) < |l_2|} \left\{ \left[a_{jj_1}^{ll_1}(\Pi) + \nu_{jj_1}^{ll_1} \right] \left[\frac{\partial}{\partial \Lambda} J(\Pi) \right]_{j_1 j_2}^{l_1 l_2} \left[\left(1 - \nu \frac{1}{4} J(\Pi)\right)^{-1} \nu \right]_{j_2 i}^{l_2 k} \right. \\ &+ \left. \left[\left(1 - \nu \frac{1}{4} J(\Pi)\right)^{-1} \nu \right]_{jj_1}^{ll_1} \left[\frac{\partial}{\partial \Lambda} J(\Pi) \right]_{j_1 j_2}^{l_1 l_2} \left[\left(1 - \nu \frac{1}{4} J(\Pi)\right)^{-1} \nu \right]_{j_2 i}^{l_2 k} \right\} \\ &+ \sum_{L_d(\Pi) < |l_1|, |l_2|} \left[\left(1 - \nu \frac{1}{4} J(\Pi)\right)^{-1} \nu \right]_{jj_1}^{ll_1} \left[\frac{\partial}{\partial \Lambda} J(\Pi) \right]_{j_1 j_2}^{l_1 l_2} \left[\left(1 - \nu \frac{1}{4} J(\Pi)\right)^{-1} \nu \right]_{j_2 i}^{l_2 k}. \end{aligned} \quad (\text{A.109})$$

In the second line, we inserted definition (5.4) wherever possible, i.e. whenever both short indices of a vertex factor are in the dynamical range. What is left is the evaluation of quantities of the form

$$\left[\left(1 - \nu \frac{1}{4} J(\Pi)\right)^{-1} \nu \right]_{ji}^{lk}, \quad (\text{A.110})$$

with $l \leq L_d(\Pi)$ and $L_d(\Pi) < k$, i.e. where one short index is inside and the other one is outside of the dynamical range. For this, we make use of the structure of our bare vertex: ν is of Coulomb type, i.e. the positions of the outgoing particles have to be the same as the ingoing ones. In our short index formulation this implies that $\nu_{ji}^{lk} \neq 0$ only if $|k| = |l|$. Using this property, we can decompose (A.110)

$$\left[\left(1 - \nu \frac{1}{4} J(\Pi)\right)^{-1} \nu \right]_{ji}^{lk} = \sum_{l_1 < L_d(\Pi)} \left[\left(1 - \nu \frac{1}{4} J(\Pi)\right)^{-1} \nu \right]_{jj_1}^{ll_1} \left[\left(1 - \frac{1}{4} J(2\mu) \hat{\nu}\right)^{-1} \right]_{j_1 i}^{l_1 k}, \quad (\text{A.111})$$

where

$$\hat{\nu}_{ji}^{lk} = \begin{cases} \nu_{ji}^{lk} & \text{if } |l|, |k| > L_d(\Pi) \\ 0 & \text{else.} \end{cases} \quad (\text{A.112})$$

The last factor of (A.111) itself can be computed from the analog decomposition at the feedback frequency 2μ

$$\left[\left(1 - \frac{1}{4} J(2\mu) \nu\right)^{-1} \nu \right]_{ji}^{lk} = \sum_{|l_1| < L_d(\Pi)} \left[\left(1 - \frac{1}{4} J(2\mu) \nu\right)^{-1} \nu \right]_{jj_1}^{ll_1} \left[\left(1 - \frac{1}{4} J(2\mu) \hat{\nu}\right)^{-1} \right]_{j_1 i}^{l_1 k}, \quad (\text{A.113})$$

and thus, under the assumption that the first factor in (A.113) can be inverted in dynamical block-matrix space, we obtain

$$\left[\left(1 - \frac{1}{4} J(2\mu) \hat{\nu}\right)^{-1} \right]_{ji}^{lk} = \left[\left(\left(1 - \frac{1}{4} J(2\mu) \nu\right)^{-1} \nu \right)^{-1} \right]_{jj_1}^{ll_1} \left[\left(1 - \frac{1}{4} J(2\mu) \nu\right)^{-1} \nu \right]_{j_1 i}^{l_1 k}. \quad (\text{A.114})$$

This inversion is here denoted by the red “ -1 ” and is e.g. possible if the bare vertex ν itself is invertible in block-matrix space. Note that for our model P3:(1) this is per se not the case, due to the vanishing contribution at the sites coupling to the leads. However it can be made invertible by adding a infinitesimal small contribution on the diagonal: $\nu_{ji}^{lk} \rightarrow \nu_{ji}^{lk} + \epsilon \delta_{lk} \delta_{ji}$.

For our numerical results presented in Sec. 5.3 we added such a small additional term, the resulting physics of the model does not change under such a small addition. Using (A.114), we finally obtain

$$\begin{aligned}
& \left[\left(1 - \nu \frac{1}{4} J(\Pi) \right)^{-1} \nu \right]_{ji}^{lk} \\
&= \sum_{|l_1|, |l_2| < L_d(\Pi)} \left[\left(1 - \nu \frac{1}{4} J(\Pi) \right)^{-1} \nu \right]_{jj_1}^{ll_1} \left[\left(\left(1 - \frac{1}{4} J(2\mu) \nu \right)^{-1} \nu \right)^{-1} \right]_{j_1 j_2}^{l_1 l_2} \left(1 - \frac{1}{4} J(2\mu) \nu \right)^{-1} \nu \right]_{j_2 i}^{l_2 k} \\
&= \sum_{|l_1|, |l_2| < L_d(\Pi)} \left[a(\Pi) + \nu \right]_{jj_1}^{ll_1} \left[(a(2\mu) + \nu)^{-1} \right]_{j_1 j_2}^{l_1 l_2} \left[a(2\mu) + \nu \right]_{j_2 i}^{l_2 k}. \tag{A.115}
\end{aligned}$$

A completely analog expression can be obtained when the rolls of l and k are interchanged, $|l| > L_d(\Pi)$ and $|k| \leq L_d(\Pi)$. In a final step, we replace terms of this type in (A.109) via (A.115) and obtain exactly the modified flow introduced in Sec. 5.3.

List of Figures

- 1.1 (a) Schematics of an experimental implementation of a layered semiconductor QPC. The 2DEG is depicted in red, the electrodes (gates on the top, source-drain electrodes on the side) in black. (b) electron microscope picture of the surface of a QPC, reproduced from [ILK⁺13]. The device here has three pairs of attached gates, enabling the tuning of the effective QPC length. 6
- 1.2 (a) Illustration of the parabolic saddlepoint potential $V(x, y)$ in the center of the QPC with positive y-curvature and negative x-curvature. The horizontal lines indicate the transversal energy levels $n = 1, 2, \dots$ in the center of the QPC. (b) First measurement of a quantized QPC conductance as function of gate voltage by Van Wees et al., reproduced from [vWvHB⁺88]. 6
- 1.3 First observation of the 0.7 anomaly by Thomas et al., reproduced from [TNS⁺96]. (a) With increasing temperature, a conductance shoulder emerges around $G = 0.7G_Q$. (b) With increasing magnetic field this shoulder develops into a spin split plateau. 7
- 1.4 First observation of conductance quantization in a metallic (quantum) point contact, reproduced from [KvRF⁺95]. The conductance is plotted as function of the distance between the source and drain electrodes in the break junction (lower horizontal axis). This distance can be varied changing the voltage of a Piezo element (upper horizontal axis). Note that here $2e^2/h$ as well as $4e^2/h$ conductance steps occur. Inset: Schematic of the experimental setup. 8
- 1.5 (a) Scanning electron microscopy picture of a graphene stripe with attached electrodes [TVJ⁺11]. Segment “C” is just the full unconstricted strip, whereas segments “A” and “B” show constrictions of varying size. (b,c) Observed quantization of the conductance G as a function of the Fermi momentum k_F , for the hole branch (blue) and the electron branch (red). The conductance is quantized in integer plateaus, clearly pronounced for the first plateau and then becoming weaker with increasing plateau number. (d) Conductance as function of gate voltage and finite magnetic field. Note the structure at $G/G_Q \approx 0.6$, developing at small magnetic fields and resembling the 0.7-shoulder in regular QPCs. Figures (a)-(d) were reproduced from [TVJ⁺11]. 9
- 1.6 (a) Conductance quantization of a gated graphene sheet, reproduced from [KCL⁺16]. Between $G = 10G_Q - 22G_Q$ one can observe clear conductance steps with height $G = 4G_Q$, i.e. the valley symmetry of graphene is in this regime conserved. (b) Conductance quantization of a single-walled carbon nanotube, reproduced from [BMM⁺05]. Interestingly, quantization occurs here with steps $G = 0.5G_Q$, indicating that spin-symmetry is broken. 10
- 1.7 (a) First observation of quantized conductance in a nanowire, observed by Lu et al., reproduced from [LXT⁺05]. (b) Highly controllable multigate nanowire device, reproduced from [HPS⁺16], and (c) observed conductance within that device. Note that in both (a) and (c) a pronounced 0.7-shoulder is observable. 11

- 1.8 (a),(b) Schematics of the experimental setup used for the cold atom QPC experiment in [KSH⁺14]. (c) Image of the resulting QPC constriction. (d) Quantized conductance observed in the steady state of the setup in (a), for a tighter (red curve, for clarity offset by $2\tilde{G}_Q$) and a wider QPC constriction (blue curve). Note the possible candidate for a 0.7-shoulder in the first conductance step of the blue data. The inset shows the conductance curves for a frequency axis scaled by ν_z , demonstrating the overall universality of the (non-interacting) conductance quantization. Figures (a)-(d) were reproduced from [KSH⁺14] . 12
- 1.9 Conductance $g = G/G_Q$ as function of gate voltage V_g for a single subband. (a) With varying temperature the conductance is smeared out symmetrically around the $g = 0.5$ point. (b) Finite magnetic field lifts the spin degeneracy and leads to a development of a spin-split plateau. Note that also here the splitting occurs symmetrically around the $g = 0.5$ point 15
- 1.10 Conductance as function of bias voltage V_{sd} for several values of the gate voltage V_g . Note that for a closed QPC an increase in V_{sd} leads to an increase of conductance, while for an open QPC it leads to a decrease. 16
- 1.11 Measurements of the first conductance step, reproduced from [BHS⁺13]. Development of the 0.7 anomaly for varying magnetic fields (a) and temperatures (b). Note that for very small temperature and zero magnetic field the 0.7-shoulder vanishes. 17
- 1.12 (a) Measured bias dependence of the conductance for various gate voltages. Note the zero bias anomaly (ZBA) occurring at $V_{sd} = 0$ and small conductance g . (b) Temperature dependence of the ZBA and the side peaks. Figures (a) and (b) were reproduced from [CLGG⁺02] 17
- 1.13 Illustration of the development of the QPC energy levels with increasing magnetic field. The region of the 0.7-analog at the intersection of the spin-up branch of the first subband and the spin-down branch of the second subband is marked in red, whereas the region of the ordinary 0.7-anomaly is marked in blue. 19
- 1.14 Conductance as function of gate voltage for increasing magnetic fields as measured in [GTP⁺03], reproduced from our publication in Sec. 4.2. The dashed and solid ellipses mark the 0.7-region and the similar shoulder structure appearing at the 0.7-analog, respectively. Note the asymmetry in the magnetic field dependence of the 0.7-analog, depending whether it is approached from lower or higher magnetic fields. 20
- 1.15 (a-c) Development of the magnetic field dependence of the QPC conductance with increasing dimensionless SOI strength R . (d-f) QPC transconductance in presence of SOI. Note that at large R , the splitting of the double step is not linear in B but almost constant (see arrow in (f)). Figures (a)-(f) were reproduced from [GBHvD14] 20
- 1.16 Detection of spin polarization via spin orbit interactions, reproduced from [YKT⁺18]. (a) Detector voltage as function of perpendicular magnetic field. Note the splitting of odd peaks arising from SOI. Inset: Focusing geometries with longer (90deg shape of split gates) and shorter QPC (60deg shape of split gates). (b) First focusing peak (blue circles) with fitted Lorentzian subpeaks (green and magenta curves). Note that the amplitude difference of the subpeaks, indicating a spin polarization of the QPC. (c) Resulting polarization (computed from the amplitude of the subpeaks in (b)) and conductance as function of gate voltage. 21

1.17	Local density of states $\mathcal{A}_j(\omega)$ of a QPC barrier, reproduced from [BHvD14], (a) as colorplot of site j and frequency ω and (b) $\mathcal{A}_j(\omega)$ at different sites j . Note that at the QPC center ($j = 0$) the LDOS attains its maximum at a small but finite value above 0. The oscillating structure in the flanks of the QPC are due to Friedel oscillations.	24
2.1	Schematic of our generic physical setup, consisting of an interacting, inhomogeneous center region described by H_C , connected via the coupling terms H_{LC} and H_{CR} on both sides to non-interacting leads H_L and H_R	29
2.2	Double time contour with forward “-” branch and backward “+” branch and initial distribution ρ_0	30
2.3	Illustration of a diagram that contributes to G_{ij} and after the exchange T of all internal incoming and outgoing spatial and spin indices yields a diagram contributing to G_{ji}	44
2.4	Illustration of the analytic continuation of $G(\omega)$ to either $G^R(\omega)$ for $\omega > \mu$ or $G^A(\omega)$ for $\omega < \mu$	47
2.5	Illustration of the correlation function (2.117) that can not be represented on the usual double contour (a). On the four branch contour (b) this is possible without a problem.	47
2.6	Schematic of the three different channels, the particle-particle channel (a), and the exchange and the direct part of the particle-hole channel (b) and (c).	52
5.1	Comparison between the RPA, the standard and the modified vertex flow result for the vertex component $a^{D\sigma\sigma}(\Omega)$. We used a small system with $N = 5$, i.e. 11 sites and a finite-ranged interaction ($L_U = 3$) with (a) a smaller and (b) a bigger interaction strength. Case (b) is close to the divergence of the RPA and the differences between the RPA/modified flow and the standard flow become apparent.	139
6.1	(a) Schematic plot of the system with two non-interacting tight-binding leads as well as a disordered, interacting central region. (b) Random potential V_i (black) and interaction U_i for one disorder realization and system size $N = 61$ sites with $V_d = 1.2\tau$ and $U = 0.8\tau$. Dotted lines illustrate properties of a smaller system. Note that the interaction is suppressed at the boundary of the central region.	142
6.2	The typical dephasing temperature, T_{deph} , (blue) and the MBL-transition temperature, T_c (red), depending on the dimensionless interaction strength λ	143
6.3	DOS $\mathcal{A}_\alpha(\omega)$ (positiv) and corresponding $\text{Im}\Sigma(\omega)$ (negativ) for six different α in the middle of the spectrum. The dashed line denotes the value of the chemical potential. Note that the values of the DOS have been divided by 10^2	145
6.4	Same setting as in Fig. 6.3, but we plot only the DOS and the self-energy for the occupied level closest to the chemical potential (the blue curves from Fig. 6.3) for equally spaced temperatures $T = 0.0, 0.02, \dots, 0.2$. The dashed line indicates the DOS maximum for $T = 0$	146
6.5	Dependence of $\text{Im}\Sigma$ on T , extracted with the method described above. We have plotted here data for three different system sizes $N = 31$ (blue), $N = 41$ (green) and $N = 61$ (red). The bars at the datapoints are not errorbars in a classical sense but indicate the magnitude of the two-particle vertex, and thus serve as a internal sanity check for our fRG approximation.	147
6.6	Same plot as in Fig. 6.5 but using a log-log scale. Straight lines have been fitted to the linear part of the plots (only shown for the $N = 31$ case, c.f. blue solid and dashed lines) and were used to extract powerlaw exponents.	147

- 6.7 (a) Grayscale plot of the interacting LDOS $\mathcal{A}_i^g(\omega)$ as function of site and frequency. (b-d) LDOS at site $i = -5$ in the non-interacting case (b) and in the interacting case (c-d) for different temperatures. Black markers indicate the non-interacting eigenenergies, colored markers the detected peaks in the LDOS. The inset in (d) shows the number of these peaks per site. (e-f) show the DOS in energy space for three different eigenenergies (colored markers) for two different temperatures. Black markers indicate again the non-interacting eigenenergies. 148

Bibliography

- [AH09] K. Aryanpour and J. E. Han, *Ferromagnetic spin coupling as the origin of 0.7 anomaly in quantum point contacts*, Phys. Rev. Lett. **102** (2009), 056805. See page: [1](#)
- [ANP⁺00] N. J. Appleyard, J. T. Nicholls, M. Pepper, W. R. Tribe, M. Y. Simmons, and D. A. Ritchie, *Direction-resolved transport and possible many-body effects in one-dimensional thermopower*, Phys. Rev. B **62** (2000), R16275–R16278. See page: [16](#)
- [BAA06] D.M. Basko, I.L. Aleiner, and B.L. Altshuler, *Metal–insulator transition in a weakly interacting many-electron system with localized single-particle states*, Annals of Physics **321** (2006), no. 5, 1126 – 1205. See pages: [3](#), [141](#), [142](#), and [145](#)
- [Bau14] Florian Bauer, *Microscopic origin of the 0.7-anomaly in quantum point contacts*, Ph.D. thesis, Ludwig-Maximilians-Universität München, 2014. See pages: [13](#), [23](#), [27](#), [48](#), [49](#), and [51](#)
- [BF06] L. Brey and H. A. Fertig, *Electronic states of graphene nanoribbons studied with the dirac equation*, Phys. Rev. B **73** (2006), 235411. See page: [8](#)
- [BHS⁺13] Florian Bauer, Jan Heyder, Enrico Schubert, David Borowsky, Daniela Taubert, Benedikt Bruognolo, Dieter Schuh, Werner Wegscheider, Jan von Delft, and Stefan Ludwig, *Microscopic origin of the ‘0.7-anomaly’ in quantum point contacts*, Nature **501** (2013), no. 7465, 73–78. See pages: [1](#), [2](#), [16](#), [17](#), [19](#), [21](#), [22](#), [77](#), [101](#), and [172](#)
- [BHvD14] Florian Bauer, Jan Heyder, and Jan von Delft, *Functional renormalization group approach for inhomogeneous interacting fermi systems*, Phys. Rev. B **89** (2014), 045128. See pages: [1](#), [24](#), [57](#), [64](#), [77](#), [78](#), and [173](#)
- [BJY05] Karl-Fredrik Berggren, Peter Jaksch, and Irina Yakimenko, *Effects of electron interactions at crossings of zeeman-split subbands in quantum wires*, Phys. Rev. B **71** (2005), 115303. See page: [101](#)
- [BKdV⁺93] D. S. Bethune, C. H. Kiang, M. S. de Vries, G. Gorman, R. Savoy, J. Vazquez, and R. Beyers, *Cobalt-catalysed growth of carbon nanotubes with single-atomic-layer walls*, Nature **363** (1993), no. 6430, 605–607. See page: [10](#)
- [BKF⁺12] A. M. Burke, O. Klochan, I. Farrer, D. A. Ritchie, A. R. Hamilton, and A. P. Micolich, *Extreme sensitivity of the spin-splitting and 0.7 anomaly to confining potential in one-dimensional nanoelectronic devices*, Nano Letters **12** (2012), no. 9, 4495–4502. See page: [1](#)
- [BMM⁺05] M. J. Biercuk, N. Mason, J. Martin, A. Yacoby, and C. M. Marcus, *Anomalous conductance quantization in carbon nanotubes*, Phys. Rev. Lett. **94** (2005), 026801. See pages: [10](#) and [171](#)

- [Büt90] M. Büttiker, *Quantized transmission of a saddle-point constriction*, Phys. Rev. B **41** (1990), 7906–7909. See page: [14](#)
- [CGP⁺08] T.-M. Chen, A. C. Graham, M. Pepper, I. Farrer, and D. A. Ritchie, *Bias-controlled spin polarization in quantum wires*, Applied Physics Letters **93** (2008), no. 3, 032102. See page: [18](#)
- [CGP⁺09] T.-M. Chen, A. C. Graham, M. Pepper, F. Sfigakis, I. Farrer, and D. A. Ritchie, *Odd-even spin effects and variation of g factor in a quasi-one-dimensional subband*, Phys. Rev. B **79** (2009), 081301. See page: [151](#)
- [CLGG⁺02] S. M. Cronenwett, H. J. Lynch, D. Goldhaber-Gordon, L. P. Kouwenhoven, C. M. Marcus, K. Hirose, N. S. Wingreen, and V. Umansky, *Low-temperature fate of the 0.7 structure in a point contact: A kondo-like correlated state in an open system*, Phys. Rev. Lett. **88** (2002), 226805. See pages: [16](#), [17](#), [18](#), and [172](#)
- [CNP⁺06] O. Chiatti, J. T. Nicholls, Y. Y. Proskuryakov, N. Lumpkin, I. Farrer, and D. A. Ritchie, *Quantum thermal conductance of electrons in a one-dimensional wire*, Phys. Rev. Lett. **97** (2006), 056601. See page: [16](#)
- [COK98] Sara M. Cronenwett, Tjerk H. Oosterkamp, and Leo P. Kouwenhoven, *A tunable kondo effect in quantum dots*, Science **281** (1998), no. 5376, 540–544. See page: [23](#)
- [Con68] J.N.L. Connor, *On the semi-classical description of molecular orbiting collisions*, Molecular Physics **15** (1968), no. 6, 621–631. See page: [14](#)
- [dPPBW04] R. de Picciotto, L. N. Pfeiffer, K. W. Baldwin, and K. W. West, *Nonlinear response of a clean one-dimensional wire*, Phys. Rev. Lett. **92** (2004), 036805. See page: [18](#)
- [DZM⁺06] L. DiCarlo, Y. Zhang, D. T. McClure, D. J. Reilly, C. M. Marcus, L. N. Pfeiffer, and K. W. West, *Shot-noise signatures of 0.7 structure and spin in a quantum point contact*, Phys. Rev. Lett. **97** (2006), 036810. See page: [16](#)
- [EHG⁺03] J. M. Elzerman, R. Hanson, J. S. Greidanus, L. H. Willems van Beveren, S. De Franceschi, L. M. K. Vandersypen, S. Tarucha, and L. P. Kouwenhoven, *Few-electron quantum dot circuit with integrated charge read out*, Phys. Rev. B **67** (2003), 161308. See page: [1](#)
- [EHW⁺04] J. M. Elzerman, R. Hanson, L. H. Willems van Beveren, B. Witkamp, L. M. K. Vandersypen, and L. P. Kouwenhoven, *Single-shot read-out of an individual electron spin in a quantum dot*, Nature **430** (2004), no. 6998, 431–435. See page: [1](#)
- [Eis13] Katharina Eissing, *Functional renormalization group applied to a multimode quantum point contact*, Master’s thesis, LMU München, 2013. See page: [78](#)
- [Fes58] Herman Feshbach, *Unified theory of nuclear reactions*, Annals of Physics **5** (1958), no. 4, 357–390. See page: [12](#)
- [FKK⁺12] Alexandra C. Ford, S. Bala Kumar, Rehan Kapadia, Jing Guo, and Ali Javey, *Observation of degenerate one-dimensional sub-bands in cylindrical inas nanowires*, Nano Lett. **12** (2012), no. 3, 1340–1343. See page: [11](#)

- [FPWH98] Stefan Frank, Philippe Poncharal, Z. L. Wang, and Walt A. de Heer, *Carbon nanotube quantum resistors*, *Science* **280** (1998), no. 5370, 1744–1746. See page: [10](#)
- [FSP⁺93] M. Field, C. G. Smith, M. Pepper, D. A. Ritchie, J. E. F. Frost, G. A. C. Jones, and D. G. Hasko, *Measurements of coulomb blockade with a noninvasive voltage probe*, *Phys. Rev. Lett.* **70** (1993), 1311–1314. See page: [1](#)
- [GBHvD14] Olga Goulko, Florian Bauer, Jan Heyder, and Jan von Delft, *Effect of spin-orbit interactions on the 0.7 anomaly in quantum point contacts*, *Phys. Rev. Lett.* **113** (2014), 266402. See pages: [19](#), [20](#), [21](#), and [172](#)
- [GmcUJB09] A. D. Güçlü, C. J. Umrigar, Hong Jiang, and Harold U. Baranger, *Localization in an inhomogeneous quantum wire*, *Phys. Rev. B* **80** (2009), 201302. See page: [22](#)
- [GMP05] I. V. Gornyi, A. D. Mirlin, and D. G. Polyakov, *Interacting electrons in disordered wires: Anderson localization and low- t transport*, *Phys. Rev. Lett.* **95** (2005), 206603. See page: [142](#)
- [GNC⁺10] E. Grémion, D. Niepce, A. Cavanna, U. Gennser, and Y. Jin, *Evidence of a fully ballistic one-dimensional field-effect transistor: Experiment and simulation*, *Applied Physics Letters* **97** (2010), no. 23, 233505. See page: [1](#)
- [GTP⁺03] A. C. Graham, K. J. Thomas, M. Pepper, N. R. Cooper, M. Y. Simmons, and D. A. Ritchie, *Interaction effects at crossings of spin-polarized one-dimensional subbands*, *Phys. Rev. Lett.* **91** (2003), 136404. See pages: [18](#), [19](#), [20](#), [101](#), and [172](#)
- [GTP⁺04] A.C. Graham, K.J. Thomas, M. Pepper, M.Y. Simmons, D.A. Ritchie, K.-F. Berggren, P. Jaksch, A. Debnarova, and I.I. Yakimenko, *0.7 analogue structures and exchange interactions in quantum wires*, *Solid State Communications* **131** (2004), no. 9, 591 – 597, New advances on collective phenomena in one-dimensional systems. See page: [101](#)
- [GUJB09] A. D. Güçlü, C. J. Umrigar, Hong Jiang, and Harold U. Baranger, *Localization in an inhomogeneous quantum wire*, *Phys. Rev. B* **80** (2009), 201302. See page: [1](#)
- [HBS⁺15] Jan Heyder, Florian Bauer, Enrico Schubert, David Borowsky, Dieter Schuh, Werner Wegscheider, Jan von Delft, and Stefan Ludwig, *Relation between the 0.7 anomaly and the kondo effect: Geometric crossover between a quantum point contact and a kondo quantum dot*, *Phys. Rev. B* **92** (2015), 195401. See pages: [2](#), [14](#), and [77](#)
- [HBSvD17] Jan Heyder, Florian Bauer, Dennis Schimmel, and Jan von Delft, *Derivation of oguri’s linear conductance formula for interacting fermions within the keldysh formalism*, *Phys. Rev. B* **96** (2017), 125141. See page: [33](#)
- [HCC⁺18] Sheng-Chin Ho, Heng-Jian Chang, Chia-Hua Chang, Shun-Tsung Lo, Graham Creeth, Sanjeev Kumar, Ian Farrer, David Ritchie, Jonathan Griffiths, Geraint Jones, Michael Pepper, and Tse-Ming Chen, *Imaging the zigzag wigner crystal in confinement-tunable quantum wires*, *Phys. Rev. Lett.* **121** (2018), 106801. See page: [18](#)

- [Hey14] Jan Heyder, *The 0.7 anomaly in quantum point contacts; a microscopic model for the first conductance step*, Ph.D. thesis, Ludwig-Maximilians-Universität München, 2014. See pages: [14](#), [64](#), and [77](#)
- [HPS⁺16] S. Heedt, W. Prost, J. Schubert, D. Grützmacher, and Th. Schäpers, *Ballistic transport and exchange interaction in inas nanowire quantum point contacts*, *Nano Lett.* **16** (2016), no. 5, 3116–3123. See pages: [11](#) and [171](#)
- [IAS⁺98] S. Inouye, M. R. Andrews, J. Stenger, H. J. Miesner, D. M. Stamper-Kurn, and W. Ketterle, *Observation of feshbach resonances in a bose–einstein condensate*, *Nature* **392** (1998), no. 6672, 151–154. See page: [12](#)
- [Iij91] Sumio Iijima, *Helical microtubules of graphitic carbon*, *Nature* **354** (1991), no. 6348, 56–58. See page: [10](#)
- [ILK⁺13] M. J. Iqbal, Roi Levy, E. J. Koop, J. B. Dekker, J. P. de Jong, J. H. M. van der Velde, D. Reuter, A. D. Wieck, Ramón Aguado, Yigal Meir, and C. H. van der Wal, *Odd and even kondo effects from emergent localization in quantum point contacts*, *Nature* **501** (2013), no. 7465, 79–83. See pages: [1](#), [5](#), [6](#), [16](#), [18](#), and [171](#)
- [IZ07] S. Ihnatsenka and I. V. Zozoulenko, *Conductance of a quantum point contact based on spin-density-functional theory*, *Phys. Rev. B* **76** (2007), 045338. See page: [1](#)
- [IZ09] ———, *Origin of the “0.25 anomaly” in the nonlinear conductance of a quantum point contact*, *Phys. Rev. B* **79** (2009), 235313. See page: [18](#)
- [Jak09] Severin Jakobs, *Functional renormalization group studies of quantum transport through mesoscopic systems*, Ph.D. thesis, RWTH Aachen, 2009. See pages: [27](#), [33](#), [34](#), [36](#), [37](#), [40](#), [41](#), [44](#), [45](#), [46](#), [48](#), [49](#), [50](#), [51](#), [54](#), [65](#), and [111](#)
- [Kar06] Christoph Karrasch, *Transport through correlated quantum dots - a functional rg approach*, PhD thesis, RWTH Aachen (2006). See pages: [35](#), [36](#), [51](#), and [64](#)
- [Kar10] ———, *The functional renormalization group for zero-dimensional quantum systems in and out of equilibrium*, Ph.D. thesis, RWTH Aachen, 2010. See pages: [27](#), [33](#), [34](#), and [48](#)
- [KBH⁺00] A. Kristensen, H. Bruus, A. E. Hansen, J. B. Jensen, P. E. Lindelof, C. J. Markckmann, J. Nygård, C. B. Sørensen, F. Beuscher, A. Forchel, and M. Michel, *Bias and temperature dependence of the 0.7 conductance anomaly in quantum point contacts*, *Phys. Rev. B* **62** (2000), 10950–10957. See page: [16](#)
- [KCL⁺16] Minsoo Kim, Ji-Hae Choi, Sang-Hoon Lee, Kenji Watanabe, Takashi Taniguchi, Seung-Hoon Jhi, and Hu-Jong Lee, *Valley-symmetry-preserved transport in ballistic graphene with gate-defined carrier guiding*, *Nature Physics* **12** (2016), no. 11, 1022–1026. See pages: [10](#) and [171](#)
- [KEB17] Sebastian Krinner, Tilman Esslinger, and Jean-Philippe Brantut, *Two-terminal transport measurements with cold atoms*, *Journal of Physics: Condensed Matter* **29** (2017), no. 34, 343003. See pages: [12](#) and [13](#)

- [KHP⁺08] C Karrasch, R Hedden, R Peters, Th Pruschke, K Schönhammer, and V Meden, *A finite-frequency functional renormalization group approach to the single impurity anderson model*, Journal of Physics: Condensed Matter **20** (2008), no. 34, 345205. See page: [53](#)
- [KLH⁺16] Sebastian Krinner, Martin Lebrat, Dominik Husmann, Charles Grenier, Jean-Philippe Brantut, and Tilman Esslinger, *Mapping out spin and particle conductances in a quantum point contact*, Proceedings of the National Academy of Sciences **113** (2016), no. 29, 8144–8149. See page: [13](#)
- [KOS⁺15] Minoru Kawamura, Keiji Ono, Peter Stano, Kimitoshi Kono, and Tomosuke Aono, *Electronic magnetization of a quantum point contact measured by nuclear magnetic resonance*, Phys. Rev. Lett. **115** (2015), 036601. See page: [23](#)
- [KRA⁺08] H. Kothari, A. Ramamoorthy, R. Akis, S. M. Goodnick, D. K. Ferry, J. L. Reno, and J. P. Bird, *Linear and nonlinear conductance of ballistic quantum wires with hybrid confinement*, Journal of Applied Physics **103** (2008), no. 1, 013701. See page: [18](#)
- [KSH⁺14] Sebastian Krinner, David Stadler, Dominik Husmann, Jean-Philippe Brantut, and Tilman Esslinger, *Observation of quantized conductance in neutral matter*, Nature **517** (2014), 64–. See pages: [11](#), [12](#), and [172](#)
- [Kub57] Ryogo Kubo, *Statistical-mechanical theory of irreversible processes. i. general theory and simple applications to magnetic and conduction problems*, Journal of the Physical Society of Japan **12** (1957), no. 6, 570–586. See page: [44](#)
- [Kub66] R Kubo, *The fluctuation-dissipation theorem*, Reports on Progress in Physics **29** (1966), no. 1, 255–284. See page: [44](#)
- [KvD18a] Fabian B Kugler and Jan von Delft, *Derivation of exact flow equations from the self-consistent parquet relations*, New Journal of Physics **20** (2018), no. 12, 123029. See pages: [48](#), [78](#), [111](#), [141](#), [149](#), and [151](#)
- [KvD18b] Fabian B. Kugler and Jan von Delft, *Multiloop functional renormalization group for general models*, Phys. Rev. B **97** (2018), 035162. See pages: [48](#), [78](#), [111](#), [141](#), [149](#), and [151](#)
- [KvD18c] ———, *Multiloop functional renormalization group that sums up all parquet diagrams*, Phys. Rev. Lett. **120** (2018), 057403. See pages: [48](#), [78](#), [111](#), [141](#), [149](#), and [151](#)
- [KvRF⁺95] J. M. Krans, J. M. van Ruitenbeek, V. V. Fisun, I. K. Yanson, and L. J. de Jongh, *The signature of conductance quantization in metallic point contacts*, Nature **375** (1995), no. 6534, 767–769. See pages: [7](#), [8](#), and [171](#)
- [Lan57] R. Landauer, *Spatial variation of currents and fields due to localized scatterers in metallic conduction*, IBM Journal of Research and Development **1** (1957), no. 3, 223–231. See pages: [5](#) and [13](#)
- [LD98] Daniel Loss and David P. DiVincenzo, *Quantum computation with quantum dots*, Phys. Rev. A **57** (1998), 120–126. See page: [1](#)

- [LMS⁺09] A M Lunde, A De Martino, A Schulz, R Egger, and K Flensberg, *Electron–electron interaction effects in quantum point contacts*, New Journal of Physics **11** (2009), no. 2, 023031. See pages: [1](#), [22](#), and [23](#)
- [LXT⁺05] Wei Lu, Jie Xiang, Brian P. Timko, Yue Wu, and Charles M. Lieber, *One-dimensional hole gas in germanium/silicon nanowire heterostructures*, Proceedings of the National Academy of Sciences **102** (2005), no. 29, 10046–10051. See pages: [11](#) and [171](#)
- [Mat04] K. A. Matveev, *Conductance of a quantum wire at low electron density*, Phys. Rev. B **70** (2004), 245319. See pages: [1](#) and [22](#)
- [MHW02] Yigal Meir, Kenji Hirose, and Ned S. Wingreen, *Kondo model for the “0.7 anomaly” in transport through a quantum point contact*, Phys. Rev. Lett. **89** (2002), 196802. See pages: [1](#), [22](#), and [23](#)
- [Mic11] A P Micolich, *What lurks below the last plateau: experimental studies of the $0.7 \times 2e^2/h$ conductance anomaly in one-dimensional systems*, Journal of Physics: Condensed Matter **23** (2011), no. 44, 443201. See pages: [1](#) and [16](#)
- [MML07] Julia S. Meyer, K. A. Matveev, and A. I. Larkin, *Transition from a one-dimensional to a quasi-one-dimensional state in interacting quantum wires*, Phys. Rev. Lett. **98** (2007), 126404. See page: [18](#)
- [MnRJFRP06] F. Muñoz Rojas, D. Jacob, J. Fernández-Rossier, and J. J. Palacios, *Coherent transport in graphene nanoconstrictions*, Phys. Rev. B **74** (2006), 195417. See page: [8](#)
- [Moo65] Gordon E. Moore, *Cramming more components onto integrated circuits*, Electronics (1965). See page: [1](#)
- [Mor94] Tim R. Morris, *The exact renormalization group and approximate solutions*, International Journal of Modern Physics A **09** (1994), no. 14, 2411–2449. See page: [49](#)
- [MS59] Paul C. Martin and Julian Schwinger, *Theory of many-particle systems. i*, Phys. Rev. **115** (1959), 1342–1373. See page: [44](#)
- [MSH⁺12] Walter Metzner, Manfred Salmhofer, Carsten Honerkamp, Volker Meden, and Kurt Schönhammer, *Functional renormalization group approach to correlated fermion systems*, Rev. Mod. Phys. **84** (2012), 299–352. See page: [47](#)
- [MSMK18] L. Markhof, B. Sbierski, V. Meden, and C. Karrasch, *Detecting phases in one-dimensional many-fermion systems with the functional renormalization group*, Phys. Rev. B **97** (2018), 235126. See pages: [2](#) and [78](#)
- [NFDD96] Kyoko Nakada, Mitsutaka Fujita, Gene Dresselhaus, and Mildred S. Dresselhaus, *Edge state in graphene ribbons: Nanometer size effect and edge shape dependence*, Phys. Rev. B **54** (1996), 17954–17961. See page: [8](#)
- [NGM⁺04] K. S. Novoselov, A. K. Geim, S. V. Morozov, D. Jiang, Y. Zhang, S. V. Dubonos, I. V. Grigorieva, and A. A. Firsov, *Electric field effect in atomically thin carbon films*, Science **306** (2004), no. 5696, 666–669. See page: [8](#)

- [NM19] Engineering National Academies of Sciences and Medicine, *Quantum computing: Progress and prospects*, The National Academies Press, Washington, DC, 2019. See page: [1](#)
- [PCG06] N. M. R. Peres, A. H. Castro Neto, and F. Guinea, *Conductance quantization in mesoscopic graphene*, Phys. Rev. B **73** (2006), 195411. See page: [8](#)
- [PJT⁺05] J. R. Petta, A. C. Johnson, J. M. Taylor, E. A. Laird, A. Yacoby, M. D. Lukin, C. M. Marcus, M. P. Hanson, and A. C. Gossard, *Coherent manipulation of coupled electron spins in semiconductor quantum dots*, Science **309** (2005), no. 5744, 2180–2184. See page: [1](#)
- [PNMM⁺91] N. K. Patel, J. T. Nicholls, L. Martn-Moreno, M. Pepper, J. E. F. Frost, D. A. Ritchie, and G. A. C. Jones, *Evolution of half plateaus as a function of electric field in a ballistic quasi-one-dimensional constriction*, Phys. Rev. B **44** (1991), 13549–13555. See page: [18](#)
- [Rei05] D. J. Reilly, *Phenomenological model for the 0.7 conductance feature in quantum wires*, Phys. Rev. B **72** (2005), 033309. See pages: [1](#) and [22](#)
- [RM06] Tomaž Rejec and Yigal Meir, *Magnetic impurity formation in quantum point contacts*, Nature **442** (2006), no. 7105, 900–903. See pages: [1](#), [22](#), and [23](#)
- [RSG⁺04] P. Roche, J. Ségala, D. C. Glattli, J. T. Nicholls, M. Pepper, A. C. Graham, K. J. Thomas, M. Y. Simmons, and D. A. Ritchie, *Fano factor reduction on the 0.7 conductance structure of a ballistic one-dimensional wire*, Phys. Rev. Lett. **93** (2004), 116602. See page: [16](#)
- [RYF⁺10] Y. Ren, W. W. Yu, S. M. Frolov, J. A. Folk, and W. Wegscheider, *Zero-bias anomaly of quantum point contacts in the low-conductance limit*, Phys. Rev. B **82** (2010), 045313. See page: [18](#)
- [SBvD17] Dennis H. Schimmel, Benedikt Bruognolo, and Jan von Delft, *Spin fluctuations in the 0.7 anomaly in quantum point contacts*, Phys. Rev. Lett. **119** (2017), 196401. See pages: [1](#), [2](#), [3](#), [22](#), [25](#), [33](#), [53](#), [111](#), and [143](#)
- [Sch93] H. J. Schulz, *Wigner crystal in one dimension*, Phys. Rev. Lett. **71** (1993), 1864–1867. See page: [22](#)
- [Sch17] Dennis H. Schimmel, *Transport through inhomogeneous interacting low-dimensional systems*, Ph.D. thesis, Ludwig-Maximilians-Universität München, 2017. See pages: [3](#), [14](#), [18](#), [37](#), [49](#), [50](#), [70](#), [72](#), [111](#), and [143](#)
- [SDG⁺79] H.L. Störmer, R. Dingle, A.C. Gossard, W. Wiegmann, and M.D. Sturge, *Two-dimensional electron gas at a semiconductor-semiconductor interface*, Solid State Communications **29** (1979), no. 10, 705–709. See page: [5](#)
- [SK17] Björn Sbierski and Christoph Karrasch, *Second-order functional renormalization group approach to one-dimensional systems in real and momentum space*, Phys. Rev. B **96** (2017), 235122. See page: [78](#)
- [SMS08] C. Sloggett, A. I. Milstein, and O. P. Sushkov, *Correlated electron current and temperature dependence of the conductance of a quantum point contact*, The European Physical Journal B **61** (2008), no. 4, 427–432. See pages: [1](#), [22](#), and [23](#)

- [SYB03] Anton A. Starikov, Irina I. Yakimenko, and Karl-Fredrik Berggren, *Scenario for the 0.7-conductance anomaly in quantum point contacts*, Phys. Rev. B **67** (2003), 235319. See pages: [22](#) and [23](#)
- [TD94] Weidong Tian and Supriyo Datta, *Aharonov-bohm-type effect in graphene tubules: A landauer approach*, Phys. Rev. B **49** (1994), 5097–5100. See page: [10](#)
- [TNS⁺96] K. J. Thomas, J. T. Nicholls, M. Y. Simmons, M. Pepper, D. R. Mace, and D. A. Ritchie, *Possible spin polarization in a one-dimensional electron gas*, Phys. Rev. Lett. **77** (1996), 135–138. See pages: [7](#), [15](#), [16](#), [22](#), and [171](#)
- [TVJ⁺11] Nikolaos Tombros, Alina Veligura, Juliane Junesch, Marcos H. D. Guimarães, Ivan J. Vera-Marun, Harry T. Jonkman, and Bart J. van Wees, *Quantized conductance of a suspended graphene nanoconstriction*, Nature Physics **7** (2011), 697–. See pages: [8](#), [9](#), [10](#), and [171](#)
- [vWvHB⁺88] B. J. van Wees, H. van Houten, C. W. J. Beenakker, J. G. Williamson, L. P. Kouwenhoven, D. van der Marel, and C. T. Foxon, *Quantized conductance of point contacts in a two-dimensional electron gas*, Phys. Rev. Lett. **60** (1988), 848–850. See pages: [5](#), [6](#), [7](#), [13](#), and [171](#)
- [Wak01] Katsunori Wakabayashi, *Electronic transport properties of nanographite ribbon junctions*, Phys. Rev. B **64** (2001), 125428. See page: [8](#)
- [Wel05] H. Arthur Weldon, *Thermal four-point functions with analytic extensions*, Phys. Rev. D **72** (2005), 096005. See page: [46](#)
- [Wet93] Christof Wetterich, *Exact evolution equation for the effective potential*, Physics Letters B **301** (1993), no. 1, 90 – 94. See page: [47](#)
- [YKT⁺17] Chengyu Yan, Sanjeev Kumar, Kalarikad Thomas, Michael Pepper, Patrick See, Ian Farrer, David Ritchie, J. P. Griffiths, and G. A. C. Jones, *Direct observation of exchange-driven spin interactions in one-dimensional system*, Applied Physics Letters **111** (2017), no. 4, 042107. See page: [13](#)
- [YKT⁺18] C Yan, S Kumar, K Thomas, P See, I Farrer, D Ritchie, J Griffiths, G Jones, and M Pepper, *Engineering the spin polarization of one-dimensional electrons*, Journal of Physics: Condensed Matter **30** (2018), no. 8, 08LT01. See pages: [1](#), [2](#), [10](#), [21](#), [22](#), [151](#), and [172](#)